YEARBOOK

2024

INSTITUTE OF TECHNICAL PHYSICS AND MATERIALS SCIENCE
HUN-REN CENTRE FOR ENERGY RESEARCH
PART OF THE HUNGARIAN RESEARCH NETWORK

http://www.mfa.kfki.hu/

Published by the
Institute of Technical Physics and Materials Science
HUN-REN Centre for Energy Research
Part of the Hungarian Research Network

HUN-REN EK MFA Yearbook 2024

Director: Prof. Béla Pécz, corr. member of HAS

Address: Konkoly-Thege Miklós út 29-33, H-1121 Budapest, Hungary
Postal: P.O.Box 49, H-1525 Budapest, Hungary
Phone: +36-1-392 2224
E-mail: info@mfa.kfki.hu
URL: http://www.mfa.kfki.hu/
Editor: Krisztina Szakolczai, Ph.D.
Published by: HUN-REN EK MFA, Budapest, Hungary, 2025.

TABLE OF CONTENTS

GENERAL INFORMATION

Director's foreword

As the director of MFA, it is my pleasure to welcome the reader. I recommend browsing the present yearbook which continues the series of the former ones and contains results achieved in 2024.

In that year our headquarter of HUN-REN, i.e. Hungarian Research Network, organized an assessment with a broad international committee composed from distinguished scientist from disciplines which fit to the subject of our research centre. We had to submit them a self assessment, i.e. a long description of our activity including the history of our institute and give a lot of data on our publication, collected independent citations, international research cooperation. We had to provide specific data on homeland cooperation and even on common jobs within our HUN-REN network members. Foreign institutions with similar research activity were also named for benchmarking purposes. During the personnel visit we learned each other and we tried to give appropriate answers for the questions of the committee members. All of these gave us a lot of work, however, I believe it was very useful for us as we had to sum up the results we achieved and think over our strategic goals as well. Later when we receive the written opinion and suggestions of the committee we accepted their suggestions and answered their further questions.

After this we were involved into the planned transition of our research network, which however, will be realized in 2025. The same is true for raising the salaries of our colleagues, we have a good hope and a promise to get that in 2025. This is essential to keep our team and to be able to attract new young researchers.

It was a pleasure for us to receive more foreign researchers than before including PhD students from Italy and Spain, but also one senior researcher from Jülich Forschungszentrum, Germany.

Unfortunately, we lost some of our colleagues: Dr. Gábor Vértessy (who died at the very end of 2023) and István Borsos, whom we lost in 2024 December both of them happened very suddenly and not expected although we knew that they were ill - the loss is very painful for us.

We could modernize the electrical network of our clean room facility and later we were very happy to learn that by an application they also get the Outstanding research facility Hungary title. By now we run two of them: Micro and Nanotechnology Research Laboratory and Aberration corrected transmission electron microscopy Laboratory.

Between September 1 and 4, 2024, the 36th EUROSENSORS Conference was held in Debrecen. The conference was co-organized by our institute, under the co-chairmanship of Dr. Gábor Battistig (Scientific Advisor at the Nano-sensors Laboratory of HUN-REN EK MFA and Head of the Department of Electrical Engineering at the Faculty of Science and Technology, University of Debrecen) and Dr. Péter Fürjes (Head of the Microsystems Laboratory of HUN-REN EK MFA), with the University of Debrecen providing the venue. Nearly 300 researchers attended the conference to discuss leading topics in materials science and technology, as well as sensor research, with a particular focus on physical, chemical, and biomedical sensors and their integration challenges. Accompanying events included more than 120 posters, industry exhibition stands, and a mini photo exhibition showcasing sensors developed by HUN-REN EK MFA. At the HUN-REN EK MFA booth, visitors had the opportunity to view and test prototypes of the latest sensors developed in the Microsystems and Nano-sensors Laboratories. These results are related to the recently completed Moore4Medical project, as well as to our ongoing projects TKP2021-EGA-04, TKP2021-NVA-03, and UNLOOC. https://akcongress.com/eurosensors/

Another international event the 14th International Conference on Ceramic Materials and Components for Energy and Environmental Systems (CMCEE14) was held in Budapest, between 18-22 August 2024 - truly one of the most important world ceramic events organized by our colleagues.

https://akcongress.com/cmcee14/ This year there were closely 550 participants from more than 35 countries. The extensive scientific program consisted of 4 plenary lectures, 42 keynote, 215 invited and 160 oral presentations divided into 9 parallel sessions. 42 posters have been presented in digital poster sessions.

The World Academy of Ceramics (WAC) induction ceremony took place on August 19 where newly elected Academicians were presented and awarded with the WAC Diploma: www.waceramics.org I was very happy to learn that our Dr. Katalin Balázsi received the academic title from the World Academy of Ceramic for her outstanding contributions to ceramic science for biomedical applications, international collaborations and promotion of under-represented groups.

Although the R&D spending in Hungary was not increased in 2024, thanks to our projects we gained before, we could work without any big obstacles. Furthermore, an Excellence and a Starting Grant form the Hungarian Research office was gained by colleagues. We learned that also the HCHIP project will start in 2025 providing good research and development opportunity for two of our research groups.

In 2024 some of our colleagues achieved successful scientific qualification. Levente Tapasztó got the Prize of the Hungarian Academy of Sciences, and we had also three successful PhD candidates, namely: Péter Kun, Timea Török, Géza Szántó, we are very proud of them and congratulate to the supervisors as well. Ildikó Cora and Zsolt Fogarassy successfully fulfilled a habilitation process and became senior research fellow. Our post-doc colleague, Marcell Gajdics gained the Outstanding Young researcher award of the Hungarian Academy of Sciences. MFA could continue to pay publication award for the young authors of the best publications.

We are also proud of the scientific results achieved by our colleagues, I hope you will enjoy learning them in this book. Here I note that the former MFA Yearbooks are available electronically at http://www.mfa.kfki.hu/hu/yearbook.

Prof. Béla Pécz
Director

Organizational structure

Director: Prof. Béla Pécz

Scientific departments	
Thin Film Physics Department	Katalin BALÁZSI, Ph.D.
Complex Systems Department	Géza ÓDOR, D.Sc.
Photonics Department	Péter PETRIK, D.Sc.
Nanobiosensorics Department	Róbert HORVÁTH, Ph.D.
Microsystems Department	Péter FÜRJES, Ph.D.
Nanosensorics Department	János VOLK, Ph.D.
Nanostructures Department and "Lendület" group - 2D Materials	Levente TAPASZTÓ, D.Sc.
"Lendület" group - Topological Nanostructures	Péter NEMES-INCZE, Ph.D.

Directly supervised functions	
Head of Scientific Advisory Council	Levente TAPASZTÓ, D.Sc.
Scientific secretary, projects and PR	Krisztina SZAKOLCZAI, Ph.D.
Quality control, patents, MTMT, REAL admin	Andrea BOLGÁR
Technical support	Károly BODNÁR
Financial administration	Zsuzsanna KELEMEN
Innovation manager, patents	Valéria OSVÁTH
Technology transfer (IPR)	Antal GASPARICS, Ph.D.

Infrastructure

Excellent Research Infrastructures

The Thin Film Physics Department is strong at national and even international level at transmission electron microscopy (TEM), what they use in order to determine relationships between the microstructure and other physical properties. They main facility the Aberration Corrected Transmission Electron Microscope Laboratory was selected as Excellent Research Infrastructure by the National Research and Innovation Office.

The Microsystems and Nanosensors Laboratories run a unique semiconductor manufacturing facility in Hungary comprising two clean labs (300 m2 + 160 m2 – Class 100-10000) with complete Si-CMOS technology line together with a mask shop, the only complete Si CMOS technology. The laboratory was also selected as Excellent Research Infrastructure by the National Research and Innovation Office.

Nondestructive characterization Laboratory:

The Institute of Technical Physics and Materials Science of the Centre for Energy has decades of experience in non-destructive testing certified according to the ISO 9001: 2009 quality assurance system.

Material characterization methods offered for external users and partners: Non-destructive optical and magnetic measurement of surface nanostructures and materials including: spectroscopy; magnetic material testing; biosensors; curvature of surfaces; surface contamination and quality; water pollution tests

Sample properties to characterize:

- layer thickness (0.5-1000 nm);
- optical refractive index (accuracy: ~ 0.001);
- homogeneity;
- quality of interfaces;
- porosity (e.g., voids content in the porous layer);
- surface nanoroughness;
- layer composition in some cases (e.g., Si nanoparticle content in silica);
- measurement of carbon phases;
- crystallinity (lattice disorder of single crystals, disintegration);
- brittleness and material properties of steel structures
- crystal and band structure of semiconductors

Other main facilities and equipments:

- Electron Microscopy, Auger and Scanning Probe Lab
- Thin film, Surface Physics and Structures
- Ion Implantation and Ion Beam Analysis
- Semiconductor Lasers and different LPE Techniques
- Porous silicon preparation and studies
- Carbon nanotubes, preparation and studies
- Ceramics, high pressure, high temperature press, refractory metals

Excellent Research Infrastucture - Aberration Corrected Transmission Electron Microscope Laboratory

Description of the RI:
New generation of aberration corrected electron microscope, the open laboratory of the Hungarian Materials Science. Sub-nanometer resolution in TEM imaging providing atomic arrangement and analytical (EDS) information on a few nanometer scale with the four EDS detectors built into the column. Elemental maps can be taken by EDS. Heating holder (with precise MEMS chip) and study of reactions inside the microscope. Helping the university teaching and partner in industrial development.

Activities and Services:
Research of thin films exploring the growth mechanism and properties. Materials science analysis using transmission electron microscopy (TEM). Sample preparation, atomic resolution images with a resolution below 0.1 nm in TEM mode thanks to the spherical aberration corrector built in. Several detectors in Scanning Transmission Electron Microscopy mode for example giving images in which the contrast is proportional with the (square) atomic number. Preparation of elemental maps taken by EDS detector based on characteristic X-Ray lines. Plan view and Cross sectional specimens, depth profiling. Determination of phases, failure analysis. Investigation of semiconductors, metals, insulators and alloys.

Specification:
FEI Titan THEMIS 200 200 kV aberration corrected TEM/STEM microscope with image corrector
STEM modes: BF, DF, HAADF images
4 SDD EDS detectors built into the column
Image corrector energy spread: 0.8EV, information limit: 90pm, STEM resolution 164pm
Specimen tilting in double tilt analytical holder: X direction ± 35o, Y direction ±30o.
Field emission gun
CETA 16M camera

Excellent Research Infrastucture - Microsystems and Nanosensors Laboratories

Description of the RI:
The main tasks of the Departments and the RI are the research and development of physical, chemical/biochemical sensors and integrated systems:

- Si Microtechnology with special emphasis on development of MEMS devices and related technologies, materials, structural and functional characterizations.
- Development and fabrication of microfluidic systems, their application in new fields of medical diagnostics and lab-on-a-chip systems – BioMEMS.
- Sensor development with special emphasis on autonomous sensor systems, physical, chemical, mechanical, opical and thermal microsensors – MEMS.
- Development of semiconductor nanodevices, the sythesis and charactirization of quasi-one-dimensional semiconducting nanostrucrures, their integratation into functional sensoric, optoelectronic and photovoltaic devices – NEMS.
- Development and small scale production of NIR LEDs of unique physical parameters

Activities and Services:
The Department runs two clean labs (300 m2 + 160 m2 – Class 100-10000) comprising a complete Si-CMOS processing line and a mask shop, unique facility in Hungary. The technology allows to manufacture layers, patterned structures and devices with line resolution of 1 μm by optical and down to ≈10 nm by e-beam lithography on 3" and 4" Si and glass wafers. Competences available as service for partners:

- High temperature annealing, diffusion and oxidation; Rapid Thermal Treatment;
- Low Pressure Chemical Vapour Deposition of poly-Si, SiO2 and Si3N4 layers;
- Low Temperature Chemical Vapour Deposition;
- Plasma Enhanced Atomic Layer Deposition;
- Physical Thin Film Depositions – Electron beam evaporation, DC and RF Sputtering;
- Ion implantation;
- Reactive Ion Etching, Deep Reactive Ion Etching;
- Photolithography with back-side alignment and Nanoimprinting;
- E-beam lithography;
- Nanopatterning, deposition and etching by Focused Ion-Beam;
- Wafer-bonding;
- Wet chemical treatments;
- Electro-chemical porous Si formation;
- Liquid Phase Epitaxy of III-V compound semiconductors;
- Mask design, laser pattern generator;
- Polymer (PDMS, SU8, Polyimide) structuring by photolithography and micro-molding techniques,
- Chip dicing, packaging especially for sensor applications;
- Materials and structural analysis & characterization:, SEM, FIB, EDX, Atomic Force Microscopy, Electrochemical Impedance Spectroscopy, Stylus Profiler;
- Electrical and functional modelling and characterization.

Key Figures of MFA

You can follow the budget of MFA in the last 20 years in the chart below. Basic subsidy is growing slightly, but far from following inflation. The periodicity of large calls for tenders - eg. EU grants and domestic innovation grants from different ministrys- can be observed in the evolution of the institute's budget. These have major effect on our everyday life. Fortunatelly the last few years were successful in terms of grant applications. Three Thematei Excellence Programmes (TKP2021) projects have started in the beginning of 2022 and last till the end of 2025. The government supports our research in ceramics, dedicated for the chips industry (CHIPCER). Also the EU Key Digital Technology project, the ECSEL JU project, MSCA fellowships, and a Pathfinder project, together with ERA-NET grants provided international visibility and utilization of the results. These grants gave legal stability for major research lines in our laboratories for 3-4 years, however, the prefinancing from the Hungarian grant office (NKFIH) stopped for the large projects, which causes noticable cashflow issues.

MFA budget 2003-2024 (million HUF)

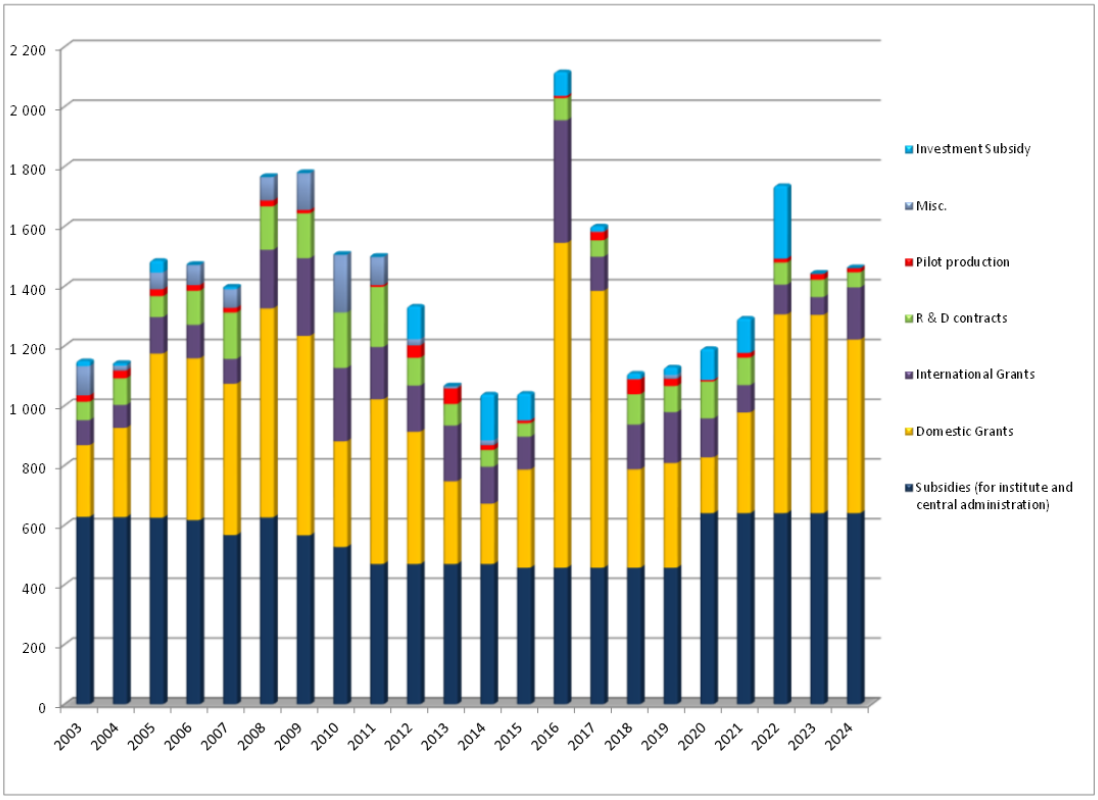

According to the Thomson-Reuters ISI "Web of Knowledge", and MTMT2 databases, the Institute has an average publication activity of ca. 120 scientific papers in IF journals a year (link). Recently MFA researchers tend to publish in journals with higher IF and the number of citations are constantly increasing. The total IF in 2024 was approx 610, the independent citations are over 7200.

MFA and its predecessor's publications and citations per year since 1998

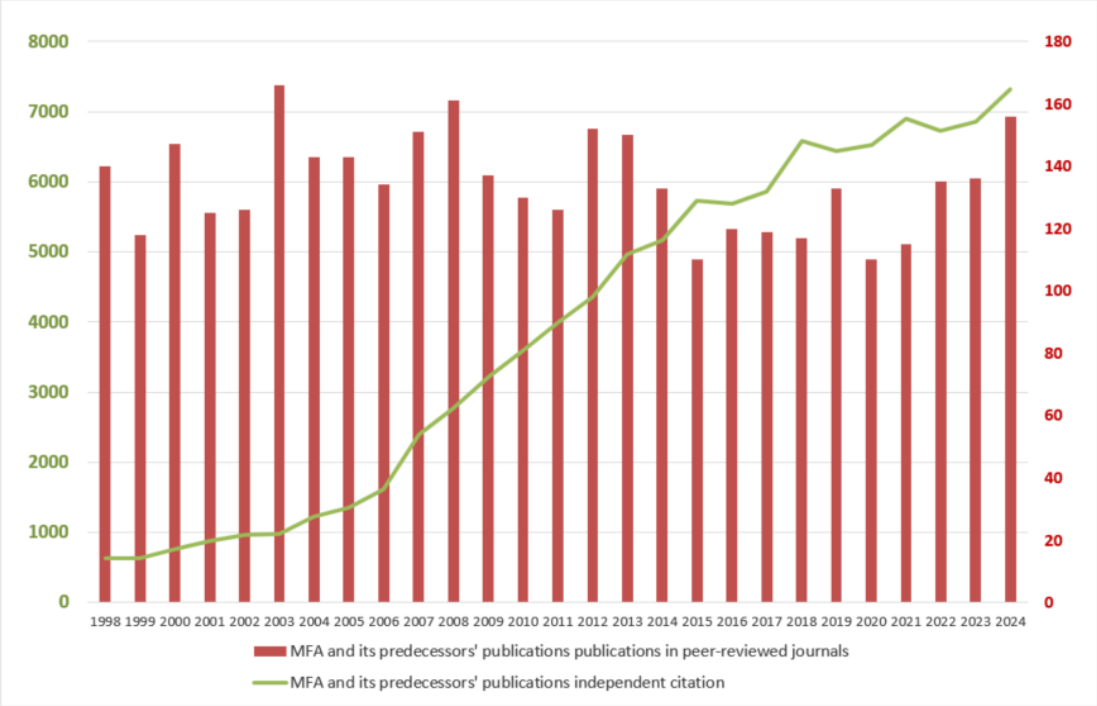

Prizes and Distinctions

	Levente TAPASZTÓ	Prize of the Hungarian Academy of Sciences
	Katalin BALÁZS	Academic title from the World Academy of Ceramic
	Marcell GAJDICS	Young researcher award of the Hungarian Academy of Sciences
	Inna SZÉKÁCS	MFA postdoc researchers prize
	András PÁLINKÁS	MFA postdoc researchers prize
	Antal GASPARICS	MFA prize for excellent research support
	János FERENCZ	MFA prize for excellent research support

Lilia BATÓ — MFA young researchers prize

György KÁLVIN — E-MRS Young researcher award

Highlights of the year

The participants of the 14th International Conference on Ceramic Materials and Components for Energy and Environmental Systems (CMCEE14), Budapest

The participants of the 36th EUROSENSORS Conference, Debrecen

Dr. Katalin Balázsi received the academic title from the World Academy of Ceramic (August 19, 2024)

Dr. Levente Tapasztó got the Prize of the Hungarian Academy of Sciences

György Kálvin receives the E-MRS Young researcher award

The Ultrabalaton trail running competition was completed by 2 teams and 10 members of the Microsystems and Nanosensors Laboratory

SCIENTIFIC REPORTS

Nanostructures Department

Head: Dr. Levente TAPASZTÓ, D.Sc., research advisor

Research Staff:

Prof. László Péter BIRÓ, Member of the HAS
Zsolt Endre HORVÁTH, D.Sc., Deputy Head of Laboratory
Mátyás DABÓCZI, Ph.D.
Gergely DOBRIK, Ph.D.
Krisztián KERTÉSZ, Ph.D.
Antal Adolf KOÓS, Ph.D.
Péter KUN, Ph.D.
Géza István MÁRK, Ph.D.
Péter NEMES-INCZE, Ph.D.
Zoltán OSVÁTH, Ph.D.
András PÁLINKÁS, Ph.D.
Gábor PISZTER, Ph.D.
Péter SÜLE, Ph.D.
Zoltán TAJKOV, Ph.D.
Péter VANCSÓ, Ph.D.

Students:

Konrád KANDRAI, Ph.D. student
Soma KESZEI, Ph.D. student
Krisztián MÁRITY, Ph.D. student
Márton SZENDRŐ, Ph.D. student
György KÁLVIN, Ph.D. student

The research activity of the Nanostructures Laboratory is based on the two-decade-long expertise in the synthesis, characterization and engineering of various nanostructures using scanning probe microscopy as the main experimental technique. Since more than a decade, our research efforts are focused on the investigation of two-dimensional materials. Besides graphene, in the last couple of years, novel 2D materials, mainly form the family of transition metal chalcogenides (TMC) have been intensely studied. Recently, we have further extended our activity with the investigation of layered topological insulator crystals. We have also successfully continued our research on bioinspired photonic nanoarchitectures.

Mapping all possible graphene stacking configurations by electronic Raman scattering

TKP2021-NKTA-05, Élvonal KKP 138144, Lendület LP2024-17, NKFIH K 146156, PD 146479, FK 142985, 2022-1.2.5-TÉT-IPARI-KR

A. Pálinkás, Z. Tajkov, K. Márity, P. Vancsó, L. Tapasztó, and P. Nemes-Incze

After the isolation of monolayers of 2D materials, it was apparent that the stacking order of the subsequent layers can be tuned as a new degree of freedom to engineer the crystal's physical properties. In natural graphite, the great majority of the layers are in hexagonal stacking, aka. ABAB sequence, and the ABC ordering, the rhombohedral phase only came up as stacking faults (Figure 1.1.a). This unusual stacking has gained prominence recently, as in thin layers with rhombohedral ordering superconductive, magnetic and Chern-insulating phases have been found. Importantly, this rhombohedral ordering is far more robust for exploring correlated phases, than the twisted graphene layers owing to the lack of twist angle inhomogeneity. Moreover, some combinations of partly rhombohedral and partly hexagonal ordered stacking sequences (as an example see Figure 1.1.c) are weak ferroelectric materials.

Beyond the defect free hexagonal and rhombohedral stackings there is an exponentially increasing number stacking configurations, which are yet to be explored. To explore the correlated electronic phenomena in these stackings of graphite first and foremost we need to be able to identify them. Until now there were no fast and reliable methods to exactly determine a given sample ordering of 5+ layers. Last year, we showed the electronic Raman scattering (ERS) can be used to directly identify defect free rhombohedral graphite (RG) from 3 to 12 layers, and beyond [Ref.1.1.].

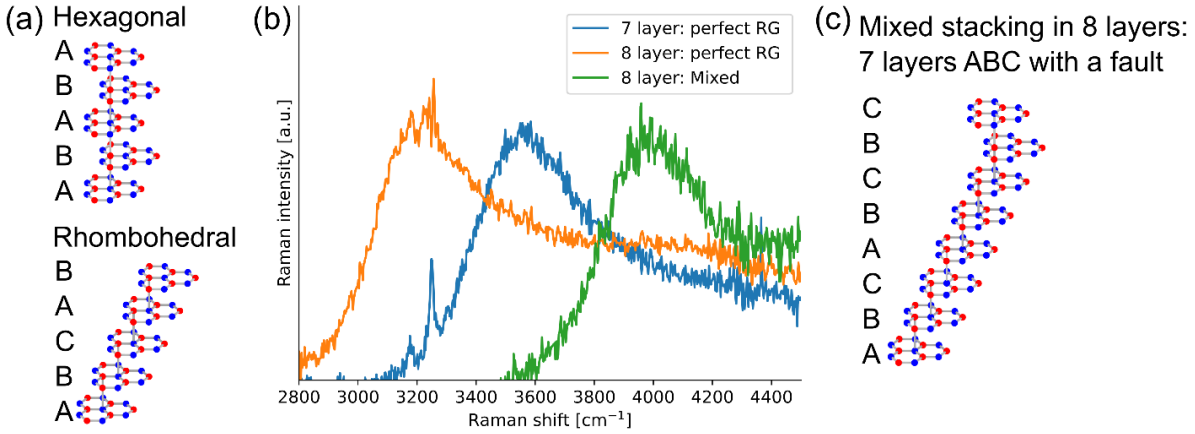

Figure 1.1 (a) Schematic structure of the perfect hexagonal and rhombohedral stackings of 5 layer graphite. (b) ERS signal of perfect rhombohedral 8 (orange) and 7 (blue) layers, and a mixed stacking (green) in an 8-layer thick stack. The first order peak in the ERS signal is at 3328, 3586 and 4005 cm^{-1}, respectively. (c) Structure of the identified mixed stacking, green ERS signal on (b).

This year we started to extend this method to every possible (mixed) configuration by predicting their ERS peaks by tight-binding calculations. We successfully identified various mixed stackings experimentally. This is particularly challenging because the number of possible stacking configurations grows exponentially with layer number.

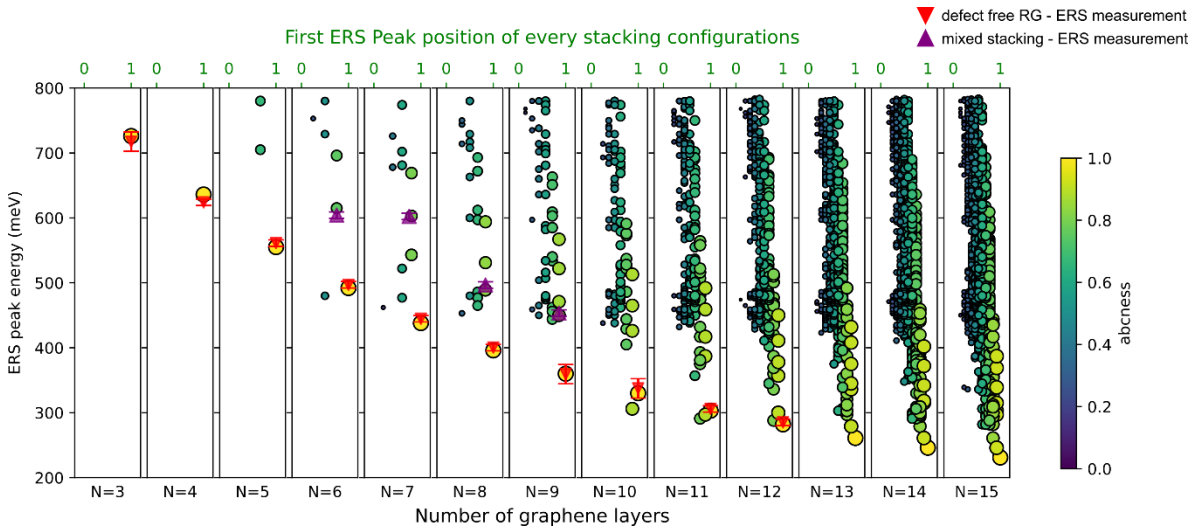

Figure 1.2 Calculated ERS peak energies in every possible stacking sequence of graphene layers up to 15 layers. The size and color of the circles corresponds to the relative ABC stacking content ("abcness") of the given sequence. Experimentally identified perfect RG stacks of 3-12 layers marked with red, and the mixed stackings with purple triangles.

The ERS process is an inelastic scattering event of photons, in which the photon loses energy solely due to electronic excitations of the given crystal, following specific selection rules determined by symmetry, without involving lattice vibrations (phonons). Despite being of very small probability, this process enables us to map the high density of states points in the electronic dispersion relation of various graphite structures. By tight-binding and subsequent ERS calculations we were able to predict the ERS signal of every possible layer sequence. For example, in the case of N=15 layers we examined 4160 configurations and more than 8300 in total. Whereas the hexagonal graphite's ERS spectrum is rather featureless, full or partial rhombohedral ordering results in peaks in the ERS spectrum. We demonstrated the validity of the calculations by experimentally identifying the structure of mixed stackings in the 6- and 7-layer system and narrowing down to a few candidates in the 8 and 9 layer case.

We have shown that the ERS process can directly fingerprint not only the perfectly stacked rhombohedral graphite, but also mixed stackings. This method offers the capability to unambiguously identify specific graphite stackings, thereby facilitating their detailed examination. Since rhombohedral graphite is one of the simplest crystals exhibiting strong electronic correlations, these findings could play a crucial role in advancing our understanding of the rich physics associated with electronic correlation phenomena.

Biomimetic hydrogen evolution with 2D MoS_2 crystals

Élvonal KKP 138144, Korea-Hungary bilateral TÉT-IPARI-KR-2022-00006, TKP2021-NKTA-05

S. Keszei, P. Vancsó, G. Dobrik, A. Koós, M. Németh, J.S. Pap, L. Tapasztó

Electrochemical hydrogen production can only be a possible alternative for hydrogen production if low-cost and efficient electrocatalysts are prepared. In the pursuit of new catalysts, it is beneficial to explore natural hydrogen production systems and take inspiration from their mechanisms. Hydrogenases are a class of metalloenzymes, that play crucial roles in the metabolism of certain microorganisms and well-known for their activity in hydrogen evolution reaction (HER), although no noble metals can be found in the active sites.

MoS_2 is considered a suitable catalyst in HER, reasoning that the edge-site sulphur atoms behave similarly to the bridge-positioned ones, found in hydrogenase and nitrogenase enzyme models. This resemblance may be used to build bioinspired catalysts by chemical modification of the basal plane sulphur atoms of MoS_2. Recently, we have shown that heteroatoms in the vicinity of metal centres can fundamentally influence the performance of biomimetic organoiron catalysts. In this work we present a convenient method to fabricate Mo-S-Fe structural moieties by combining a selected iron complex with the basal plane of MoS_2, thus creating highly active catalytic sites with atomic configuration mimicking those that can be formed at the edges.

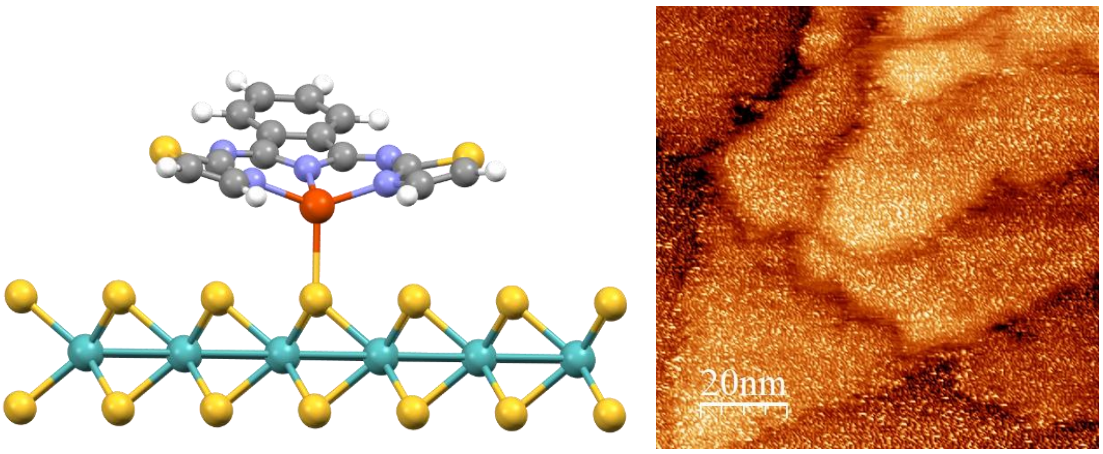

Figure 1.3 DFT structure of iron(III) complex anchored to a basal plane S atom of the 2D MoS_2 crystal (left). Experimental evidence for the presence of the iron(III) complex on the MoS_2 surface STM (right)

MoS_2 basal plane is generally considered rather inert towards chemical functionalization, however the weak nucleophilic character of the surface sulphur atoms enables to react with electron-rich reagents (eg.: organic halides, diazonium salts or maleimide derivatives) to form covalent bonds. It is also known that these sulphur atoms can act as electron donating ligands towards metal ions. We exploited this feature of basal plane sulphur atoms in few-layer MoS_2 nanostructures, utilizing them as binding sites for the immobilization of an iron(III) complex with the structurally rigid and redox-mediating 1,3-bis(2'-thiazolylimino)isoindolinate($^-$) (thia-BAI$^-$) ancillary ligand. The complex is attached to the MoS_2 by a coordinative bond between the surface sulphur atom and the Fe(III) centre, resulting Mo-S-Fe structural motifs. DFT-optimized geometries suggest high-spin tetrahedral iron(III) species, in consistence with the experiments. The Fe(thia-BAI) could be detected on the surface by IR and Raman spectroscopy, as well as XPS. STM confirmed the presence and stable binding of Fe(thia-BAI) moieties on the surface, corroborating with the DFT-derived DFT-derived adsorption energy of 1.6 eV (Figure 1.3).

The catalytic properties in HER of the novel hybrid materials were also investigated. Polarization curves (Figure 1.4.a) reveal an enhanced catalytic activity of the iron-decorated MoS_2, revealing a Tafel slope of 152 mV/dec. Surface modification resulted in a drastically lowered overpotential (from 1.24 to 0.2 V) and an increased turnover frequency for the HER. Constant potential electrolysis at the higher, as well as the lower overpotentials resulted an increased amount of hydrogen production with high Farradic efficiencies (91.2 and 83% for η = 1.54 and 0.2 V, respectively, Figure 1.4.c). EIS analysis showed a substantially decreased charge transfer resistance (R_{ct}), compared to the bare MoS_2 sample (Figure 1.4.d) and suggested multiple charge transfer processes taking place parallel during the catalytic reaction of the modified MoS_2 sample.

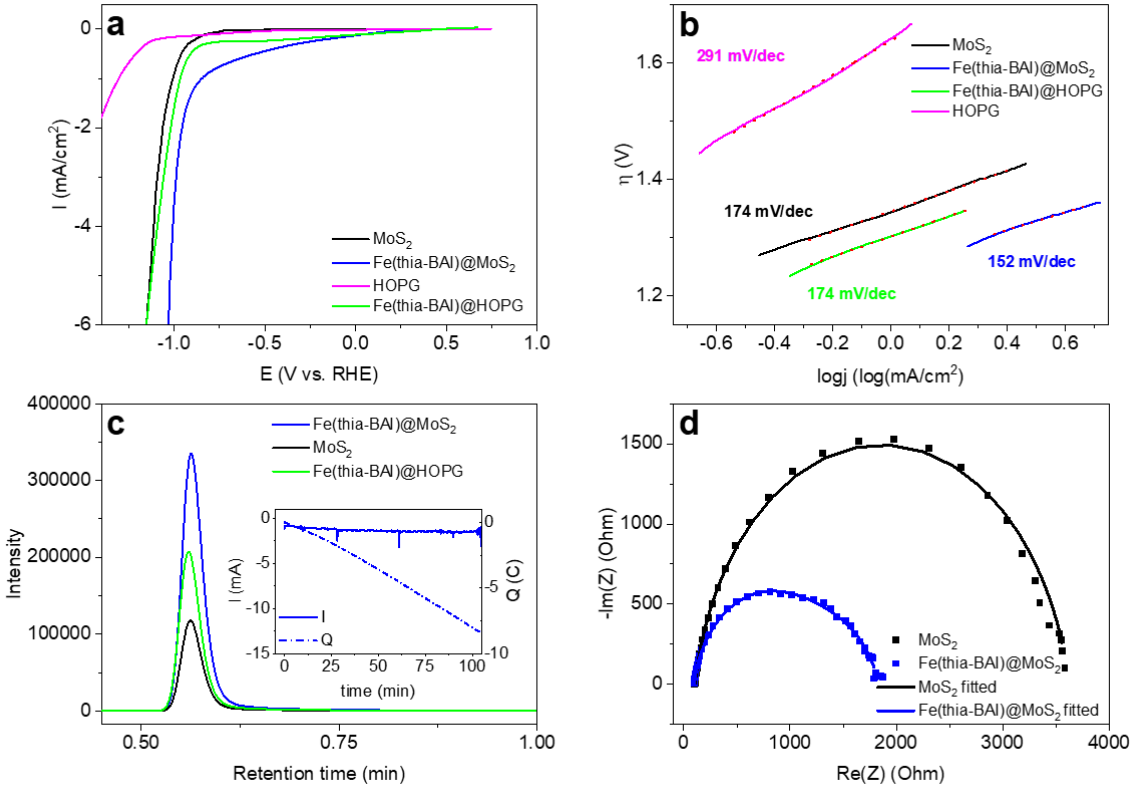

Figure 1.4 (a) HER polarization curves of MoS_2/Fe(thia-BAI)@MoS_2/ Fe(thia-BAI)@HOPG and HOPG in 0.1 M NaClO4 (b) Tafel plots of of MoS_2/Fe(thia-BAI)@MoS2/ Fe(thia-BAI)@HOPG and HOPG in 0.1 M $NaClO_4$ (c) Gas chromatogram of derected hydrogen after 1 hour of constant potential electrolysis (η = 1.54 V) (d) EIS responses at the overpotential of 1.14 V

It is well-known feature of MoS_2 that the catalytically relevant sites are the edge site sulphur atoms, however, based on our findings, the confinement of iron coordination compounds to the surface can lead to the establishment of new active sites for catalysis, therefore the activation of the basal plane of MoS_2. Based on our results, other transition metals with various organic ligands, bound to the MoS_2 surface are feasible, enabling the precise tuning of the chemical structure and behaviour of the resulting active sites, that may be the subject of our further research.

Engineering strain in MoS_2 monolayers using gold nanoparticles

OTKA K 134258

Z. Osváth, A. Pálinkás, Gy. Molnár, P. Kun, A. A. Koós

The study of strain-induced effects in monolayer molybdenum disulfide (MoS_2) is essential for tailoring its physical properties. For example, tensile strain can significantly reduce the direct bandgap of MoS_2 monolayers, which can enhance photogenerated charge carriers in photodetectors. In this work we applied gold nanoparticles (NPs) to induce local strain in MoS_2 monolayers. A thin gold film, with a nominal thickness of 15 nm, was first deposited onto a Si/SiO_2 (285 nm) substrate, followed by the mechanical exfoliation of MoS_2 onto the gold-coated surface (Figure 1.5.a and Figure 1.5.b). The sample was subsequently annealed in an electric furnace at 400 °C under an argon atmosphere. During the annealing process, the gold film restructured into flat NPs exhibiting lateral dimensions on the order of several hundred nanometres and heights typically ranging between 50 and 100 nm (Figure 1.5.c).

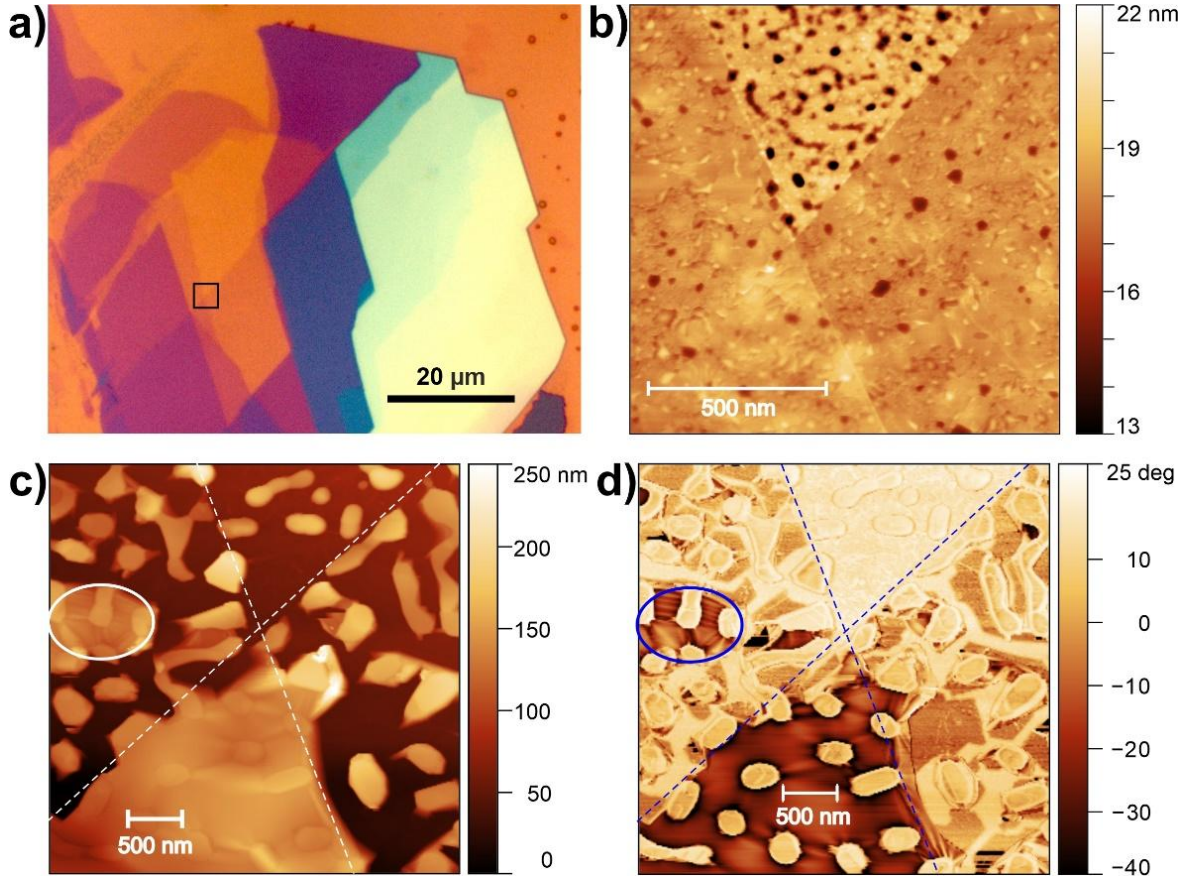

Figure 1.5 (a) Optical microscopy image of MoS_2 layers exfoliated on thin gold film. (b) AFM topography measured on the area marked with black square in a), showing two overlapping MoS_2 monolayers. (c)-(d) AFM topography and phase images measured simultaneously on the same area as in b) after annealing at 400 °C, showing that the thin gold film transformed into nanoparticles. The region with phase values > 15 degrees (light toned) corresponds to bare Au NPs on the SiO_2 substrate, while the region with values < -10 degrees (dark toned) corresponds to a double layer (overlapped monolayers) suspended on the gold NPs. Suspended monolayer parts are marked with ellipses in c)-d).

The AFM measurements showed that the MoS_2 monolayers do not cover perfectly the SiO_2 substrate and the Au NPs. There are extended regions where the MoS_2 monolayers are suspended between Au NPs (see for example the region marked with ellipses in Figure 1.5.c and Figure 1.5).

The annealed samples were investigated by confocal Raman spectroscopy using excitation laser of 488 nm with power of 0.5 mW and beam diameter of ≈1 μm^2. Raman maps were recorded in areas that were already characterized by AFM (shown for example in Figure 1.5) to study the space dependence of the MoS_2 A_{1g} and E^1_{2g} modes. The analysis of Raman maps revealed areas with reduced A_{1g} and E^1_{2g} peak frequencies (data presented with blue symbols in Figure 1.6). Comparing the Raman maps with the AFM topographic images we found that these spectra correspond to the MoS_2 monolayer parts suspended between Au NPs.

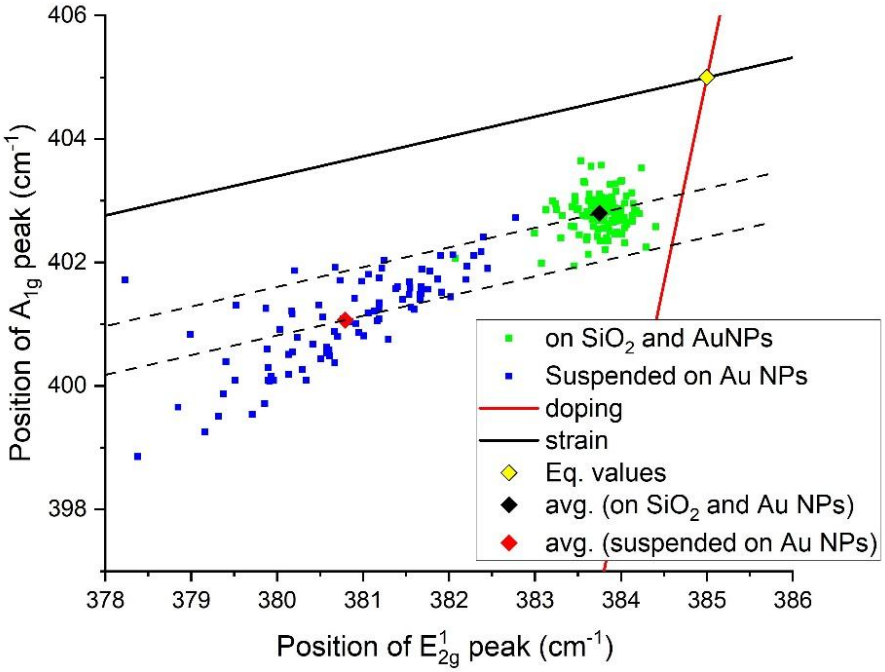

Figure 1.6 Correlative plot of Raman A_{1g} and E^1_{2g} peak frequencies showing the peak positions measured on MoS_2 monolayers covering the nanoparticle-decorated SiO_2 substrate (green symbols), and on MoS_2 monolayers suspended between Au NPs (blue symbols). The corresponding averages are marked with black and red symbol, respectively. The slopes denoting strain (black line) and doping (red line) are also plotted. The yellow symbol indicates the reference values of undoped and unstrained MoS_2 monolayer.

The correlative analysis of the A_{1g} and E^1_{2g} peak frequencies (Figure 1.6) demonstrated significant strain in the MoS_2 monolayer regions suspended over Au NPs. The local strain in these suspended areas ranged from 0.38% to 1.26%, with an average strain of 0.73% and n-type doping of 1.24×10^{13} cm^{-2}. In contrast, the MoS_2 regions conformally coating the nanoparticle-decorated SiO_2 substrate exhibited lower average strain and doping levels of 0.18% and 0.86×10^{13} cm^{-2}, respectively.

Photocatalytic bioheteronanostructures by integrating multicomponent Cu_2O-Au nanoparticles into ZnO-coated butterfly wings colored by photonic nanoarchitectures

OTKA PD 142985, TKP2021-NKTA-05

G. Piszter, K. Kertész, G. Nagy, D. Kovács, D. Zámbó, Zs. Baji, J. S. Pap, and L. P. Biró

A systematic study is reported on biotemplated heteronanostructures produced by coating blue-colored male *Polyommatus icarus* butterfly wings using ZnO thin films and depositing hybrid nanoparticles (NPs) from the Cu_2O–Au heteronanostructures family. The resulting composite material is designed to enhance the efficiency of photocatalysis using the visible part of the solar spectrum. The effect of various NPs (Cu_2O octahedra, Cu_2O octahedra with Au nanograins grown on their facets, Cu_2O octahedra with a centrally incorporated Au nanorod, and spherical Au NPs) was thoroughly tested and compared (Figure 1.7).

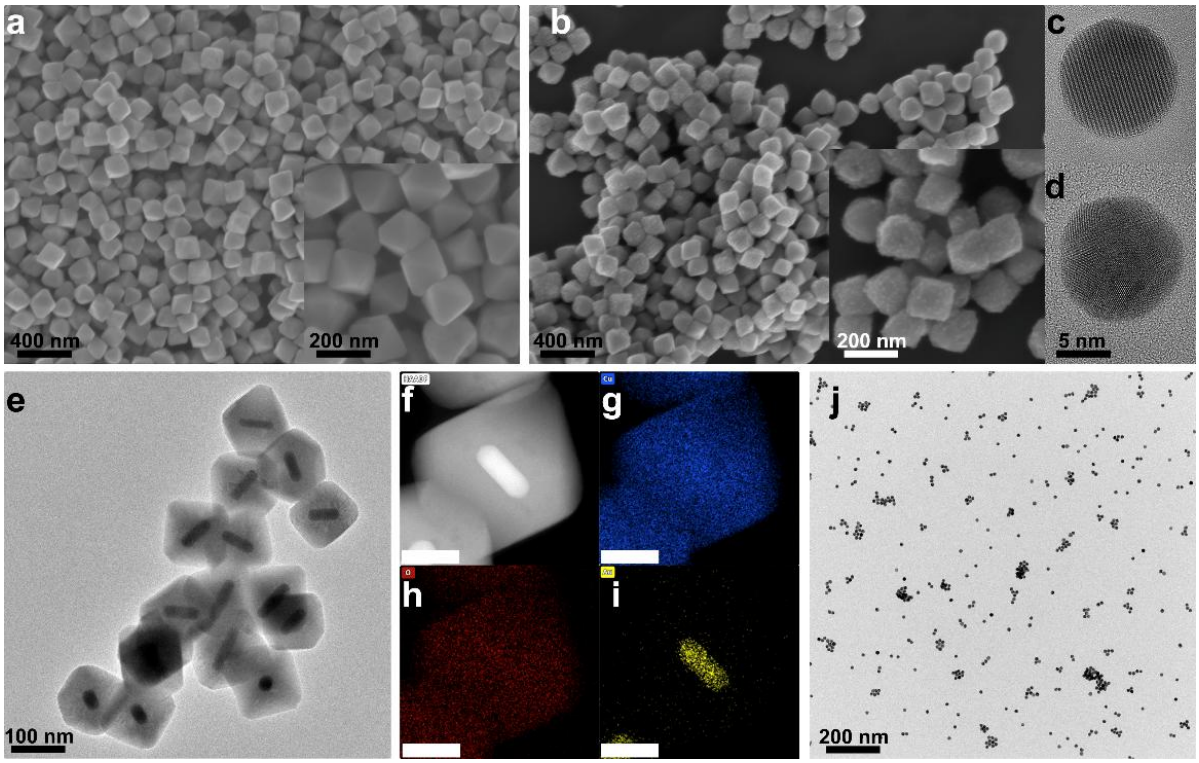

Figure 1.7 Morphology of the used NPs: (a) SEM image of Cu_2O NPs; (b) SEM image of Au@Cu_2O NPs, note in the right lower corner inset the rough surface of the facets due to the Au nanograins grown on the Cu_2O NPs; (c) and (d) two Au NPs shown in high-resolution TEM images; (e) TEM image of AuR@Cu_2O NPs, note the contrast difference due to the Au nanorod inside the Cu_2O octahedra; (f) HAADF image; (g) Cu, (h) O, and (i) Au distribution of a AuR@Cu_2O NP measured with EDS, scale bars: 5 nm; and (j) TEM image of spherical Au NPs.

Cu_2O has the advantage of being abundant, environmentally safe, and minute amounts of Au can be efficiently used to tune its properties. Au decoration of the Cu_2O NPs can enhance their structural stability even during long-time light exposure in aqueous environment. When aiming at environmental protection applications, and water remediation in particular, the immobilization of the NPs on an appropriate substrate is of great importance. Due to their complex hierarchical structure from tens of nanometers to centimeters, butterfly wings are particularly well suited for this purpose and an important question is to what extent and in which ways the properties of the hybrid photocatalytic NPs are affected by the interaction with such substrates.

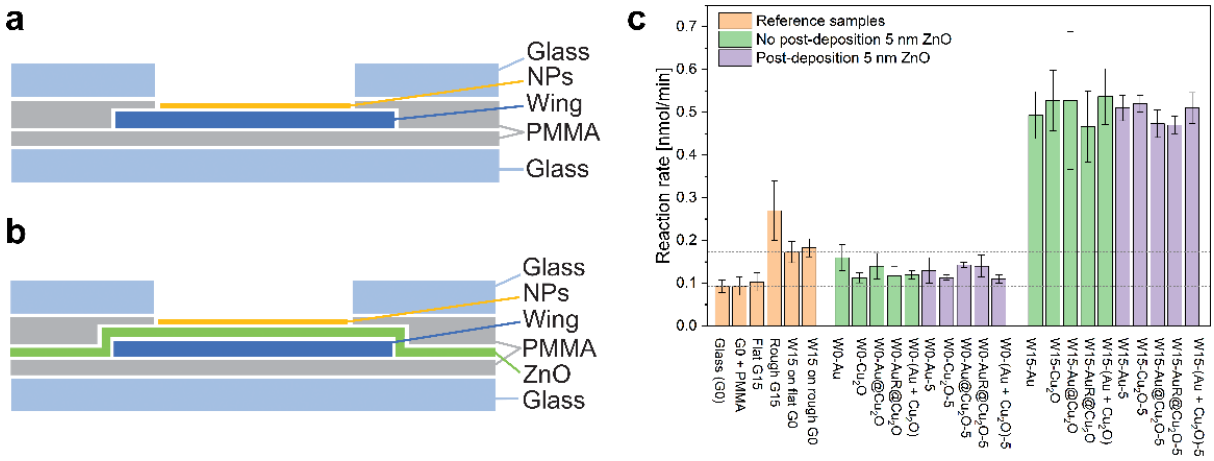

Figure 1.8 Schematic sample structure (a) without or (b) with ZnO adlayer; (c) average reaction rates after three consecutive photocatalytic tests on reference samples (orange), samples without post-deposition of 5 nm of ZnO (green), and samples with post-deposition of 5-nm ZnO (purple) after the deposition of the NPs.

We used butterfly wing-based substrate *i)* to immobilize the NPs, *ii)* to provide increased contact surface between the solute and the photocatalytic surface, and *iii)* to exploit structural complexity by using the hierarchical nanoarchitecture. The chemical and plasmonic complexity are provided by the conformal ZnO adlayer and the deposited NPs used for doping. After the deposition of the different NPs, the photocatalytic performance of the samples under visible light illumination was tested by the photodegradation of methyl orange dye in aqueous solution monitored continuously by an immersion probe. It was found that the components of the biological hetero-nanoarchitecture, ZnO-coated wings and wings without ZnO with deposited NPs (Figure 1.8.a), exhibited poor catalytic performance. But the combined system, ZnO-coated wings with NPs deposited onto them (Figure 1.8.b), exhibited a sixfold to eightfold increase in their catalytic performance (Figure 1.8.c). This increase is attributed to the extension of the ZnO absorption into the visible range and to the formation of the heterojunction between the n-type ZnO and the p-type Cu_2O NPs which resulted in the charge transfer of the photogenerated carriers. As the samples exhibited good stability under the continuous magnetic stirring, they can be used in real-world applications as prototypes, e.g., in flow-through systems suitable for wastewater remediation using sunlight illumination.

Photonics Department

Head: Dr. Peter PETRIK, D.Sc., scientific advisor

Research Staff:

Miklós Fried, D.Sc., Head of Ellipsometry Laboratory
András Deák, Ph.D., Head of Chemical Nanostructures Laboratory
Antal Gasparics, Ph.D.
Zoltán Lábadi, Ph.D.
Norbert Nagy, Ph.D.
Boglárka Nyerges
Ferenc Riesz, C.Sc.
Dániel Zámbó, Ph.D.
Géza Szántó, Ph.D.
Miklós Serényi, D.Sc., retired
György Kádár, D.Sc., Prof. Emeritus
Tivadar Lohner, D.Sc., Prof. Emeritus
János Makai, C.Sc., retired
András Hámori, dr. Univ., retired
György Juhász, dr. Univ., retired

Students:

Noor Taha Ismael, Ph.D. student
Noémi Jakab,
Dávid Kovács, Ph.D. student
Deshabrato Mukherjee, Ph.D. student
Berhane Nugusse, Ph.D. student
Máté Podráczki
Alekszej Romanenko, Ph.D. student
Máté Stift

The Photonics Department develops unique methods and tools for non-destructive optical and magnetic measurement of surface nanostructures and materials (spectroscopy; magnetic material testing; biosensors; surface curvature measurement; surface testing; water contamination). One of the most important tasks of the Department is patenting and application of the methods in international projects with partners representing the industry and the high technology.

Key achievements of the Photonics Department in 2024 (detailed summaries of the research results can be found in the following project descriptions):

- Creation of multicomponent, multi-metal nanoparticles for optoelectronic, photocatalytic, and electrocatalytic applications
- Investigation of the formation and properties of metal–semiconductor and copper oxide shell-structured nanoparticles
- Advancement in the industrial application of solid–liquid adhesion work
- Further development of Makyoh topography evaluation using the Schlieren setup, and by comparing the rear-side visual image with the front-side projected image
- Development of an in-situ investigation method for studying the electrochromic properties of combinatorial TiO_2–SnO_2 layers
- Combinatorial deposition of metal oxides for electrochromic applications
- Development of sputtering techniques for the fabrication of gallium oxide and aluminum oxynitride layers
- Qualification of sensor-targeted layers using simultaneous ellipsometric and electrochemical methods
- Microscopic ellipsometer patent from a proof-of-concept grant
- Development of materials for nuclear applications
- Formation and sensoric properties of combinatorial plasmonic nanoparticles
- Dániel Zámbó received the EK Youth Award
- Antal Gasparics received the MFA Science Support Award

Cryoaerogel electrodes from Pd/Pt nanoparticles for electrocatalytic application

OTKA FK 142148

D. Zámbó

In general, platinum has been considered as one of the best – or even the best – electrocatalyst in hydrogen evolution reaction and fuel cell-related reactions. The main challenge in this field is to reduce the use of this precious metal, however, its total exclusion is not a technically promising concept. In contrast, partial substitution of Pt with other elements, such as Pd opened new ways in the preparation of nanocatalysts. Electronic properties, resistance against CO poisoning, oxophilicity as well as C-C bond cleavage can be positively modified by adding palladium to the systems containing reduced amount of Pt.

In this work, a novel electrode preparation concept called cryogelation was employed to fabricate nanocrystal gel structures from mixed Pd and Pt colloidal solutions. Prior to the gel formation, Pd and Pt nanoparticles (diameter of 6.2 and 3.8 nm) were synthesized in aqueous medium. Based on the important findings regarding the correlation between the gelation parameters and the gel structures in the recent years, pure and mixed Pd/Pt cryogels were prepared by freezing the colloidal solution in isopentane medium (at -160 °C) after drop-casting onto the substrate. This had a positive impact both on the attachment and stability of the porous gel network on the conductive ITO substrate as well as on its pore structure (Figure 2.1). [Ref.2.1]

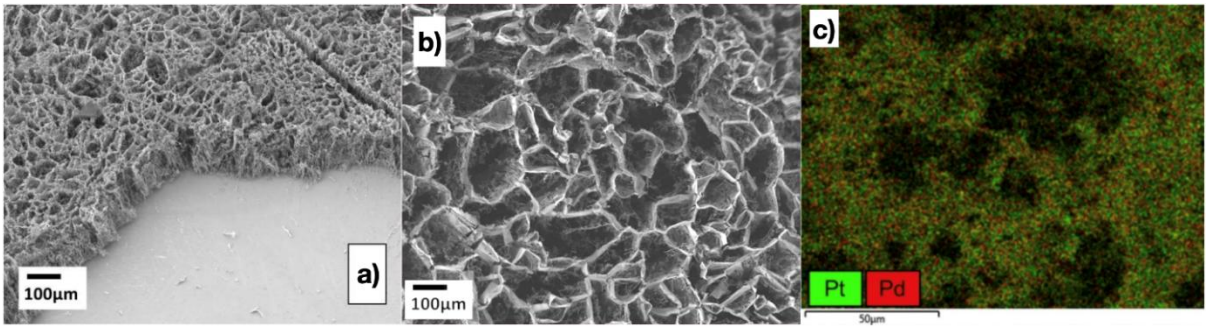

Figure 2.1 Structure of the cryogel electrode on ITO and its dendritic, open-pore structure (a,b). Elemental mapping proving the homogeneous distribution of the small Pd and Pt nanoparticles (c). [Ref.2.1]

Cryogel structures were characterized by scanning and transmission electron microscopy as well as their exact compositions were determined by atomic absorption spectroscopy. Mixing of the colloidal solutions were prepared in different Pt:Pd ratios: 1:0, 1:1, 1:2, 1:4 and 0:1. A new approach further increased the applicability of the cryogels: the frozen gel structures were stored in liquid nitrogen overnight and then thawed in the electrochemical cell without freeze drying. Thus, the gels can be transferred to the cell in the form of cryohydrogels, which have the same structure and composition as their dried counterparts. The thickness of the cryogels have a profound impact on the structural and catalytic properties, hence it was also optimized during the preparation process just like the concentration of the ethanol. The catalytic performance of the structures was investigated in a three-electrode configuration using the ITO-supported gels as working electron in the electrooxidation of ethanol (EOR). The measured mass activity highly depended on the mixing ratio of the initial metal colloidal solutions and the highest value belongs to the Pt:Pd=1:4 mixing ratio (345 mA/mg). Overpotential of the ethanol oxidation decreased with increasing Pd content. The catalytic activity of

all bimetallic cryogels over performed that of the pure metal (Pd or Pt) gels which justifies the use of the mixing approach to increase the performance of the gel networks (Figure 2.2).

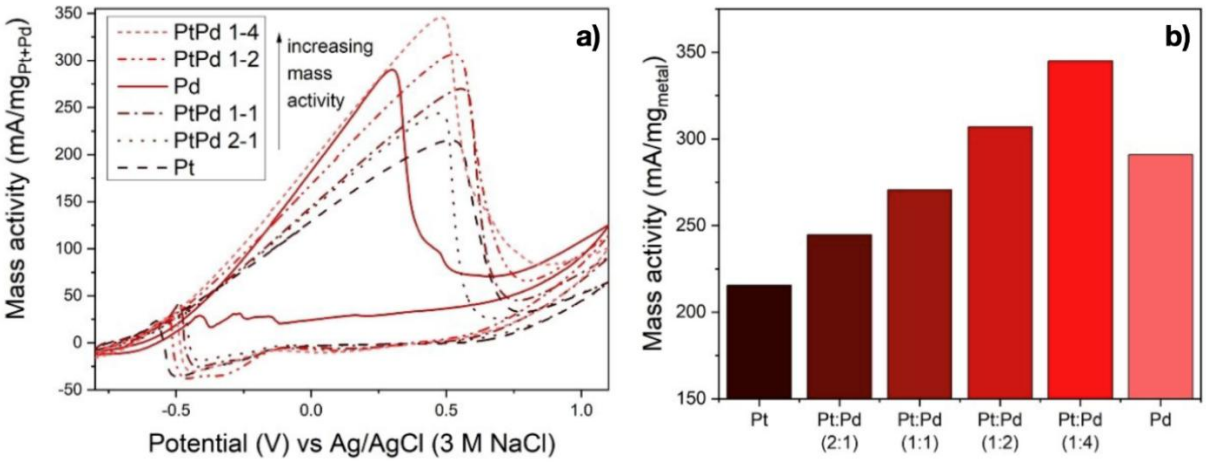

Figure 2.2 Cyclic voltammograms of the cryogels as a function of the mixing ratio (a). Summarized results on the EOR mass activities of the synthesized model systems (b). [Ref.2.1]

Comparing the mass activity of these novel mixed noble metal cryogels with the previously reported ones revealed that Pd/Pt mixed nanocrystal cryogels show higher activity than Pt/γ-Fe_2O_3, Pd/γ-Fe_2O_3, monometallic Pd and Pt_xPd_y alloys. Nevertheless, the performance might be able to be further boosted by incorporating a third metal (e.g. Au or Ag) into the gel matrix. This study showed the importance of multielemental synergy in gel structures and offered a simple and straightforward preparation method for multicomponent metal working electrodes. The work was published in ChemElectroChem. [Ref.2.1]

Porous tetrametallic nanorods for catalytic applications

OTKA FK 142148, TKP2021-NKTA-05

D. Kovács, Gy. Z. Radnóczi, Zs. E. Horváth, A. Sulyok, I. Tolnai, A. Deák, D. Zámbó

Noble metal (especially Au, Pd, Pt and Ir) nanoparticles are widely used in various applications in the field of optics, sensing and catalysis. Although platinum is one of the benchmark catalysts for hydrogen evolution and water splitting, the use of precious metals is intended to be reduced in the recent decade. A promising strategy to decrease the amount of noble metals used as catalyst is *(i)* to prepare nanoparticles with highly accessible surface sites and *(ii)* to combine more than one metal into a multimetallic system. Synergistic properties between the elements are able to extend the functionalities of the synthesized nanocatalyst by altering the electronic properties of the incorporated metals. Moreover, preparation of porous nanoparticles with proper morphological control enables achieving significantly higher surface area, where interfacial catalytic transformations can take place.

Integration of more than two metals into a tailored nanoparticle matrix is a synthetic challenge. Reduction potentials determine the elemental structure of the built-up nanoparticles, while the direct contact between the metals has an impact on the overall electronic properties. Our aim was to utilize the multielemental synergy in tetrametallic nanoparticles consisting of a gold nanorod core and a trimetallic PdPtIr shell. To enhance the specific surface area of the particles, the shell was constructed to be micro- and mesoporous (Figure 2.3).

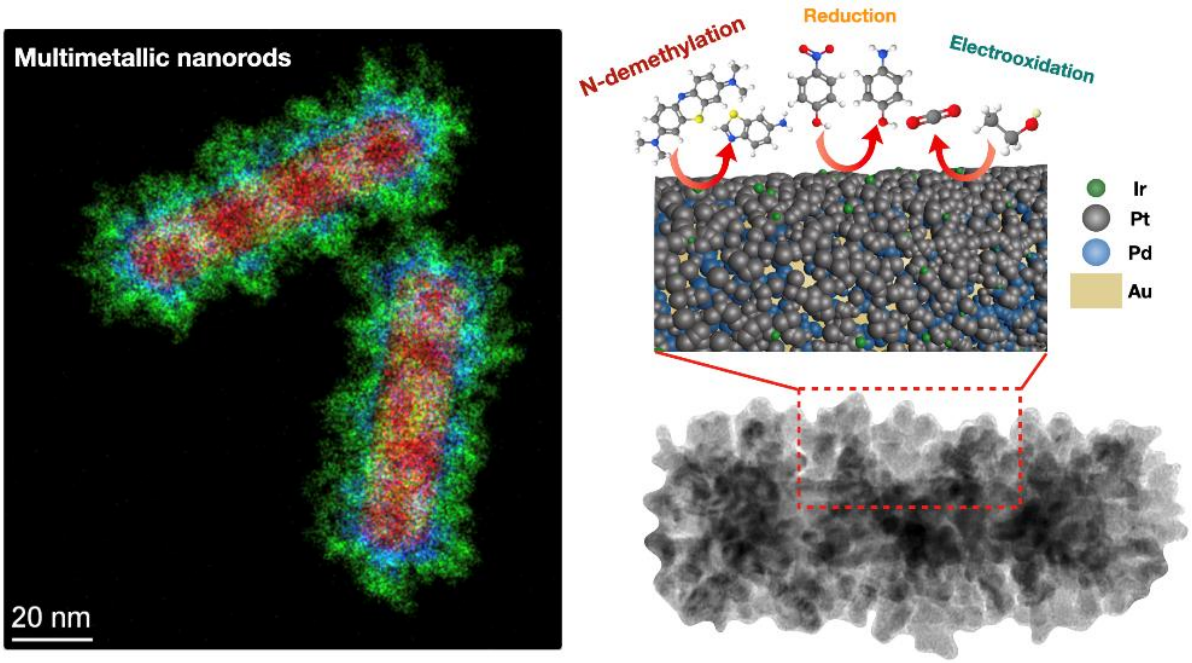

Figure 2.3 TEM-EDX elemental maps of the Au@mPdPtIr nanorods (left), and the catalyzed test reaction on the surface of their porous shell (right). [Ref.2.2]

We demonstrated that the conditions of the particle synthesis (i.e. pH, temperature, order of chemical additions, micellar template) are critical for ensuring the robust preparation of the particles with excellent shape, size and elemental uniformity. The multielemental composition and the position of the Fermi levels of the metals ensure the formation of a negatively charged particle surface which was found to be active in various catalytic reactions such as N-demethylation, nitro group reduction and ethanol electrooxidation. Nanocatalyst electrodes were successfully fabricated by depositing the porous

particles onto a conductive substrate in a straightforward manner at room temperature. The multimetallic nanoparticles possess outstanding morphological stability and reusability in the investigated test reactions. The particles can act as catalyst in p-nitrophenol amination, methylene blue degradation reaction, as well as in a direct liquid fuel cell-related application (ethanol electrooxidation, EOR). For the former, the particles contributed in the preparation of OH radicals, while in the latter, electrodes with low catalyst loading enabled the decrease of the overpotential in alkaline medium.

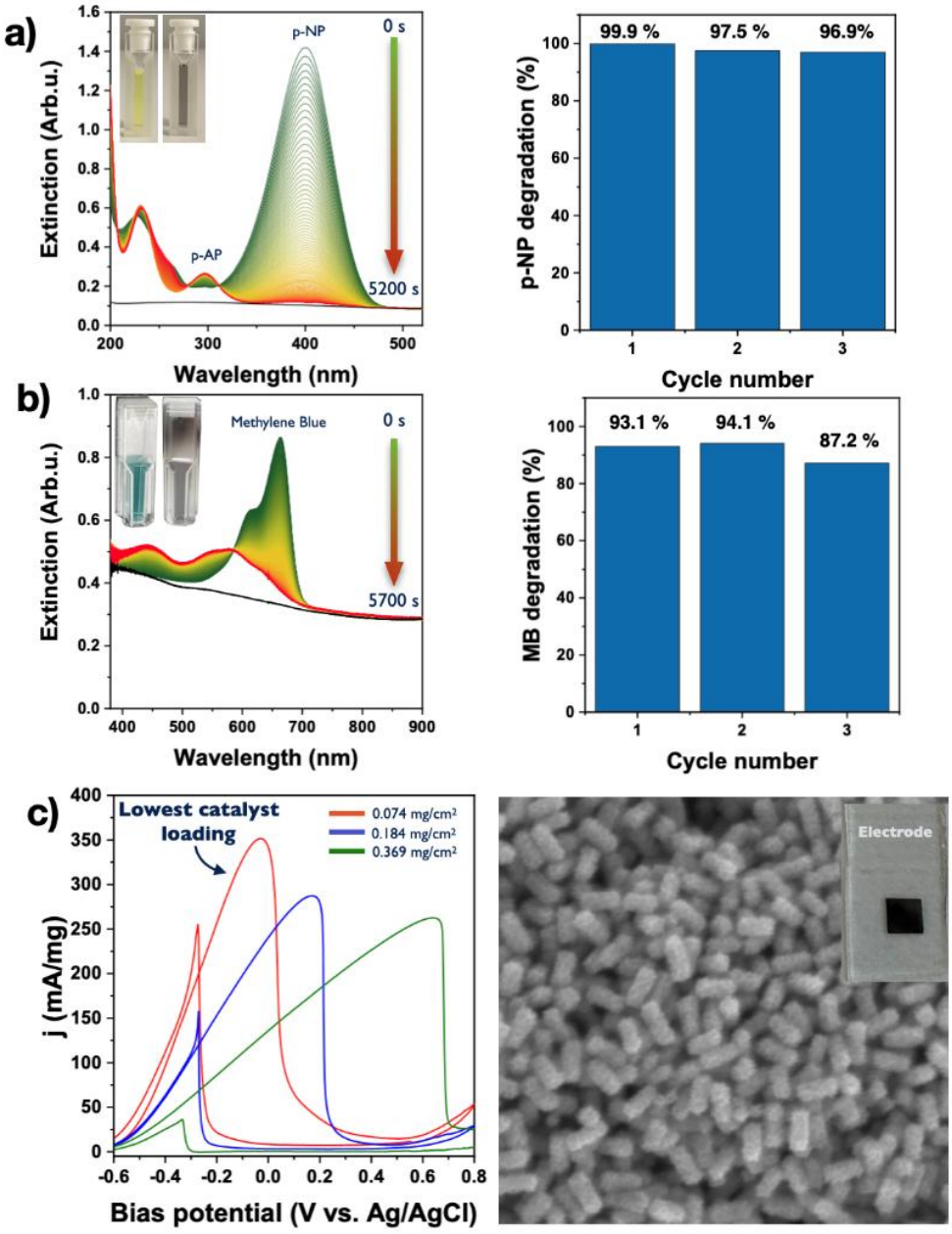

Figure 2.4 Performance of the porous tetrametallic nanorods in p-nitrophenol to p-aminophenol conversion (a), N-demethylation of methylene blue dye (b) and EOR (c).[Ref.2.2]

The work was selected as the "*Publication of the month*" by the Hungarian Academy of Sciences – VII. Section of Chemical Sciences in March, 2024. The paper was published in Small as a part of the Hot Topic: Mesoporous materials. [Ref.2.2]

Enhancing the catalytic activity of multimetallic nanoparticles by symmetry breaking

OTKA FK 142148, TKP2021-NKTA-05

*A. S. Omondi, D. Kovács, Gy. Z. Radnóczi, Zs. E. Horváth, I. Tolnai, A. Deák, D. Zámbó**

The library of noble metal nanoparticles has been expanded in the recent decade by elaborating their synthesis in numerous morphology such as spheres, rods, prisms, octahedra, stars and bipyramids. Symmetry breaking (*i.e.* preparation of anisometric particles) enables the tuning of their optical properties and catalytic activity due to the presence of crystal planes with different surface energies. Complementing this strategy with the integration of various noble metals as well as with improved accessibility of surface sites by preparing porous metal particles can further enhance their catalytic performance in heterogeneous catalysis and electrocatalysis.

The work aimed for the robust synthesis of tetrametallic Au@PdPtIr (core@shell) nanoparticles with excellent morphological purity to monitor the effect of the core morphology on the optical and catalytic properties. Proper synthetic control and symmetry breaking procedures during the particle growth ensured the preparation of novel porous tetrametallic nanocatalysts with spherical, rod-shaped, prism-shaped, octahedral and bipyramidal morphology (Figure 2.5).

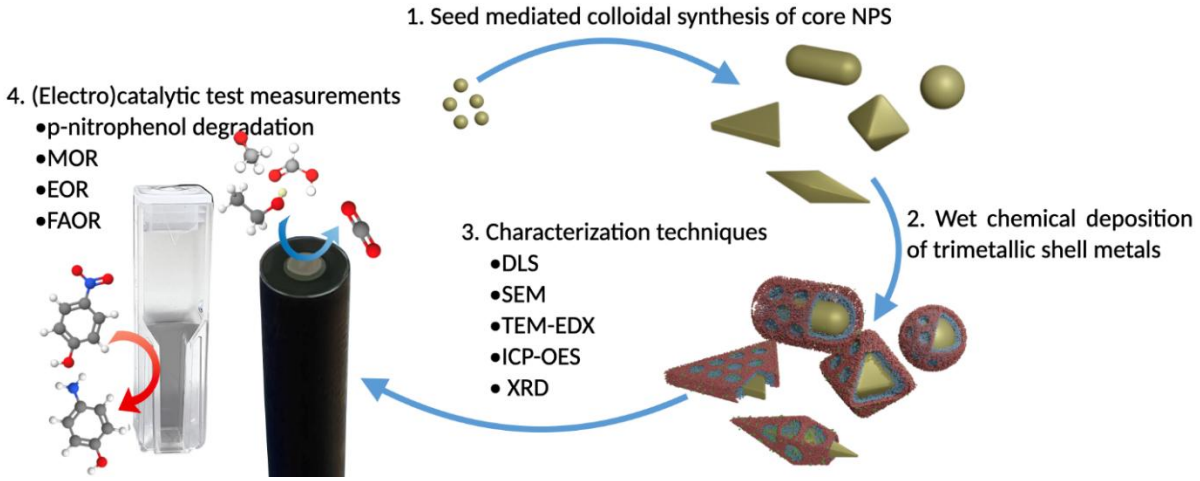

Figure 2.5 Schematics on the synthesis and application of morphologically-controlled tetrametallic nanoparticles. [Ref. 2.3]

Spherical and symmetry-broken gold nanoparticles cores where post-synthetically covered by a trimetallic (PdPtIr) porous shell to obtain the different model systems. As a key novelty, the work intended to compare the catalytic performance of such model systems by keeping the volume of the seed particle, the composition of the shell as well as the surface chemistry and catalyst loading identical. Tetrametallic nanoparticles possess highly negatively charged surfaces due to the intraparticle charge transfer. Dispersed nanoparticles were used as catalyst in p-nitrophenol conversion in aqueous medium without applying external trigger (e.g. heat or light). Moreover, electrodes were fabricated by depositing the particles onto glassy carbon electrode (GCE) to compare their activity in alcohol and formic acid oxidation reactions (direct liquid fuel cell-relevant model reactions). Electrode preparation neither involved binding agent nor Nafion as additive, thus, it is a clean and straightforward procedure. All particle types catalyzed the model reactions, however, symmetry-broken morphologies performed significantly better (Figure 2.5). This can be attributed to the higher electrochemically active surface areas as well as the presence of different facets on the gold cores.

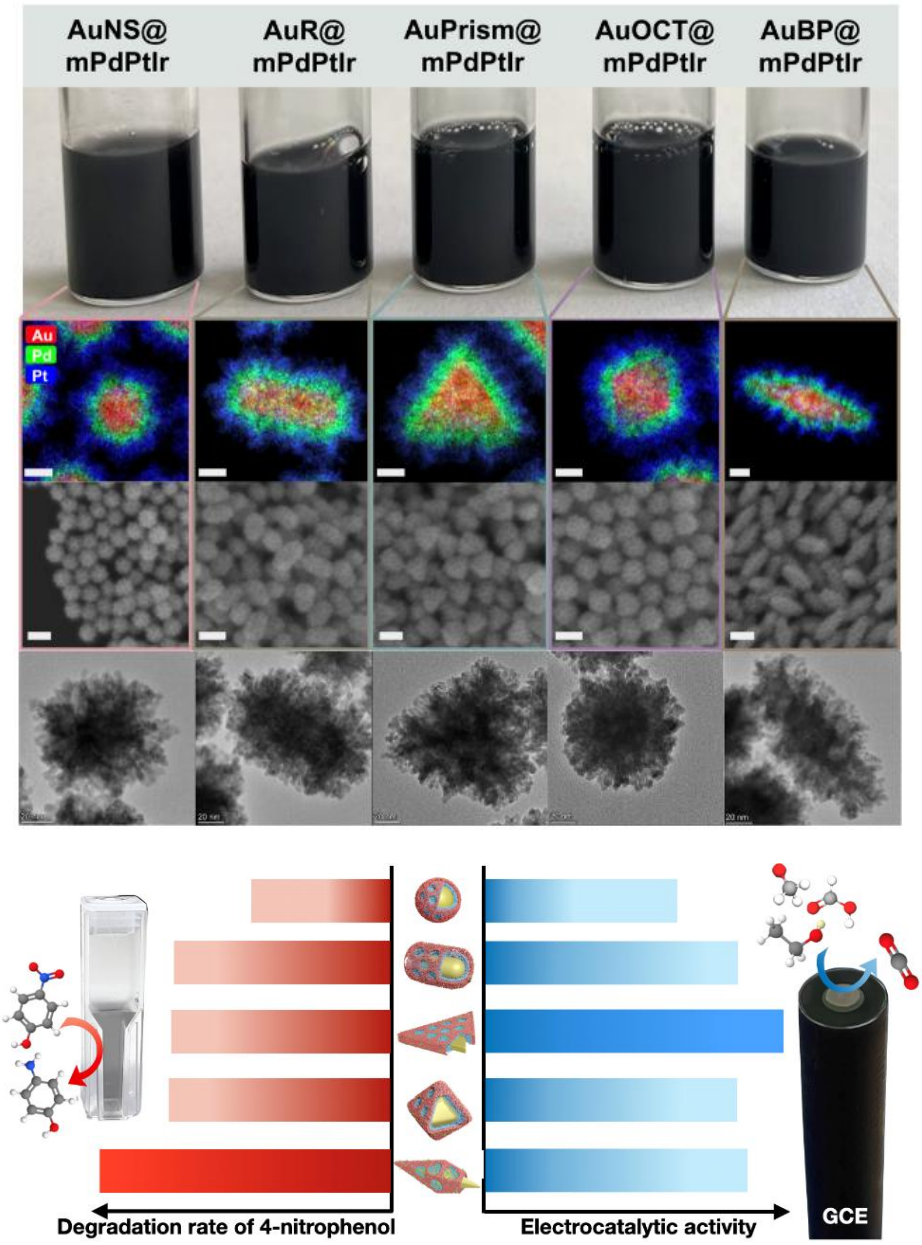

Figure 2.6 Synthesized model systems with different morphologies and their elemental maps (top). Performance of the particles in 4-nitrophenol degradation and electrooxidation according to their shape. [Ref.2.3]

Importantly, all tetrametallic particles significantly outperforms their monometallic counterparts highlighting the importance of proper compositional control and the intraparticle charge transfer upon constructing multielemental particles. These novel nanocatalysts show excellent morphological robustness down to the fine structural level. This work sheds light on the correlation between the morphology and the application potential underlining the importance of the proper selection of the particle shape for a specific catalytic reaction. This study was published in *Nanoscale* of the Royal Society of Chemistry as an invited paper. [Ref.2.3]

The growth and structure of cuprous oxide shell of gold nanoprisms

TKP2021-NKTA-05, OTKA FK 142148

D. Zámbó, D. Kovács, A. Deák

Hybrid nanostructures derived from semiconductors and noble metals can show improved charge generation and separation properties, that are useful for various catalytic and optoelectronic applications. The combination of cuprous oxide (Cu_2O) with gold is especially interesting, as such a nanostructure unites the earth-abundance of copper with the outstanding stability and inertness of gold, whereas Cu_2O is a p-type semiconductor with its optical band-gap located in the visible wavelength range. Additionally, both materials can be used to prepare size and shape controlled nanoparticles *via* wet-chemical synthetic routes. In one of our earlier works we have shown that separation and localisation of photogenerated charge carriers in a Cu_2O/gold heteroparticles depend heavily on the morphology of the particles [Ref 2.4]. Up to now, various shapes of Cu_2O/gold core/shell nanoparticles have been reported in the literature, where as a general rule the gold core morphology was matching the symmetry of the Cu_2O shell grown around the particles.

In our recent work we were investigating in detail how cuprous oxide shells can be grown on prism shaped gold nanoparticles [Ref.2.5]. As there is an inherent mismatch between favoured crystal structure and she shape of the gold core, the evolution of the deposited shell's structure was investigated in detail.

High-purity gold nanoprisms were obtained by wet-chemical synthesis and depletion-interaction mediated post-synthetic purification process. The cuprous oxide shell growth was carried out in alkaline aqueous media from $CuCl_2$, using either hydrazine or hydroxylamine as reducing agent. Both reducing agents are known from the literature to be able to deliver Cu2O/Au core/shell nanoparticles, but hydrazine is a stronger reducing agent usually leading to shell formation with faster kinetics. To characterize the morphology and optical properties of the particles, electron microscopy (SEM, TEM), an optical spectroscopy was employed. To obtain more detailed information about the development of the cuprous oxide shell morphology, the growth reaction was deliberately quenched at different time instances and correlative electron microscopy/single nanoparticle spectroscopy experiments were carried out.

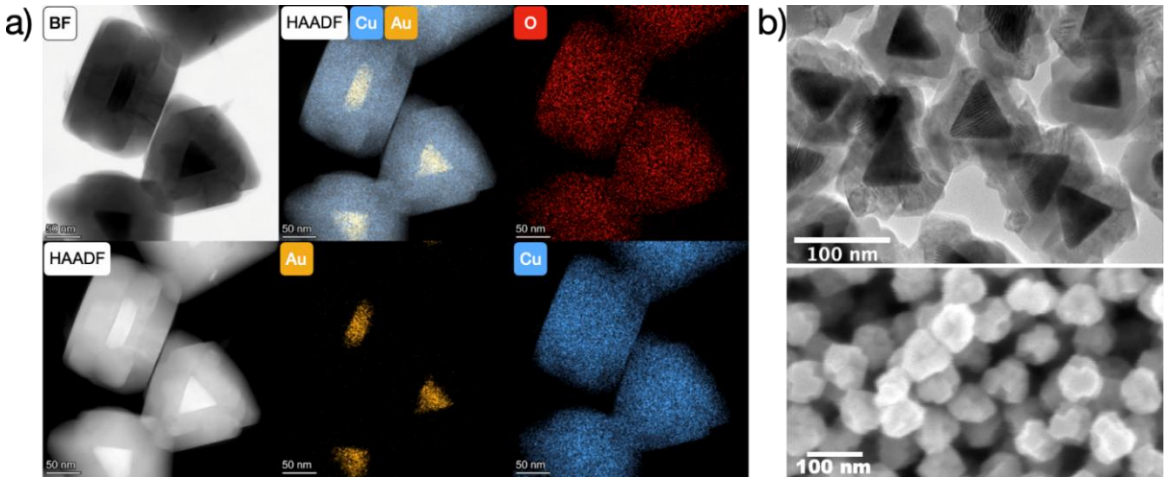

Figure 2.7 TEM images and elemental map of the Cu2O/Au nanoparticles prepared suing hydrazine as reducing agent (a). TEM and SEM pictures of the particles when hydroxylamine was introduced to initiate the shell growth (b).

Both hydrazine and hydroxylamine are able to produce core/shell type particles (Figure 2.7), but there is an inherent difference between the shell structures. While hydrazine results in twisted slab-like Cu2O coating, where the slabs run parallel to the flat planes of the gold nanoprisms, hydroxylamine produces a multi-grain shell, which (especially on the SEM images) features a complex 3D structure. It can be inferred, that while hydrazine induces the shell growth on the prisms' face region, for hydroxylamine the shell deposition starts in the curved regions of the core particles (tips and edges) and as the reaction commences, it transforms into the observed complex 3D structure. This would also imply that some degree of region-selective growth takes place in the presence of hydroxylamine. This has been investigated in detail and confirmed by looking at the time-evolution of the optical and structural properties of the core/shell particles. The spectra recorded during the growth show a fast shell deposition (Figure 2.8.a), and the 2D projection in the TEM indicate a multi-crystalline, but conformal shell growth with some structural inhomogeneity developing at later stages (Figure 2.8.b). From the SEM image (Figure 2.8.c) it is also obvious that in reality the shell starts to grow at the tips and edges of the particles, and the faces are covered only at later growth stage. This leads to a complex 3D shell morphology observed at the final stages of the growth (Figure 2.7.b).

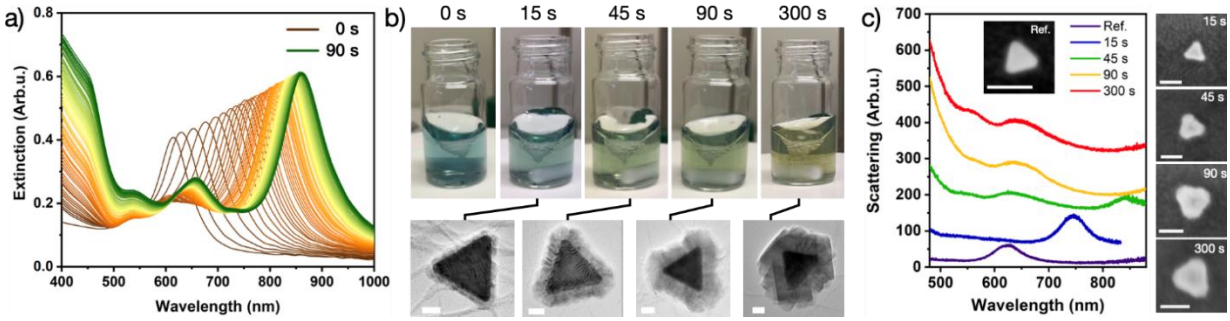

Figure 2.8 Ensemble optical spectra of the nanoprisms during the Cu2O shell growth using hydroxylamine in the first 90 seconds (a). The time-evolution of the shell morphology as observed in TEM (b). Correlative SEM/single-particle spectroscopy of the particles as a function so shell growth time (spectra have been vertically shifted for clarity) (c).

Determination of solid-liquid adhesion work in a direct and absolute manner by the Capillary Bridge Probe

OTKA FK 128901, TKP2021-EGA-04

N. Nagy

The need of the determination of solid-liquid adhesion work is as old as Dupré's definition of the reversible work of adhesion. In addition to its scientific importance, this quantity is a critical factor affecting product quality and performance in many industrial fields. In general, it plays crucial role if the liquid should completely cover a solid surface (e.g. coatings, paints, inks, lubricants, adhesives, pesticides) or, on the contrary, the liquid should not remain on the surface at all (liquid repellency, anti-icing, etc.).

According to Dupré's definition, the adhesion work is the reversible thermodynamic work required to separate unit area of two phases in contact. Applying this definition to solid and liquid phases, the solid-liquid adhesion work (W_a) can be written as

$$W_a \equiv \gamma_{LV} - (\gamma_{SL} - \gamma_{SV}) \quad (1)$$

where γ_{LV} is liquid's surface tension, γ_{SL} is solid-liquid interfacial tension, and γ_{SV} is the surface free energy of the solid. The last two quantities cannot be measured directly. However, their difference is included in the Young equation, which describes the condition for equilibrium of the contact line at the solid-liquid-vapor interface:

$$\gamma_{SV} - \gamma_{SL} - \gamma_{LV} \cdot \cos\vartheta = 0 \quad (2)$$

where ϑ is the contact angle at the contact line. The combination of these two equations eliminates the unknown difference term and results in the Young–Dupré equation:

$$W_a = \gamma_{LV} \cdot (1 + \cos\vartheta) \quad (3)$$

which relates the measured contact angle to adhesion work. Traditionally, the work of solid-liquid adhesion has been determined through the measurement of contact angle. This contact angle based approach is very convenient and effective, however, it raises several theoretical and practical questions.

During a measurement cycle of capillary bridge probe, the capillary force is measured as a function of the change of bridge length that is as a function of the vertical displacement of the cylinder.
This work is only spent on changing the interfacial areas, if gravitational force is negligible. During approach and retraction, both the area of the liquid-vapor interface (A) and that of the solid-liquid interface (B) change. Consequently, the energy balance can be written as

$$-\int \vec{F} d\vec{z} = \Delta A \cdot \gamma_{LV} + \Delta B \cdot (\gamma_{SL} - \gamma_{SV}) \quad (4)$$

where $\overrightarrow{F}$ is the measured capillary force, $\vec{z}$ is the displacement of the cylinder, ΔA is the change of interfacial area between the liquid and vapor phase, and ΔB is the area change between the solid and the liquid, see Figure 2.9. (The value of ΔA and ΔB are also dependent on the start and end points of the interval (z-range), over which the integration is performed.)
After rearranging Equation (4), the difference term in the bracket can be expressed as:

$$(\gamma_{SL} - \gamma_{SV}) = -\frac{\int \overrightarrow{F}\, d\vec{z} + \Delta A \cdot \gamma_{LV}}{\Delta B}. \quad (5)$$

One can substitute this experimentally otherwise unattainable term into the definition of adhesion work (Eq. (1)). Furthermore, considering that the net force and the displacement have only z-component, the vector notation can be omitted.
This resulting formula gives the value of the solid-liquid adhesion work without the need of including any contact angle in the equation:

$$W_a = \gamma_{LV} + \frac{\int F\, dz + \Delta A \cdot \gamma_{LV}}{\Delta B}. \quad (6)$$

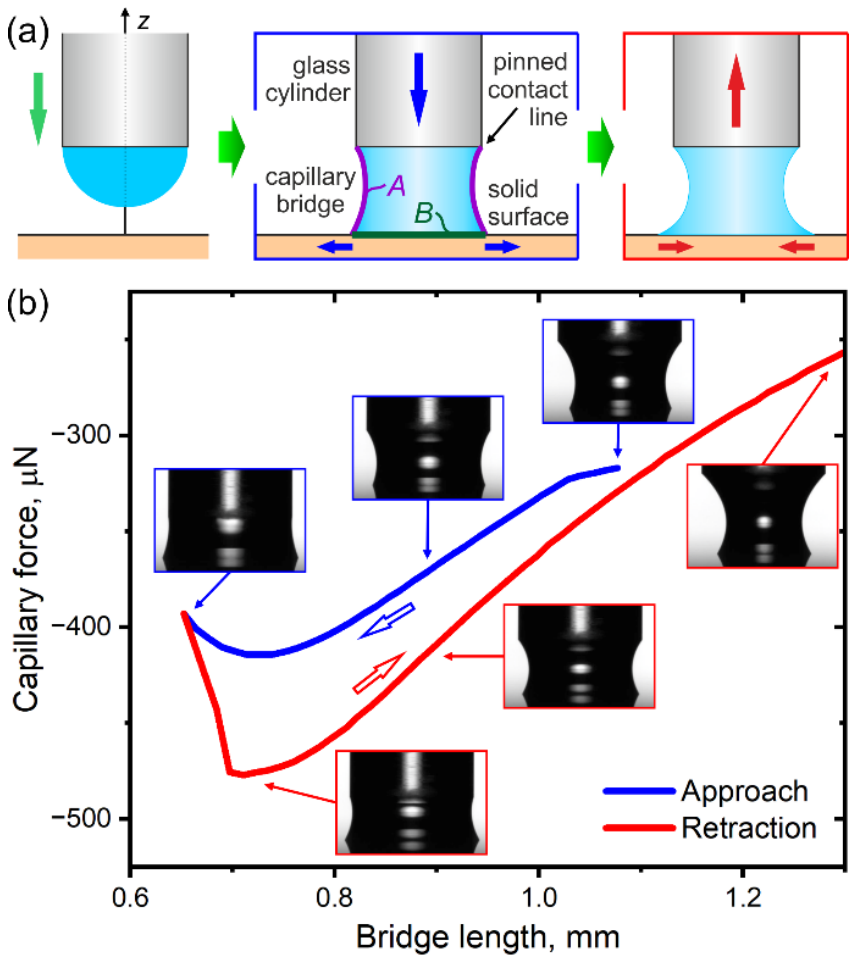

Figure 2.9 (a) Schematics of the measurement steps. The liquid bridge is formed from a pedant drop. The contact line advances and recedes on the investigated surface, as the bridge length is decreased and then increased. During the length change, the image of the liquid bridge is captured and the capillary force is measured. The z axis is the axis of cylindrical symmetry. (b) Capillary force as a function of the bridge length measured on a hydrophilic (Si_3N_4) surface. The insets show captured images of the water capillary bridge. The diameter of the cylinder is 2 mm.

Integration between the start and end points of approach and retraction gives the mechanical work done in the advancing and receding phases, respectively. The change of interfacial areas can be determined by simple image analysis in cylindrically symmetric case. Therefore, the solid-liquid adhesion work can be calculated according to Equation (6) for both the advancing and receding contact lines.

In conclusion, there is a century-old need for directly measured adhesion work values. The method determines the solid-liquid adhesion work directly and both for advancing and receding scenarios without any model assumptions. In advancing situation, the adhesion work quantifies the driving force behind spreading, while it gives the work required to remove the liquid from a unit of solid surface in receding case. The presented method provides an absolute, thermodynamic quantity, hence it is insensitive to the measurement parameters, and furthermore the resulting values can be used directly for further calculations, e.g. in the various surface free energy models. The method can be applied easily using commercial tensiometers equipped with an optional commercial camera module or with a laboratory-built one. [Ref.2.6-Ref.2.8]

Optical calibration of the ellipsometric mapping tool from cheap parts

VOC-DETECT M-era-Net project, OTKA NNE 131269

B. Nugusse[1,2], Gy. Juhász[1], Cs. Major[1], P. Petrik[1,4], S. Kálvin[1], Z. Gy. Horváth[3], M. Fried[1,2]

[1]Institute of Technical Physics & Materials Science, Centre for Energy Research, Hungary
[2]Institute of Microelectronics and Technology, Obuda University, Hungary
[3]Institute for Solid State Physics & Optics, Wigner Research Centre for Physics, Hungary
[4]Department of Electrical Engineering, University of Debrecen, Debrecen, Hungary

Non-destructive techniques are important methods to use during all stages of the thin film processes. Spectroscopic Ellipsometry (SE) is one of such methods. SE is a non-destructive, noninvasive and non-intrusive optical technique. It is a technique that measures the change in polarization state of the measurement beam induced by reflection from or transmission though the sample. Ellipsometry measures the amplitude ratio (tan ψ) and phase difference (Δ) between the parallel (p) and normal (s) polarizations. During data analysis, information about the system under the study is obtained by fitting measured ellipsometric spectra to optical and structural models, as ellipsometry does not give a direct information of the sample in consideration.

The purpose of this work is to make a well calibrated prototype optical mapping tool for thin film measurements using only cheap parts such as an LCD monitor and a pinhole camera [1-3] with CMOS Sensor with Integrated 4-Directional Wire Grid Polarizer Array (Sony's IMX250MYR CMOS), shown in Figure 2.10. Our arrangement shows similarity to the solution of Bakker et al [Ref.2.12], using a computer screen as a light source and a webcam as a detector in an imaging off-null ellipsometer.

During the conventional ellipsometric mapping, the data collection is relatively slower and use a scanned small spot, while our new optical mapping tool from cheap parts measures a big area in one shot. Specifically, in this paper the special focus is on a newly developed calibration method. The thickness map result is independently cross checked using a commercial Woollam M2000 ellipsometer and the agreement is within 1 nm, which makes our optical mapping tool a good candidate for industrial purposes.

We know two industrial systems which are capable to measure big (square meter size) samples: Semilab FPT system (https://semilab.com/hu/product/799/fpt) and the Woollam AccuMap (https://www.jawoollam.com/download/pdfs/accumap-se-brochure.pdf) system. Both systems use “traditional” SE device (100 kUSD price) in special big moving/scanning system, measuring point-by-point the big samples. The Woollam brochure writes that "Data Acquisition Rate: < 6 seconds per point (includes time for movement to new point, automated alignment, and data collection)" so it can measure one big area during several 10 minutes. Our system can measure within seconds during one shot. The new concept of the non-collimated beam ellipsometer prototype is set up as shown in Figure 2.10

A LED-LCD monitor (or a TV), see Figure 2.10.a (C) serves as a polarized RGB colored light source for the built-in polarizer sheet, number 4 in Figure 2.10.b and a polarization sensitive camera behind a pinhole (7&8) together. The LCD monitor (Dell UltraSharp™ U2412M, GB-LED) is used in a 45-degree rotated position, measured by a digital angle gauge with 0.1 deg precision. In straight-through position, we can detect the extinction of the polarization sensitive camera better than 10^{-2}.

The polarization sensitive camera sensor (The Imaging Source Company’s DYK 33UX250 USB 3.0 Polarsens camera), see in Figure 2.10.a (A) and in Figure 2.10, serves the polarization state data, from 0, 45, 90, 135-degree rotation positions (plus 3 RGB colors in each position). This arrangement is equal to a conventional static photometric rotating analyzer ellipsometer.

The sample is illuminated by a non-collimated light through a fixed polarizer at an azimuth of 45 degrees to the plane of incidence. The reflected light passes through a virtual “rotating analyzer” and the intensity is captured by a two-dimensional position sensitive photodetector system at four different angular positions of the analyzer.

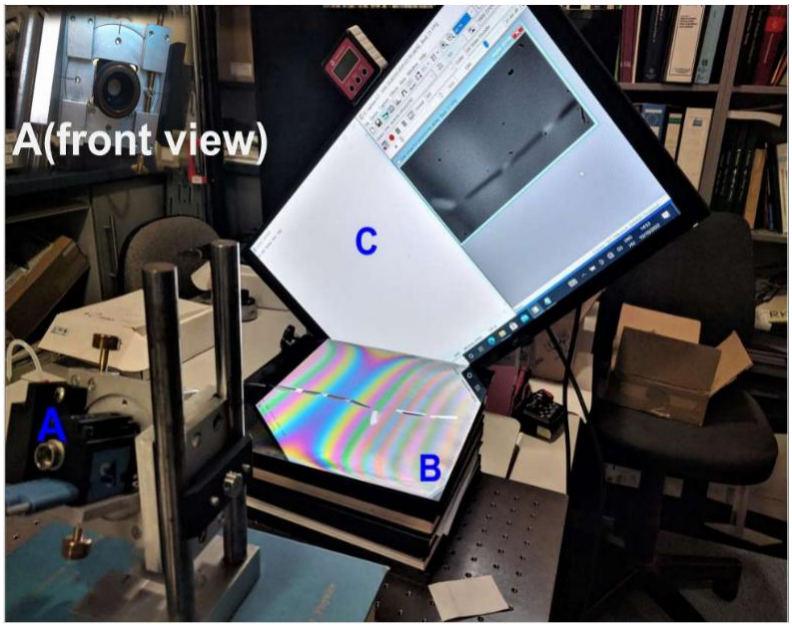

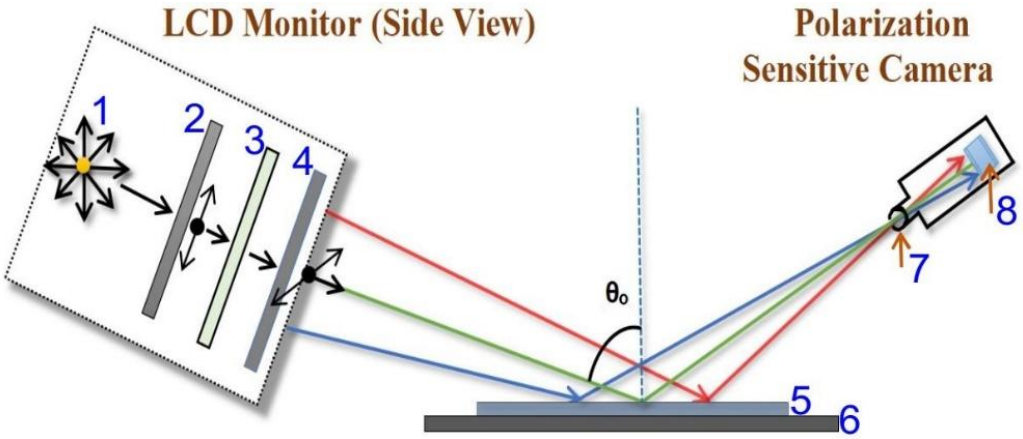

Figure 2.10 (a) Experimental set-up: A) Polarization sensitive camera B) Sample + Sample holder C) LCD monitor rotated into 45° position – Upper-left: the pinhole in front of the camera (b) Schematics of the non-collimated beam ellipsometer: 1) Light source 2) Vertical polarizer 3) Liquid crystal cell 4) Horizontal polarizer - (C) 5) Sample - (B) 6) Sample holder 7) Pinhole (sub-mm size) 8) Camera sensor (A)

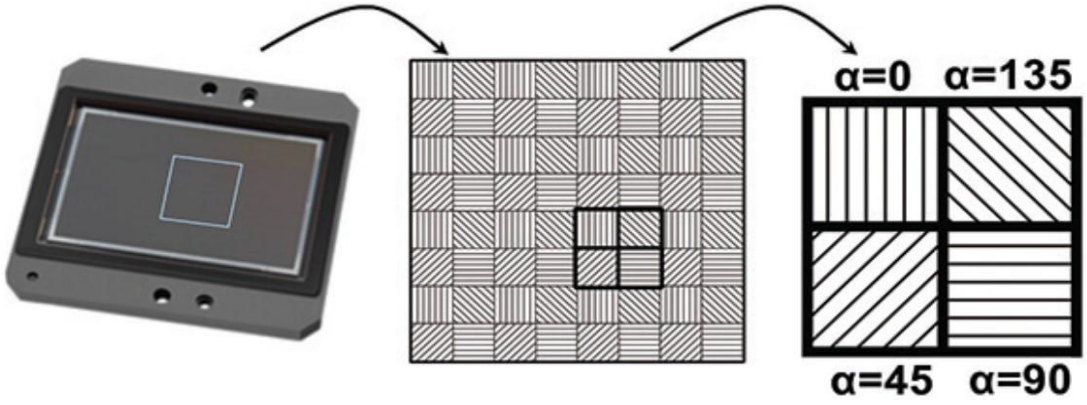

Figure 2.11 Schematic structure of a 2/3 inch Sony CMOS Pregius Polarsens sensor (IMX250MZR) a). Camera sensor b). Polarizer array matched to detector pixels c). Unit cell (Super pixel)

Minimum 3 different analyzer positions are required. These four polarization states (intensity) data (at 0, 45, 90, 135-degree rotation positions) are enough (the fourth date is good to reduce the error) to determine the ellipsometric angles: ψ and Δ. Our camera serves the data for 3 colors, so we have 3x2 measured ψ and Δ. Schematic structure of a 2/3-inch Sony CMOS Pregius Polarsens sensor (IMX250MZR) is shown in Figure 2.11.b and Figure 2.11.c. The main advantage of the assembly is that no moving parts in the system!).

It is a common scientific practice to check any device or a setup for an accuracy and precision and trying to correct any errors or malfunctions on the setup through calibration and comparing with other corresponding standard models. Accordingly, a direct monitor measurement is taken in our setup and we noticed, rather confirmed, that we need error correction and calibration of the experiment setup.

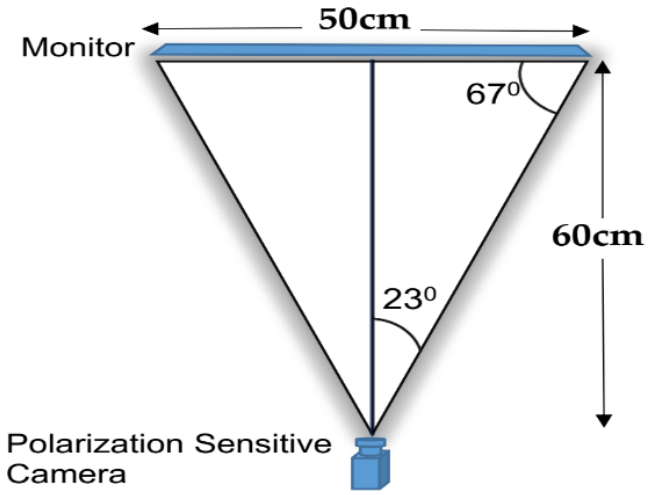

Figure 2.12 Schematic drawing of the direct ellipsometric measurement of monitor.

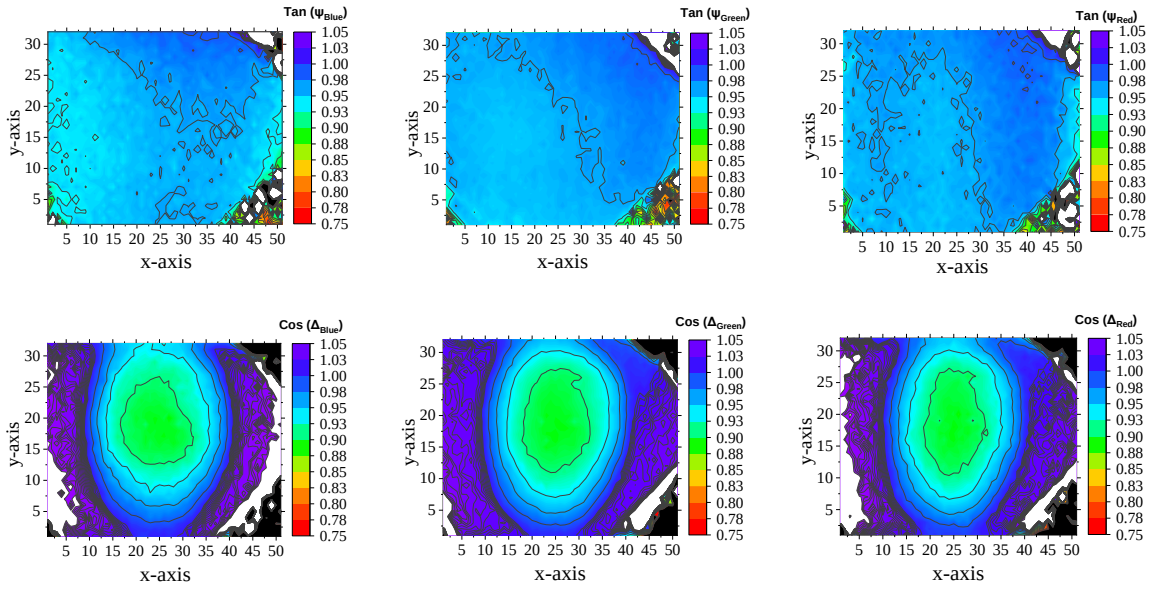

Figure 2.13 3D experimental results of tan ψ and cos Δ values for each color from the direct monitor measurement. Note that the x and y-axes of our figures represent the pixel group in the sample, 51x32 and the z-axis (color band) shows the range of the measurement values in each corresponding category, depending on the type of the map.

Theoretically, perfect linearly polarized light is coming from the monitor at 3 different (red, green, blue) light-bands. We directed the camera to the monitor performing a direct ellipsometric measurement without a sample, see Figure 2.12. If we have an ideal sample which do not change the polarization state then we measure tan ψ and cos Δ values to 1 in each point. This measurement shows the fact that a point-by-point ρ-correction calibration is needed.

Figure 2.13 shows the result of direct-monitor measurements, tan ψ and cos Δ values for each color, Red, Blue and Green. The systematic alterations from 1 in the maps show systematic measurement errors in our optical mapping tool that justify the need for a special calibration. Three SiO_2/Si samples of nominally 40, 60 and 100 nm thickness were used for the calibration process and another nominally 80 nm SiO_2/Si sample was analyzed using the calibration values from the three oxide samples. The experimental data is collected for each three oxide samples and then, six different positions of each sample was used in the calibration process. The experimental figures shown in this paper are mostly deduced by excluding pixels with high MSE values that deviate the results from the true expected values, prioritizing points of only low MSE. Figure 2.14.b shows the MSE-map of the central 20x15 cm part where the measurement proved to be reliable.

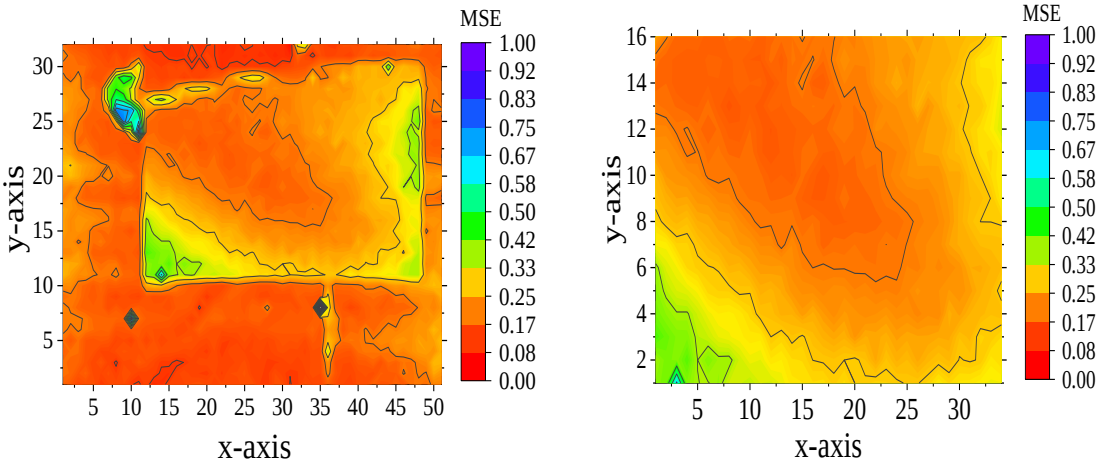

Figure 2.14 (a). Merged MSE full map and (b)low MSE pixels map

Monitor-correction are calculated using the following equation:

*ρopt=ρmeas*ρmonitor (different for each point and each wavelength)*

where ρ_{opt} is the measured value with perfect light source, ρ_{meas} is the actually measured value and $\rho_{monitor}$ is the ρ-correction. We measure three SiO_2/Si samples with different thicknesses. We determine 3*N*2 ψ and Δ (where N is the number of different wavelengths, presently 3) and we should calculate (fit) 2*N+3+1 unknown calibration values for a full calibration: N*real ($\rho_{monitor}$) and N*im($\rho_{monitor}$) + 3 thicknesses + 1 actual angle of incidence in each points and each wavelength. Each thickness and angle-of-incidence in the sample depends only on location, but the ρ-corrections ($\rho_{monitor}$) are location and wavelength dependents. This implies ρ-corrections give more insight on the nature and status of the sample measurement.

The result of the angle-of-incidence calibration is shown in Figure 2.15. Using the same criterions (low MSE, smooth map), we refined the angle-of-incidence map (Figure 2.17.b) from the angle-of-incidence full map (Figure 2.17.a). As it can be seen in Figure 2.17.b, the angle-of-incidence varies smoothly across the surface, which agrees with the theoretical values. This refined angle-of-incidence map was used later to evaluate the nominally 80 nm SiO_2/Si sample thickness map.

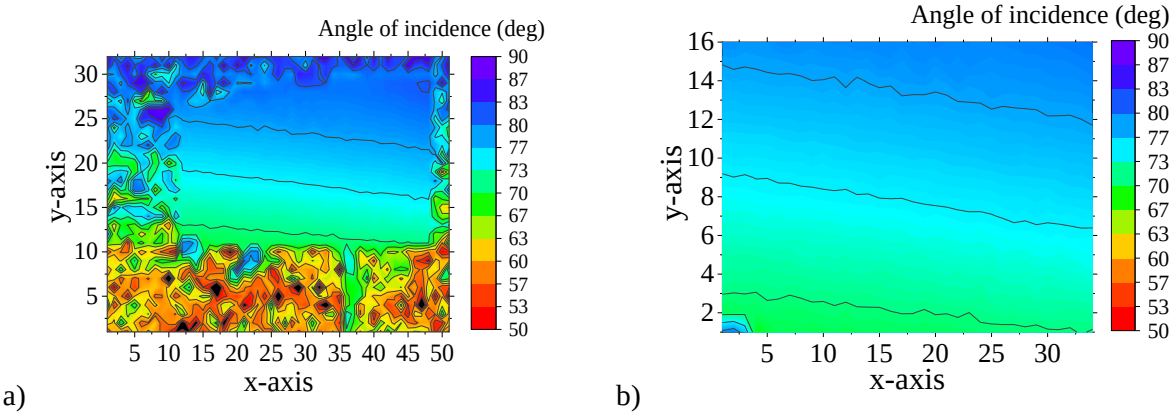

Figure 2.15 a). Angle of incidence full map b). Angle of incidence with high MSE pixels removed

The same calibration process resulted the thickness maps of our calibration oxide samples (nominally 40, 60 and 100 nm thickness) which are shown in Figure 2.16

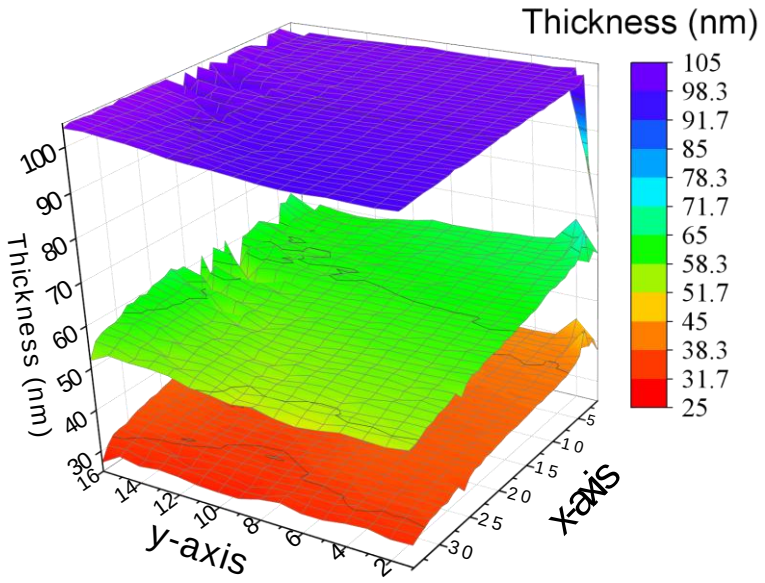

Figure 2.16 Thickness maps of nominally 40 nm, 60 nm and 100 nm of SiO2/Si samples (low MSE areas) from the refined central 20x15 cm part.

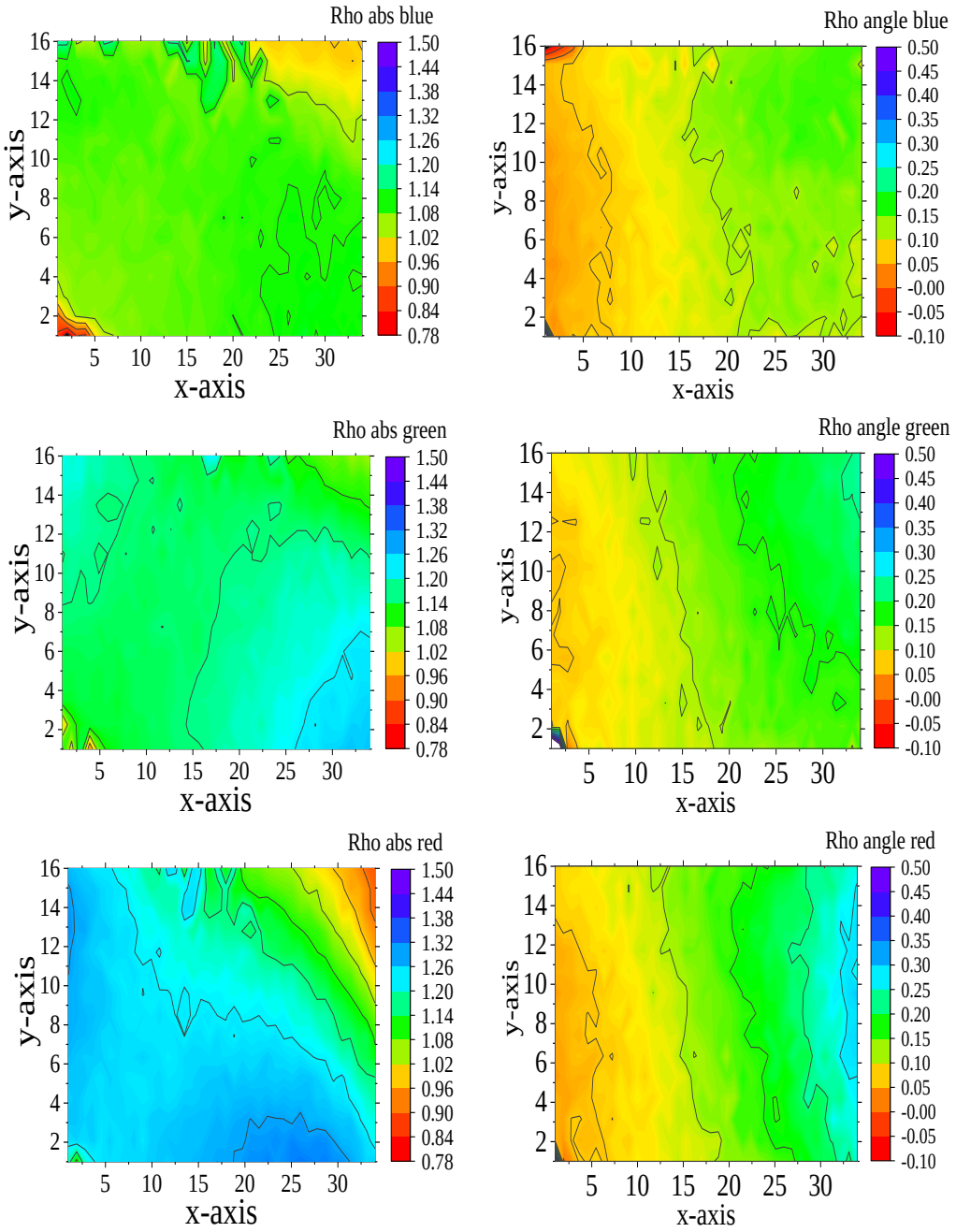

Figure 2.17 The calibrated $\rho_{monitor}$ values. Left column: real ρmonitor, right column: phase shift-correction in rad. Upper row: blue (450 nm), Middle row: green (550 nm), Lower row: red (650 nm).

The calibrated ρmonitor values for the specific setting of the device are also mapped, see Figure 2.17. These values differ only by less than 0.3 from the ideal values, so we can use them to evaluate independent measurements.

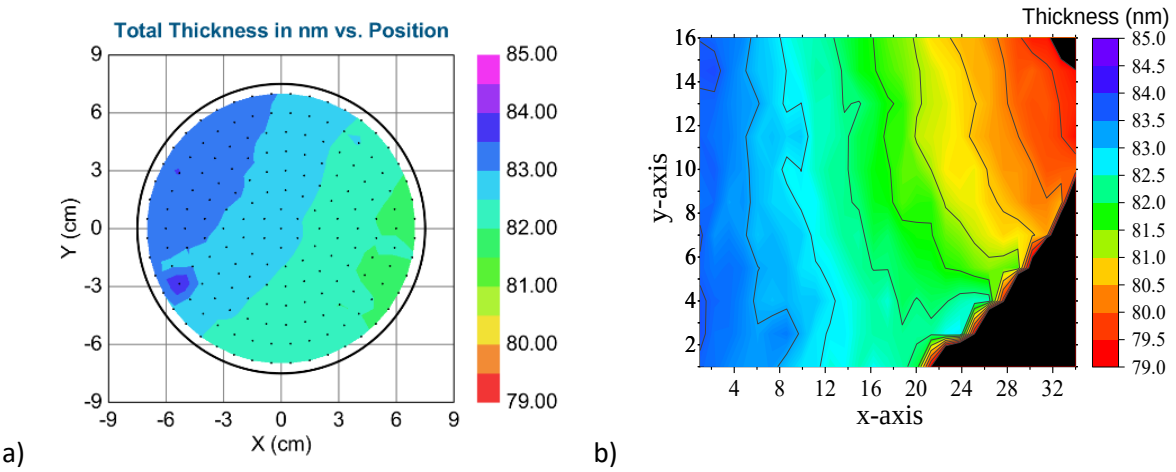

Figure 2.18 (a) Nominally 80 nm oxide sample thickness map by Wollam M2000 SE (Note, that our M2000 can map only the central 14 cm diameter area of the 20 cm diameter sample (b) Thickness map of same SiO2/Si sample 20x15 cm area by the non-collimated, calibrated mapping tool.

We used a nominally 80 nm thick, 20 cm diameter SiO_2/Si sample to check the results of the calibration. We used the calibrated $\rho_{monitor}$ values to correct the measured ellipsometric angles and used the corrected values to determine the thickness map. The thickness map of the 80 nm oxide sample in Figure 2.18.b appears to be smooth enough. Note, that one color in Figure 2.18 is only 0.5 nm.

An independent checking measurement of the same sample was also made by the Wollam M2000 ellipsometer, as shown in the Figure 2.18.a The agreement of the thickness measurement made between our non-collimated ellipsometer after correction, and the conventional Wollam M2000 ellipsometer is only within 1 nm, which is a good agreement. [Ref.2.9-Ref.2.11, Ref.2.13]

Optimized Sensing on Gold Nanoparticles Created by Graded-Layer Magnetron Sputtering and Annealing

TKP2021-EGA-04, OTKA K 131515, OTKA K 146181, EMPIR POLight 20FUN02

D. Mukherjee, K. Kertész, Z. Zolnai, Z. Kovács, A. Deák, A. Pálinkás, Z. Osváth, D. Olasz, A. Romanenko, M. Fried, S. Burger, G. Sáfrán, P. Petrik

Gold nanoparticles (GNPs) possess optical properties making them especially suitable for plasmonic sensing. They are less than pristine, however, when it comes to the most common methods for fabricating them. These methodologies—electrochemical deposition, chemical methods, and physical vapor deposition—almost always yield GNPs with a uniform layer of gold. We know from working with metal nanoparticles in general that the optical properties of a particle are not just a function of the material, but also of its structure. That is why this work aims to methodically vary the deposition thickness, and the subsequent annealing (heating) of the deposited material to explore the three-dimensional structural evolution of GNPs [Ref.2.14, Ref.2.15]. The GNPs produced because of these explorations have been used to perform a series of optical characterizations that themselves serve as a basis for understanding the appearance and disappearance of the GNPs' optical sensing capabilities.

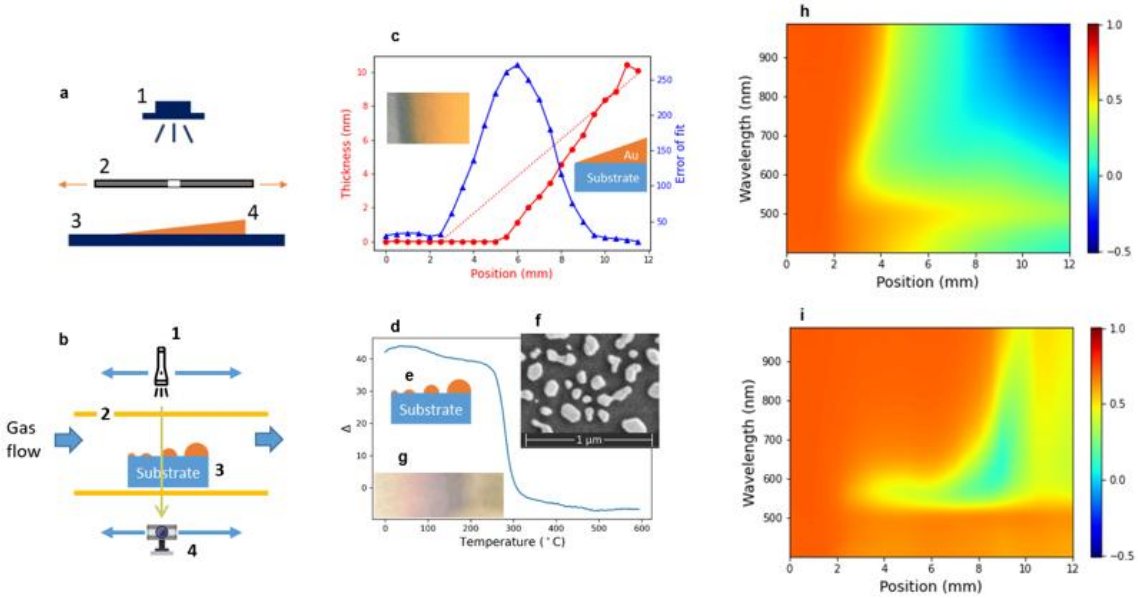

Figure 2.19 (a) Schematic view of the micro-combinatorial sputtering method [Ref.2.17] (b) Configuration of the optical transmission cell. (c) Thickness (red circles), effective thickness [Ref.2.18] corresponding to the deposited amount of material (dotted line), and error of fit for the as-deposited graded Au sample measured by ellipsometry. (d) Change of Δ measured by ellipsometry as a function of temperature during annealing at the λ = 632.9 nm and position of 8 mm on sample (e) Schematic, (f) SEM (at a position of 8 mm), and (g) optical images on the sample after annealing. (h) and (i) show m33 spectra on sample over the range of positions from 0 to 12 mm for the as deposited and 300 ◦C annealed state, respectively.

A graded-layer deposition approach was employed, where gold thickness varied from 0 to 20 nm across the substrate. After thermal annealing, the gold layers self-assembled into nanoparticles, forming distinct size and spacing distributions along the substrate [Ref.2.16]. At thin deposited layers (~1–2 nm), the nanoparticles were small and well-dispersed. At 3–7 nm, the particles coalesced into interconnected island-like structures. Beyond 7 nm, a continuous gold film formed, and the plasmonic properties of the system were reduced (Figure 2.19). Scanning electron microscopy (SEM) was used to confirm that the

mass thickness of deposition affected particle shape: the particle shape transitioned from oblate to hemispherical as thickness (and deposited mass) increased, affecting the near-field optics. The electron oscillation that resulted in the appearance of the local surface plasmon resonance (LSPR) peak was timelined to the onset of a hydrodynamic regime in finite element method (FEM) calculations [Ref.2.19].

Ellipsometry and transmission spectroscopy were used to analyse the optical response of the layers. The LSPR effect was observed, where electrons oscillated collectively at specific wavelengths depending on nanoparticle size and spacing. The LSPR peak appeared at ~550–600 nm for thinner layers (2–4 nm effective thickness). For thicker layers (>7 nm), LSPR diminished, indicating a loss of discrete plasmonic behaviour (Figure 2.20). The experimental results were validated by FEM simulations predicting similar trends.

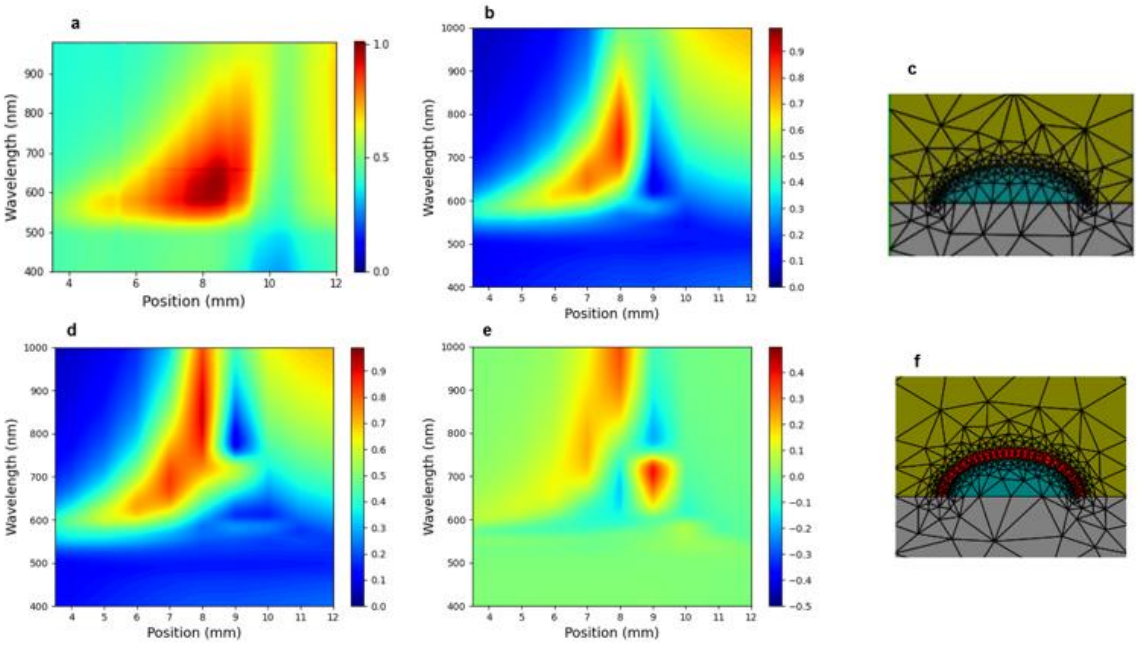

Figure 2.20 Reflectance spectra measured along the sample and (b) simulated at normal incidence using (c) a FEM model. (d) Reflectance spectra calculated for the same structure with (f) a model using an overlayer with a thickness of 2 nm and $n=1.45+0.01/\lambda^2$, where the unit of λ is in μm. The differences between (b) and (d) are plotted in (e).

We also conducted systematic evaluations of ethanol, water, and Raman reporter molecules as test analytes, correlating sensing efficiency with the deposited gold thickness and nanoparticle morphology. Optical transmittance spectroscopy was used to show that the refractive index altered upon ethanol and water adsorption, shifting the LSPR peak accordingly [Ref.2.20]. The best performance was recorded at a gold thickness of ~3.2 nm. This was the transition region where the nanoparticles were still discrete but had strong plasmonic coupling. Above ~ 7 nm, the sensing capability declined, as we moved into a region that behaved more like bulk gold and had less plasmonic enhancement.

Surface-enhanced Raman Spectroscopy (SERS) was then used to probe our system and to see if we could take advantage of the intense electric fields to observe molecular signals. The most intense signals were recorded at 1.6-2 nm gold thickness, under the same conditions where we were getting near-field enhancement. The interparticle gap, most importantly its ratio to the particle size, was also critical. FEM calculations were performed to model the optical responses of gold gratings under various conditions. We were able to successfully corroborate with the simulations the limits of detection based on the geometry of the nanoparticles and the changes in refractive index.

We confirmed the shifts in the LSPR peak as a function of the size, spacing, and environmental refractive index of the nanoparticles, along with the surface coverage effects on resonance behaviour and the enhancement factors for SERS-based molecular detection. This research demonstrated that the combinatorial sputtering technique can theoretically be applied to the scalable, precise, and reproducible fabrication of optimized gas and molecular sensors based on plasmonic structures. Optimized gold nanoparticle thicknesses of about 2-3 nm offered the best overall performance.

These research findings also have implications for bimolecular (virus, protein) detection applications. Therefore, the anisotropic control of the GNPs along with the precise control of the gap widths significantly enhances the gas and molecular detection capabilities of the plasmonic sensors.

Optimization of SnO2/ZnO Films for Electrochromic Coloration Efficiency

OTKA K 143216, OTKA K 146181 and TKP2021-EGA-04

Z. Lábadi, N. T. Ismael, P. Petrik, M. Fried

Electrochromic applications for metal oxides, such as smart windows and displays, have been widely studied recently. Electrochromic films decrease the extra absorption of heat in buildings. The electrochromic process is based on a reversible redox process and characterized by coloration efficiency (CE). Transition metal (titanium, tungsten, nickel, vanadium, molybdenum and others) oxide films are the most interesting and most widely studied materials for this purpose [Ref.2.21]. Nevertheless, relatively few publications have studied the possible advantages (higher CE) of the mixtures of different metal oxides as electrochromic materials. The change in light absorption for the same electric charge represents the electrochromic effectiveness, and it can be higher in mixed metal oxide layers.
Spectroscopic Ellipsometry (SE) has been used as an investigation method for combinatorial or pure materials since it is a cost-effective, non-destructive and fast method for the mapping of mixed oxide layers. A thickness map and a composition map have been achieved by the developed optical models of the sample layers.

The objective of this work was to determine the CE and to investigate the electrochromic effectiveness of SnO_2-ZnO mixed layers in the full compositional range. Mixed oxide layers were prepared by reactive DC magnetron sputtering. It should be noted that we apply a combinatorial approach for composition-graded layer deposition to allow study samples chosen from a full and continuous $SnO_{2(x)} - ZnO_{(1-x)}$ composition range. The deposited films were characterized using spectroscopic ellipsometry (SE), Scanning Electron Microscopy (SEM) with Energy-Dispersive X-ray Spectroscopy (EDS) and coloration efficiency (CE) measurements. We expected that mixing metal oxides with different sizes in films can enhance the CE.

Metallic Sn and Zn targets were placed separately from each other, and indium–tin-oxide (ITO)-covered glass and Si-probes on a glass substrate (30 cm × 30 cm) were moved under the two separated targets (Sn and Zn) in a reactive argon–oxygen (Ar-O_2) gas mixture (see Figure 2.21). The tin-zinc oxide layers were deposited onto ITO-covered 100 × 25 mm glass surfaces. Layer depositions were carried out by reactive sputtering in an (Ar + O_2) gas mixture at a ~2×10^{-4} Pa base pressure and at a ~10^{-1} Pa process pressure. The target–substrate working distance was 6 cm. Volumetric flow rates of 30 sccm/s Ar and 70 sccm/s O_2 were applied in the magnetron sputtering chamber. The plasma powers of the Sn and Zn metal targets were set to 800 and 1000 W, respectively. The samples were moved back and forth at a 25 cm/s walking speed between the Sn and Zn targets, and a mixed oxide film was deposited onto the ITO surface. A 5 min cooling interruption was applied after every 50 walking cycles.

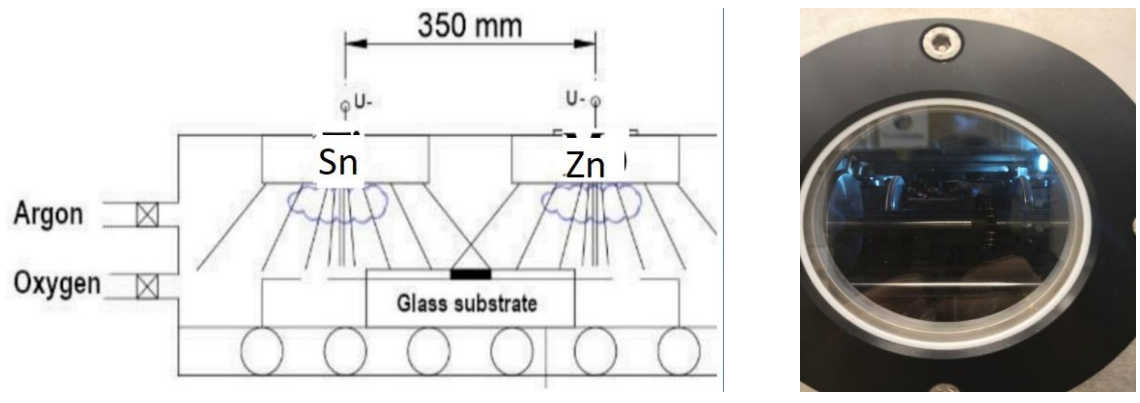

Figure 2.21 Target arrangement for combinatorial deposition and an insight into the chamber

Coloration Efficiency η is given by the following equation:

$$\eta(\lambda) = \frac{\Delta OD(\lambda)}{q/A} = \frac{\ln(\frac{T_b}{T_c})}{Q_i}$$

where Q_i is the electrical charge inserted into the electrochromic material per unit area, ΔOD is the change in optical density, T_b is the transmittance in the bleached state, and T_c is the transmittance in the colored state. The unit of CE is cm^2/C (square centimeters per Coulomb).

The CE was determined in a transmission electrochemical cell (see Figure 2.22). The cell was filled with 1 M lithium perchlorate ($LiClO_4$)/propylene carbonate electrolyte. A 5 mm width masked (Sn-Zn oxide-free) ITO strip of the slides remained above the liquid level, allowing direct electric contact with the cell. A Pt wire counter electrode was placed into the electrolyte alongside a reference electrode. This arrangement was a fully functional electrochromic cell. The applied current was controlled through the cell using a Farnell U2722 Source Measurement Unit (SMU). A constant current was applied through coloration and bleaching cycles of the electrochromic layer, and simultaneous spectral transmission measurements were performed by using a Woollam M2000 spectroscopic ellipsometer in transmission mode.

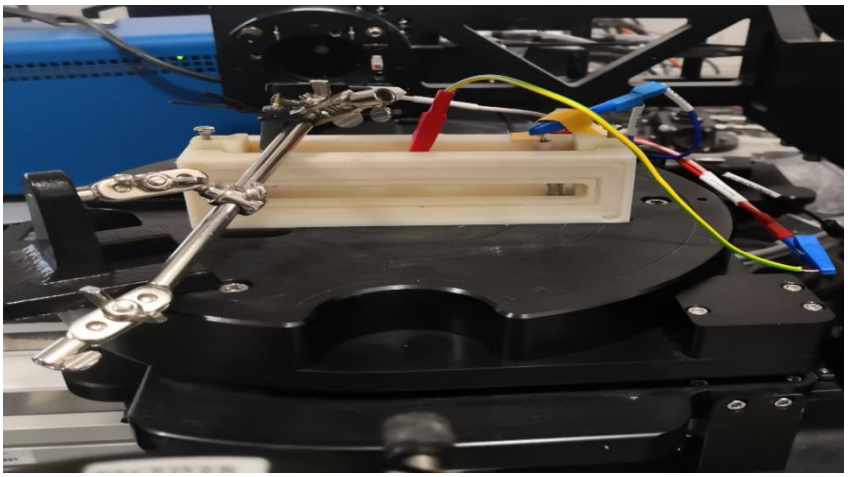

Figure 2.22 Setup for transparency measurements during coloration – bleach cycles

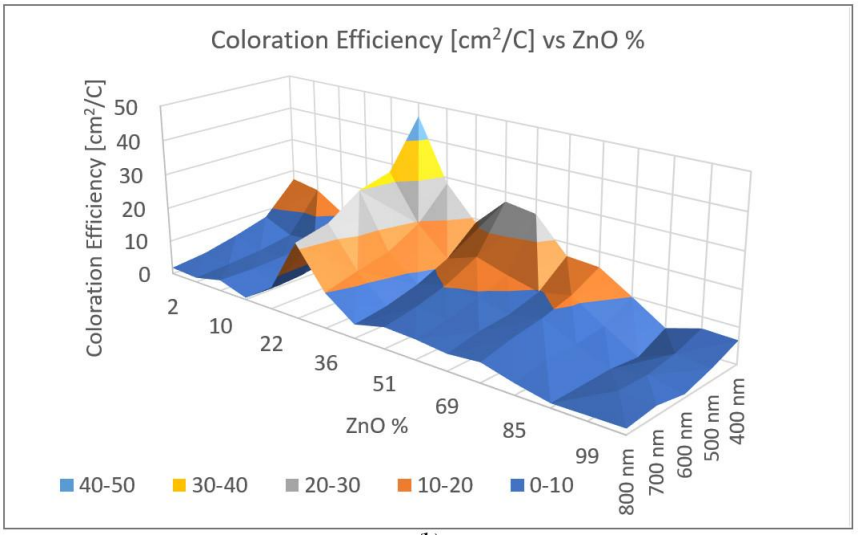

Figure 2.23 Three-dimensional diagram of CE data of SnO_2-ZnO vs. Zn % for wavelengths from 400 to 800 nm in visible spectral range.

Figure 2.23 shows the 3D representation of the calculated CE data as a function of the ZnO fraction of the film and the wavelength. Individual points were calculated from the average of three independent measurements. The error is estimated to be 3%, calculated based on the accuracy of sample positioning in the measuring cell and the spot size of the optical beam.

The CE maximum was found to be 29% Zn for each wavelength between 20 and 50 cm^2/C. This 29% is very close to the optimum value of 30% in the case of the TiO2-SnO2 mixture which was investigated in our earlier paper [Ref.2.22]. We expected that mixing metal atoms with different diameters in the layers can enhance the CE. This (70–30)% mixture of different metal oxides seems to be the optimum for Li-diffusion in these sputtered materials.

The influence of mixing metal atoms with different diameters in the layers on EC behavior can be attributed to several factors. Mixing can create new pathways for charge carriers, enhancing the overall electrical conductivity. This increased conductivity can support faster ion intercalation and deintercalation processes, causing quicker color changes. Mixing can alter the electronic structure of the layer, affecting the way it absorbs and transmits light. These factors can explain the enhanced CE values [Ref.2.23].

Magic mirrors of the Orient: analogies and inspirations in optics

F. Riesz

Magic mirrors (in Japanese, Makyoh) are ancient metallic mirrors with a backside relief pattern, originating from China and Japan. If a light beam falls on the mirror surface, an image is projected on a distant wall that resembles the back pattern as if the mirror was transparent (Figure 2.24) [Ref.2.24]. These mirrors fascinated laymen and scholars alike during centuries, and from the 19th century, when Western scholars became aware of these mirrors, till recent days, they have been actively studied. It was clarified that a nearly invisible surface relief is formed on the polished front face during manufacturing by mechanical means of the back relief, and the image is created by the local deflection of the reflected rays by this front relief [Ref.2.24]

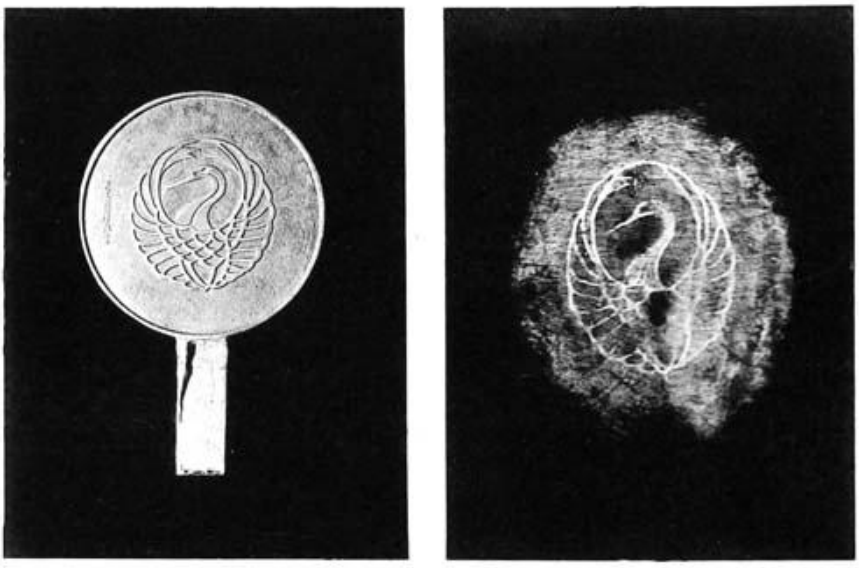

Figure 2.24 A Japanese magic mirror: backside and projected image (from [Ref.2.24] public domain).

Analogies to ancient, pre-technology artifacts have always played a significant role in modern scientific and technological advances by providing foundational insights, inspiring new ideas and presenting complex problems in accessible ways. Magic mirror related phenomena also represent an interesting chapter of optics: In addition to the well-known ‘Makyoh topography’ application, used mostly for the visualisation of surface defects of semiconductor wafers, magic mirrors and their fabrication method serve as analogies of several optical and other technological phenomena. In the following, we briefly review the most important analogies and connections to problems in optics and other areas of technology.

Optical modulators—The traditional fields of optics deal with ray/wavefront propagation through lenses and mirrors, that is, spherical surfaces/interfaces arranged in rotational symmetry along an axis. However, areas of advanced optics aim at direct manipulation or structuring a wavefront, changing its intensity, phase or polarisation in a spatially addressed arbitrary manner. Magic mirror thus appears as an ancient form of a 2D light modulator, as well as serves as a useful and illustrative analogy [Ref.2.25]. It is not an exaggeration to state that the ancient magic mirror was the first high-tech optical device, achieving spatially resolved control of wavefronts with phase changes in a wavelength-range precision, using the backside height relief as the ‘input data’.

Freeform optics—Magic mirrors satisfy the basic definition of freeform optical elements defined most simply as having surface shape that lacks translational or rotational symmetry [Ref.2.26].

Flat optics—Certain magic mirrors can be regarded as flat optical elements (although most magic mirrors are convex, the convexity is not a prerequisite of operation and globally flat magic mirrors do exist).

Mechanical fabrication method—Backside patterning and subsequent polishing of a metallic plate can induce small deformations in the front surface, similarly to the ancient magic mirror [Ref.2.27]. With carefully chosen materials and processing parameters, reproducible, high-precision shaping in the submicron range can be achieved.

Deformation induced by buried stressors—Subsurface (or interface) inclusions or voids induce a surface deformation of a plate or layered system, especially if the surface is machined in some way. This effect, which is basically the main principle of the magic mirror operation, is frequently observed in machining and technology. Notable examples are backside (or interface) contaminant particles in wafer polishing (wafer bonding), and surface bulging in metal foams at near-surface pores [Ref.2.28].

Non-visible and non-photonic imaging—Analogies to magic mirror imaging extend beyond light optics to other fields where the same governing laws are in effect. Mirror electron microscopy is such a method [Ref.2.29] here, the object is illuminated by an electron beam, and the sample is electrically biased to reflect the electrons before reaching the sample. Variations of surface height and chemical composition cause variations of the equipotential surfaces, causing reflection of different angles across the sample, similarly to a magic mirror surface, thus the reflected beam then forms an image. Another analogous method is the propagation-based X-ray phase-contrast imaging [Ref.2.30] used as an extension of traditional radiography. The studied object is illuminated by X-rays and the transmitted beam is imaged by a screen placed some distance away. The beam, in addition to the absorption, suffers local deflections due to changes in the net refractive index of the material along the X-ray path due to changes in density and chemical composition (Figure 2.25). The mechanism of image forming is thus similar to that of the magic mirror, improving the imaging of weakly absorbing samples.

Optics education—the catchy and intriguing principles of magic mirrors aid in understanding of ray optics and image formation principles [Ref.2.31].

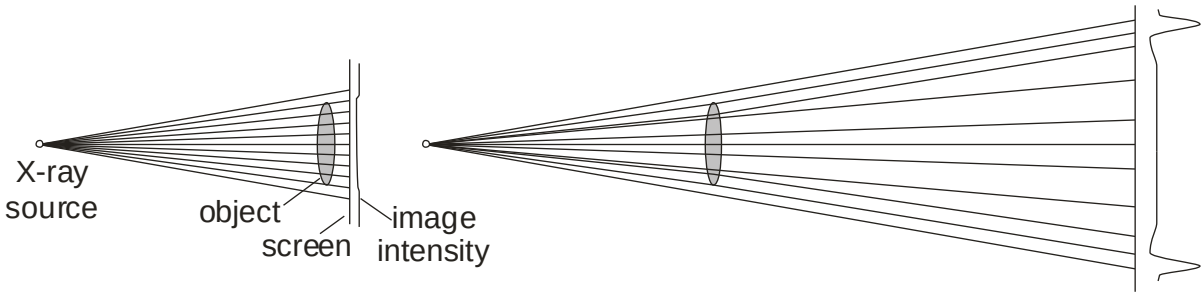

Figure 2.25 Propagation-based X-ray phase-contrast imaging: traditional method; weak absorption contrast (left), improved imaging due to edge enhancement—'magic mirror' effect (right).

Thin Film Physics Department

Head: Dr. Katalin BALÁZSI, Ph.D., senior scientist

Research Staff
Alaa Almansoori, Ph.D.
Csaba Balázsi, D.Sc.
Ildikó Cora, Ph.D.
Zsolt Czigány, D.Sc.
Zsolt Fogarassy, Ph.D.
Klára Hajagos-Nagy, Ph.D.
Mónika Furkó, Ph.D.
Tamás Kolonits, Ph.D.
Viktória Kovácsné-Kis, Ph.D.
Béla Pécz, D.Sc., deputy general director of HUN-REN EK, MFA director
György Zoltán Radnóczi, Ph.D.
Adél Rácz, Ph.D.
György Sáfrán, C.Sc.
Attila Sulyok, Ph.D.
Péter B. Barna, D.Sc., Prof. emeritus
Miklós Menyhárd, D.Sc., Prof. emeritus
György Radnóczi, D.Sc., Prof. emeritus
János Lábár, D.Sc, Prof. emeritus

Ph.D. students
Dániel Olasz
Erzsébet Dódony
Maroua H. Kaou (Hungaricum stipendium)
Wasan Alkaron (Hungaricum stipendium)

Technical Staff
Andrea Jakab-Fenyvesiné
Andor Kovács
Balázs Erki
Valéria Osváth
Boglárka Ódor
Noémi Szász
Viktor Varga

The scientific results of the Thin Film Physics Department are related to thin film and ceramic fields. The main research topics are in line with modern trends of material science with the respect to a 50 years long history of the department.

The development of the 2D semiconductor, multicomponent thin films and technical ceramics were the important base research fields supported by several international basic scientific projects and collaborations in 2024.

The uniqueness of the Department in national and international level as well was the structural investigation of various materials by transmission electron microscopy (TEM). The effect of the structure on the developed material´s properties was demonstrated by TEM. It was demonstrated that the optimal structure can be directed in a controlled way. All topics were supported by methodical developments based on electron diffractions.

In 2024, 66 scientific publications (17 pc D1, 26 pc Q1) appeared in refereed journals with a cumulative impact factor of 309. In addition, 5 papers were published with no impact factor conference proceedings. Members of the group presented invited lectures, oral talks at national and international conferences. The group received ~ 4000 independent citations in the examined interval of the last two years.

Research members of the group lectured some courses at universities and held few laboratory practices. All courses were for full semester (Eötvös Lóránd University - ELTE, and Budapest University of Technology and Economics - BME, and University of Pannonia- UP and Óbuda University - OE). In addition, 4 PhD students were supervised.

A few national and international conferences were organized by Thin Film Physics group members:

- 48th International Conference and Expo on Advanced Ceramics and Composites (ICACC2024) USA – Balázsi Csaba, Balázsi Katalin (symposium lead org.)) Daytona Beach, USA 2024 January 23-February 2
- 14th International Conference on Ceramic Materials and Components for Energy and Environmental Systems (CMCEE14), HU - Balázsi Csaba, Balázsi Katalin (conference chairs) Budapest, 2024 August 18-22
- Annual conference of the Hungarian Microscopic Society 2024 (MMT) Siófok 2024 May – Pécz Béla, Lábár János Radnóczi Gy. Zoltán
- European Microscopy Congress, Copenhagen, 2024. August 25-30, International committee member, Kovácsné Kis Viktória
- 2ND International Summit on Graphene & 2D Materials (ISG2DM2024) Germany Munich 2024 May 20 –Balázsi Katalin (conference chair)

Social activity of the group is landmarked by nearly 20 memberships in different committees of the Hungarian Academy of Sciences and in boards of international societies (European and American Ceramic Society, International Ceramic Society, International Union for Vacuum Science).

Laser annealing improves quality of thin superconducting CoSi2 films

2019 2.1.7-ERA-NET-2022-00032 (QuantERA II SIQUOS)

J. L. Lábár, B. Pécz, Dumas[1], P., F. Gustavo1, M. Opprecht[1], G. Freychet[1], P. Gergaud[1], S. Kerdilès[1], S. Guillemin1, F. Lefloch[2] and F. Nemouchi[1]

[1] Université Grenoble Alpes, CEA LETI, 38000 Grenoble, France
[2] Université Grenoble Alpes, CEA IRIG, 38000 Grenoble, France

Quantum technology is regarded as a great promise for revolutionizing computational power. Its cornerstone is the practical realization of Qubits, the basic parts of quantum computers and additionally promising units as new type of sensors. Out of the many physically very different realizations of Qubits, solid state electronic devices using superconducting elements seem to be the most developed. The most serious question from the point of view of future applications is if mass production of reliable Qubits can be realized. The SIQUOS project promises to bring this goal closer by manufacturing Qubits compatible with standard Silicon CMOS technology. For that reason, only Si-compatible materials and technology-steps are used in the project. The Qubit developed in SIQUOS is a gatemon, which contains a single gate-controlled Josephson junction (JJ) with superconductor/semiconductor hybrid nanostructure. Such a JJ follows the geometry of a metal-oxide-semiconductor (MOS) field-effect transistor (FET) with superconducting source and drain (S/D) contacts. When transparency is good between the S/D contacts and the semiconductor channel and the length of the gate is short enough, a non-dissipative super current flows in the device whose amplitude can be controlled by the gate. This is the working principle of a JoFET.

SIQUOS project experiments are carried out with different superconducting materials to obtain the best performance JoFET. One of those superconductors is CoSi2. Best parameters require thin (≤10nm) CoSi2 films with uniform thickness and as smooth Si/CoSi2 interface as possible. Standard self-aligned-silicidation (SALICIDE) process is based on a two-step rapid thermal annealing (RTA) of the layer first at 500°C (to form CoSi) and the second at 700°C (to transform CoSi to CoSi2). Although this process is good for standard transistors with thicker layers, the wavy Si/CoSi2 interface and the ensuing varied layer thickness formed by this process is unfavourable for the JoFET. The new laser annealing heat treatment developed in the project solves this problem by producing smoother interface and more uniform layer thickness [Ref.3.1]. Electrical measurements proved better superconductivity, too. The improvement is explained by single-step formation of CoSi2 (skipping CoSi phase). The Figure 3.1 illustrates this improvement. SREF: CoSi2 layer made by standard SALICIDE process; S1: CoSi2 layer made by a single laser shot; S100: CoSi2 layer made by 100 laser shots.

The SIQUOS project (grant no. 2019-2.1.7-ERA-NET-2022-00032) was supported by the National Research, Development and Innovation Fund.

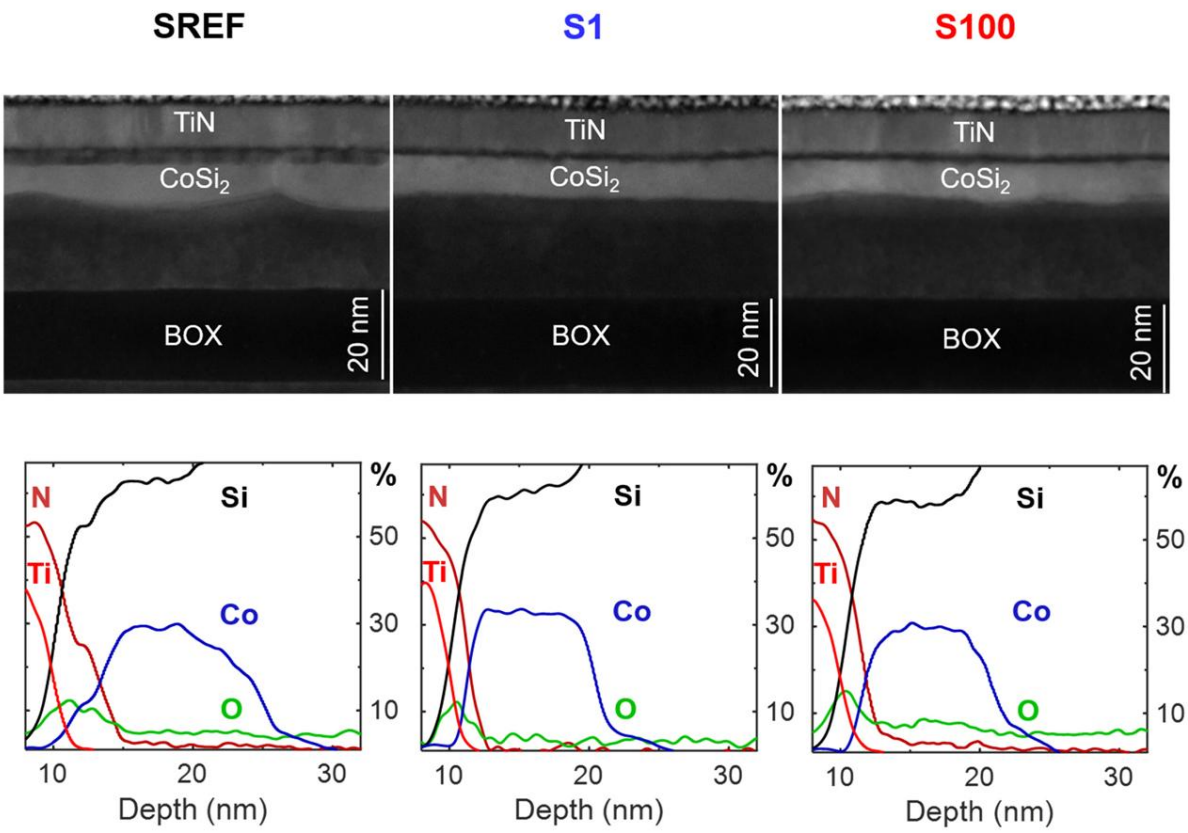

Figure 3.1 Cross-sectional STEM image and EDS element profiles related to SREF, S1 and S100. The depth origin in EDS profiles is situated at the TiN surface.

Synthesis and Properties of Cr-Hf-Mo-Ta-W Multicomponent Carbide Thin Films

Zs. Czigány, T. Stasiak[1], S. Debnárová[1], S. Lin[1], N. Koutná1, K. Balázsi, V. Buršíková[1], P. Vašina[1], P. Souček[1]

[1] *Department of Physical Electronics, Faculty of Science, Masaryk University, Brno, Czech Republic*

This study demonstrates the synthesis of multicomponent carbides with NaCl-type fcc structures using reactive DC magnetron sputtering and explores the influence of deposition conditions on the structural and mechanical properties of thin films in the Cr-Hf-Mo-Ta-W system [1]. The deposition process was conducted in an argon atmosphere with varying acetylene flows (0–12 sccm) at ambient and elevated temperatures (700 °C). These conditions either hindered or promoted adatom diffusion, significantly affecting the resulting film structures and phases.

Structural analysis (XRD; TEM in Fig.3.2.) revealed that films deposited without acetylene formed a bcc metallic phase with lattice parameters ranging from a = 3.188–3.209 Å, in agreement with density functional theory (DFT) calculations of lattice parameters as a function of carbon content. A bcc-to-fcc phase transition occurred with increasing acetylene flow, facilitated by the formation of an amorphous intermediate phase likely caused by limited a mobility. At higher acetylene flows, an fcc multielement carbide phases grew with lattice parameters of a = 4.33–4.49 Å. Crystalline films exhibited a columnar morphology, whereas amorphous films were dense and featureless.

Mechanical testing revealed exceptional properties, with hardness values reaching 25 ± 1 GPa and indentation moduli up to 319 ± 6 GPa. These results were consistent with DFT predictions, demonstrating the correlation between carbon content and mechanical performance. The calculated H/E and H^3/E^2 ratios indicated superior wear resistance, positioning these materials as promising candidates for demanding applications.

The study highlights the possibility to synthesize Cr-Hf-Mo-Ta-W multicomponent thin films with either bcc or fcc structures by controlling the acetylene flow. Notably, the films maintained high deposition rates (38–64 nm/min) under all tested conditions. The successful preparation of fcc carbide phases at intermediate acetylene flows (3–6 sccm) underscores the versatility of this multielement system in forming stable single-phase carbides.

In conclusion, this work demonstrates the potential of hybrid PVD-PECVD magnetron sputtering for fabricating high-entropy carbide thin films. These materials combine advanced microstructural characteristics with excellent mechanical properties encouraging further exploration and application of Cr-Hf-Mo-Ta-W multicomponent carbides for high-performance applications in harsh environments.

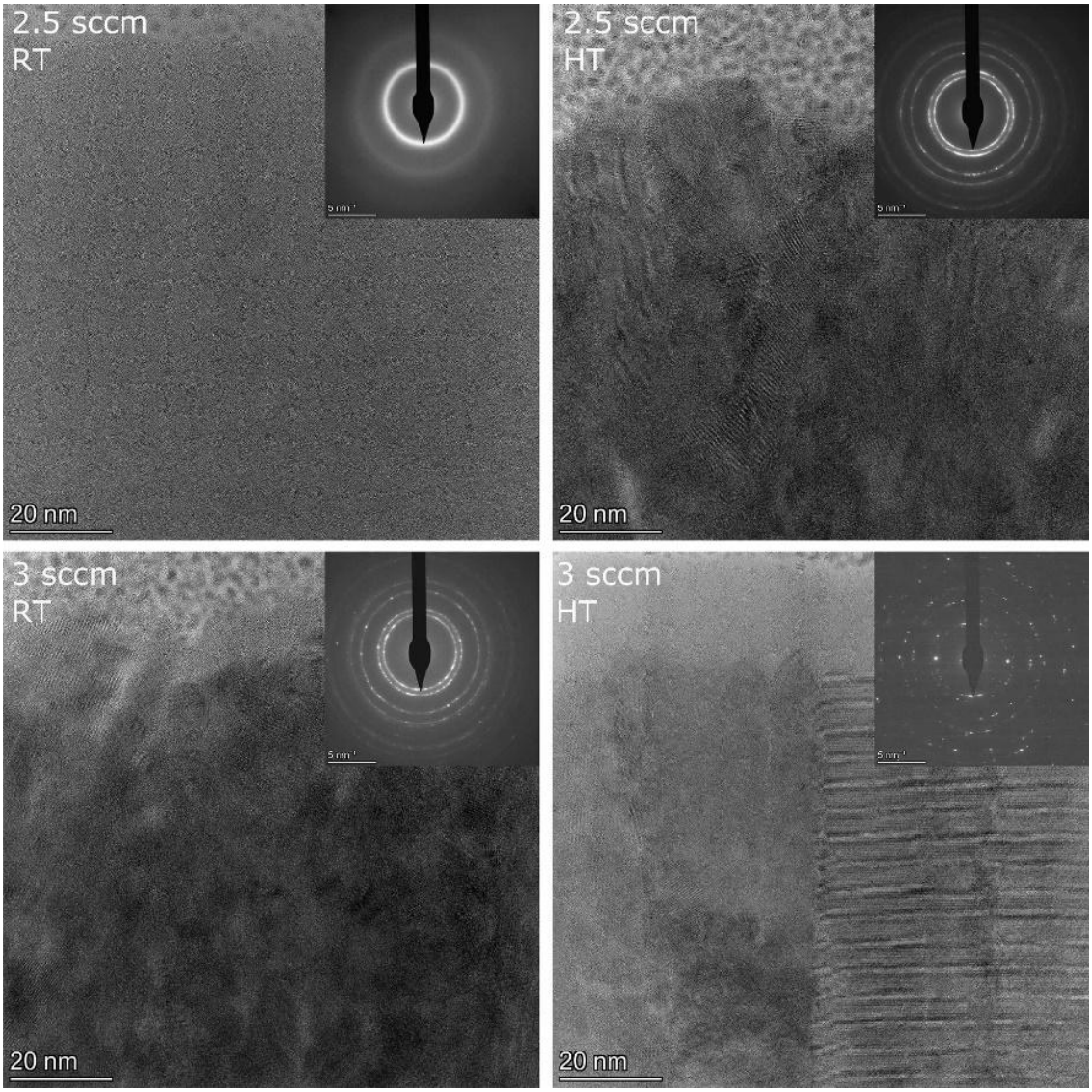

Figure 3.2 High-resolution TEM images of samples prepared at 2.5 sccm and 3 sccm of acetylene at ambient room temperature (RT) and high temperature (HT). The SAED patterns are shown as insets of the images of the corresponding coatings. The sample prepared at 2.5sccm at RT sample is amorphous, while all the others are polycrystalline with fcc crystal structure

Cr-Al spinel phase formation in 316L alumina dispersed stainless steel during spark plasma sintering

OTKA K 146076

Zs. Czigány, H. Rachid Ben Zine[1], K. Balázsi, C. Balázsi
[1]Biskra Universtity, Biskra, Algeria

Oxide dispersion strengthening (ODS) of stainless steel alloys is generally applied to improve the mechanical properties of steel alloys. This paper is intended to present an interesting phenomenon that the alumina additive has completely transformed to a Cr rich spinel [Ref.3.3.]. The composites were prepared with two different compositions of 0.33 wt% Al2O3 and 1wt% Al2O3. The alumina particles were located at grain boundaries mixed with micrometer sized steel debris from milling after attrition milling (Figure 3.3.a and Figure 3.3.b).

After spark plasma sintering (SPS) the α-Al2O3 additive has completely transformed to a Cr rich spinel (Figure 3.3.c) surrounded by an amorphous silica phase in both sintered composites. This phenomenon is not only surprising but it is also remarkable that transformation occurs at a relatively low process temperature (900°C). Both Cr component of Cr-Al spinel phase and Si in silica could diffuse from the 316L steel during the spark plasma sintering process.

It is well known, that formation of silica scale plays a crucial role in the high-temperature oxidation resistance of austenitic stainless steels. Amorphous silica is thermodynamically stable at low and moderate temperatures compared to crystalline forms like quartz or cristobalite. The energy barrier for the transition from amorphous to crystalline phases is relatively high and would require sustained elevated temperatures over extended periods.

In case of 316L steel the formation of this protective scale is accompanied by formation of chromia. Chromium oxide (Cr2O3 or possibly CrO) formation may take place during attrition milling and SPS processes at the surface of steel grains. Spinel phase formation by reaction of oxide of surface segregated Cr and the dispersed α-Al2O3 nanoparticles can take place during SPS process performed at 900°C sintering temperature.

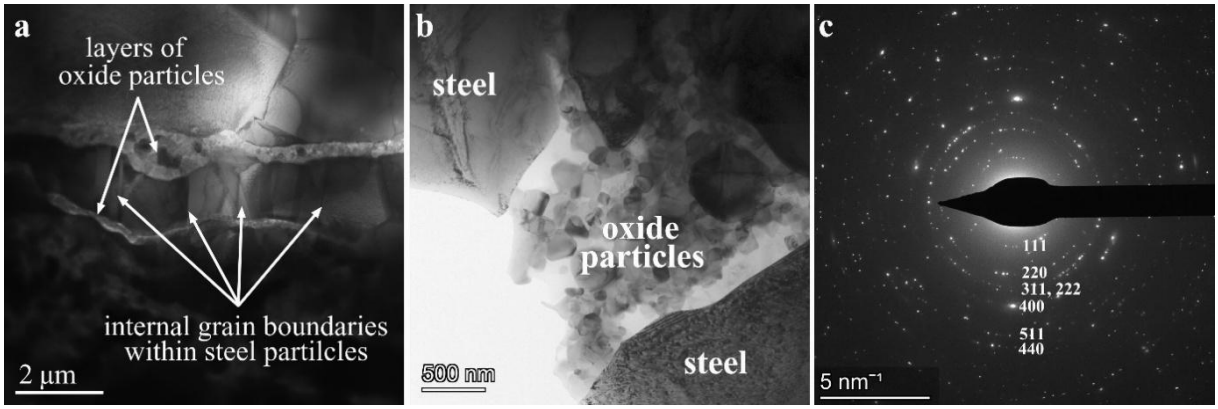

Figure 3.3 a) overview and b) medium magnification TEM images of the sintered composite 316L/0.33 wt% Al2O3. c) The SAED pattern of the oxide particles is indexed as a spinel phase with a lattice parameter of 8.36Å. The diameter of selected area was ~600nm.

The finding that the transformation occurs in presence of amorphous silica is consistent with literature describing both geological occurrence of chromite and phases with spinel structure in annealed glass composites in the presence of silica phase (e.g. [Ref.3.4.]). Those publications sometimes suggest the promoting effect of silica on spinel phase formation without explaining its mechanism. The phase transition may be also promoted by local temperature increase at the grain boundaries of steel during the spark plasma sintering. The main reason for local temperature increase is that the current of the pulses is concentrated at the surfaces of the sintered grains which can result that conditions (including temperature, mechanical pressure and oxygen content) at the grain boundaries of steel grains and at current transit points between the grains may deviate from the nominal experimental parameters applied during the spark plasma sintering. This phenomenon occurs at any process temperature during current pulses applied in spark plasma sintering.

The lattice parameter of the spinel phase is 8.36Å independent of the local cation composition variation. The lattice parameter of the spinel phase is relatively large among synthetic Cr-Al spinels [Ref.3.5, Ref.3.6.] which implies that octahedral sites of spinel structure are mainly occupied by Cr^{3+} cations replacing a portion of Al.

Microcombinatorial TEM for more efficient catalytic methanepyrolysis

EK internal project

A. Horváth, Gy. Sáfrán

The project is about the applicability of a worldwide new method, microcombinatorial TEM sample preparation in catalysis research, which could be a very exciting but so far unknown toolbox in catalysis. Anita Horváth reported on our partial results at international catalysis conferences in China and Austria in 2024, and both times there was a great interest in the topic. At home, she presented the main experiences and the way forward at the MFA Materials Science Seminar organised by Miklós Fried.

The basic idea of the research is to form alloy nanoparticles on a TEM grid (a 3 mm diameter metal grid covered with a thin substrate membrane), whose composition varies linearly along the grid axis. We then investigate the methane dissociation ability of the alloys, as this depends mainly on the metal composition. Methane decomposition should be carried out at 700-800 °C, because this is the temperature needed for the dissociation of methane and the formation of pure H2 and carbon nanotube growth. The resulting carbon specieson the grid were planned to be studied by TEM. The idea was very promising, however, it presented even more practical difficulties than expected. A major part of the work plan was already implemented, but only after thorough investigations did a problem emerge: the TEM grid material itself (Au) and the sample holder contaminate our formed metal particles during high-temperature annealing, so that the catalytic methane decomposition ability and carbon-forming tendency of the metal particles are drastically reduced, and the methane does not become H2 and carbon as in our conventional powder catalyst samples. Therefore, the following steps have been performed according to the outline below.

Grid holder development steps (the original steel grid holder Ge introduced pollution into our samples):
No grid support - filling, grid is very sensitive to physical impacts, membrane on grid tears easily
Quartz grid support - due to thermal expansion differences, grid can sink, bend, but at least it can be cleaned

Increase sputtering temperature: particle size can be varied, reduced, real particles instead of layered morphology (should approach smaller size range of powder catalysts)

Commercially available grids that we have worked with:
Cu grid300 mesh/C membrane - copper is very mobile, combines with our metal particles
Mo grid 200 mesh/C membrane - Mo content within the alloy is indeterminate, as the grid is also Mo, the membrane ruptures because of the large meshes
Au 300 mesh/lacey C membrane - carbon shell not stable even at 600 °C treatments
Au 300 mesh/C membrane - presence of carbon should be excluded

In-house modification of commercial grids (to simulate the substrate oxide of a powder catalyst)
Mo/C/NaCl on RF sputtered Al2O3 mantle, then floated on grid - NaCl contamination, which is forbidden for catalysis
RF sputtered Al2O3 layer on Au/C
Au/C on RF sputtered MgO layer from commercial MgO target

TEM analysis:
2 steps after reduction and methanation or
1 step after reduction + methanation. Methanation and reduction were varied between 600-800 °C to preserve mebrane stability or to promote carbon formation.

Au 400 mesh/SiO2 membrane – unfortunately, no longer produced by SPI, but was the basis of many of our experiments

The challenge with the catalytic reaction was that high temperatures are needed for the catalytic reaction, reduction, but this can cause instability and rupture of the grid membrane, and the grid material becomes inert and mobile, contaminating the metal particles (in the case of Au grids, although the literature describes it as stable up to 850 °C). Apparently, the Al2O3 and MgO coating (simulation of oxide carrier) was not enough to inhibit the mobility of Au, but the metals were difficult to reduce on the oxide layer, so they remained partially in oxide state. Based on our observations and considerations, the next step was to test a 3 mm diameter Si-framed Si3N4 membrane and Ti/C grid, which were obtained.

The sputtering of the Mo-Ni islet metal layer (particles) onto the new -Si-nitride- substrates was performed successfully. TEM studies show that the particles are well separated on the substrate, with sizes ranging from 3-10 nm and showing a linear variation in composition along the TEM grid. This is therefore a good quality sample for the following catalysis experiments.

Our next step is to carry out the methane decomposition reaction, followed by TEM, XPS and Raman studies.

The effect of impurities on the structure and mechanical properties of CoCrCuFeNi alloy films

OTKA K 143216

K. Hajagos-Nagy; Gy. Z. Radnóczi; Gy. Radnóczi

High-entropy alloy (HEA) films are often used as protective coatings; therefore their mechanical and anticorrosion properties are of main interest. Mechanical properties of films are fundamentally determined by their structure and morphology. Impurities, especially oxygen can inhibit structure evolution in vapour deposited films. Consequently, mapping their effect on film growth and structure is of outmost importance. At the same time financial aspects must also be taken into account. Our goal was to find optimum between the cost of film deposition and the properties of the films.

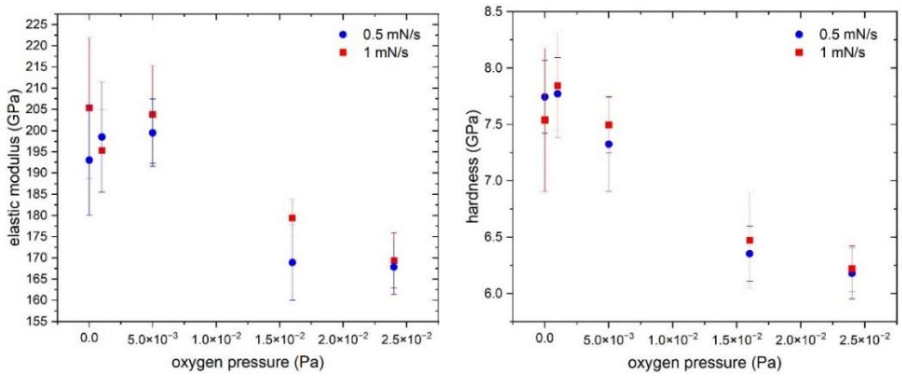

Figure 3.4 Changes of elastic modulus and hardness of CoCrCuFeNi films with oxygen pressure.

CoCrCuFeNi films were deposited by DC magnetron sputtering on thermally oxidized Si wafers. First we used different sputtering speeds (by changing the magnetron power) at 5x10-5 Pa background pressure. Then we used different types of ultra-high vacuum and high vacuum deposition conditions by introducing oxygen to the chamber before sputtering (from 5x10-5 Pa to 5x10-2 Pa). Lowering the sputtering speed increases the chance of impurities being adsorbed on the growth surface. That is, in theory it has the same effect as increasing the background pressure. CoCrCuFeNi films exhibit a T zone structure when they are deposited in ultra-high vacuum and ~0.4 nm/s speed. We found that decreasing the deposition rate at 5x10-5 Pa oxygen pressure does not inhibit the formation of T zone structure, only increases the thickness of the random layer that forms at the beginning of growth. Increasing the background pressure (1.6x10-2 Pa) first decreases the elastic modulus and the hardness of the films (Figure 3.4) through the fragmentation of columnar grains. By further increasing the background pressure (2.4x10-2 Pa) a globular, two phase structure forms (Figure 3.5) which has further decreased mechanical properties. We concluded that 5x10-3 Pa background pressure is sufficient to grow T zone structured CoCrCuFeNi films with adequate mechanical properties. Providing a better vacuum than this is not cost-effective.

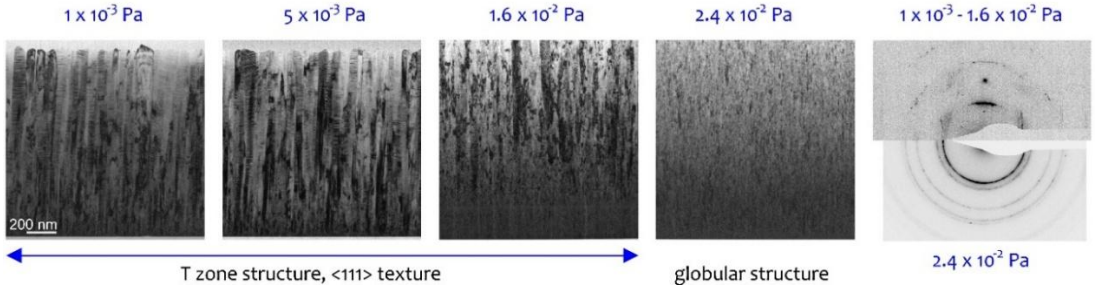

Figure 3.5 The effect of oxygen pressure on the growth of CoCrCuFeNi films.

Evolution of structural and photoluminescent properties of sputter-deposited Ga2O3 thin films during post-deposition heat treatment

TKP2021-NKTA-05

M. Gajdics, I. Cora, D. Zámbó, Zs.E. Horváth, A. Sulyok, K. Frey and B. Pécz

Gallium oxide as an ultrawide bandgap semiconductor material has several potential applications in the field of optoelectronics and high-power electronics. Among the many deposition techniques radio frequency sputtering is a common technique to prepare Ga2O3 thin films. Sputtering can be performed at elevated temperature or at room temperature and in this latter case the layers will be amorphous. Post-deposition annealing is frequently applied to crystallize these films. Studying the phase evolution and the high-temperature behavior is important from the perspective of applications. In situ characterization methods, such as in situ transmission electron microscopy, may provide better understanding than ex situ measurements. However, earlier investigations indicated that the annealing atmosphere is a major factor influencing the photocurrent characteristics of Ga2O3.

We have demonstrated an in situ method, namely in situ spectroscopic ellipsometry that can be performed in various atmospheres during annealing. This method (coupled with ex situ characterization techniques) enabled to determine the phase transition temperatures through the change of the optical parameters. Beside the study of the phase evolution of RF-sputtered amorphous Ga2O3, the optical and photoluminescent properties of the layers were also investigated at the various heat treatment steps.

It was shown that the relatively abrupt changes in the ellipsometric parameters and in the calculated refractive index can indicate the occurrence of phase transformations. X-ray diffraction and transmission electron microscopy were used to confirm the appearance of the new phases. The amorphous layer first crystallizes into the metastable γ-Ga2O3 phase at 390-400 °C and at higher temperatures (530-570 °C) the stable β-Ga2O3 phase appears during the annealing in air. It was also found that the γ-Ga2O3 and β-Ga2O3 phases coexist in a wide temperature range.

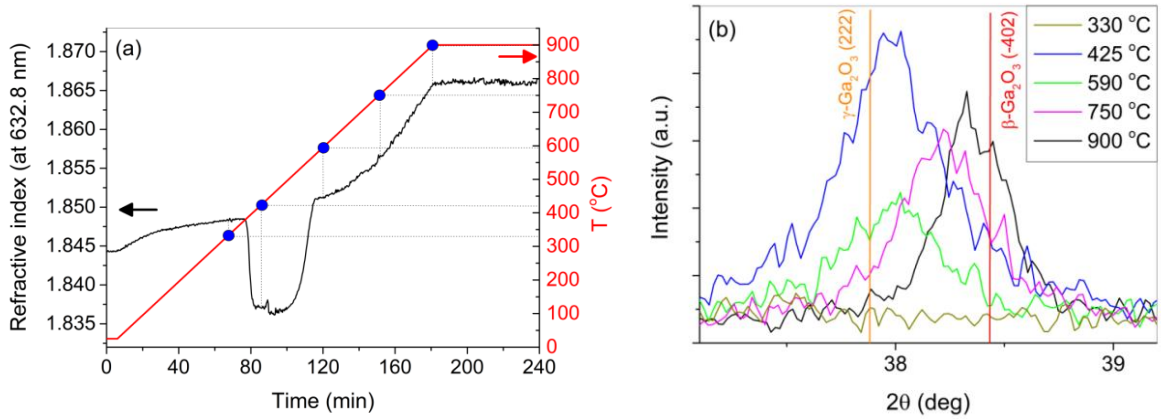

Figure 3.6 The variation of the refractive index and the applied temperature ramp (a). The shift of the X-ray diffraction peak of around 38° of 2θ indicating the change of the relative volume fraction between the two crystalline phases (b).

The optical transmission measurements showed that all the heat treated samples has an absorption edge in the UV wavelength region. The bandgap of the samples was determined based on reflective electron energy loss spectroscopy and the optical measurements. Even though the films have significantly different structural characteristics, no significant change in the bandgap could be observed as a result of heating at different temperatures.

Photoluminescence measurements were also performed and it was found that the annealing temperature and the annealing atmosphere have a significant effect on the emission properties of the layers. A broad green luminescence band emerged after the crystallization of the layer and it can be associated with the presence of the γ-Ga2O3 phase, which is characterized by partially occupied cation sites. The temperature of 750 °C seems to be a transition point where the sample shows green (~519 nm), blue (424 nm) and red (765 nm) emission as well. Upon further heating only either the blue or the red emission remains beside the green one.

The position of the appearing emission band depends on the annealing atmosphere, i.e. in argon the blue band emerges, while in air and nitrogen the red one can be observed. The blue luminescence can be related to donor-acceptor pair recombination mechanism, while the red luminescence can be related to the formation of gallium vacancies. It is proposed that by changing the composition of the annealing atmosphere, it is possible to tune the photoluminescence emission of Ga2O3.

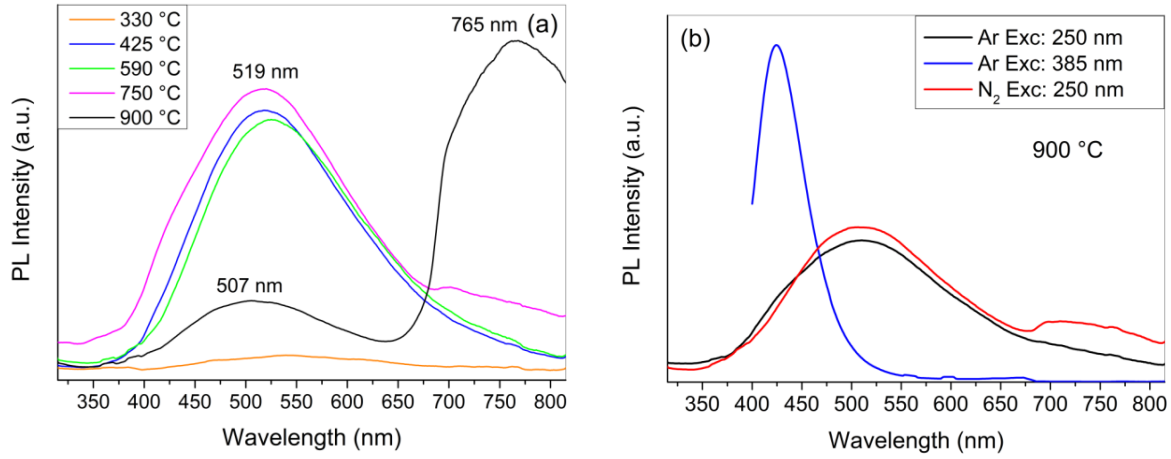

Figure 3.7 Photoluminescence emission spectra of the Ga2O3 films annealed in air at different temperatures (a). Emission spectra of the samples annealed at 900 °C in argon and nitrogen (b).

Indentation size effect for ultrafine-grained materials

OTKA K 143216, KDP-2021 (C1792954)

Nguyen Quang Chinh, Olasz Dániel, Sáfrán György, Terence G. Langdon

Indentation measurements are fundamental to the study of mechanical properties in materials science. In general, however, measurements are subject to the so-called Indentation Size Effect (ISE), which describes the scale-dependent behaviour of the hardness of a material. At lower loading forces, and thus lower indentation depths, the material exhibits higher strength. Unfortunately, this makes it difficult to compare the results of measurements at different indentation loads. The most accepted theory of this phenomenon was provided by Nix and Gao, who explained it in terms of geometrically necessary dislocations (GND) and described the relationship between hardness (H) and indentation depth (h) by the following simple relation:

$$\frac{H}{H_0} = \sqrt{1 + \frac{h^*}{h}},$$

where H0 is a material constant (the hardness of the material at h→∞), h* is a material-specific constant that expresses the rate at which the hardness increases/decreases with depth.
Based on our results [Ref.3.7.] of indentation measurements on Al matrices of different grain sizes, we have shown that the theory is valid for polycrystalline materials [Ref.3.8.]. The following relationship holds for the characteristic length h* of ISE:

$$h^* = \frac{C}{H_0^2},$$

where C is a constant including Burgers vector, shear modulus and indenter geometry. This implies that h* is small for higher strength materials, so that the indentation size effect is not significant. In ultrafine-grained materials, the Hall-Petch relationship suggests that the strength of the material increases significantly as the grain size decreases so that the ISE will not be detectable in the measurements, as shown in Figure 3.8.

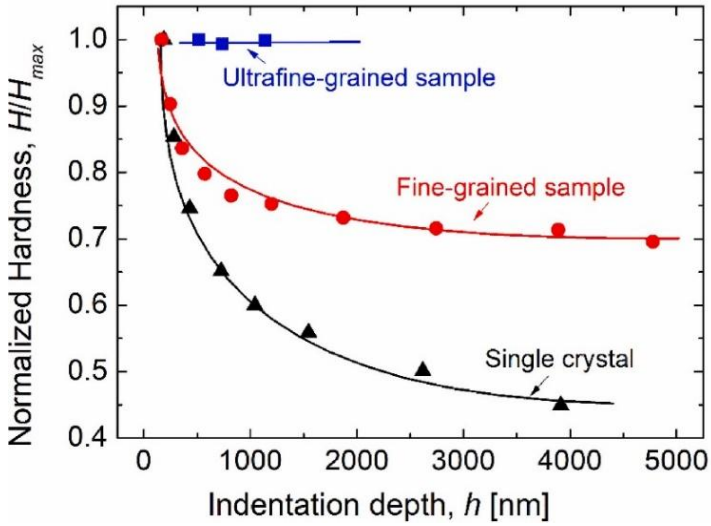

Figure 3.8 Normalized hardness values as a function of indentation depth in different Al matrices (ultrafine-grained d~350 nm, fine-grained d~ 1200 nm and single crystal).

"GHOST III: Graphene and transition metal dichalcogenides HeterOstructures with wide bandgap SemiconducTors for advanced electronics"

MTA NKM2023-15/2023

B. Pécz

During the second year of the project, the Italian and Hungarian research teams continued the collaboration on the following subjects:

Synthesis and characterization of MoS2 thin films on sapphire and GaN substrates

During 2024, the CNR and MFA groups continued the activity on the synthesis and characterization of MoS2 thin films on substrates of interest, such as insulating sapphire and the wide bandgap semiconductor gallium nitride (GaN). Starting from previous joint results of the two research teams, thermal sulfurization of ultra-thin Mo-based films has been further explored as a promising approach for large-area growth of MoS2. In particular, they demonstrated that the crystalline quality (domains size and defects density), strain, doping, and light emission properties of monolayer (1L) MoS2 obtained from sputter deposited MoOx films on a c-sapphire substrate can be tailored by the sulfurization temperature (Ts) in the range from 700 to 800 °C [Ref.3.9.].

Starting from a continuous film with a nanocrystalline domains structure at Ts=700 °C (Figure 3.9.a and Figure 3.9.b), a distribution of 1L MoS2 triangular domains with 2.1±0.6 μm and 2.6±1.6 μm average sizes was obtained by increasing Ts to 750 °C (Fig.3.9.c and Fig 3.9.d) and 800 °C (Fig.3.9.e and Fig 3.9.f), respectively.

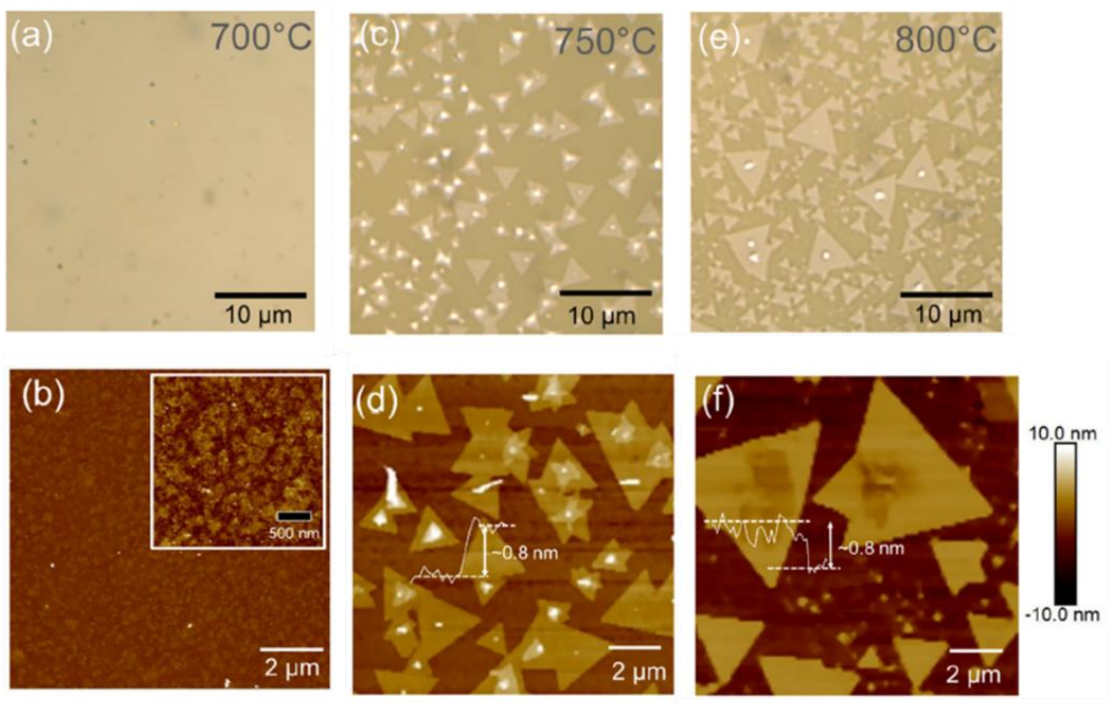

Figure 3.9 Optical and morphological (AFM) images obtained for the MoS2 on sapphire grown at 700 °C (a,b), 750 °C (c,d), and 800 °C (e, f).

The increase in Ts was accompanied by a strong (25 times) enhancement of the photoluminescence (PL) intensity (Figure 3.10.a). Furthermore, as illustrated in Figure 3.10.b, the average doping of MoS2,

evaluated from Raman analyses, evolved from a strong p-type doping (~1×1013 cm-2) after Ts=700 °C, ascribed to residual MoO3 in the film, to a low average n-type doping (~0.04×1013 cm-2) after Ts=800 °C. The wide tunability of doping and PL of 1L MoS2 by the sulfurization temperature can be exploited to tailor material properties for different specific applications.

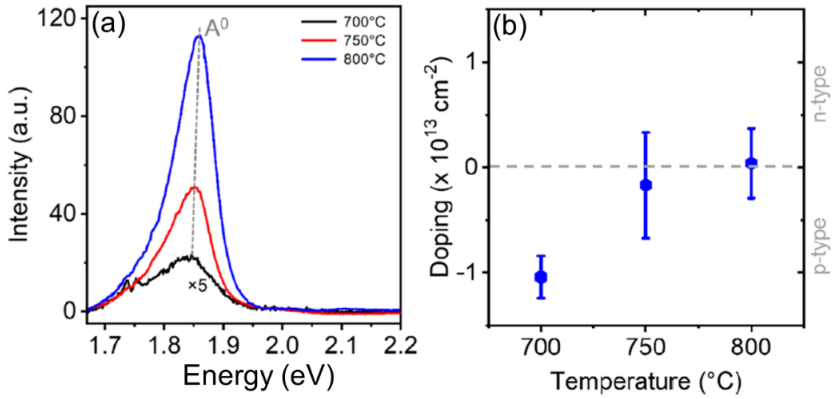

Figure 3.10 (a) PL spectra for 1L-MoS2 on sapphire at 700 °C (black line), 750 °C (red line), and 800 °C (blue line), where all the spectra are normalized with respect to the Raman MoS2 peaks.

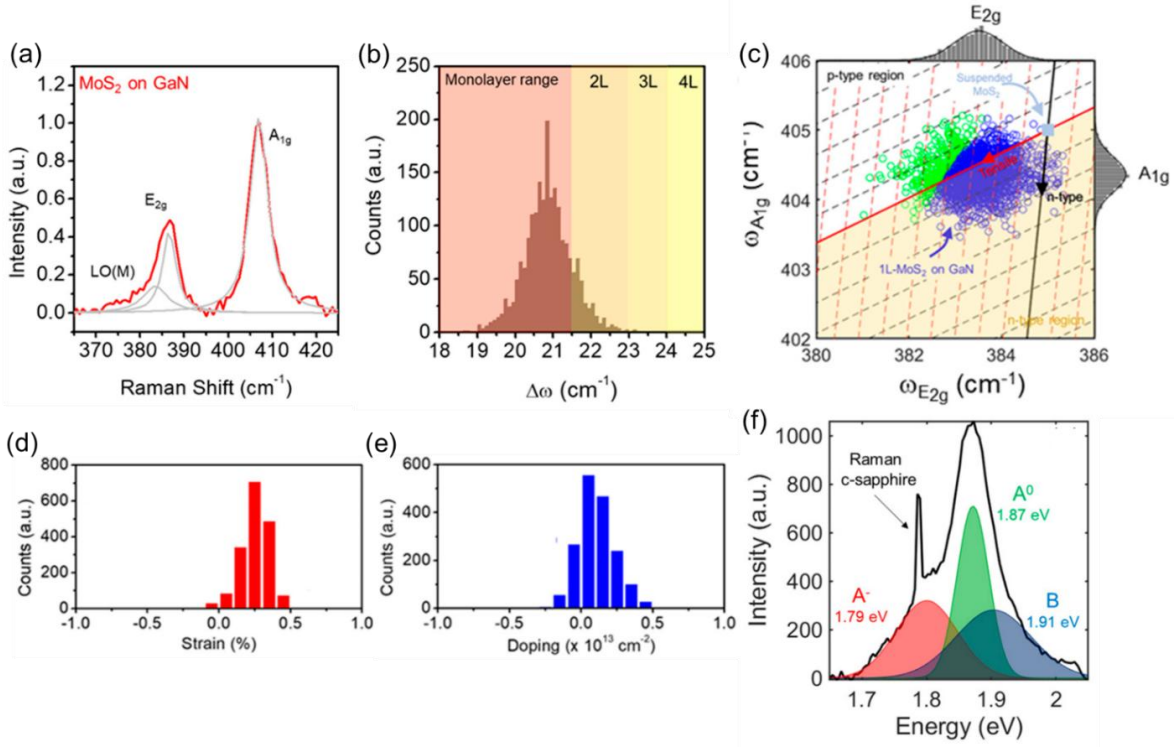

Figure 3.11 (a) Raman spectrum of CVD-grown MoS2 on GaN, showing MoS2 vibrational modes E2g and A1g, in addition to a further small LO(M) component deduced after a deconvolution analysis. (b) Histogram of the difference between the two peaks (Δω = ωA1g − ωE2g), related to the number of layers, deduced from a large number of Raman spectra collected at different positions. (d) Correlative E2g vs A1g plot to evaluate the strain and doping effects induced on the MoS2 flakes by the growth conditions and the interaction with GaN substrate. Evaluated distributions of strain (d) and doping (e) for 1L of MoS2. (f) Photoluminescence spectrum of MoS2 on GaN, where the two excitons (A0 and B) and trion (A−) components were extracted after deconvolution analysis.

The combination of the unique physical properties of MoS2 with those of GaN and related group-III nitride semiconductors have recently attracted increasing scientific interest for the realization of innovative electronic and optoelectronic devices. A deep understanding of MoS2/GaN interface properties represents the key to properly tailoring the electronic and optical behavior of devices based on this heterostructure. During 2024, the CNR and MFA-EK teams worked on the growth of 1L MoS2 on GaN-on-sapphire substrates by chemical vapor deposition (CVD) at 700 °C.

The structural, chemical, vibrational, and light emission properties of the MoS2/GaN heterostructure were investigated in detail by the combination of microscopic/spectroscopic techniques and ab initio calculations [Ref.3.10.]. X-ray photoelectron spectroscopy analyses on as-grown samples showed the formation of stoichiometric MoS2. Statistical analysis of a large number of micro-Raman spectra collected at different sample positions showed the deposited film on GaN is mostly composed by monolayer MoS2 domains (see Figure 3.11.a and Figure 3.11.b). Furthermore, from a correlative plot of the frequencies of characteristic vibrational peaks of MoS2 (illustrated in Figure 3.11.c), it was deduced that these domains exhibit an average n-type doping of $(0.11 \pm 0.12)\times 1013$ cm−2 (Figure 3.11.d) and a small tensile strain $\varepsilon \approx 0.25\%$ (Figure 3.11.e). Finally, an intense light emission at 1.87 eV was revealed by PL analyses (Figure 3.11.f). High-resolution Transmission Electron Microscopy (HR-TEM) and atomic resolution Scanning Transmission Electron Microscopy (STEM) analyses on cross-sectioned samples (illustrated in Figure 3.12.a and Figure 3.12.b, respectively) demonstrated the presence of a gap at the interface between MoS2 and GaN, confirming the formation of a van der Waals (vdW) heterostructure.

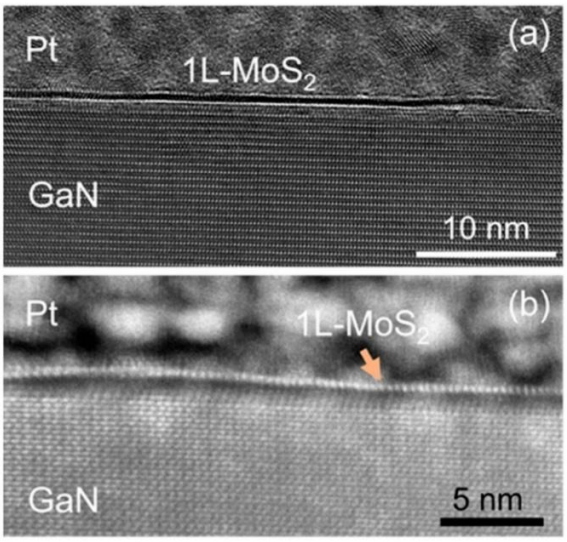

Figure 3.12 . (a) Overview the HR-TEM image showing 1L of MoS2 conformal to the (0001) basal plane of GaN. (b) Atomic resolution STEM image showing the presence of a van der Waals gap between 1L of MoS2 and the underlying GaN surface.

Finally, density functional theory (DFT) calculations of the heterostructure were carried out, considering three different configurations of the interface, i.e., (i) an ideal Ga-terminated GaN surface, (ii) the passivation of Ga surface by a monolayer of oxygen (O), and (iii) the presence of an ultrathin Ga2O3 layer. This latter model predicts the formation of a vdW interface and a strong n-type doping of MoS2, in closer agreement with the experimental observations.

Schottky contacts on sulfurized silicon carbide (4H-SiC) surface

Besides demonstrating the formation of monolayer or few-layers MoS2 by sulfurization of pre-deposited MoOx films on different substrates (including SiO2, sapphire, GaN and SiC), the CNR and MFA-EK groups partner of the GHOST-III project evaluated the effect of the sulfur annealing process

on the electrical properties of the bare 4H-SiC substrate. This investigation is relevant, since sulfur (S) impurities in the 4H-SiC lattice have been shown in different studies to work as donor levels. In particular, the effect of a sulfurization treatment carried out at 800 °C on silicon carbide (4H-SiC) surface has been studied by detailed chemical, morphological, and electrical analyses [Ref.3.11.]. X-ray photoelectron spectroscopy confirmed S incorporation in the 4H-SiC surface at 800 °C (see Figure 3.13.a), while atomic force microscopy showed that 4H-SiC surface topography is not affected by this process (see Figure 3.13.b and Figure 3.13.c). Notably, an increase in the 4H-SiC electron affinity was revealed by Kelvin Probe Force Microscopy in the sulfurized sample with respect to the untreated surface.

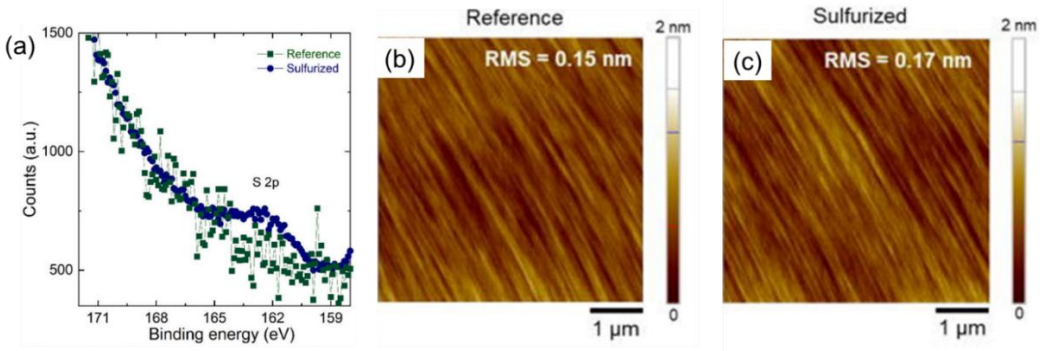

Figure 3.13 (a) XPS-spectra recorded on the reference 4H-SiC sample and after sulfurization at 800 °C. AFM morphology of 4H-SiC before (b) and after (c) the sulfurization process.

Current-voltage characterization of Ni/4H-SiC Schottky contacts fabricated on sulfurized 4H-SiC surfaces (Figure 3.14.a) revealed a significant reduction (~0.3 eV) and a narrower distribution of the average Schottky barrier height with respect to the reference untreated sample (see histograms in Figure 3.14.b). This effect was explained in terms of a Fermi level pinning effect induced by surface S incorporation.

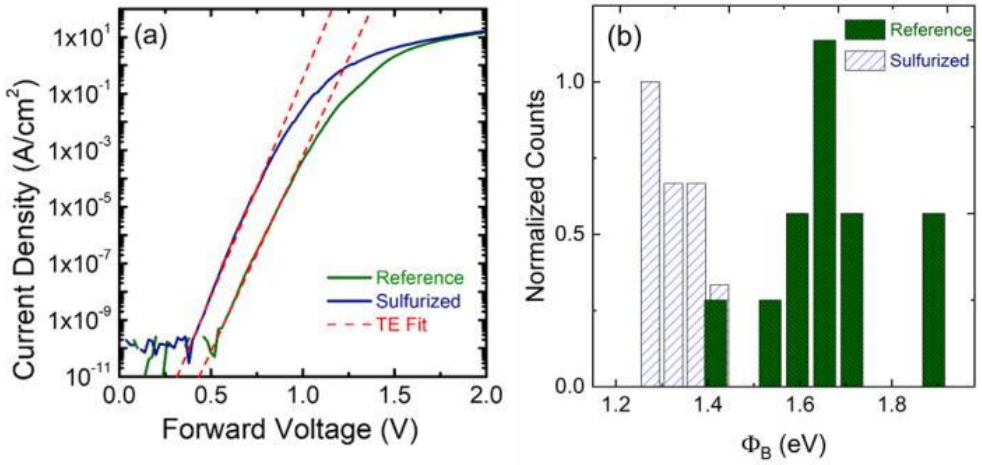

Figure 3.14 (a) Representative forward I-V curves of Ni/4H-SiC Schottky diodes fabricated on an untreated surface (reference) and on a surface subjected to the sulfurization process at 800 °C (sulfurized). The dashed lines represent the linear fits of the curves obtained by the thermionic emission model. (b) Statistical distributions of the Schottky barrier height values determined in the reference and for the sulfurized diodes.

These results provide a better understanding of the electrical impact of S incorporation on SiC surfaces and can be particularly useful both for 4H-SiC power device technology and for integrating MoS2 layered materials on SiC surfaces in advanced devices concepts.

Examination of calcium phosphate-based biopolymer composites doped with bioactive elements

OTKA FK 146141

M. Furkó

In various biomedical and orthopedic fields, bioactive ceramics and scaffolds play a crucial role due to their beneficial interactions with human tissues.

Calcium phosphates stand out among various bioceramics as the most appropriate choice, given that hydroxyapatite, a specific form of calcium phosphates (CaPs) or apatites, is the primary inorganic component found in human bones. The CaPs can be applied as bone substitutes, types of cement, drug carriers, implants, or coatings. Furthermore, bioceramics that can be absorbed by the body show significant promise in the field of tissue engineering, as they are commonly utilized as frameworks that facilitate the natural healing process of bones during tissue repair. A significant breakthrough in CaPs occurs when they are combined with active biomolecules such as magnesium, zinc, and strontium.

In our work, amorphous or nanocrystalline calcium phosphates (CaPs) and their combination with biopolymers are prepared as coatings or scaffold matrices. The innovative types of resorbable coatings for load bearing implants that can promote the integration of metallic implants into human bodies. Owing to the bioactive mineral additions (Mg, Zn, Sr) in optimized concentrations, the base Cafxps

P particles became more similar to the mineral phase in human bones. To prepare the composites, the doped CaP powders were mixed into two types of biopolymers. One is cellulose acetate (CA) as a natural polymer, the other is polycaprolactone (PCL) as an artificial polymer. The morphology of the composites with the element maps is shown in Figure 3.15.

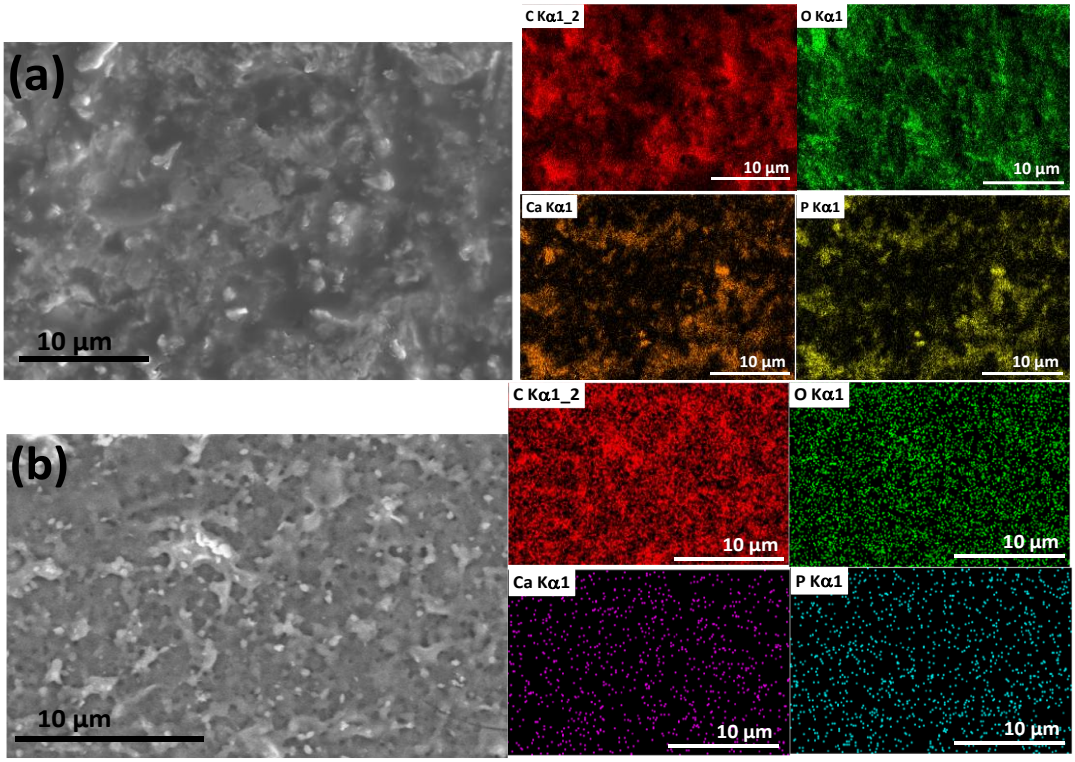

Figure 3.15 Scanning electron microscope image and the corresponding elemental mapping of PCL-mCP composite (a) and CA-mCP composite (b).

Figure 3.15 shows that the morphology of the composite made with two types of polymers is different, but both have a porous structure with smaller holes and cracks. The distribution of added CaP powders is uniform in both cases.

We investigated the morphology and structure of the basic CaP and the doped mCaP (Figure 3.16). CP powder, produced from the salt of organic calcium gluconate by a wet chemical process, consists of very small, randomly arranged needle-like particles, which sometimes form larger agglomerates. On the other hand, in the case of powder added with organic bioactive components, it consists of even smaller, dense, very thin, thorn-like particles. This small morphological change can be attributed to the incorporation of minerals into the CaP core structure.

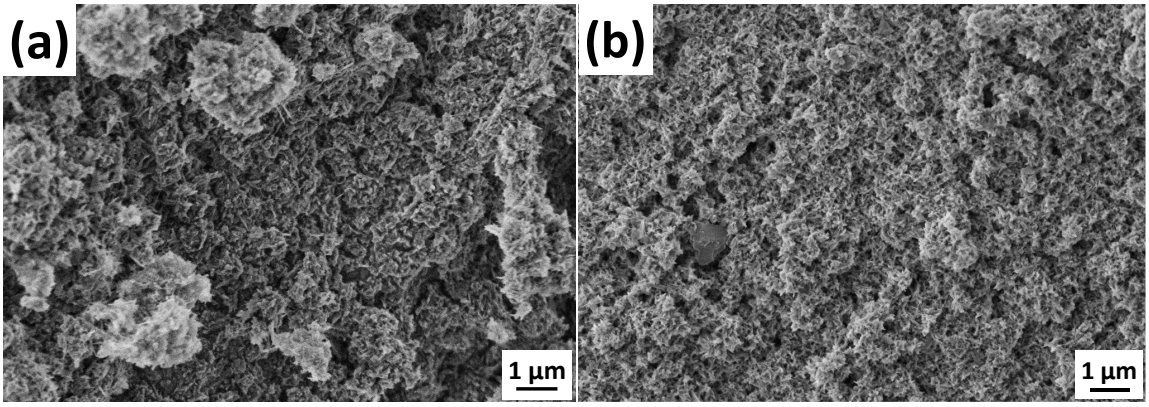

Figure 3.16 SEM images of nanocrystalline calcium-phosphate powder (CaP) (a) and bioactive element added mCaP (b).

The XRD measurements (Figure 3.17) confirmed that with wet chemical precipitation and alkaline post-treatment, the calcium phosphate phase has a nanocrystalline structure and is amorphous. The addition of bioactive elements further increased the amorphous nature of the powder. It can be said that this amorphous structure is favorable for biological degradation.

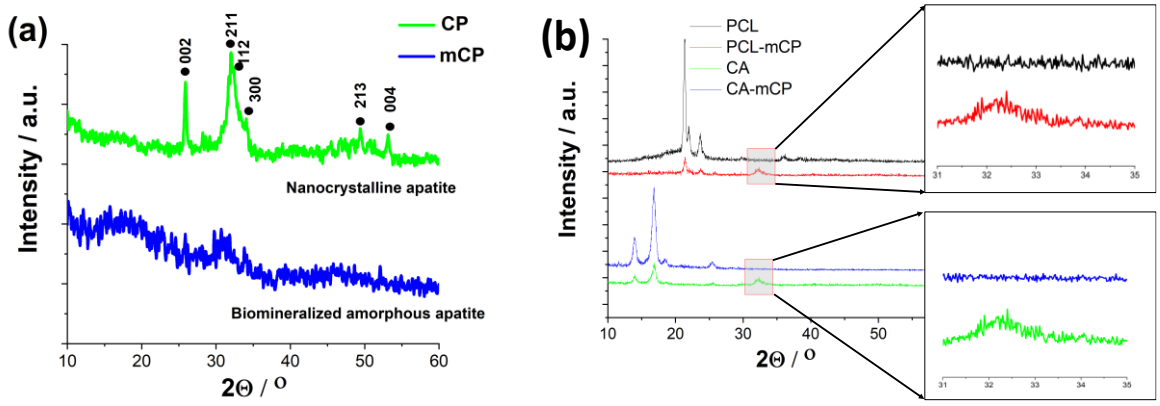

Figure 3.17 XRD patterns of CP and mCP powders (a) prepared by wet chemical method and the PCL-mCP, CA.mCP composites (b).

XPS depth profiling of nano-layers by a novel trial-and-error evaluation procedure

A.S. Racz, M. Menyhard

In spite of its superior chemical sensitivity, the usage of XPS depth profiling is limited due to the alteration introduced by the sputter removal process and the resulting inhomogeneous in-depth concentration distribution. Moreover, the application of XPS becomes increasingly challenging in the case of the analysis of thin layers, if the thickness is in the range of 2–3 inelastic mean free paths (IMFP) of the photoelectrons. We will show that even in these unfavorable cases the XPS depth profiling is applicable. Herein the XPS depth profiling of a model system tungsten-carbide-rich nano-layer of high hardness and corrosion resistance is presented. We will show that the problems arising because of the relatively high IMFP can be corrected by introducing a layer model for the calculation of the observed XPS intensities, while the alteration, e.g. ion mixing, compound formation and similar artefact, introduced by the sputter removal process can be handled by TRIDYN simulation. The method presented here overcomes the limitation of XPS depth profiling.

We have applied XPS depth profiling in an unfavorable case; the C/W multilayer system studied had thin layers, compared to the IMFP of the used photoelectrons, and is sensitive to the ion bombardment used for depth profiling. Accordingly, the as measured depth profiles were strongly distorted, and routine evaluation resulted in an erroneous result for the initial structure. We proposed a trial-and-error protocol for deriving the initial concentration distributions from the distorted XPS depth profile. The problem arising from the relatively high IMFP values was handled by simulating the XPS signal, considering its attenuation in matrices of varying composition. The effect of the ion bombardment was accounted for by using TRIDYN simulation. We have demonstrated for a sample of well-known structure that the method works properly, then the same protocol was applied for the study of the ion beam mixing and carbide formation in the case of medium energy (40 keV Ar+, 120 keV Xe+) ion irradiation of a C/W multilayer system. The study showed that the irradiation produced W2C instead of the previously assumed WC. This work demonstrates that despite of the high IMFP of the analyzed photoelectrons and artefact production due to the sputter removal process, XPS depth profiling can be still a powerful tool for analyzing the composition of nano-multilayer films. [Ref.3.15.].

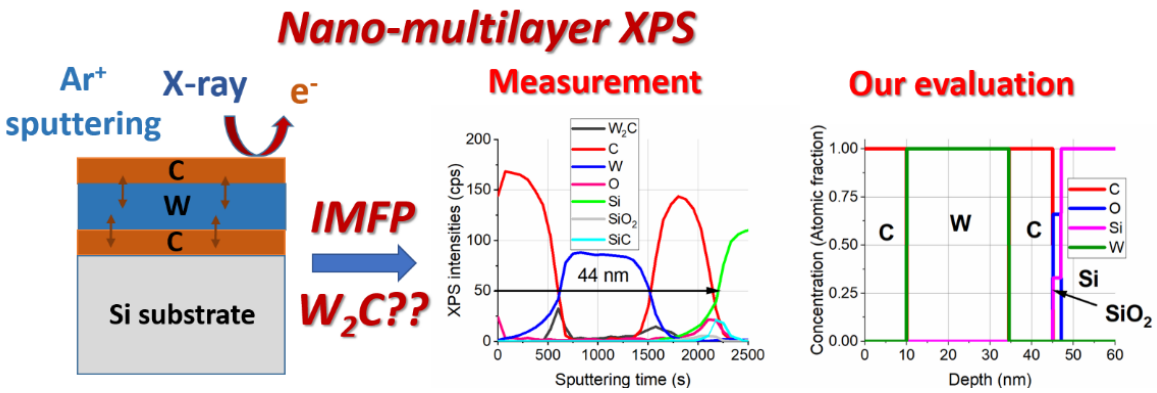

Figure 3.18 Summary of the trial-and error evaluation method for XPS depth profiling.

Atomistic insights into salicylic acid treatment on human keratinized skin by XPS combined with argon gas cluster sputtering: A pilot study.

A.S. Racz

Stratum corneum is the skin's outermost layer, whose main constituent is keratin. The treatment of dermatological diseases showing hyperkeratosis is a serious problem in dermatology and cosmetics seriously affecting the population showing increasing prevalence. One of the treatment is a peeling agent like salicylic acid (SA), categorized as a keratolytic agent, however its mode of action is not fully understood. X-ray photoelectron spectroscopy (XPS) is a method for monitoring the changes of surface composition at atomistic level in 5–10 nm depth. The development of argon cluster sputtering enabled the investigation of deeper regions (nanometric level) even for biomaterials.

In this pilot study, the mode of action of SA has been studied at atomistic level for the first time. Different concentrations of SA (3, 5, 10 wt%) in different time frames (1 day, 1 week, 1 month) was applied on human keratinized skin. The carbon, nitrogen and oxygen peak have not shown changes during the treatment, not showing the suggested desmolytic mechanism of SA. However, significant changes were observed in the sulfur peak, with increasing time and concentration the rate of sulfonate and sulfate was increased compared to thiol group indicating the break of sulfide bonds between the polypeptide chains in keratin, indicating that keratolysis happens at nanometric level. Already a 1 week-10 wt% SA treatment resulted in higher rate of sulfate compared to sulfonate indicating further oxidation of the keratolytic product. However, 1 month-10 wt% treatment resulted in the same surface composition as 3 wt%-1-month treatment indicating that enough time with low concentration can exert the same effect as higher concentrations.

These findings have relevance in the design of future SA-based dermatologic therapies and that XPS can contribute to medical therapy monitoring. The measurement method and XPS results related to the sulfur peak is summarized in Figure 3.19. [Ref.3.16.]

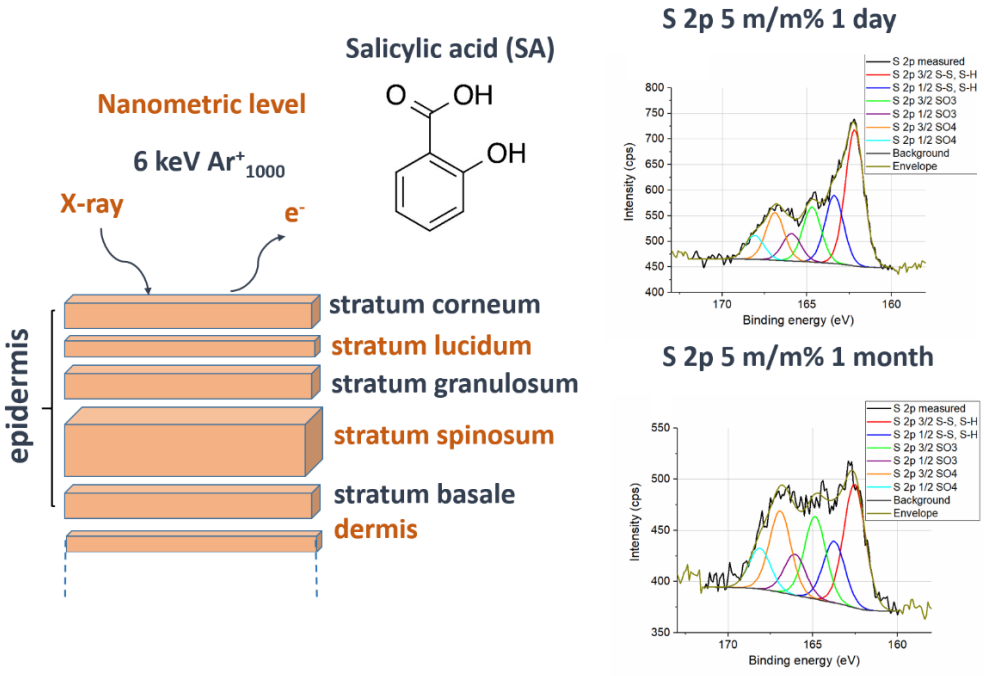

Figure 3.19 Following the effect of salicylic acid treatment of keratinized skin by XPS

R+D+I development and utilization of high-performance electronic chips

"CHIPCER" Phase 1. ÁFF/96/1/2023

K. Balázsi, Cs. Balázsi, T. Kolonits, E. Dódony, A. Jakab Fenyvesiné, B. Erki, V. Varga, A. Kovács

The government has accepted the Ministry of Economic Development's proposal to launch an R+D+I project for chip-carrying ceramic wafers, so Hungary is also starting to enter the semiconductor manufacturing market.

The project, whose partners are the Bay Zoltán Nonprofit Ltd. (PI), Neumann Ltd., Budapest Technical University (BME) and the Thin Film Physics Laboratory of HUN-REN EK MFA, started from December 2023.

Our task is to develop thin (several hundred micrometers) ceramics as a chip substrate used in the automotive industry and high-performance electronics and to facilitate their production on an industrial scale. In the first year of the project, we determined the ceramic to be tested, silicon nitride, an important parameter of which is that European suppliers provide the raw materials, thereby making the production process independent of various external influences.

All novel results are confidential.

Digitalization of Power Electronic Applications within Key Technology Value Chains

2022-1.2.8-KDT-2022-00001, Horizon Europe KDT 101096387 PowerizeD

K. Balázsi, C. Balázsi, T. Kolonits, M. Furkó, K. Hajagos-Nagy, E. Dódony, A. Fenyvesiné Jakab, V. Osváth, V. Varga, A. Kovács, B. Erki

PowerizeD is an innovative EU funded project aiming to develop breakthrough technologies of digitized and intelligent power electronics to enable sustainable and resilient energy generation, transmission and applications.

The project is supported by the Chips Joint Undertaking and its members, including the top-up funding by the national Authorities of Germany, Belgium, Spain, Sweden, Netherlands, Austria, Italy, Greece, Latvia, Finland, Hungary, Romania and Switzerland, under grant agreement number 101096387. Co-funded by European Union.

The project focuses on improving the way energy is produced and transmitted through the use of digitized and intelligent electronic energy, which will greatly contribute to the decarbonisation of European society and the protection of our climate.

The research results so far are not yet public, scientific publications can only be published after the permission of the project leader, Infineon.

Nanosensors Department

Head: Dr. János Volk, Ph.D., Senior Research Fellow

Research Staff:

Zsófia Baji, Ph.D.
Gábor Battistig, D.Sc. (60%)
Szabolcs Csonka, Ph.D. (20%)
György Molnár, D.Sc.
Nguyen Quoc Khánh, Ph.D.
Péter Lajos Neumann, Ph.D. (50%)
László Pósa, Ph.D.
Zsolt Zolnai, Ph.D. (75%)

Engineers:

Ferenc Braun, Engineer
János Ferencz, Engineer
Levente Illés, Engineer
Attila Nagy, Technician
Zoltán Kovács, Engineer
Áron Vándorffy, Engineer

Ph.D. Students / Diploma Workers:

- László Kelemen, B.Sc. Student
- János Márk Bozorádi, Ph.D. Student (50%)
- Bertalan Németh, B.Sc. Student
- Hanna Stephan, M.Sc. Student
- Máté Sütő, Ph.D. Student (50%)
- Anett Szeledi, B.Sc. Student
- Bence Vasas, Ph.D. Student (40%)
- Tímea Nóra Török, Ph.D. Student (50%)
- Tamás Zeffer, Ph.D. Student (40%)

The Nanosensors Department was established at the beginning of 2019, following the split of the former Microtechnology Department. The group jointly maintains two semiconductor clean rooms (nanofabrication and Si MEMS) and several complementary labs with the Microsystems Department.

The Nanosensors Department aims to develop practical sensors based on new principles of operation using the results of basic research. To this end, the group exploits the unique experimental infrastructure and the diverse expertise of the research/engineering team. In the following topics our results are presented, covering i) the characterisation of functional thin films; ii) nanoscale electronic devices and novel readout systems; and iii) a short summary in the field of quantum technology research. These research topics are conducted mainly in the framework of four domestic, one EU projects:

- TKP2021-NVA-03: Environmental monitoring sensors for emergency and extreme conditions;
- OTKA FK 139075: Atomic layer deposition and applications of functional sulfide nanolayers;
- OTKA K 143263– Investigation of luminescence and ionization energy deposition processes in microstructured semiconductors based on neutral and charged particle conversion phenomena;
- OTKA K 143282: Development of Nanometer Scale Resistive Switching Memory Devices,
- HORIZON-EIC-2022-PATHFINDERCHALLENGES-01-06-101115315 EU research project: Quantum bits with Kitaev Transmons (QuKIT).

Besides, the Nanosensors Department provided electronmicroscopy services for several industrial partners (Semilab, Lighttech, Technoorg Linda, Bosch, Visola), nanofabrication infrastructure for the Quantum Information National Laboratory (QNL), and was engaged in university education as well (Budapest University of Technology and Economics, Óbuda University, University of Debrecen).

Growth and nucleation of vanadium-sulphide layers with atomic layer deposition

OTKA FK 139075

Zs. Baji, Zs. Fogarassy, A. Sulyok, Zs. E. Horváth, O. Hakkel, and Z. Szabó

Transition metal sulphides are gaining a huge interest, due to their abundance, the many different possible morphologies, and their cheapness. Vanadium chalcogenides have outstanding optical characteristics combined with high electrical conductivity, low resistivity, and excellent catalytic performance.

ALD is a thin film deposition method based on the introduction of precursor materials into the vacuum chamber separately, and their chemisorption of the heated substrate surface. As the reagents can only meet and react on the substrate, the growth actually proceeds in a monolayer-by-monolayer layer fashion. This level of control promises to be the ideal approach to the preparation of ultra-thin, or even 2D materials.

The present work explored the preparation of VS layers with a novel precursor combination: TEMAV and H_2S and also examined the growth and nucleation characteristics- The use of the TEMAV with H_2S resulted in a growth rate of 0.45Å/cycle between 200°C and 300°C. The deposited layers were homogeneous and uniform, thus they are ideal atomic layer deposited films. The prepared vanadium-sulphide layers were very smooth with an RMS roughness of 0.7 nm, as measured by AFM. XPS measurements showed that the as-deposited layers have an internal composition of 63% V, 37% S. The structure and crystallinity of the films was examined with (S)TEM, which showed that the deposited material is amorphous.

To improve the layer quality, post deposition annealing procedures were performed at 500°C in a sulphur containing atmosphere. A 5-hour long treatment resulted in crystalline and stoichiometric VS. According to the XPS results, the top few nanometres consisted of a mixture of VS and VS_2, below which, the composition was pure VS. The stoichiometric VS produced by sulphur treatment proved to be more stable and has a better resistance to oxidation than the as-deposited layer with a lower sulphur content.

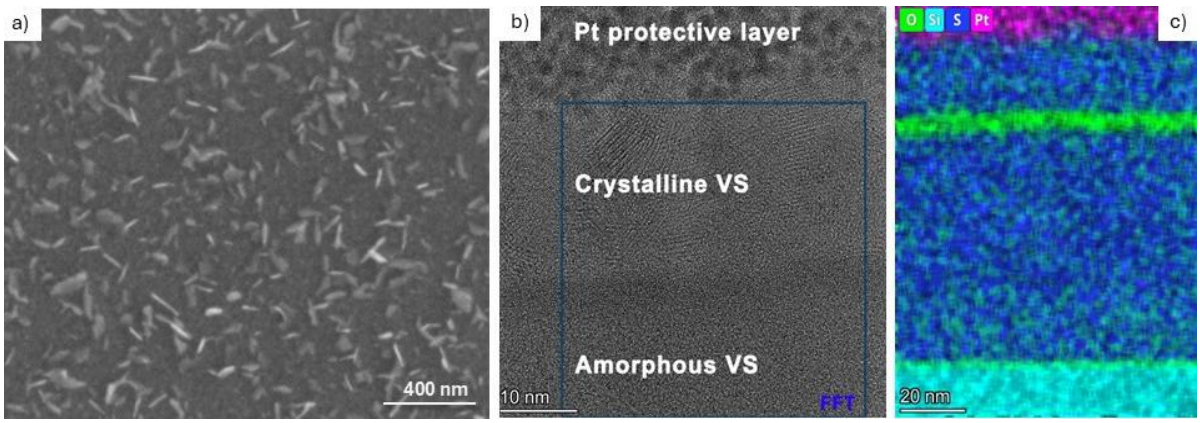

Figure 4.1 The morphology and structure of the VS films annealed in H2S atmosphere for 5 hours.

The SEM image in Figure 4.1.a shows that the surface of the layer has roughened during annealing, as the crystallization took place. From the STEM EDS mapping (Figure 4.1.c), it can be seen, that during the annealing, the oxygen containing front, which was initially the surface of the film, moved

inwards to the layer, while the crystallization took place based on the HRTEM images (Figure 4.1.b). After the annealing, the top of the layer is polycrystalline VS, while the part of the layer which is under the oxide, is still amorphous. This suggests that the presence of the Vanadium-oxide thin film enhanced the crystallization of the layer, perhaps by the oxygen diffusing towards the depth of the layer taking up the excess vanadium. It is also clear from the TEM images, that the sulphidised, stoichiometric VS layer did not oxidise after the removal from the vacuum chamber on the top part of the sample.

Optical transmission measurements were performed on the as-deposited and the 5 hours annealed samples. The layers showed a wavelength-independent absorption throughout the visible spectrum. The as-deposited layer showed absorption in the region under 400 nm, and was a mixture of metallic and semiconducting components, with the latter showing a band gap of 3.37 eV according to the Tauc-plot. The annealed film, however, proved to be a semiconductor with a band-gap of 2.84 eV. This material is absorbing under 600 nm and has a slightly higher transmittance.

The nucleation, and more generally, the growth of vanadium sulphide films is limited by the size of the precursor molecule. The radius of the TEMAV precursor molecule is around 5Å. When it binds to the surface, it binds chemically either to one SH^- group, forming a V-S bond and releasing one ligand, or it binds to two surface SH^- groups, forming two V-S bonds and releasing two ligands. In some cases, more than two ligands may be released upon arrival. If a vanadium-oxide film has already formed, and a steady growth has been established, the surface is covered by vanadium sulphide. The growth rate of vanadium sulphide, in the case of a well-established growth, is only 0.45 Å/cycle, which means 1/9 of a monolayer per cycle, which corresponds to the TEMAV precursor chemisorbing on the surface and releasing only one ligand and thus covering 9 binding sites. The TEMAV precursor in this case attaches to one SH^- group, resulting in a larger steric hindrance and a lower growth rate and the nucleation must also be slower for VS layers.

The control of the nucleation of ALD growth is crucial, on the one hand, for research aiming at the deposition of few atomic layer thick continuous layers and for the fabrication of functional nanoparticles. The nucleation of ALD films is hindered by the number of reactive sites on the surface. In a well-established layer growth this barrier is not present, however, in most ALD processes, especially in the case of Si or sapphire substrates, the growth starts by the chemisorption of the precursor molecule to the surface OH^- species If there are no reactive sites on the surface, initially, the nucleation does not start, however, after a few cycles, some precursor molecules that are physisorbed, or bound to the surface, stay left behind after the purge step, or reactive sites might also be generated as a side effect of the ALD process, for instance, by the chemical modification of the surface by the precursors. These can then act as nucleation centres for the following growth cycles.

The initial growth of VS was island-like both on sapphire and on Silicon. The lattice mismatch between VS and Al_2O_3 is 33%, which is far from sufficient to ensure an epitaxial growth. The adhesion even proved insufficient for a layer-by-layer growth. Figure 4.2 shows the VS sublayers nucleated on sapphire (a) and Si (b) and the surface coverages vs growth cycles on native oxide covered Si. The growth data were compared to a mathematical model published by Puurunen et al., which provided a phenomenological growth model with the following basic assumptions:

- The nucleation begins on active defect sites on the surface, apart from these the substrate is unreactive.
- The active defect areas expand during growth, but no new nucleation centres are generated.
- The islands grow laterally symmetrically from the nucleation centre.

The model uses basic material constants of the grown material (bulk density and molar mass) as input and has four independent parameters: the growth rate on the activated substrate, the growth rate on the ALD grown material, the number of cycles needed for the islands to touch each other, and the initial radius of the active areas. From these parameters, the model gives the surface coverage, the growth-per-cycle and the total amount of material depo sited as a function of the number of ALD cycles.

This ALD growth model was interpreted in python language, and the independent input parameters were optimized by fitting the measured surface coverage data of the samples. The GPC on the ALD-grown material was estimated from the experiments, assuming that the resulting layer has the same stoichiometry and density as the bulk material. Surface coverage values derived from the AFM measurements were used as input data points in the parameter optimization process.

The parameters obtained from the fitting based on the phenomenological ALD growth model are the following:

- The chemically active sites on native oxide are at about 6-7 nm distance, which is less than on the surface of thermally or chemically grown oxides. These are not point-like defects, from the calculations, the defect areas are 2.5-2.8 nm in diameter. However, the nucleation is different in the case of the oxide and sulphide films, which reflects the difference in growth chemistry.
- The growth of the islands is 0.5 nm/cycle in radius, and from the calculation, around 13 cycles are needed for the islands to start to merge.

The nucleation could be improved by an oxygen plasma, piranha or the nitric acid pretreatment before deposition, and it proved to increase the nucleation centres on the surface. The nucleation could be further improved by longer initial pulses. This meant that the very first ALD cycle (both the precursor exposures and the purges) was 50 times longer than the ones used for flat samples. This longer exposure ensured that all the available binding sites could be occupied by the precursor atoms. The pretreatment combined with long initial exposures resulted in a 79% surface coverage, which is about the same as after 20 cycles in the case of an untreated surface [Ref.4.1, Ref.4.2].

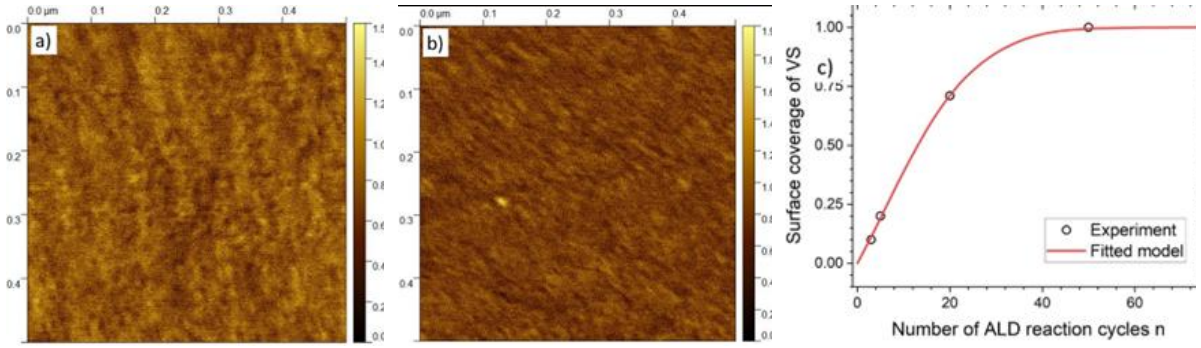

Figure 4.2 ALD cycles of VS2 on sapphire (a) and silicon (b) and the experimental and calculated surface coverage on Si (c)

Optimization of selective phase growth during vanadium thin film oxidation

OTKA FK 139075

Gy. Molnár, Zs. Baji, Zs. Fogarassy, J. Volk

VO_2 shows a first-order insulator-metal phase transition around 68°C, which is accompanied by the structural transformation from monoclinic to tetragonal phase. Different methods, physical and chemical, are used to prepare VO_2 films. We have been used a rational fabrication method: oxidation of evaporated vanadium thin films in low-pressure air at elevated temperatures to produce electrically active vanadium dioxide layer. Former transmission electron microscopy investigations reveal that our vanadium-oxide layers contain two phases. V_2O_5 phase at the substrate and on the top of it a VO_2 phase, which ensures the electrical activity of our samples for memristive devices. The applications of the reversible phase transition in VO_2 are not restricted to electrical use, but it can be utilized for wide range of thermal, optical and multi-stimuli devices. That is why, it is essential to eliminate the V_2O_5 phase, and synthesize clean VO_2 phase layer.

As a start-up, we used a general model describing the solid phase reaction in thin films [Ref. 4.3]. According to the model, only one phase develops (in our case VO_2, which contains less oxygen) until one of the reaction components exhausts (in our case the vanadium film). The next phase (V_2O_5, which contains more oxygen) can grow only at the expense of the first phase. This indicates, that the oxidation process should be interrupted at the moment, when the vanadium oxidized totally to VO_2, but the VO_2 > V_2O_5 transformation could not start.

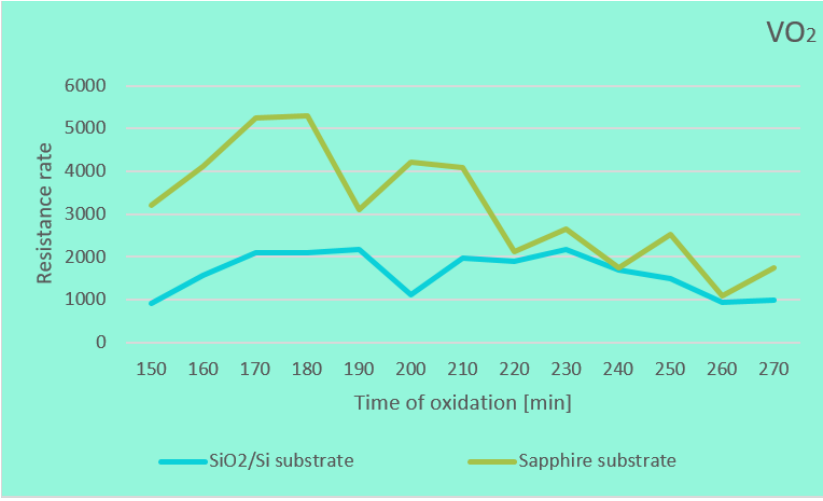

Figure 4.3 Resistance rate as a function oxidation time of vanadium oxides on SiO_2 and sapphire substrates. The temperature of oxidation was 400°C, and the pressure of oxidizing air was 1.0 x 10^{-1} mbar for all samples.

Numerous samples were prepared both on SiO2/Si and sapphire substrates to find the correct oxidation parameters to achieve the best VO_2 layer. The temperature of oxidation was 400°C, and the pressure of oxidizing air was 1.0x10^{-1} mbar for all samples. The time of oxidation varied between 150 and 270 minutes. Earlier we used samples with 270 min oxidation time, which resulted double phase layers, but as a consequence of the upper VO_2 phase, they were excellent for memristor experiments.

As a first test for sample qualification, we used resistance measurements to determine the switching ratios for the vanadium-oxide samples. Figure 4.3 shows the resistance rate of samples measured at

20°C/100°C (under and above the insulator-metal phase transition). As can be seen, the best switching rates were measured at about 180 min. oxidation time. The rates are better for films grown on sapphire than on SiO_2/Si substrate, and the best switching rate was more than five thousand.

Transmission electron microscopy investigations showed that on sapphire substrate only VO_2 phase formed at 180 min oxidation time. The layer consists of large grains of VO_2 (Figure 4.4.a), which are epitaxially matched to the sapphire substrate as can be seen on high-resolution image (Figure 4.4.b).

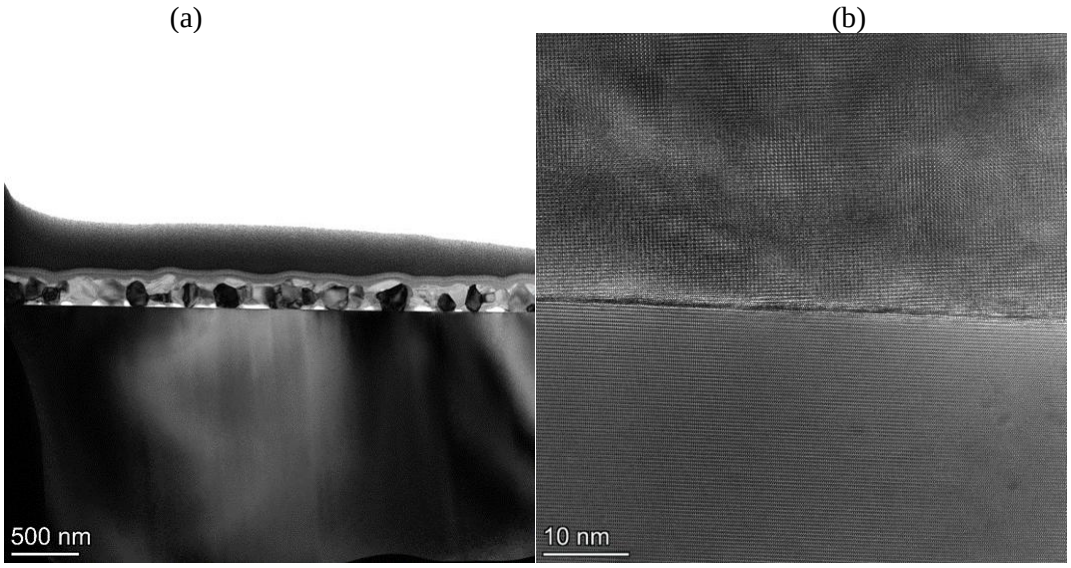

Figure 4.4 Transmission electron microscopy images of VO_2 layers on sapphire substrate. (a) The layers consist of large grains of VO_2, (b) VO_2 grains match epitaxially to the sapphire lattice.

We were succeeded in growth of clean VO_2 films by the optimization of the oxidation parameters of vanadium layers. The deeper understanding of the phase selection rules and the role of the different substrates during oxidation needs further experiments and careful discussions.

Nanoscale Mapping of Electrical Conduction of Thin VO_2 Film by Conductive Atomic Force Microscopy

TKP2021-NVA-03

N. Q. Khánh, L. Kelemen, and J. Volk

In study of temperature dependent conductance of thin polycrystalline VO_2 layer conductive AFM (cAFM) could be very helpful tool because it is able to give an insight into the process taking place at nanoscale, i.e. inside the crystal grains. However, one of the challenges for reliable cAFM performance is the surface contamination which can prevent electrical conduction between the probe and the sample. Both sample's surface, and the AFM probe are exposed to surface contamination during storage, and even during the measurement itself.

Generally, surface contaminants are mostly hydrocarbon which are very tough to clean. We've found radio frequency ion bombardment the most effective for sample cleaning, but not suitable for conductive probe's, because it would blunt the tip, and remove the tip's conducting layer by sputtering and overheating, Conductive tip in contrast, can be cleaned effectively by using mixture of sulfuric acid and hydroperoxide (Piranha solution). However, this approach is not compatible with VO_2 thin layer, as it can be etched well in H_2O_2. Furthermore, we've applied dry N_2 ambient to prevent contamination during cAFM performance.

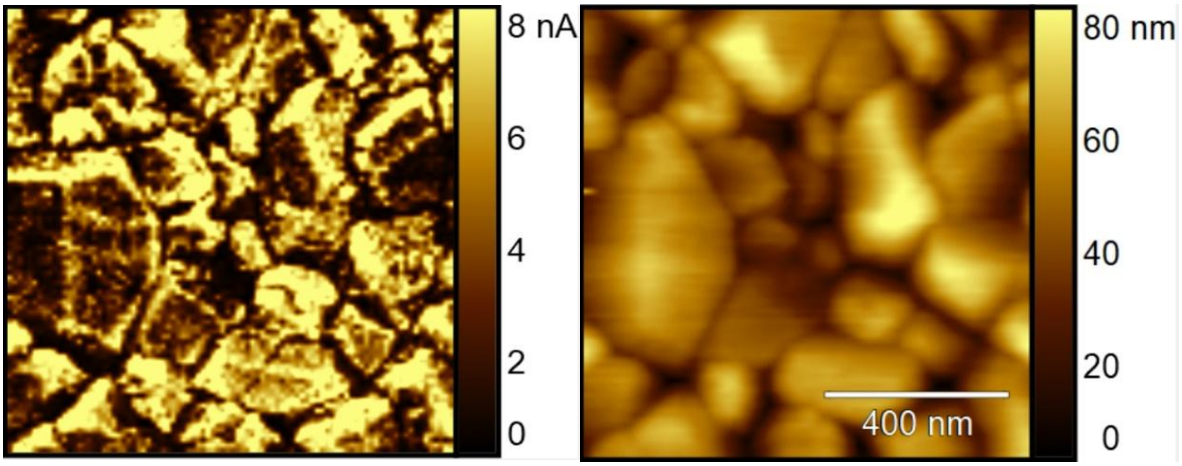

Figure 4.5 Current map measured by cAFM (left), and corresponding surface morphology (right) on thin VO_2 film deposited using magnetron reactive ion sputtering.

0 shows the current map measured by cAFM using cleaned tip at slightly elevated temperature of 36 ^oC (left), and the corresponding surface morphology (right) obtained simultaneously on the also cleaned thin VO_2 film. Our VO2 film was deposited using magnetron reactive ion sputtering. Taking the current distribution, the crystallites seem to have different electrical conductivity even by a factor of 8, probably due to their crystal quality. Furthermore, most of them show the core shell characteristics, i.e. the conductivity of the shell region is higher than that at the core of the grain. This behavior may be associated with the enhanced oxygen vacancy concentration along grain boundary region, and indicates the existing of other monoclinic phase in the core region.

Size-Dependent Study on Nanosized VO_2 Phase Change Memory Devices

OTKA K 143282, János Bolyai Research Scholarship, ÚNKP Bolyai+

L. Pósa, L. Bakos[1], S. W. Schmid[1], T. Török, M. Csontos[2], and A. Halbritter[1]
[1]Department of Physics, BME, Budapest, Hungary
[2]EMPA, Dübendorf, Svájc

Volatile Mott memristors are key components of neuromorphic circuits alongside conventional non-volatile resistive switches. While non-volatile devices primarily function as artificial synapses in neural network applications, volatile Mott memristors act as artificial neurons, capable of implementing diverse neural spiking patterns. Furthermore, Mott memristors are well-suited for oscillating neural networks, where information processing occurs in the dynamic domain, with computation encoded in the oscillators' phase.

In our study, we fabricated devices with ultrasmall electrode spacings ranging from approximately 30 to 110 nm. The asymmetric, V-shaped electrode configuration (SEM image in the inset of Figure 4.6.a) focuses the switching region into a well-defined spot [Ref.4.4], allowing us to systematically analyze the impact of device size on operation. A representative current-voltage (I(V)) trace is shown in Fig. 1a. The device transitions from an initially high-resistance OFF state to a low-resistance ON state at $V_{set} \approx 1.7$ V and reverts to the OFF state at $V_{reset} \approx 0.5$ V during the reversed voltage sweep. Due to the unipolar behavior of the device, the same characteristic is observed at the negative polarity. The resistance-voltage (R(V)) characteristics of the OFF and ON states (black curves in the right panels) exhibit significant nonlinearity, particularly in the ON state near the reset voltage. To model the device operation, we employed a two-dimensional resistor network approach [Ref.4.5]. The simulated R(V) traces (blue curves) closely align with the experimental results. Additionally, the red curves represent the maximum local temperature, which increases significantly in the ON state and likely contributes to the pronounced nonlinearity.

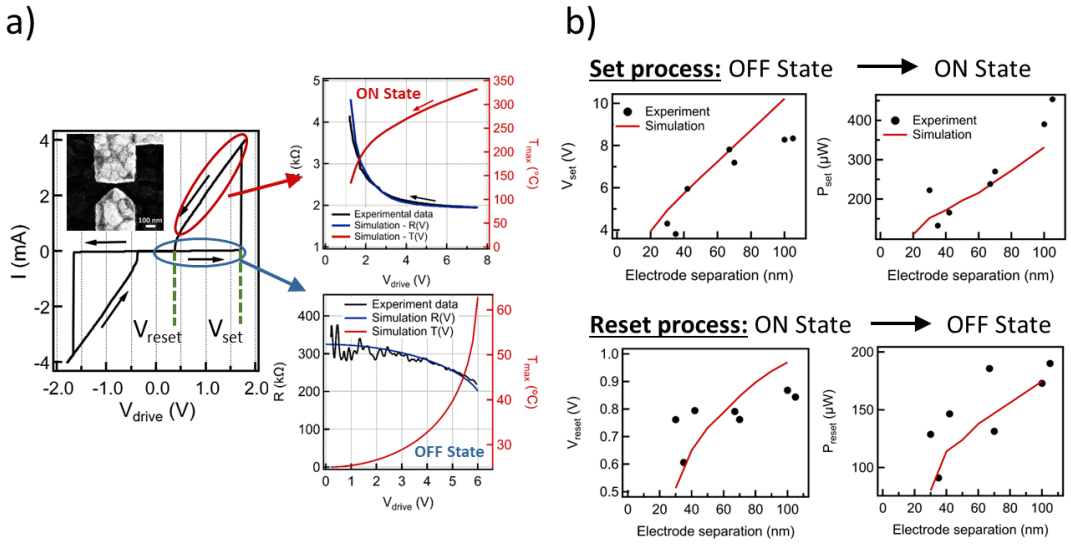

Figure 4.6 a) Switching I(V) trace of the nanogap device, the inset panel shows the SEM image of the active region. The experimental R(V) traces for the ON and the OFF states are plotted in the adjacent graphs (black curves). Simulated results are also presented, including the R(V) curve (blue) and the bias voltage dependence of the maximum local temperature (red curve). (b) Dependence of switching voltages (left panels) and switching powers (right panel) on device size. The red lines represent fittings based on the two-dimensional resistor network model.

Integrating the VO_2 device into a circuit requires the ability to tune its switching voltages to match the circuit's signal levels. The most straightforward approach to achieve this is by adjusting the distance between the metal electrodes (gap size). To minimize the effect of the layer's inhomogeneity, the devices were fabricated within only a few square micrometers large area, with gap sizes ranging from 30 to 110 nm. A clear trend was observed in the set and reset voltages (V_{set}, V_{reset}) as well as the corresponding switching powers (P_{set}, P_{reset}), see black dots in Figure 4.6.b. Notably, simulations accurately reproduced the experimental trends, further validating our findings (red curves).

By applying time-resolved measurements, we revealed the switching dynamics of the device. Last year, we demonstrated that a 20 ps long voltage pulse could already induce the set transition, which was supported by our simulation [Ref.4.5]. The set transition was explained using a pure electrothermal model, accounting for Joule heating caused by the electrical current and the thermal conductivity of the device.

The simulation predicted a nanosecond-scale relaxation process for the reset transition, driven by the thermal relaxation of the device. However, the experiment showed a much longer reset time, extending to several hundreds of nanoseconds, as shown in Figure 4.7.a. During the experiment, the device was set to the ON state by applying a voltage pulse with t_{pulse} length and V_{pulse} amplitude. Upon removing the pulse, the voltage was adjusted to a readout level $V_{readout}$, lower than V_{reset} to monitor the resistance of the device. The measurements revealed that the device maintained its low-resistance state (see the bottom panel of Figure 4.6.a for a relaxation period (t_{relax}), after which it rapidly returned to the high-resistance state.

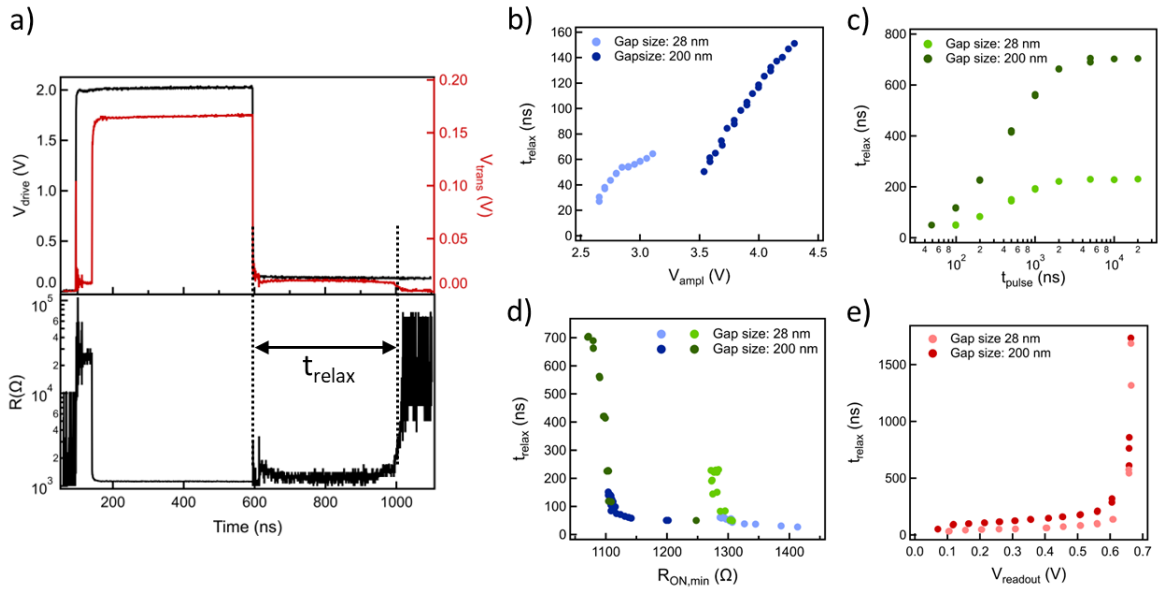

Figure 4.7 (a) Time-resolved pulsed measurement of nanometer-sized VO_2 devices. The upper panel depicts the driving voltage signal (black curves) and the transmitted voltage signal (red curve). Upon applying a 500 ns voltage pulse with a 2 V amplitude, the device switches to a low resistance state after a delay of a few tens of nanoseconds delay. Following releasing the voltage pulse, the device retains its low-resistance state for approximately 400 ns. The bottom panel presents the corresponding time-resolved resistance data, indicating the length of the relaxation time (t_{relax}) of the reset process. (b)-(e) Dependence of the relaxation time on various parameters: (b) pulse amplitude, (c) pulse length, (d) minimum device resistance, and (e) readout voltage.

To study the relaxation phenomenon in detail, we first varied the amplitude and length of the set pulses (see Figure 4.7.b-Figure 4.7.c) using two devices with significantly different gap sizes (28 and 200 nm). The relaxation time increased with both parameters; however, for the pulse length, a saturation effect was observed in both devices. The measurement data can be scaled together when the relaxation time was plotted as a function of the device's minimum resistance during the set pulse, which is typically measured at the end of the pulse.

This indicates that the relaxation time depends solely on the size of the metallic filament. The observed saturation in pulse length beyond microsecond range arises because the device resistance stabilizes at its steady-state value. Additionally, we investigated the relaxation time as a function of the readout voltage. While a slight increase was observed at low voltage, the relaxation time increased significantly near the reset voltage exceeding the microsecond range. This steep rise is likely due to variations in the local temperature. High readout voltages elevate the local temperature near the phase-change temperature (≈65 °C), significantly prolonging the lifetime of metastable metallic grains.

Towards fully hardware-based neuromorphic encoding for efficient vibroacoustic signal recognition

TKP2021-NVA-03

T. Zeffer, T. N. Török, F. Braun, and J. Volk

Neuromorphic signal processing can enhance IoT sensor efficiency and support edge computing by mimicking biological systems. However, preprocessing encoded signals for spiking neural networks (SNNs) often requires significant computational resources.

Here, we propose an energy-efficient, hardware-based solution for analyzing rapidly changing vibration and acoustic signals. Inspired by human cochlear implants — which achieve clear speech recognition with limited frequency channels (16–22) — our approach minimizes energy costs while maintaining performance. Beyond conventional MEMS chip design, sensor parameters are optimized to align with the computational neural network, analogous to higher auditory neural pathways. Our adaptive co-design methodology jointly optimizes preprocessing filters and SNN parameters, ensuring unified hardware-software integration for energy-efficient neuromorphic systems. The proposed hardware consists of a frequency-selective MEMS cantilever array paired with a VO_2 memristor nanogap oscillator for amplitude-sensitive spiking signals (Figure 4.8). We validated the system using the Google Speech Commands dataset, which includes approximately 105,000 one-second audio samples across 35 common words such as ‘yes,’ ‘no,’ ‘up,’ and ‘down.’ We plan to extend its application to vibration signals for IoT-based vibroacoustic sensor networks. The multi-cantilever array's FFT-free operation makes it ideal for low-power, place-and-forget sensor nodes, outperforming conventional MEMS microphones and accelerometers.

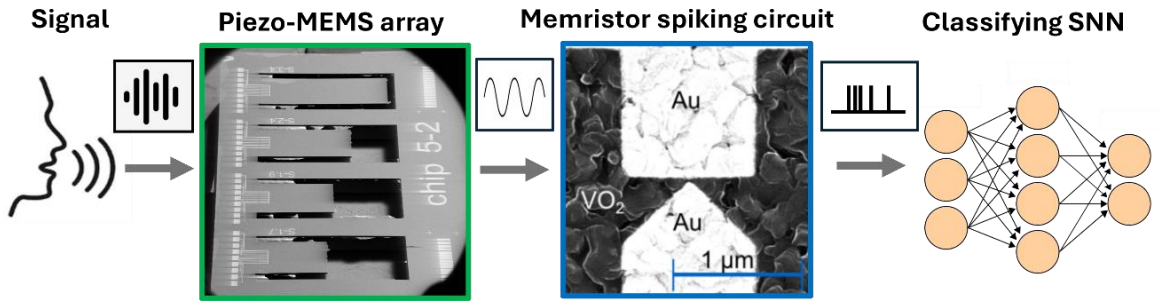

Figure 4.8 Schematics of the proposed neuromorphic vibroacoustic signal recognition system. Incoming acoustic/seismic signals are detected by an N-channel piezoelectric MEMS array, producing frequency-specific periodic signals. These signals are converted into spike trains via a VO_2 nanogap memristor circuit, enabling amplitude-encoded spike raster generation. The generated spike trains are subsequently processed by a spiking neural network (SNN) for recognition and classification. The concept is validated using Google Speech Commands dataset.

Before integrating the proposed system, our aim was to build a software-based SNN that takes into account the constraints of both the MEMS and memristor-based spike generation. The former implies limitations in the number of usable frequency channels (N). In our FFT-free sensor operation, each frequency corresponds to an individual cantilever, and their number must be kept below 100 to maintain a compact chip size. The fundamental resonant frequency of the MEMS oscillators can be finely tuned by adjusting the length of the cantilevers and the tip mass on their backside. However, single-crystal Si unimorph cantilevers typically have a high Q-factor (100–200), resulting in narrow bandwidth filtering. This causes a significant portion of the voice frequency range to be uncovered by cantilevers, potentially

leading to some information loss. In the case of memristor oscillators, the limiting factor lies in the relatively simple encoding compared to more refined software-based solutions. Nevertheless, using an oscillator with a volatile VO_2 memristor, we observed that no spike generation occurs below a certain incoming amplitude threshold. However, above this threshold, the spiking rate is proportional to the amplitude of the sinusoidal wave, enabling a simple amplitude encoding mechanism.

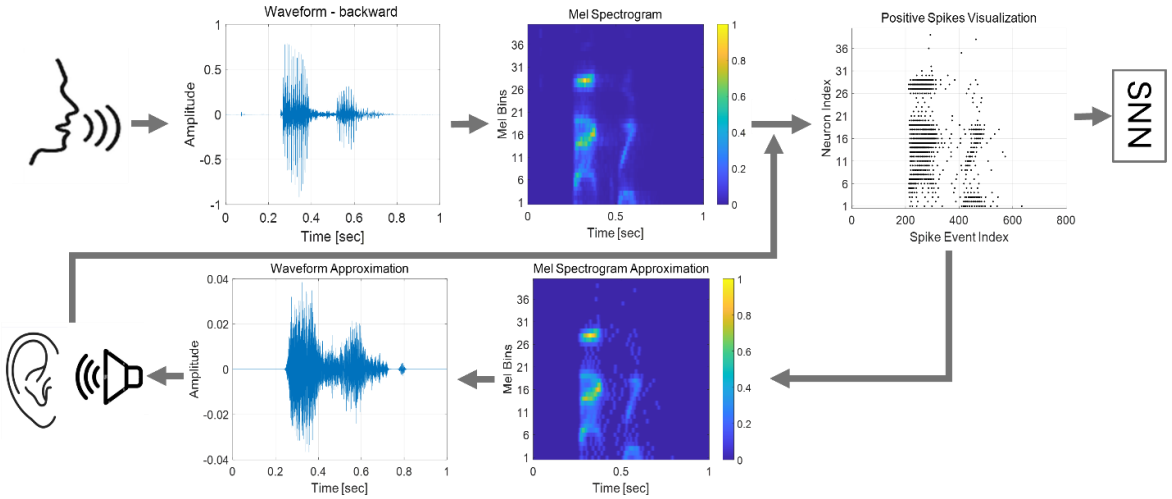

Figure 4.9 Optimization of the SNN preprocessing pipeline. Google Speech Command benchmark items are first converted to mel spectrograms and subsequently into spike rasters to feed the SNN. Higher amplitude regions on the mel spectrogram correspond to higher spike rates in the generated spike raster. Reconstruction of the spike raster using inverse transformations supports hyperparameter optimization. Critical parameters were varied until all 35 different words were recognizable by human hearing.

The full pipeline is depicted in the upper row of Figure 4.9. Audio files from the Google Speech Commands database are converted to mel spectrograms using PyTorch. Afterward, time-dependent amplitude signals for each channel are parallelly converted to spike trains using cumulative sum and step-forward algorithms. Higher amplitude regions on the mel spectrogram correspond to higher spike rates in the generated spike raster. (Later, this function will be replaced by the memristor oscillator.) The goal of the present SNN optimization was to determine if acceptable learning accuracy can be achieved despite the limitations of the minimal encoding hardware components, namely the low number of channels, the narrow frequency bandwidth, and the simple amplitude-encoding algorithm. The applied SNN consists of an input layer of N neurons, four fully connected hidden layers of 256 neurons each, and an output layer of 35 neurons corresponding to the speech commands to be classified. The successful training of the SNN relies heavily on implementing suitable hardware and appropriate tuning of hyperparameters. For the hardware simulations, we used an NVIDIA GeForce RTX 4070 GPU. To reduce the volume of the hyperparameter space, we performed audio signal reconstruction and fine-tuned preprocessing parameters (e.g., spiking threshold and hop length). These parameters were adjusted and evaluated through human recognition of the 35 command words. We assumed that successful human recognition would provide a good starting point for training the artificial SNN.

Through trial-and-error and referencing literature data, we also established the internal parameters of the SNN. To further support the final MEMS design process, we varied and compared two key parameters: the channel number (20, 40, and 60) and the filtering bandwidth of the resonators (overlapping versus fixed bands of 100 Hz). The results showed that the accuracy of the SNN on the validation dataset approached and slightly exceeded 60%. Surprisingly, the effects of both channel number and bandwidth were minimal. Although further optimization is required, the software-based simulation of preprocessing demonstrates that even with simple, energy-efficient hardware, a reasonable accuracy can be achieved using an equally energy-efficient SNN-based classification tool.

Progress toward Kitaev transmon generation

HORIZON-EIC-2022-PATHFINDERCHALLENGES-01-06-101115315 (QuKIT)

M. Sütő[1], B. Vasas[1], Z. Kovács. P. Makk[1], and Sz. Csonka[1]
[1]In collaboration with the Department of Physics, BME, Budapest, Hungary

Quantum computing has held the interest of the scientific community for years, promising algorithms orders of magnitude faster compared to classical computing, but the realizations are still in their infancy. As part of the QuKIT international collaboration, we aim to create a novel, fault-tolerant quantum bit using the combination of a Kitaev chain coupled with the well-characterized transmon qubit. The schematic of such a device is shown on Figure 4.10.a. The presence of the Kitaev chain introduces topological protection and enhances the qubit tolerance to environmental factors, while the transmon part provides a well-established platform for qubit manipulation and readout. To this end we are working with an InAs-based near-surface two-dimensional electron gas (2DEG), contacted by an epitaxial superconducting aluminum layer (Figure 4.10.b). As part of the collaboration, our work is twofold. Firstly, we aim to test out the possibility of using the epitaxial Al layer as a base for the transmon qubit, secondly, we are working on the fabrication and characterization of a minimal Kitaev chain.

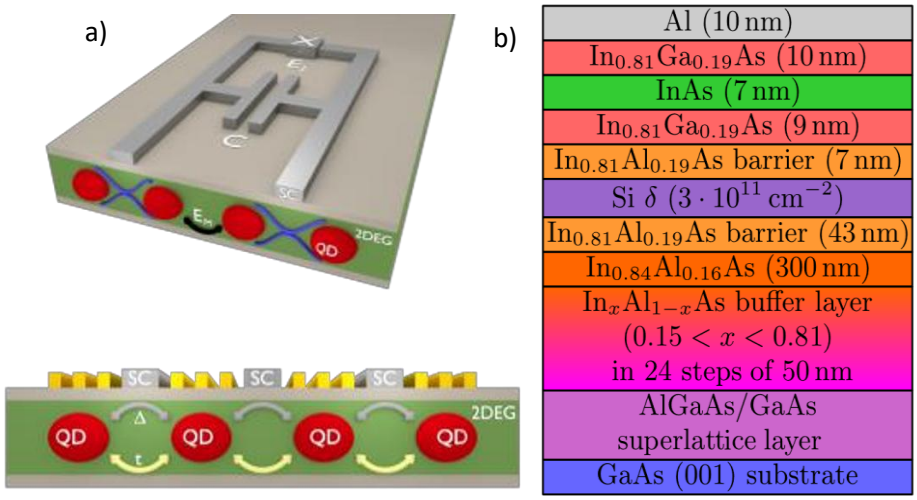

Figure 4.10 Schematics of the novel Andreev qubit formed by coupling a traditional transmon to a minimal Kitaev chain (a) (source: QUKIT Proposal Part B). Our platform for the realization of the Kitaev qubit: near-surface InAs 2DEG contacted by an epitaxial Al layer (b).

To test the quality of the epitaxial Al layer, we created a high frequency λ/4 coplanar resonator and coupled it to a Josephson junction embedded into a superconducting loop, creating an RF squid, with the goal of measuring the current-phase relations of the junction (Figure 4.11.a). In this setup we can substitute the junction as a magnetic flux tunable inductance, coupled to the resonator such, that any change in the flux will cause the resonance frequency to shift periodically by applying magnetic field. From this periodic behavior one can characterize the properties of the junction, such as the average transmission, and the supercurrent profile. As shown in Figure 4.11.b, we managed to observe the resonance frequency fluctuations, and by fitting to the individual resonance curves, we estimated an average transmission of 87%. Details about the results are shown in our paper, recently submitted, currently under review [Ref.4.6].

To create half of a minimal Kitaev chain, we need to form two quantum dots, separated by a small strip of a superconductor (Figure 4.10.a). To work towards this goal, we first tried to create a double quantum dot, using multiple layers of gate electrodes, first to restrict the 2DEG into a quasi-1D channel, then with a 2nd layer of gates, we can form the desired dots. Our first device toward this goal is presented in Figure 4.12.a, with the trapezoid gates to define the 1D channel and the thin finger-gates on the 2nd layer, for qdot creation and manipulation. The device is currently in measurement, but shows, that it is capable of hosting qdots, as is visible in the stability diagram presented in Figure 4.12.b.

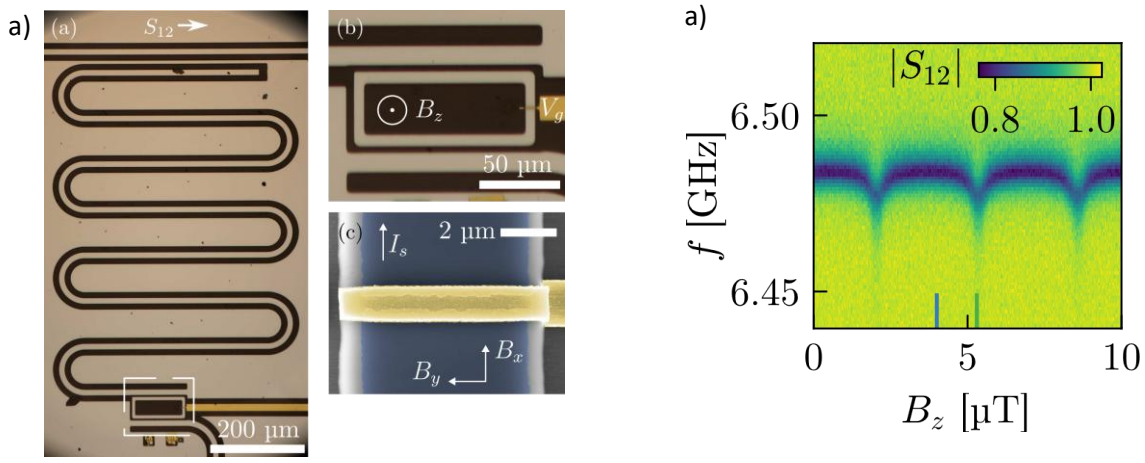

Figure 4.11 Optical (Aa and Ab) and SEM (Ac) images of a λ/4 coplanar resonator etched from the epitaxial Al layer. (A). The transmission of the resonator feedline as a function of the frequency and magnetic field. The <1 parts correspond to the resonance frequency, which shows a clear periodic behavior (B) [Ref.4.6].

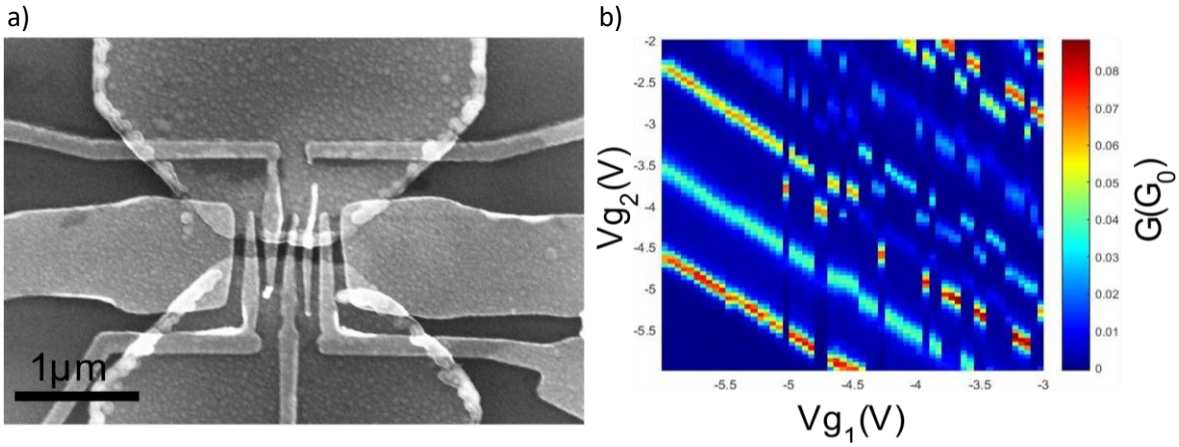

Figure 4.12 SEM image of a measured qdot device. The trapezoid electrodes define the 1D channel in the 2DEG, while the finger-gates create the qdots (a). Stability diagram of the formed qdot as a function of the two leftmost finger-gates. It shows clear conductance peaks, tuned by both gate electrodes, corresponding to the qdot regime. It also exhibits charge fluctuations, possibly indicating problems with the dielectric or the wafer (b).

Microsystems Department

Head: Dr. Péter FÜRJES, Ph.D., senior research fellow

Research Staff:

István Bársony, member of HAS
Orsolya Bálint-Hakkel, Ph.D.
Anita Bányai, Ph.D.
Barbara Beiler, Ph.D.
Ferenc Bíró, Ph.D.
Csaba Dücső, Ph.D.
András Füredi, PhD.,
Péter Fürjes, Ph.D.
Eszter Leelőssyné Tóth Ph.D.
Zoltán Szabó, PhD.
Zsófia Sztyéhlikné Bérces, Ph.D.

Engineers / technicians:

Gabriella Bíró, technician
Tibor Csarnai, electrical engineer
Magda Erős, technician
Róbert Hodován,
mechatronic engineer
István Laczkovics, technician
Csaba Lázár, electrical engineer
Margit Pajer, technician
Zsuzsanna Brigitta Sik, bioengineer

PhD Students:

Lilia Bató (ÓE Univ. Óbuda)
Dóra Bereczki (ÓE Univ. Óbuda)
János Márk Bozorádi (ÓE Univ. Óbuda)
Zsombor Szomor (ÓE Univ. Óbuda)

The main goal of the Microsystems Laboratory is to research and develop integrated sensors and sensor systems, MEMS and BioMEMS devices fabricated by silicon or polymer micro- and nanomachining technology. The activity covers the characterisation of novel functional materials, development of sensing principles, technology solutions and application-specific microsystems. The utilisation of micro- and nanomachining technology enables the miniaturisation of sensing and analytical systems and integration of various functions of sample preparation, sensing, readout, actuation or communication. The laboratory is focusing on the development of mechanical, physical, chemical (and biochemical) sensors, functional micro- and nanofluidic devices, implantable microsystems and infrared LED.

Our medium-term goal is to broaden the spectra of perspective research topics of MEMS systems and to develop a systematic organisation by forming a dynamic and growing research groups in the Microsystems Laboratory. Considering the financial environment our research directions fit to the European and Hungarian strategic roadmaps and directives (S3 - National Smart Specialisation Strategy) by the following research topics:

Health	*BioMEMS, microfluidic, Lab-on-a-Chip (LoC), Organ-on-a-Chip (OoC) systems, Point-of-Care (POC) diagnostics, therapeutic drug monitoring (TDM), personal medicine, implantable, wearable devices, continuous monitoring,*
Cutting-edge technologies	*human-machine interaction and cooperation – sensors for robotics, space technologies (microfluidics and diagnostics for space applications), biosensors, driving safety sensors, novel materials and manufacturing technologies: advanced materials, nanotechnologies, 3D manufacturing, AI based signal and data processing,*
Energy, climate	*sensors for energy industry, characterisation photovoltaic systems, environment safety sensors (water monitoring), gas sensors (smart home, smart clothes), low consumption electronics,*
Agrifood	*food safety sensors, optical (UV-VIS, infrared, Raman) spectroscopy*

Infrastructure and technological competencies

The Laboratory operates a unique infrastructure in Hungary, therefore its sustainable operation and development is a strategic goal. The infrastructure is open for academic and industrial partners to fabricate (and to characterise) complex, purpose-designed microsystems, nanocircuits, as well as Lab-on-a-Chip devices and to develop their technology solutions.

The high-tech microtechnology related fabrication and characterisation systems work in a class 10 cleanroom facility. The laboratory is dedicated for 3D processing of 4" Si / glass / polymer substrates with maximal resolution of 1μm, together with lithographic mask manufacturing. Electron beam lithography and focused ion beam (FIB) milling are also available with resolution of 20nm. Multi-domain Finite-Element Modelling (FEM), and process simulation also support the structural design and development. Wide spectra of characterisation techniques are also available: optical (fluorescent) and electron microscopy (SEM and EDS), atomic force microscopy (AFM), profilometry, optical and electrical measurements, electrochemical impedance spectroscopy, microfluidic characterisation, mechanical vibration and climate test chambers, UV-Vis / IR / FTIR / FLUORESCENT / RAMAN spectroscopy, etc.

Available micromachining techniques:

- Patterning – mask design, laser pattern generator, photolithography, (double side) alignment, electron beam lithography (E-Beam), Focused Ion Beam processing – FIB milling, nanoimprinting
- Structured polymer layers – PMMA, PI, SU8 patterning, micromoulding, soft lithography – PDMS, hot embossing technique for polymers
- Wet chemistry – chemical wafer cleaning, isotropic and anisotropic etching techniques
- Dry chemistry – deep reactive ion etching, plasma etching techniques (DRIE, RIE)
- High temperature processes – thermal oxidation, annealing, rapid thermal annealing (RTA)
- Physical thin film depositions – Thermal and electron beam evaporation, DC and RF sputtering
- Chemical thin film depositions – Atmospheric and Low Pressure Chemical Vapour Deposition (APCVD, LPCVD, LTO), thermal and plasma enhanced Atomic Layer Deposition (ALD)
- Liquid Phase Epitaxy of III-V compound semiconductors (LED manufacturing)
- Wafer bonding – Si-glass, glass-glass, polymer-glass anodic and thermal bonding
- Chip dicing, wire bonding especially for sensor applications
- Special packaging techniques and methods
- 3D printing and CNC milling for application-specific polymer packages or microfluidic structures

The Micro- and Nanotechnology Research Laboratory is recognised as one of the strategic research infrastructures (RIs) by the National Research, Development and Innovation Office with an excellent rating in its survey entitled "National Research Infrastructures 2023-2024".

R&D topics and research group structure and in the Microsystems Laboratory

The development of MEMS devices requires solid design capacity and advanced cooperation among the research and technical staffs for precise operation of the full micromachining fabrication line. Actually, 10 researchers, 5 PhD students, 4 engineers and 4 technicians work for the Laboratory with close and flexible cooperation with the colleagues of the Nanosensors Laboratory.

- **MEMS & 3D micromachining technology (Csaba Dücső, Ferenc Bíró):** Development specific MEMS (mechanical and gas) sensors for driving and environmental safety applications – with special emphasis on the advanced technology of 3D microstructuring and functional nanomaterials.
- **BioMEMS, integrated systems for biomedical applications (Péter Fürjes, Zsófia Sztyéhlikné Bérces, János Márk Bozorádi, Csaba Dücső):** Development MEMS sensors and microsystems specifically for medical applications, considering their complex electro-mechanical integration, biocompatible packaging and signal acquisition. The topic includes the

manufacturing Si and flexible implantable microstructures in connection with the National Brain Programme.

- **Microfludics, Lab-on-a-Chip & Organ-on-a-Chip devices (Péter Fürjes, Anita Bányai, Lilia Bató, Dóra Bereczki, András Füredi, Orsolya Hakkel, Zsuzsanna Brigitta Sik, Zsombor Szomor):** These are essential building blocks of Point-of-Care diagnostic and drug analytical tools in the medical field. Research of micro- and nanofluidic systems enable the development of sample preparation, molecular detection and cell analytical functions for LoC and OoC devices. The group works in active collaboration with companies, research institutes and universities in this field (Aedus Space Ltd., Budapest University of Technology and Economics, Micronit B.V., Microfluidic ChipShop GmbH, University of Pécs).
- **IRLED (Zoltán Szabó, Barbara Beiler):** Development and fabrication wavelength specific infrared LEDs (thousands per year for our partners: Anton Paar GmbH, Senop OY). We envisaged a larger scope development of broadband IRLEDs for OoC based pharmaceutical, environmental and food safety applications.
- **Technology and FEM Modelling (Eszter Leelőssyné Tóth, Zsombor Szomor):** Modelling, such as digital twin, is a widely applied method in engineering practice to speed up development and manufacturing of prototypes. These methods also effectively support the comprehension of physical and chemical processes in the microscale.

Cooperation

According to the large number of European and domestic R&D projects wide cooperative and knowledge network was established with universities (BME, DE, ÓE, PPKE, PTE, SE, TU Delft, TU Eindhoven), research centres (HUN-REN ATOMKI, HUN-REN SZBK, HUN-REN WIGNER, HUN-REN TTK, HUN-REN SZTAKI, IMEC, CSEM) or research groups and companies (77 Elektronika Ltd., Philips Research, Micronit B.V.) to perform interdisciplinary research. The Laboratory is supporting the National Laboratory Programmes (Quantum Technology, Brain Research or Human Reproduction) by our technology and expertise. Besides the scientific projects, the Lab offers technology development and manufacturing services for several industrial partners as SEMILAB, 77 Elektronika Ltd., Mirrotron, Bay Zoltán Appl. Res., Anton Paar (Austria), Senop (Finland) to achieve higher technology readiness levels (TRL 2 → 6).

Major research projects

The researchers of the Laboratories are involved in development, fabrication and integration micro- and nanosystems, sensor structures to open new perspectives in the field of medical diagnostics, Minimal Invasive Surgery techniques, energy-efficient autonomous systems. Moreover, our interest covers the topics of optical analytics (spectroscopy), environmental and safety (gas detectors) sensors.

- Development of a point-of-care microfluidic device for Therapeutic Drug Monitoring in cancer treatment (POC-TDM), Marie Skłodowska-Curie Actions - Postdoctoral Fellowships (HE MSCA PF) – András Füredi, Péter Fürjes
- Unlocking data content of Organ-On-Chips - UNLOOC, Horizon-KDT-JU-2023-1-IA-Topic-1-Global call according to SRIA 2023(IA) 101140192
- Monitoring sensors deployed in emergency situations and in harsh environment, Thematic Excellence Programme - TKP2021 National Defence and Security, TKP2021-NVA-03
- Innovative biosensing technologies for medical applications – INBIOM, Thematic Excellence Programme - TKP2021 Health, TKP2021-EGA-04
- Low-dimensional nanomaterials for the optical sensing of organic molecules on liquid and gas interfaces - OTKA K 131515 (participant)
- IR spectroscopy of extracellular vesicles: from exploratory study towards IR-based diagnostics – OTKA K 131594 (participant)
- Thin film integrity check by capillary bridge test – OTKA FK 128901 (participant)
- Atomic layer deposition and applications of functional sulfide nanolayers – OTKA-FK_139075 (participant)

Scientific cooperation:

- Providing optrode devices and their characterisation background for Implantable Microsystems Research Group of Pámány Péter Catholic University
- Development Lab-on-a-Chip technology for detection nucleic acid content in extracellular vesicles for University of Pécs (cooperative partner: BME SZAKT)

Industrial cooperation:

- Development and optimisation polymer based autonomous microfluidic cartridge, its production technology and measurement methodology for high sensitive Point-of-Care detection of bacteria and blood biomarkers for 77 ELEKTRONIKA Ltd.
- Development, manufacturing and characterisation microfluidic systems for the HUNOR Programme in cooperation with AEDUS SPACE Ltd.
- Development and manufacturing specific calibration test samples for characterisation methods of semiconductor industry for the SEMILAB Inc.
- Development and manufacturing Near InfraRed LED devices for spectroscopic applications for SENOP Ltd. (Finland)

Conference organization

Our colleagues organised the prominent European conference dedicated for the scientific community of research and development sensors and actuators, the XXXVI. EUROSENSORS Conference in Debrecen.

Scientific media appearances:

- Researchers' Night – Radio Bézs discussion - https://www.radiobezs.hu/marton-eva-fekete-feher/, https://www.radiobezs.hu/radiobezs_files/Arch%C3%ADvum/2024/0923_1500.mp3 (Péter Fürjes)
- Novum Microsystems – https://www.youtube.com/watch?v=MP38eG41AE0

Education

The Microsystems Laboratory also have an important mission to provide university students with access to micromechanical technologies and related qualification procedures, and to familiarize future engineers, physicists, chemists, and biologists with this field of science. Accordingly, the laboratory staff actively participate in higher education training as lecturers, practice leaders, and provide students with opportunities to do internships, TDK, BSc., MSc., and Ph.D. work. We have significant relationships with the Faculties of Natural Sciences, Electrical Engineering and Informatics, Chemical Technology and Biotechnology, as well as Mechanical Engineering of BME, the Faculty of Information Technology and Bionics of PPKE, the University of Óbuda, the University of Pannonia, the University of Debrecen, and several faculties and research groups of the University of Szeged.

Wearable gas sensors for emergency and extreme conditions

TKP2021-NVA-03

A. Király, K. Pankász, F. Bíró, I. Bársony, Z. Szabó, Csaba. Dücső

In the „ Chemical gas sensors" workpackage of the TKP2021-NVA-03 „Environmental monitoring sensors for emergency and extreme conditions" project we plan to develop wearable and mobile gas sensors (on drones and controlled robots) for detection dangerous gases carry high risk during natural or industrial disaster management (time frame: April 1. 2022 – September 30. 2025). The primary goal is the recognition of methane leakage; however, detection of other risky gases will also be investigated. We are intended to reach the TRL4 (in demo devices) and TRL6 for prototypes with dedicated readout and communication electronics, or commercial demo kit.

Two families of gas sensors are considered:

1) **low cost solid-state catalytic and chemoresistive sensors** for demo applications
   target gases: H_2S, HCN, NH_3, Cl_2 or HCl (1-10-100ppm - TLV level or above)
2) **moderate cost optical sensor for more accurate concentration measurements**
   target gases: CH_4, LPG, PB 1—5 %v/v (possibly CH_4 ~ 100 ppm)

Test platform for chemoresistive gas detectors

Regardless the operation principle, the calorimetric or chemoresistive sensors operate at elevated temperatures between 100 – 500°C. The basis of our calorimetric sensors is a newly developed small diameter (150µm) microhotplate exhibiting ±1% temperature uniformity on the heated area below 550°C. The stability of the heater is 5000 hours at least at the operation temperature of 530°C, thereby in pulsed mode operation ca. 5 years' operation can be achieved. The power dissipation at 500°C is 27mW/1.5V, so the chip can be utilized in portable or wearable devices for personal safety. A utility model protection was given for the microhotplate design in 2021 (*Microheater with uniform surface temperature*, U 20 001150, registration number 5279). Accordingly, we exploit our previously developed microhotplate structure as the carrier of the gas sensitive material.

In a parallel phase, a chip set for chemoresistive gas sensor's development was prepared. The main goal is to facilitate the functional characterization of the sensing layer by enabling its local deposition on the heater surface of individual chips instead of processing a complete wafer. Apart from economic issues, the set assists the laboratories active in development of sensing layers but do not have chip processing capabilities.

The 3.5x3.5 mm^2 basic chip carries three microheaters with resistance measuring electrodes on their top. The 150µm diameter microheaters are suspended on a 500 µm circular membrane. Two types of Pt read-out electrodes of 10 and 100 µm were formed to enlarge the resistance measuring range (0).

Two versions of masking elements were fabricated for better flexibility and widening the possible deposition methods of the sensing layer. A Si masking chip formed from SOI wafer is for general use and also enables the high temperature deposition methods, such as CVD and ALD (0). This version requires post processing of mounting and wire contacting. The functionality of the chip set was demonstrated by sputtering ZnO layers.

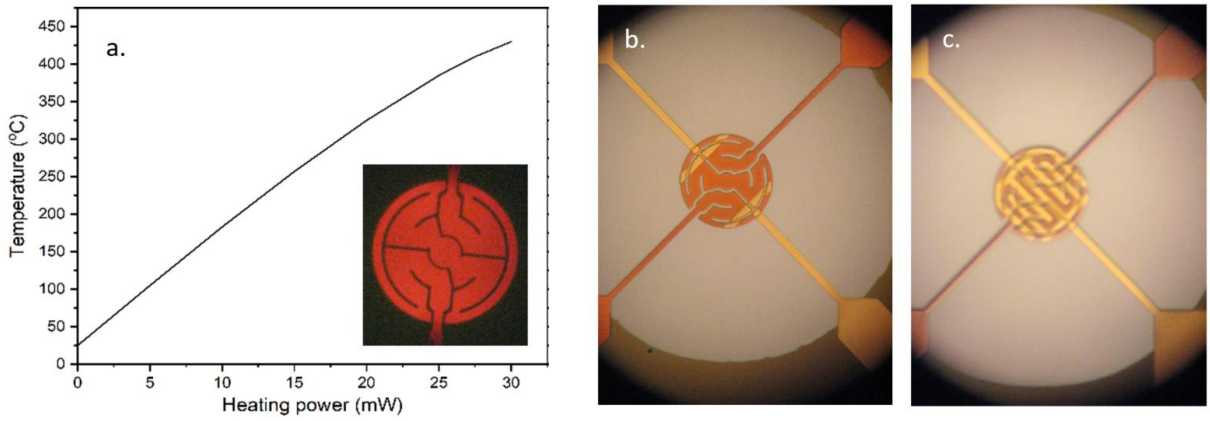

Figure 5.1 Temperature vs. power characteristics and the excellent temperature uniformity as seen from the glowing heater (a.). Suspended microheaters with resistance readout electrodes of 100µm and 10µm distances (b, c).

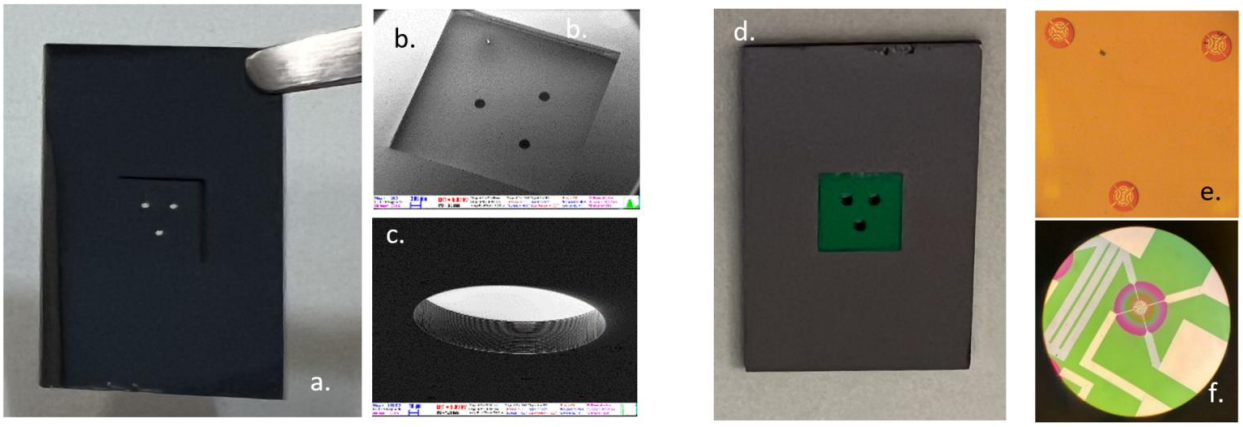

Figure 5.2 Deposition-through masking chip made from SOI wafer. Details show the cavity formed in the substrate and one of the openings in the 40µm thick device layer (a, b, c). Positioned test chip from the back (d) and the three heaters as seen from the deposition side (e). Sputtered thin ZnO layer (orange) (f).

The results and the chip set were presented at the Eureosensors XXXVI. Conference. Anna Király from BME wrote her BSc thesis from the processing technology.

Optical gas sensing

In frame of the TKP 2021-NVA-03 Grant 2nd Work package we have been investigating the construction and capability of methane detection by non-dispersive operation principle in the mid infrared region. The goal is to develop a complete setup consists of MEMS elements, such as microheaters and reflectors for IR source, optical channels and detectors. The test setup was built from commercial components, whereas the electronics was constructed in modular form for **driving the IR source** and the **appropriate read-out**. Adequate optical system was constructed to ensure high IR intensity projection on the detector and improve the achievable signal-to-noise ratio with the applied pathway (30mm). The preliminary results show that the construction is capable to detect methane in the 500 – 50000 ppm concentration range with the accuracy of 1-10%. In 2024 the development of prototypes of non dispersive infrared (NDIR) optical gas detector was continued. Due to the fact, since the last decade the sensor networks (Wireless Sensor Network - WSN) attract unstoppable rise in popularity at the markets of science & technology, industrial and consumer applications, we targeted to develop a completely digital version of the NDIR methane detector. Our development also pointed out

that, the main benefit of the digital optical gas detection is the key physical parameters which affect the response signal can be measured (for example light intensity, filament current, detector temperature, humidity) and these values can read out remotely at a control room for example through a suitable sensor network thereto the detectors are connected. Two versions of the digital NDIR methane detector with the software for sensor control and signal processing have been designed and fabricated also. These versions were calibrated and tested. According to test results we may say **digital NDIR sensors are capable to response in 7-8 seconds to 1 or 2 %v/v methane exposure as it is recommended by the industrial standard**. Meanwhile, the detector consumes 120-150mA current which is still below the maximum permissible 200mA current consumption. 0 illustrates the constructed devices and some experimental results.

Some further improvements were performed on optical channel, signal processing and device calibration procedure on the prototype of digital NDIR methane detector. Following these modifications detector prototype for portable devices was presented successfully to the members of the control group of NKFIH organization in March 2024 (First milestone of the Grant). Furthermore, the device was exhibited at the Eurosensors XXXVI. conference in Debrecen. [Ref.5.1]

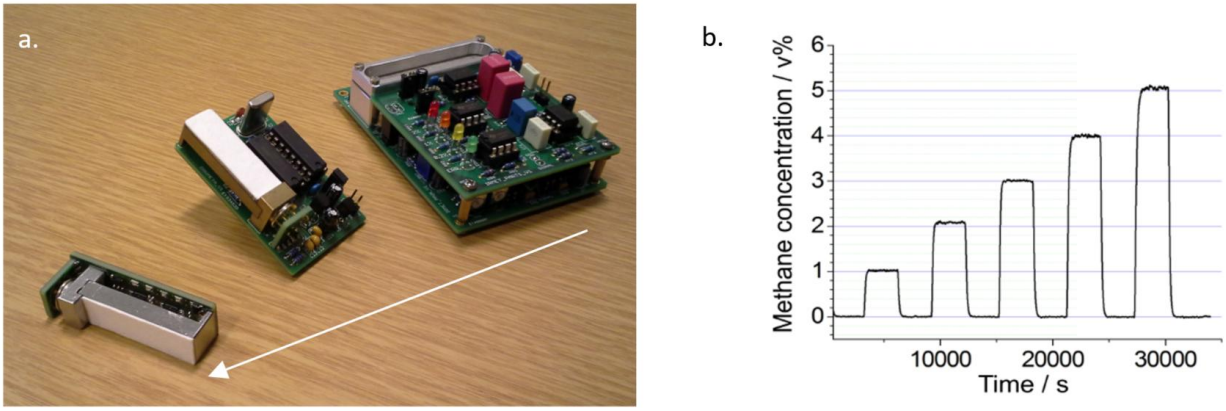

Figure 5.3 Illustration of the analogue and digital NDIR detector prototypes (a) and the typical response of the sensor (b).

Another goal in this project is to form **micro IR sources** for optical sensing – please check in section 6. Development of near infrared LEDs for spectroscopic applications.

Microcalorimeters

Having in hand the **stable heaters** we now focus on other applications also. In cooperation with the University Debrecen we have already started to develop a **micro-calorimetric measuring method** to investigate thermally indicated physical-chemical phenomena in thin films.

3D MEMS force sensor for tissue recognition

Follow up H2020-ECSEL-2017-2-783132 "POSITION-II, 2018-2.1.6-NEMZ-ECSEL-2018-00001

J. M. Bozorádi, Zs. Bérces, P. Földesy (HUN-REN SZTAKI), G. Pap (Uzsoki Hospital), P. Fürjes

Laparoscopic devices have been widely used in the past decades during surgical procedures. Currently they are the golden standard in minimal invasive surgery. Furthermore, combining these devices with robotic platforms, most notably the Da Vinci system, is more and more common. The precision, adaptability and the foreshadow of automation of such systems are promising, but the costs of their application or even maintenance put a limit on their propagation. Minimally invasive (robotic) surgery (MIS) offers several advantages for the patients, although the lack of sensory feedback for the surgeon is also a barrier in its progress. Gathering immediate multi-parametric information about the physical and anatomic conditions of tissues is crucial for the operator to precisely control the robotic actions or support the tissue recognition and pathologic characterization. Smart devices with integrated MEMS force sensors can provide such feedback and improve the safety of these interventions or help in on-site pathologic decisions.

At the Uzsoki Hospital in Budapest (Dr. Géza Pap) there is a growing interest in these sensors since they were already integrated in a laparoscope head in the previous INCITE project. Although gastric resection surgeries are among the most routine surgical procedures – more than 300 000 of them carried out in modern countries – the 1,5% rate of postoperative complications can be considered. Even with the existence of surgical robots such as the Senhance or the more known Da Vinci system there's still a great need for handheld devices with the addition of a „smart element" embedded in them to help the work of the surgeon by providing information regarding tissue thickness, stiffness, composition and the effect of the surgeon's current action.

Our goal was to develop a novel device with integrated micromachined 3D force sensors to provide tactile information about the different organs and tissues touched. Our developed 3D piezoresistive force sensors were designed and manufactured by silicon micromachining technology and mechanically integrated in the appropriate biocompatible packaging and elastic coverage. Application specific readout electronics were designed to solve the analog-digital signal conversion, initialization, noise filtering and the communication with a LabVIEW data acquisition user interface. The force sensory units were integrated with dedicated readout electronics and precisely controlled linear motors solving the accurate tissue deformation to provide more information about the mechanical (elastic) parameters of the analysed materials. Our latest work we demonstrated a complex, automatized measurement system – as well as hardware and software solutions – which is capable of implementing in vitro mechanical tissue characterization and thus provides elastomeric and pathological data. The results also demonstrated the deformation dependent and hysteretic behaviour of the artificial viscoelastic and biological samples also, as the Young modulus is continuously changing during the loading (0). We started mapping patient data that can be correlated to tissue compression curves and the outcomes of surgical procedures, as well as developing a measurement protocol for in vitro tissue testing. Our hope is that information regarding the patient's status before and after surgical procedures can be correlated with the tissue elasticity curves so an optimal stapler height can be determined by a neural network based AI supported data processing system in the future.

As of 2024 tissue testing experiments continued on mass at the Uzsoki street hospital, under ethical authorization IV/174- 2 /2022/EKU were concluded. The setup and the LabView based software package were optimized for the easy use of medical professionals. A total of 11 sensor boards were calibrated and brought to the hospital to measure human gastrointestinal tissue samples in vitro after their removal during stapling procedures. These included both healthy and tumorous samples. A Python script was developed to automatically extract information from measurements, enabling quick and easy

processing of large amounts of measurement data. Tissue thickness was identified as a key parameter, as surgeons select stapler cartridges based on this information in laparoscopic surgery. Both uncompressed thickness and thickness under a specific compressive force, as suggested by surgeons, were extracted.

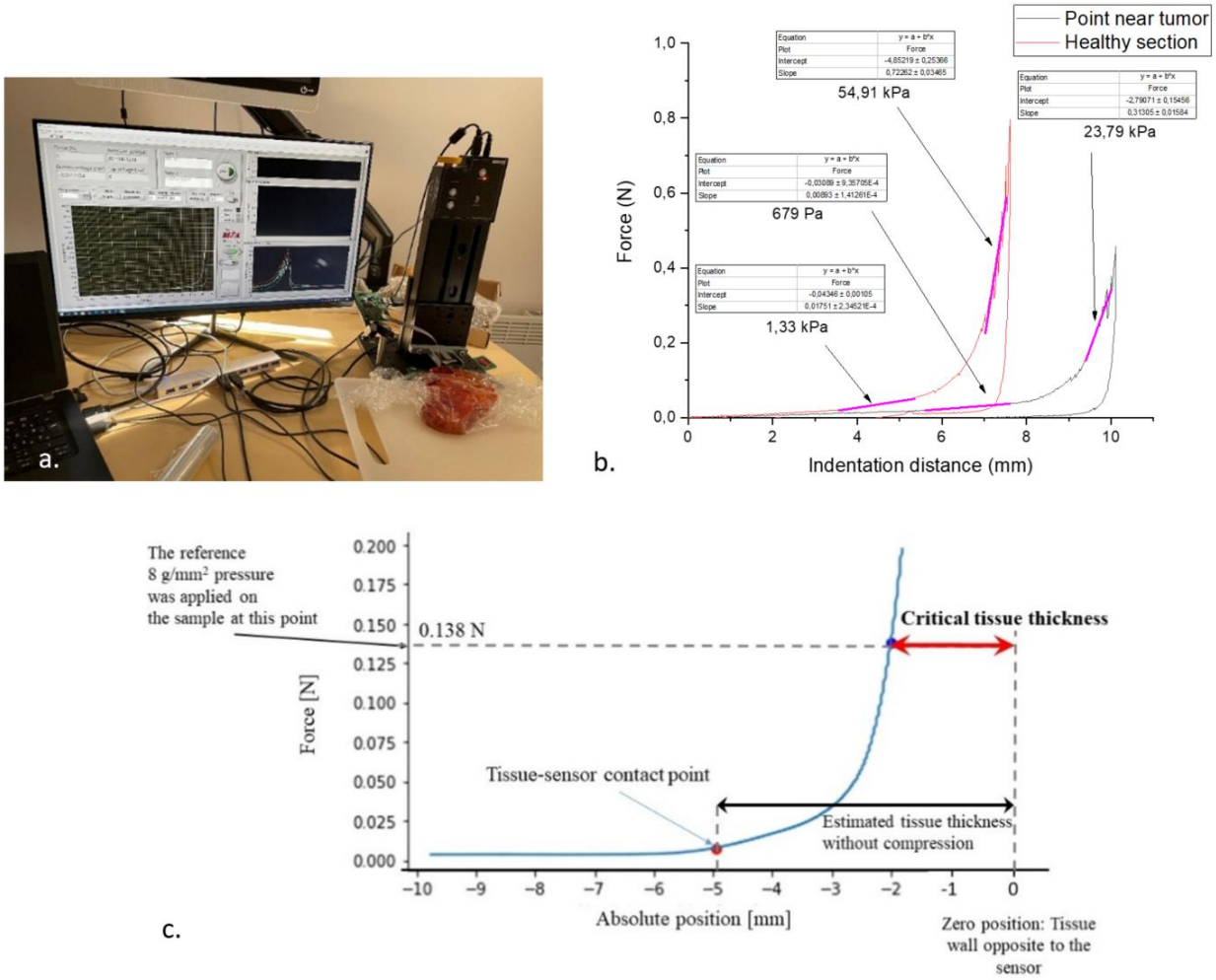

Figure 5.4 Compact automated tissue elasticity measurement setup (a) in the Uzsoki Hospital and the comparision of the mechanical characteristics (force vs. deformation function) of the healthy and cancerous gastric tissues (b) and the post processed tissue force-displacement characteristics (c).

The results of the data were published at Eurosensors XXXVI conference in September where the measurement system was also presented in the company exhibition section. And abstract, poster and video material were also published at Coloretcal THRIVE conference in April where the abstract **won 1st place best contributor**. The material and results gained approval from surgeons on the annual surgical conference in Hungary. [Ref.5.2-Ref.5.4]

Manufacturing implantable microelectrode arrays for neural research

NKP_17 National Brain Programme (subcontractor of PPKE)

Á. Horváth, Z. Fekete (PPKE Implantable Microsystems Group), P. Fürjes

The Microsystems Laboratory is working in cooperation with the PPKE Implantable Microsystems Group in the field of development neural optrode and brain surface electrodes.

The application of infrared (IR) light irradiation as a neuromodulation technique has been proven as safe and applicable in numerous studies. Either the continuous or the pulsed mode of IR stimulation (INS) showed promising neural responses under various conditions in vitro and in vivo as well. One of the advantages of INS compared to the classical electric stimulation is that INS does not induce photoelectric artefact in electrophysiological recordings. Another advantageous feature of INS is that the propagation of light can be shaped easier than in case of electrical signals. Therefore, the stimulus can be more directional, the neuromodulation impact can be – more – localized.

The optrode was made by planar and bulk micromachining (MEMS technology). The Pt wiring and contact material of the electrophysiological recording sites were realized by standard lift-off technology. The high surface roughness sidewalls of the silicon chip were polished after deep reactive ion etching. The individual optrode chips then were bonded to a custom printed circuit board (PCB). The PCB besides providing electrical connections helps the proper alignment and fixing of the optical fiber, which delivers IR light from an external source.

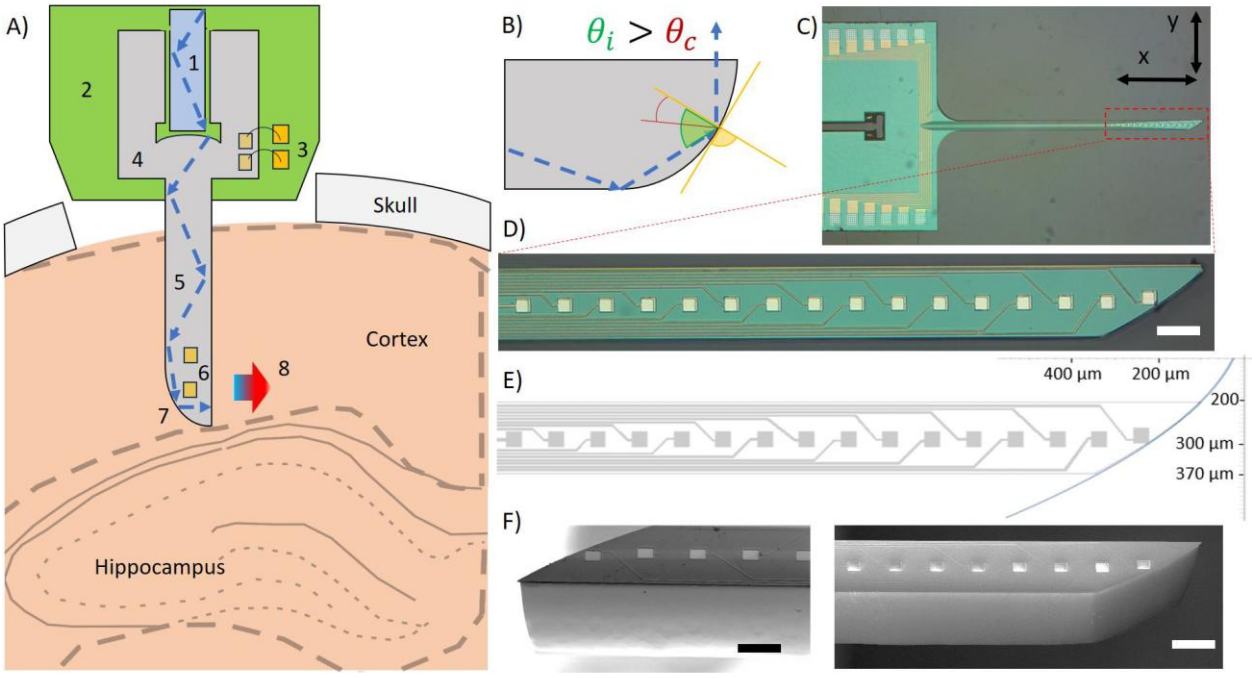

Figure 5.5 Schematic drawings represent of the principle of operation (A) and the specular property of the of the IR optrode (B). Optical microscopy view of the multimodal Si chip (C) and the Si needle (D). Technical drawing of the electrode layout (E). Scanning electron microscopy (SEM) images of the Si tip (F) - scale bars mean 100 µm.

Infrared (IR) neuromodulation holds an increasing potential in brain research, which is fueled by novel neuroengineering approaches facilitating the exploration of the biophysical mechanism in the microscale. The PPKE's group lays down the fundamentals of spatially controlled optical manipulation of inherently temperature-sensitive neuronal populations. The concept and in vivo validation of a multifunctional, optical stimulation microdevice is presented, which expands the capabilities of conventional optrodes by coupling IR light through a monolithically integrated parabolic micromirror. Heat distribution in the irradiated volume is experimentally analyzed, and the performance of the integrated electrophysiological recording components of the device is tested in the neocortex of anesthetized rodents. Evoked single-cell responses upon IR irradiation through the novel microtool are evaluated in multiple trials. The safe operation of the implanted device is also presented using immunohistological methods. The results confirm that shift in temperature distribution in the vicinity of the optrode tip can be controlled by the integrated photonic components, and in parallel with the optical stimulation, the device is suitable to interrogate the evoked electrophysiological activity at the single neuron level. The customizable and scalable optrode system provides a new pathway to tailor the location of the heat maximum during infrared neural stimulation. [Ref.5.5-Ref.5.8]

Polymer based autonomous microfluidic systems for medical diagnostics

Development of high precisity lab-on-a-chip point-of-care instrument (for 77 Elektronika Ltd.)

A. Bányai, Zs. Sik, M. Túróczi (77E), M. Varga (77E), P. Fürjes

Precise and fast PoC monitoring marker molecules or bacteria levels in body fluids or cell culture media could be crucial in effective diagnostics and design of adequate therapies. The complex, integrated, but miniaturised analytical devices, such as Lab-on-a-Chip and microfluidics systems enable cost effective although sensitive analysis of these samples. These microfluidic cartridges integrate precise sample transport, preparation, incubation and sensing functions. The sample preparation steps need a specified time, accordingly precise sample handling and flow control are crucial. The perspective of our work is to develop a polymer based microfluidic cartridge suitable to autonomously controlled sample transport or preparation for integrated bioanalytical device. To define precise sample flow rates in the microfluidic systems adequate surface modification and macro and microscale structuring of the geometry are crucial. For industrialisation the COP (cyclic-olefin-copolymer) material were chosen which can be manufactured by polymer technologies (injection moulding or hot embossing) and adequate subsequent surface treatment methods, as specific plasma treatment.

The material composition of the pre-industrial / laboratory stage cartridge was optimised according to the required sample flow rate, the optical and mechanical properties. The moulding masters of the microfluidic cartridges were fabricated. As a development of autonomous polymer microfluidic cassette of POC medical diagnostic devices, the need arose to process thermoplastic polymer instead of commonly used PDMS - glass hybrid microfluidic unit. To step forward the industrial polymer manufacturing technology the hot embossing technology was tested as promising manufacturing solution in cooperation with BME Polymer Technology Department. The Microsystems Lab developed 3D epoxy (SU8) and silicon based mould masters for the structuring tests. A novel Collin P 200 S hotembossing machine was installed in the Laboratory to establish semi-industrial manufacturing capability for supporting our industrial partner with polymer microfluidic cartridges.

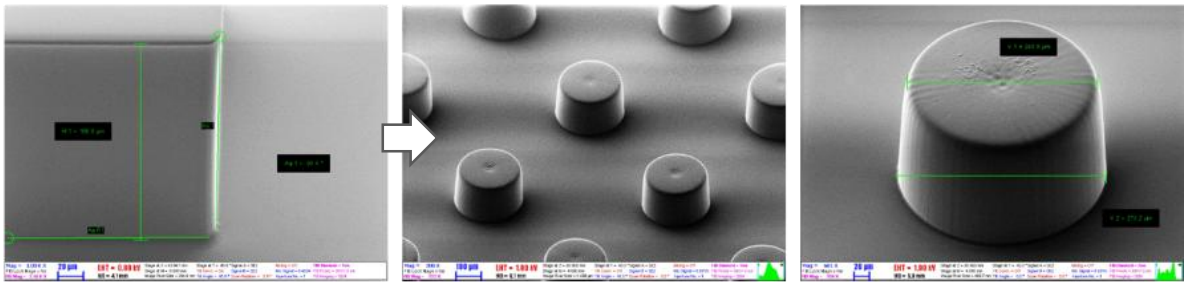

Figure 5.6 Challenges shows the negative side slope of the embossed tool; the inhomogeneous pressure that occurs in the case of dense column rotation; the chipped SU8 varnish left over from the pressing tool on the sensor patch in the COP print. Solution was the usage of the proximity mask in lithography which caused the positive slope inclination of the side for better separation.

For the Collin P 200 S hot press machine located in our clean room, the Si or epoxy (SU8) molding tool for hot press polymer processing was provided by our Laboratory. In case of Si - SU8 lithographic slides, the lifetime of the printing forms could be further increased by using a large-surface adhesive layer and the hard bake process, however, in these cases the real problem was caused by the negative side breakage of the SU8 varnish, which led to chipping of the varnish in the in print form, as well as worsened its separation from the COP. A significant improvement was achieved in easier separation of the embossed COP from the author insert and in increasing of the column heights by changing the column diameters and column density of the trace form. (see in 0) With this modification, column heights of approximately 200 µm could be achieved in the capillary pumps.

Microfluidic methods for particle and cell manipulation and analysis

TKP2021-EGA-04

A. Bányai, M. Varga (77E), L. Bató, Zs. Szomor, E. Leelőssyné Tóth, B. Beiler, M. Veres (HUN-REN Wigner), P. Fürjes

In the field of microfluidics, the development of medical diagnostic applications with the spread of Lab-on-a-chip (LOC) or miniaturized total analytical systems (μ-TAS), Point-of-Care (POC) diagnostic platforms, which can be used at the patient's bedside, ambulances or medical offices, has received great emphasis in recent decades.

Trapping and electrochemical impedance spectroscopic analysis (EIS) of single cells and cell populations

In vitro testing of cell populations or individual cells in artificial systems that model their real environment is highly prospective from a biomedical and environmental point of view. Specially designed microfluidic systems allow the development of such a controllable chemical environment that is comparable to the size of cells. The application of such Organ-on-chip devices, which integrate sensing functions, can be a significant step in the research of pharmaceutical agents, but also in facilitating the spread of personalized medicine. Cell trapping and in-vitro analysis are powerful tools that enable the investigation of cell viability and proliferation in microfluidic structures.

Specific microfluidic structure was created to achieve uniform hydrodynamics and an efficient cell trapping method, also taking into account the subsequent integrability of the electrodes. The microfluidic structure consists of two main channels and between these, additional thin cross-channels - with widths comparable to the size of the cells - have been designed. The cross-channels are used to trap particles or cells as they are thinner and lower than the main channels. In microfluidic systems, impedance spectroscopy-based measurements can be performed by integrating electrodes into the structure. A PCB was also designed and fabricated which enables measurements on electrodes in four parallel channels.

To test the device, the EIS spectrum was measured during channel filling and its frequency dependence was measured also with different concentrations of phosphate buffer solutions (PBS), nanoparticles and yeast cell solutions. Using the measurement software, the filling could be examined with the change of impedance and its phase in time. During filling a step-like jump occurs when each cross-channel is filled and the respective electrodes close, and when particles are placed between two electrodes. The concentration dependence of the EIS spectra of different PBS solutions were measured. Measurements were made with fluorescent microparticles of 6 μm diameter to pretest the trapping, and then continued with solutions of 0.05 mg/ml concentration Saccharomyces cerevisiae yeast cells solutions. To distinguish between live and dead cells propidium iodide (PI) staining was used. The cell membrane of dead cells becomes permeable to the nucleic acid dye, causing it to light up, which in the case of PI gives a red fluorescence. The effect of the number of trapped cells were also measured, as demonstrated in 0.c

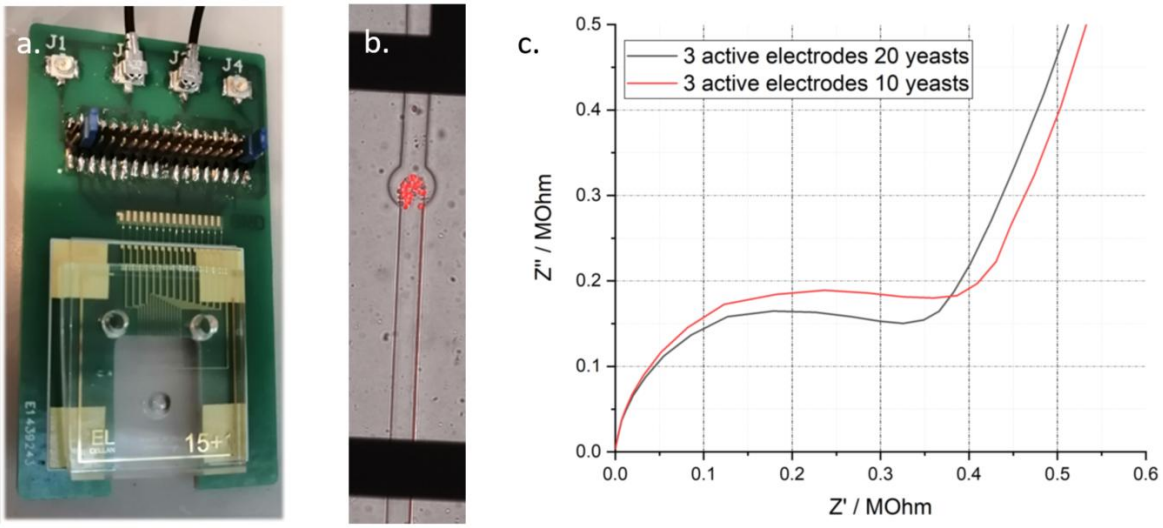

Figure 5.7 The cell analytical microfluidic system mounted on PCB (a) and the captured yeast cells (b) dyed with propidium iodide in fungicide chemical environment. The effect of the number of trapped cells (c) on the Nyquist diagram measured by EIS.

Two-phase microfluidic systems for cell analytical applications

In the last two decades, the utilization of microengineered systems has revolutionized the manner in the fields of chemical and biological sciences in which high-throughput experimentation is conducted. The capacity to construct intricate microfluidic architectures has empowered researchers to devise novel experimental formats for processing extremely small analytical volumes within short timeframes and with remarkable efficiency. These applications rely on generating small, separate droplets of the sample or reagent within a non-mixing carrier fluid, altering fluid behavior. These artificial microscopic containers enable accelerated mixing of chemical primers, prevent contamination and non-specific molecular binding on channel walls, and support highly parallelized processes with the opportunity of single cell or molecule analysis.

Achieving effective mixing in microscopic environments poses a significant challenge due to the dominance of laminar flow, which inherently limits mixing efficiency. However, passive microfluidic techniques effectively address this challenge by reducing power consumption, eliminating the need for external energy sources, and offering simplicity and cost-effectiveness through fewer components and less complex geometries. By utilizing channel geometries with intricate patterns, passive mixing induces chaotic advection and vortices via secondary transversal flows, significantly enhancing mixing efficiency. Based on these principles, the geometric design of microfluidic channels and changes in flow parameters were characterized regarding their influence on key mixing phenomena and droplet sizes, including Dean vortices, mixing efficiency, and the spatial distribution of dissolved substances within the droplets.

Numerical simulation using finite element modeling (FEM) was performed with COMSOL Multiphysics. The investigation is based on the solution of the Navier-Stokes and continuity equations, which were coupled with the Cahn-Hilliard equations to modelling of multi-phase flows. To calculate concentration distribution in microdroplets, the Transport of Diluted Species model was used alongside the Ternary Phase Field method. This method was applied to accurately resolve the interfaces among the three immiscible phases (oil, water, and fluorescent solution), considering surface tension and contact angles. In both the simulations and experiments, water and fluorescently labeled Bovine Serum Albumin (BSA) served as the dispersed phase, forming quasi-monodisperse droplets in a silicone oil-based continuous phase. The simulations demonstrated that the design of microfluidic channels and

variations in flow rates significantly affect the dynamics of mixing within the droplets and the distribution of sample solutions.

To validate the simulation results, experimental measurements were also conducted, demonstrating the presence of Dean vortices in curved channel sections, which greatly enhance mixing. These experiments used BSA sample solutions and fluorescent beads. Additionally, the concentration distribution and profile of BSA within the droplets were investigated by generating droplet populations with varying concentrations. For analysis, a custom-developed MATLAB code and the ImageJ software were utilised, enabling droplet identification from exported images, calculation of their average diameter, and examination of the BSA concentration distribution within them. By analyzing the intensity of droplets in the exported images, information about mixing efficiency and homogeneity were gathered. These findings highlight the potential of droplets as miniaturized chemical reactors and their capability to serve as isolated chemical microreactors for studying the distribution and concentration of therapeutic substances.

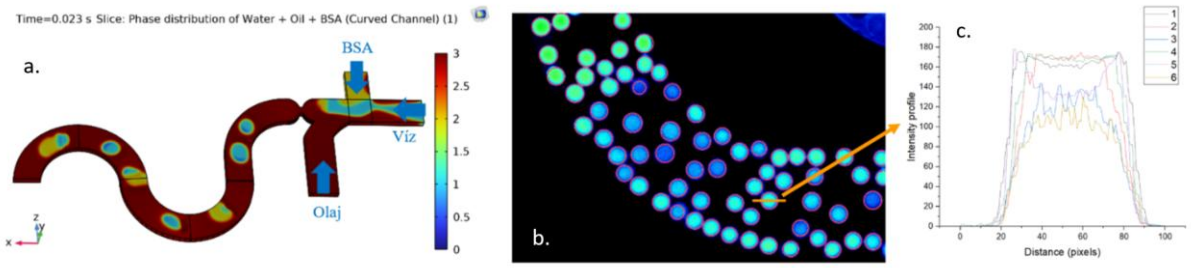

Figure 5.8 Droplet formation and mixing in the mulit-phase simulation (a), and fluorescent BSA concentration distribution analysis of droplets with solution in the laboratory measurements (b, c).

Flow control in microfluidic system using morphological changing polymers

Discovered in the early 1990s, porous polymer monoliths are a new class of materials that revolutionized liquid chromatography. These materials can be used as separation media where macropores provide the flow of the liquid and meso- and micropores are responsible for the separation. The pore sizes and their distribution can be designed by varying the preparation conditions to suit the specific application. Due to their high specific surface area, these polymers can also be used as carriers, adsorbents, solid phase reagents, enzyme carriers, etc. In recent years, their application in microfluidic, lab-on-a-chip devices for analytical purposes has also emerged.

In the conventional photo- and thermally-initiated production of monoliths, the thermal sensitivity of the initiators, the long reaction time, and also the thickness of the monolith and the material of the container wall all make the preparation and use of these monoliths difficult, especially for in situ processes and at larger scale. In contrast, gamma-irradiation initiated polymerization is an innovative alternative production method where the properties of the final product are independent of the initial temperature, no initiator is required for the polymerization (clean final product), the production time is short and the thickness of the polymer or the quality of the container material does not affect the properties of the monolith formed. Since there is no other material in the monomer mixture than the solvent and the monomer, in addition to varying their type and concentration, dose, temperature and dose rate can be used to change the pore structure and other properties.

At the HUN-REN Wigner Research Centre for Physics, in collaboration with Dr. Miklós Veres, we started to work on the gamma irradiation induced polymerization of poly-N-isopropylacrylamide hydrogels. The polymer may be suitable for use as a liquid silicon in microfluidic systems and as a carrier for gold nanoparticles in surface-enhanced Raman scattering. The morphology of the polymer pores can be monitored by SEM measurements, flow velocity measurements are performed while

changing the temperature, so that the pore size variation of the polymer can be controlled (the pore size of the hydrogel changes with temperature and pH variation.) Raman spectroscopy can be used to monitor the polymerization process and to design further functionalization of the resulting scaffolds. [Ref.5.9-Ref.5.16]

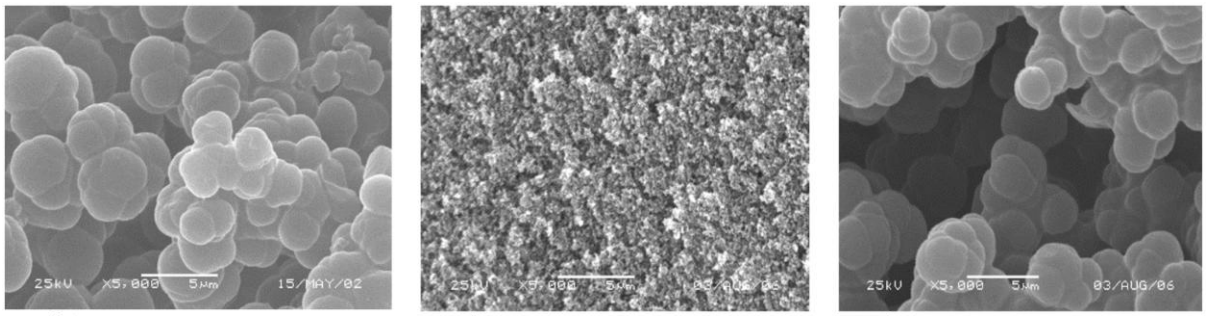

Figure 5.9 Morphology of monoliths prepared by gamma radiation initiated polymerization from different monomer mixtures.

Small scale production and development of near infrared LEDs

Horizon-KDT-JU-2023-1-IA-101140192 (UNLOOC), TKP2021-EGA-04

Barbara Beiler, János M. Bozorádi, Csaba Dücső, Péter Fürjes, Zoltán Szabó

Infrared spectroscopy is a very popular measurement technique especially in food industry, pharmaceutical industry and agriculture for the detection and measurement of organic materials. The -OH, -NH and -CH functional groups found in organic substances can frequently be detected by spectroscopy through absorbance measurements at the resonance wavelength of valence-bond vibrations. The measured wavelengths are 4-2.5μm, while the signal to noise ratio of photon detectors is low due to thermal noise at room temperature. The 1st-3rd harmonic absorption bands are located in the range of the near infrared (NIR), where smaller signals can be measured effectively in practice. NIR LEDs have narrow wavelength, therefore they are suitable for measurements at given wavelength. Further advantages of LEDs compared to incandescent lamps are their small dimensions, high efficiency, and low power consumption, which is critical in small handheld devices.

GaInAsP/InP is an ideal material system for the fabrication of double heterostructure devices as the emission wavelength is easily tuneable between 950-1650 nm. As InP has higher bandgap than the lattice-matched GaInAsP active layer the absorption losses inside the device structure can be minimized. In order to tune the emission wavelength of the LED, the composition of the semiconductor light-emitting layer has to be properly set. Our high quality single peak LED chips (1220nm) have a stable market with a sales value around 10kEUR in 2024.

Wide emission-spectrum NIR LEDs

Specific InGaAsP/InP layer structures were grown by liquid phase epitaxy (LPE) to fabricate wide emission spectrum near-infrared LEDs. Even wider emission spectrum (4 peaks) was achieved by multilayered LPE growth steps: by growing multiple photoluminescent and active layers. Samples were fabricated and characterized by optical transmittance measurements, by photo-luminescent measurements using various excitation sources in the NIR range, and by scanning electron microscopy to measure layer thicknesses and verify epitaxial crystal formation.

Therapeutic drug monitoring by optical spectroscopy

POC-TDM HE MSCA PF, Horizon-KDT-JU-2023-1-IA-101140192 (UNLOOC), TKP2021-EGA-04, OTKA K 131594

D. Bereczki, O. Bálint-Hakkel, A. Füredi, Z. Szabó, P. Fürjes

Optical Spectroscopy in microfluidic environment

The concentration of molecular markers – such as relevant amino-acids, carbohydrates and drugs – is an important signal of the metabolic or chemical processes unfolding in Organ-on-Chip applications. In recent years the advanced and miniaturized sources, detectors and spectrometers has proven the applicability of optical spectroscopy to be an excellent tool for the analysis of different sample compositions or chemical reactions. Optical spectroscopy combined with microfluidic sample transport and preparation can be a powerful, in-situ analysis method for continuous monitoring of complex cell culture media and revealing the molecular fingerprints of the relevant molecular contents. Based on the spectral characteristics the molecular concentration in the sample could be determined, however the architecture, the geometry and the optical parameters of the structural materials (glass, poly-dimethylsiloxane (PDMS), cyclo-olefin polymer / copolymer (COP / COC), etc.) of the microfluidic system have to be considered.

Considering the requirements of the specific usecases in UNLOOC project, the following drug molecules were characterized:

1. Cyclosporine: 25 mg/mL in DMSO
2. Dopamine: 29 mg/mL in distilled water
3. Diclofenac: 25 mg/mL in DMSO
4. Levodopa: 12.5 mg/mL in distilled water (adjusted with 1M HCl solution)
5. Methotrexate: 23.5 mg/mL in DMSO
6. Ibuprofen: 25 mg/mL in DMSO
7. Naproxen: 10mg/mL in MetOH

The absorption spectra of each compound were measured to determine the possible excitation regions for fluorescent measurement
The fluorescence excitation wavelengths were then selected based on the observed maxima.

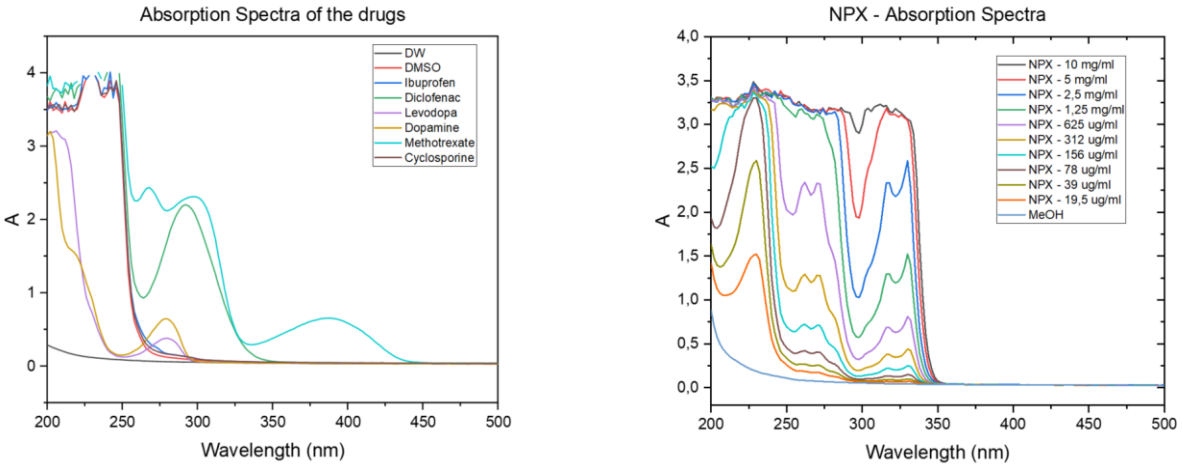

Figure 5.10 Optical absorption spectra of different drug components. Note that the UV cutoff for DMSO solvent is approximately 250 nm, below which the solvent absorbs light.

Fluorescent detection of anticancer drugs

Cancer claims almost 10 million lives annually, making it one of the major causes of death around the world. Chemotherapy is the most frequently used non-surgical method in clinical practice in cancer treatment to depress the growing, proliferation, or spreading of cancer cells. Detection of the anti-cancer drugs in patients' blood or standard cell culture media is the fundamental step forward in personal treatments or in vitro drug tests in Organ-on-Chip devices. Besides the golden standard mass spectrometry, optical spectroscopy has to be considered as a potential analytical method, although there is no extensively accessible database of the spectral characteristics of the widely applied chemotherapeutic drug compounds. There are some well-known examples of anticancer molecules with strong fluorescence like the anthracycline family, however systemic screening for fluorescent drugs used in oncology was never done before.

Fluorescence spectroscopy is a widespread method to measure concentrations of specific drug molecules such as active pharmaceutic ingredients (APIs) or their impurities. Anthracyclines (doxorubicin, daunorubicin, epirubicin, idarubicin, mitoxantrone, pixantrone) are not only the most effective anticancer chemotherapeutics, but they are also highly fluorescent. First, we showed that after sample preparation this autofluorescence is enough to detect doxorubicin (DOX, excitation: 490 nm, emission: 590 nm) in different solvents in a concentration dependent manner using 100 µl sample in a Tecan Spark fluorescent plate reader. To further reduce the required volume of sample, we designed a simple microfluidic chip with autonomous sample transport and proved the significant sample volume reduction (to ~ 7 µl) had no significant effect on the efficiency of fluorescence detection. The sensitivity and precision of the fluorescent measurements were validated by mass spectrometry based (Sciex 5600+ QTof) concentration determination. As 0b. shows, the individual pharmacokinetics of a mouse was determined, and the results were highly similar to the mass spectrometry measurements. [Ref.5.18-Ref.5.19]

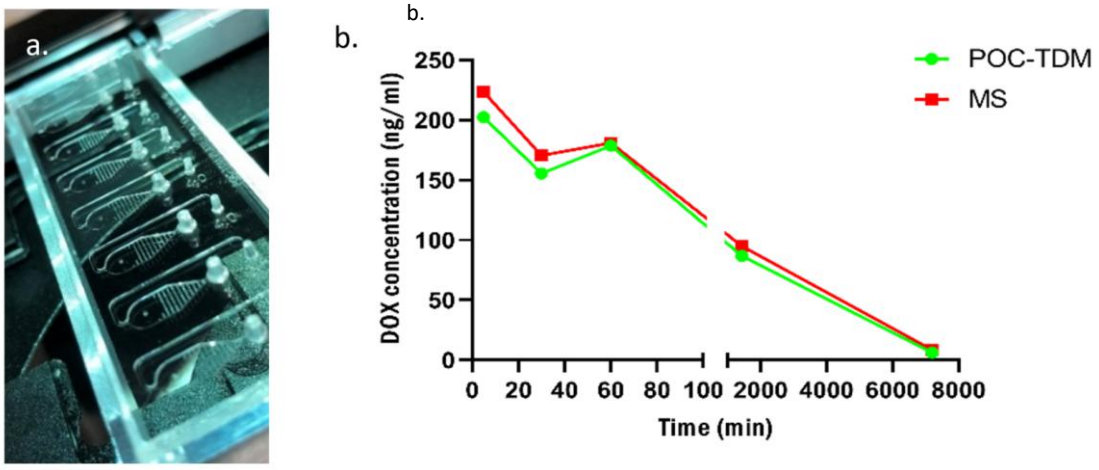

Figure 5.11 Plate Reader-compatible microfluidic cuvette (a) and a representative pharmacokinetics curve of a single mouse treated with 6 mg/kg PLD (pegylated liposomal doxorubicin). Blood concentrations (b) measured by our Point-of-Care TDM chip (POC-TDM, green) was also determined by mass spectrometry (MS, red).

Nanobiosensorics Department

Head: Róbert HORVÁTH, Ph.D., Senior Scientist

Research Staff:

Robert Horvath, Ph.D.
Sándor Kurunczi, Ph.D.
Inna Székács, Ph.D.
Beatrix Péter, Ph.D.
Boglárka Kovács, Ph.D.
Zoltán Szittner, Ph.D.
Enikő Farkas, Ph.D.

Ph.D. Students / Diploma Workers:

Kinga Dóra Kovács, Phd student
Bálint Béres, Phd student
Imola Rajmon, Ph.D. student
Anna Balogh, Ph.D. student
Igor Sallai, Ph.D. student
Péter Joó, Ph.D. student
Krisztina Borbély, Ph.D. student
Sebestyén D. Varga, Ph.D. student
Dóra Balogh, Ph.D. student
Nicolett Kanyó, Ph.D. student
Zoltán Dicső, Ph.D. student
Beatrix Magyaródi, Ph.D. student
Dorina Kiss, M.Sc. student
Szabolcs Novák, M.Sc. student
Ágoston Richárd Kiss, M.Sc. student
Bálint Legányi, M.Sc. student
Csaba Béla Váradi, M.Sc. student
Viktor Sándor Kovács, B.Sc. student

The research profile of the Nanobiosensorics Department is the development and application of label-free optical biosensors, the mathematical modeling of the relevant biological and biophysical processes. Building on their broad national and international collaborative network the group conducts research in the fields of instrument development, monitoring of cell secreted extracellular vesicles, development of protein-based functional coatings, adhesion studies on human cancer and immune cells, and theoretical modeling. In 2014, the application for an ERC Consolidator Grant by the head of the research group received qualification category “A (fully meets the ERC excellence criteria and should be funded if sufficient funds are available)” after the interview in Brussels, but the funding line did not reach this proposal due to budgetary constraints. However, using this achievement the Group could successfully apply for funding from NKFIH in the framework of the ERC_HU call. In the framework of this project they aim single cell manipulation and label-free sensing. Building on this expertise, in 2018 they won an Élvonal (NKFIH) research project for single cell biosensing. In 2020, the research group won the Tématerületi Kiválósági Program (TKP) excellence project as well in collaboration with other groups of the MFA.

Label-free biomolecular and cellular methods in small molecule epigallocatechin-gallate research

LP2012-26/2012 Lendület, OTKA ERC_HU 117755, TKP2021-EGA-04, OTKA KKP 129936, Bolyai Scholarship

B. Péter, I. Székács, R. Horvath

Affinity measurements of small molecules below 100 Da molecular weight in a label-free and automatized manner using small amounts of samples have now become a possibility and reviewed in the present work. We also highlight novel label-free setups with excellent time resolution, which is important for kinetic measurements of biomolecules and living cells. We summarize how molecular-scale affinity data can be obtained from the in-depth analysis of cellular kinetic signals. Unlike traditional measurements, label-free biosensors have made such measurements possible, even without the isolation of specific cellular receptors of interest. Throughout this review, we consider epigallocatechin gallate (EGCG) as an exemplary compound. While the direct impact of small molecules on living cells and biomolecules is relatively well investigated in the literature using traditional biological measurements, this review also highlights the indirect influence of these molecules on the cells by modifying their nano-environment. Moreover, we underscore the significance of novel high-throughput label-free techniques in small molecular measurements, facilitating the investigation of both molecular-scale interactions and cellular processes in one single experiment. This advancement opens the door to exploring more complex multicomponent models that were previously beyond the reach of traditional assays [Ref.6.1].

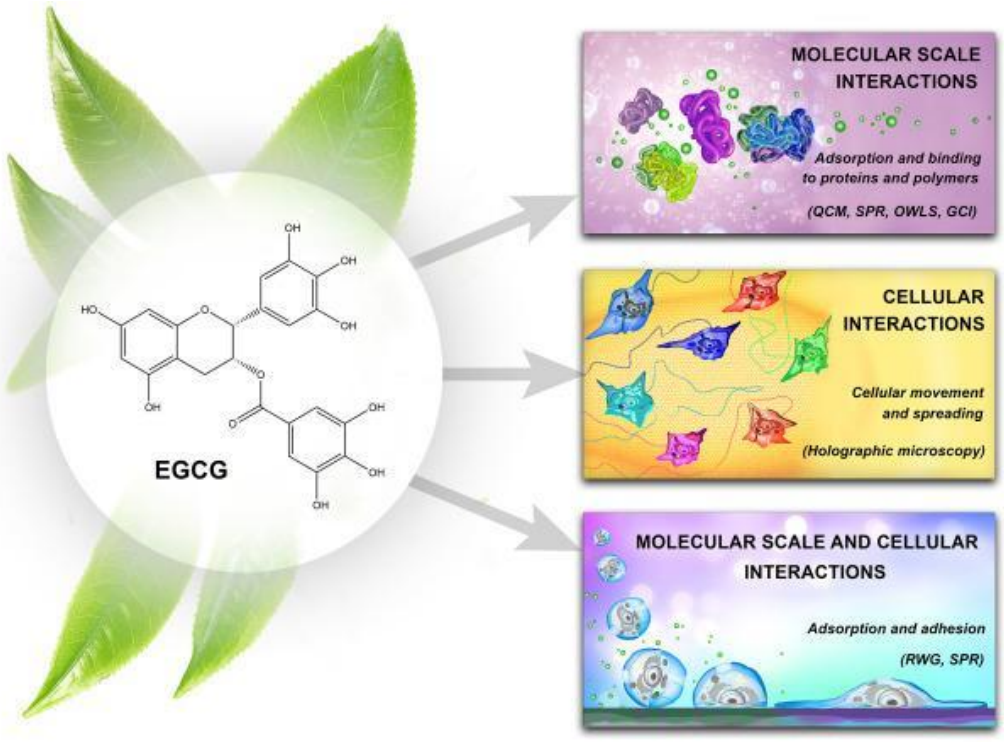

Figure 6.1 Label-free biomolecular and cellular methods in EGCG research. On the left: chemical structure of EGCG. This compound is isolated from the Camellia sinensis leaves. On the right: the label-free methods are summarized and categorized into three groups. These techniques and the results of the EGCG research are detailed in further chapters.

Hydrodynamic function and spring constant calibration of FluidFM micropipette cantilevers

LP2012-26/2012 Lendület, OTKA ERC_HU 117755, TKP2021-EGA-04, OTKA KKP 129936

A. Bonyár (BME), Á. G. Nagy, H. Gunstheimer (Nanosurf AG, Switzerland), G. Fläschner (Nanosurf AG, Switzerland), R. Horvath

Fluidic force microscopy (FluidFM) fuses the force sensitivity of atomic force microscopy with the manipulation capabilities of microfluidics by using microfabricated cantilevers with embedded fluidic channels. This innovation initiated new research and development directions in biology, biophysics, and material science. To acquire reliable and reproducible data, the calibration of the force sensor is crucial. Importantly, the hollow FluidFM cantilevers contain a row of parallel pillars inside a rectangular beam. The precise spring constant calibration of the internally structured cantilever is far from trivial, and existing methods generally assume simplifications that are not applicable to these special types of cantilevers. In addition, the Sader method, which is currently implemented by the FluidFM community, relies on the precise measurement of the quality factor, which renders the calibration of the spring constant sensitive to noise. In this study, the hydrodynamic function of these special types of hollow cantilevers was experimentally determined with different instruments.

Based on the hydrodynamic function, a novel spring constant calibration method was adapted, which relied only on the two resonance frequencies of the cantilever, measured in air and in a liquid. Based on these results, our proposed method can be successfully used for the reliable, noise-free calibration of hollow FluidFM cantilevers [Ref.6.2].

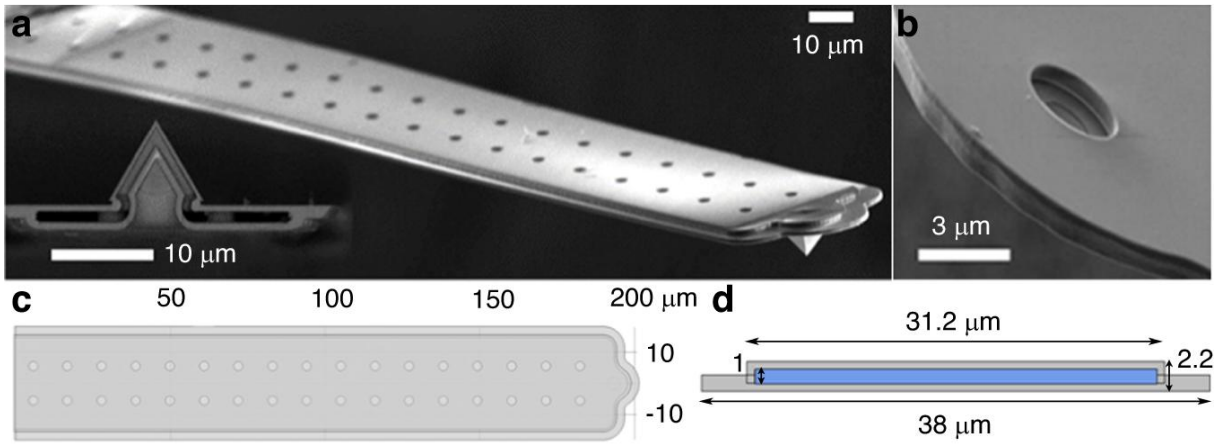

Figure 6.2 a) Scanning electron microscopy (SEM) image of a FluidFM cantilever with a nanopipette head. b) SEM image of a micropipette head with a circular aperture. ***c*** *3D reconstruction of the micropipette cantilever in the COMSOL Multiphysics environment.* ***d*** *Cross-section of the same 3D model, with the channel highlighted in blue.*

Continuous distribution of cancer cells in the cell cycle unveiled by AI-segmented imaging of 37,000 HeLa FUCCI cells

LP2012-26/2012 Lendület, OTKA ERC_HU 117755, TKP2021-EGA-04, OTKA KKP 129936

H. Cheraghi (ELTE), K. D. Kovács, I. Székács, R. Horvath, B. Szabó (Semilab)

Classification of live or fixed cells based on their unlabeled microscopic images would be a powerful tool for cell biology and pathology. For such software, the first step is the generation of a ground truth database that can be used for training and testing AI classification algorithms. The application of cells expressing fluorescent reporter proteins allows the building of ground truth datasets in a straightforward way. In this study, we present an automated imaging pipeline utilizing the Cellpose algorithm for the precise cell segmentation and measurement of fluorescent cellular intensities across multiple channels. We analyzed the cell cycle of HeLa–FUCCI cells expressing fluorescent red and green reporter proteins at various levels depending on the cell cycle state. To build the dataset, 37,000 fixed cells were automatically scanned using a standard motorized microscope, capturing phase contrast and fluorescent red/green images. The fluorescent pixel intensity of each cell was integrated to calculate the total fluorescence of cells based on cell segmentation in the phase contrast channel. It resulted in a precise intensity value for each cell in both channels [Ref.6.3].

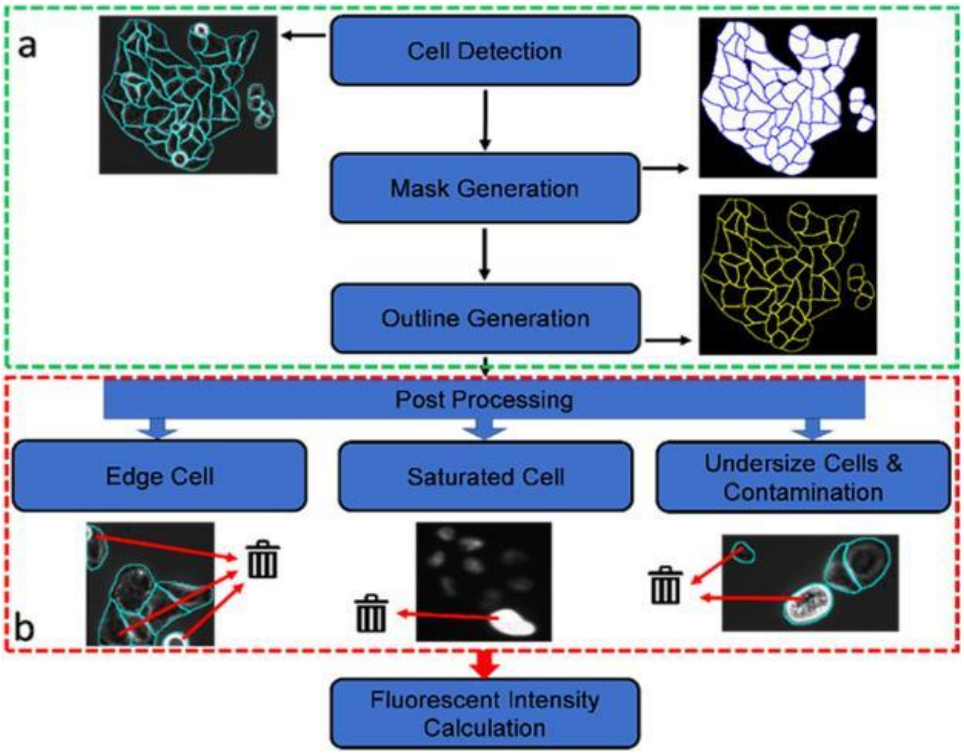

Figure 6.3 Illustrating the automated pipeline employed for measuring cellular fluorescent intensities. The process consists of two primary stages: (a) Segmentation and outline generation; and (b) Post-Processing involving the removal of contaminants and non-fluorescing cells to ensure accurate quantification.

Optical sensor reveals the hidden influence of cell dissociation on adhesion measurements

LP2012-26/2012 Lendület, OTKA ERC_HU 117755, TKP2021-EGA-04, OTKA KKP 129936 KDP, OTKA PD 134195, Bolyai Scholarship

K. Dóra Kovács, Z. Szittner, B. Magyaródi, B. Péter, B. Szabó (Semilab), A. Vörös, N. Kanyó, I. Székács, Robert Horvath

Cell adhesion experiments are important in tissue engineering and for testing new biologically active surfaces, prostheses, and medical devices. Additionally, the initial state of adhesion (referred to as nascent adhesion) plays a key role and is currently being intensively researched. A critical step in handling all adherent cell types is their dissociation from their substrates for further processing. Various cell dissociation methods and reagents are used in most tissue culture laboratories (here, cell dissociation from the culture surface, cell harvesting, and cell detachment are used interchangeably). Typically, the dissociated cells are re-adhered for specific measurements or applications. However, the impact of the choice of dissociation method on cell adhesion in subsequent measurements, especially when comparing the adhesivity of various surfaces, is not well clarified. In this study, we demonstrate that the application of a label-free optical sensor can precisely quantify the effect of cell dissociation methods on cell adhesivity, both at the single-cell and population levels. The optical measurements allow for high-resolution monitoring of cellular adhesion without interfering with the physiological state of the cells. We found that the choice of reagent significantly alters cell adhesion on various surfaces. Our results clearly demonstrate that biological conclusions about cellular adhesion when comparing various surfaces are highly dependent on the employed dissociation method [Ref.6.4].

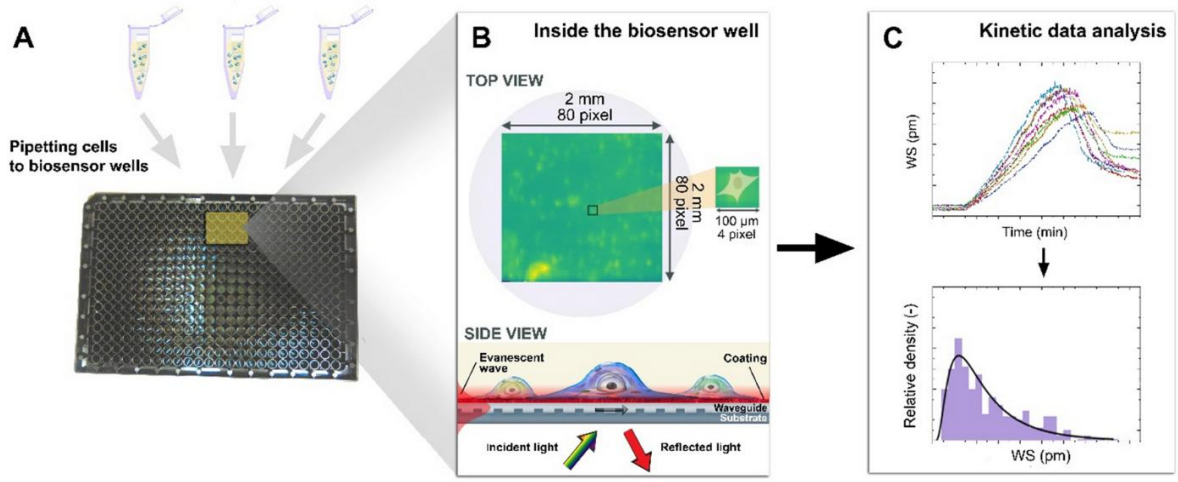

Figure 6.4 Schematic illustration of the measurement with single-cell resolution optical sensor. The cells were added to 12 wells in the microplate and measured (A). The sensor can detect refractive index change above the surface in an approximately 150 nm thick layer, which corresponds to the evanescent field [(B), 'side view' part, red zone]. The integrin-ligand binding happens in this layer, thus the sensor can monitor cell adhesion and provides kinetic data of the process (C).

Single-cell classification based on label-free high-resolution optical data of cell adhesion kinetics

LP2012-26/2012 Lendület, OTKA ERC_HU 117755, TKP2021-EGA-04, OTKA KKP 129936 KDP, OTKA PD 134195, Bolyai Scholarship

K. D. Kovacs, B. Beres, N. Kanyo, B. Szabó (Semilab), B. Peter, Sz. Bősze (ELTE), I. Szekacs, R. Horvath

Selecting and isolating various cell types is a critical procedure in many applications, including immune therapy, regenerative medicine, and cancer research. Usually, these selection processes involve some labeling or another invasive step potentially affecting cellular functionality or damaging the cell. In the current proof of principle study, we first introduce an optical biosensor-based method capable of classification between healthy and numerous cancerous cell types in a label-free setup. We present high classification accuracy based on the monitored single-cell adhesion kinetic signals.

We developed a high-throughput data processing pipeline to build a benchmark database of ~ 4500 single-cell adhesion measurements of a normal preosteoblast (MC3T3-E1) and various cancer (HeLa, LCLC-103H, MDA-MB-231, MCF-7) cell types. Several datasets were used with different cell-type selections to test the performance of deep learning-based classification models, reaching above 70–80% depending on the classification task. Beyond testing these models, we aimed to draw interpretable biological insights from their results; thus, we applied a deep neural network visualization method (grad-CAM) to reveal the basis on which these complex models made their decisions.

Our proof-of-concept work demonstrated the success of a deep neural network using merely label-free adhesion kinetic data to classify single mammalian cells into different cell types [Ref.6.5].

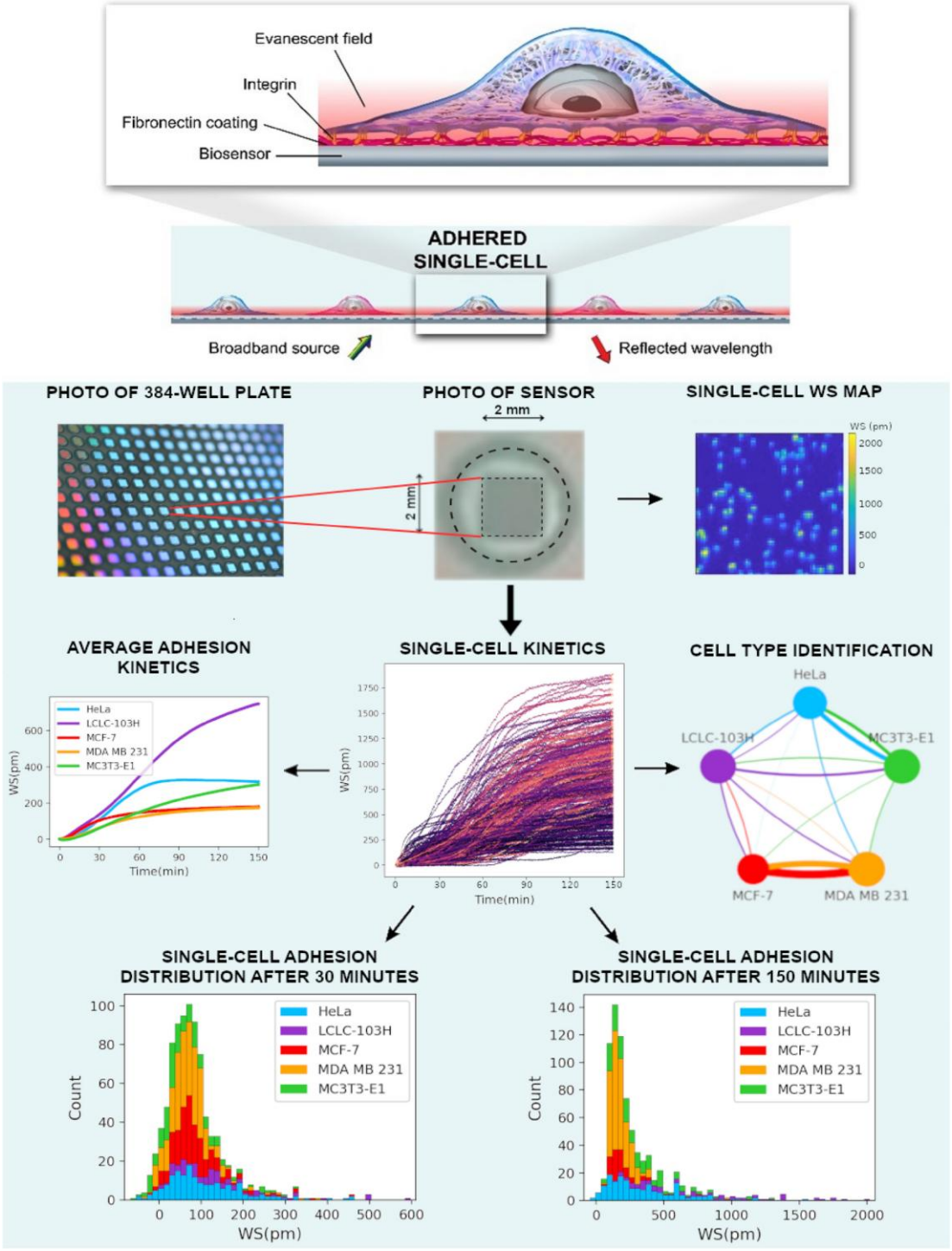

Figure 6.5 Label-free acquisition of single cell adhesion kinetics. Cells were added to a standard 384-well optical biosensor plate and functionalized with a cell adhesion-promoting coating. Representative wavelength-shift (WS) map at a given timestep of a single well in a typical single-cell RWG biosensor measurement. Peaks in the image indicate adherent cells. Single-cell signals after preprocessing. Average cell adhesion signal for every cell type. A confusion graph was obtained from the cell type classification. Distribution of cell adhesion signals at 30 (left) and 150 (right) minutes.

Label-free single-cell cancer classification from the spatial distribution of adhesion contact kinetics

LP2012-26/2012 Lendület, OTKA ERC_HU 117755, TKP2021-EGA-04, OTKA KKP 129936 KDP, OTKA PD 134195, Bolyai Scholarship

B. Beres, K. D. Kovacs, N. Kanyo, B. Peter, I. Szekacs, R. Horvath

There is an increasing need for simple-to-use, noninvasive, and rapid tools to identify and separate various cell types or subtypes at the single-cell level with sufficient throughput. Often, the selection of cells based on their direct biological activity would be advantageous. These steps are critical in immune therapy, regenerative medicine, cancer diagnostics, and effective treatment. Today, live cell selection procedures incorporate some kind of biomolecular labeling or other invasive measures, which may impact cellular functionality or cause damage to the cells. In this study, we first introduce a highly accurate single-cell segmentation methodology by combining the high spatial resolution of a phase-contrast microscope with the adhesion kinetic recording capability of a resonant waveguide grating (RWG) biosensor.

We present a classification workflow that incorporates the semiautomatic separation and classification of single cells from the measurement data captured by an RWG-based biosensor for adhesion kinetics data and a phase-contrast microscope for highly accurate spatial resolution. The methodology was tested with one healthy and six cancer cell types recorded with two functionalized coatings.

The data set contains over 5000 single-cell samples for each surface and over 12,000 samples in total. We compare and evaluate the classification using these two types of surfaces (fibronectin and noncoated) with different segmentation strategies and measurement timespans applied to our classifiers. The overall classification performance reached nearly 95% with the best models showing that our proof-of-concept methodology could be adapted for real-life automatic diagnostics use cases.

The label-free measurement technique has no impact on cellular functionality, directly measures cellular activity, and can be easily tuned to a specific application by varying the sensor coating. These features make it suitable for applications requiring further processing of selected cells [Ref.6.6].

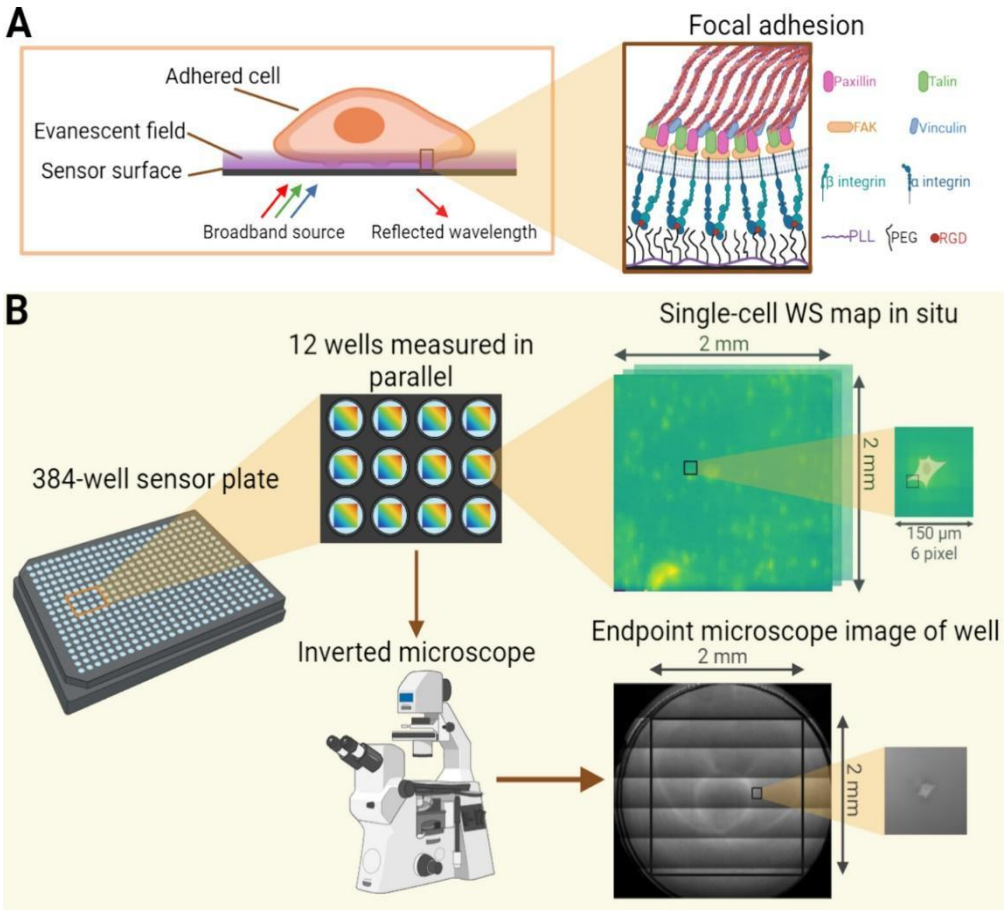

Figure 6.6 Schematic illustration of the measurement workflow, detailing the working principle of the RWG biosensor (A) and the measured adhesion complexes (B). The data is captured in two phases. First, the adhesion kinetic data is recorded using the RWG biosensor, and subsequently, each well is captured using a phase-contrast microscope for highly accurate spatial data. No changes are performed to the wells between the different measurements.

Kinetic monitoring of molecular interactions during surfactant-driven self-propelled droplet motion by high spatial resolution waveguide sensing

LP2012-26/2012 Lendület, OTKA ERC_HU 117755, TKP2021-EGA-04, OTKA KKP 129936 KDP, OTKA PD 134195, Bolyai Scholarship

E. Farkas, K. D. Kovács, I. Szekacs, B. Peter, I. Lagzi, H. Kitahata (Chiba University, Japan), N. J. Suematsu (Meiji University, Japan), R. Horvath

Self-driven actions, like motion, are fundamental characteristics of life. Today, intense research focuses on the kinetics of droplet motion. Quantifying macroscopic motion and exploring the underlying mechanisms are crucial in self-structuring and self-healing materials, advancements in soft robotics, innovations in self-cleaning environmental processes, and progress within the pharmaceutical industry. Usually, the driving forces inducing macroscopic motion act at the molecular scale, making their real-time and high-resolution investigation challenging. Label-free surface sensitive measurements with high lateral resolution could *in situ* measure both molecular-scale interactions and microscopic motion.

We employ surface-sensitive label-free sensors to investigate the kinetic changes in a self-assembled monolayer of the trimethyl(octadecyl)azanium chloride surfactant on a substrate surface during the self-propelled motion of nitrobenzene droplets. The adsorption–desorption of the surfactant at various concentrations, its removal due to the moving organic droplet, and rebuilding mechanisms at droplet-visited areas are all investigated with excellent time, spatial, and surface mass density resolution.

We discovered concentration dependent velocity fluctuations, estimated the adsorbed amount of surfactant molecules, and revealed multilayer coverage at high concentrations. The desorption rate of surfactant ($18.4\ s^{-1}$) during the microscopic motion of oil droplets was determined by *in situ* differentiating between droplet visited and non-visited areas [Ref.6.7].

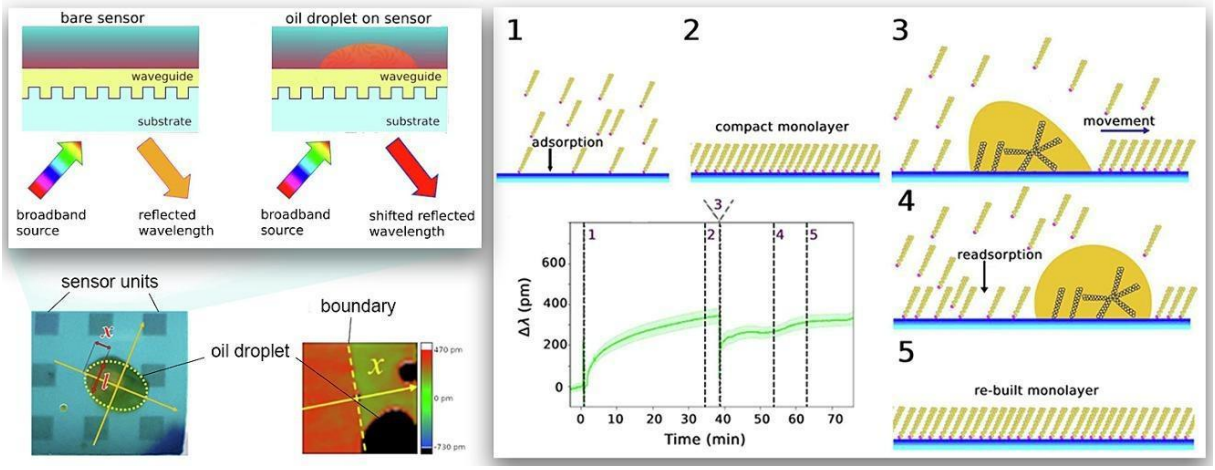

Figure 6.7 Schematic illustration of the measurement method.

Resonant waveguide grating biosensors based on label-free optical principle

LP2012-26/2012 Lendület, OTKA ERC_HU 117755, TKP2021-EGA-04, OTKA KKP 129936, KDP, OTKA PD 134195

I. Sallai

Label-free optical biosensors are powerful tools for the real-time monitoring of both molecular and cellular-scale interactions. Resonant waveguide grating biosensors are based on the detection of refractive index changes induced by molecular interactions and/or cell mass redistributions. The Epic BenchTop and Epic Cardio are two biosensors with high sensitivity and throughput that offer excellent potential for life science research. Both instruments are suitable for cell-based and biochemical assays. In this paper, we describe the principles of operation and performance of the Epic BenchTop and Epic Cardio label-free waveguide grating biosensors and discuss their applications in various research areas [Ref.6.8].

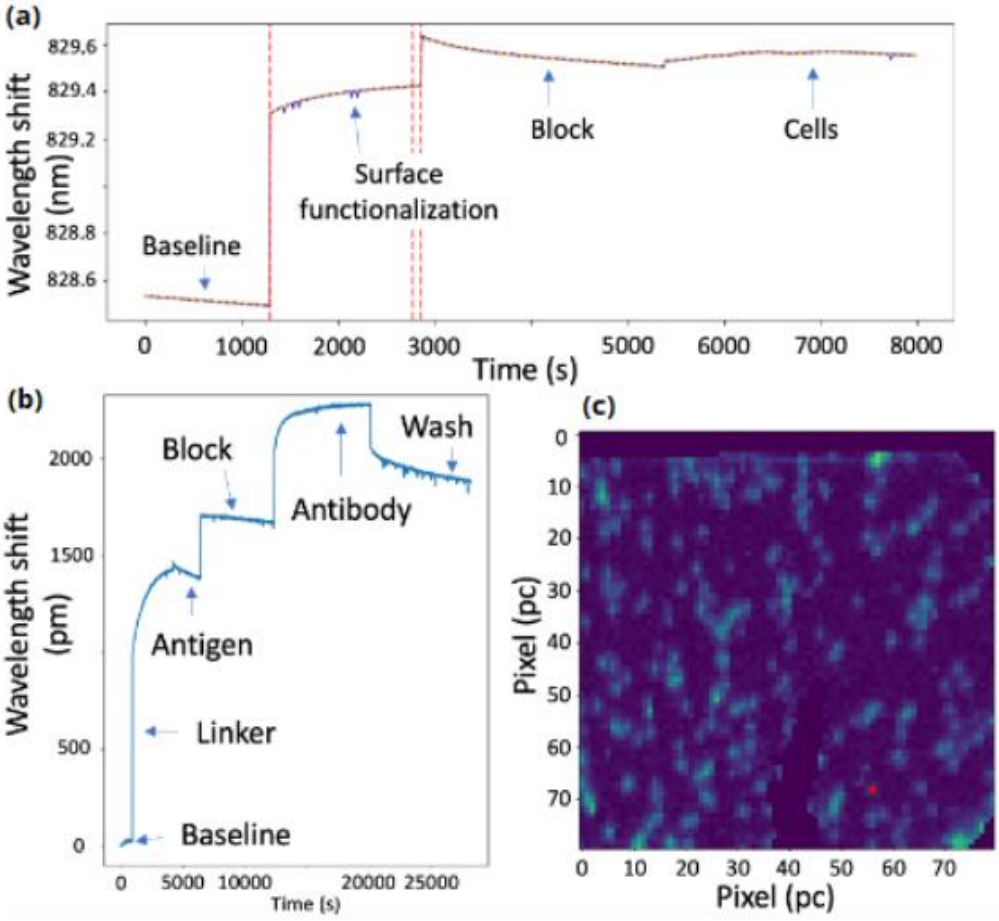

Figure 6.8 Output data of the RWG biosensor; (a) shows an example of a set of wavelength shift events averaged over a single microtiter plate hole. The procedures and surface treatment/functionalization methods used at each stage are marked in the diagram; (b) shows a set of wavelength shift events occurring on a single sensor pixel; (c) shows a 25 μm resolution image taken with a CMOS camera, with the red marker indicating the cell just detected.

Temporal pH waveforms generated in an enzymatic reaction network in batch and cell-sized microcompartments

"Lendület" (HAS) research program, ERC_HU, TKP, KKP_19

M. Itatani, G. Holló (University of Lausanne, Switzerland), P. Albanese (University of Siena, Italy), N. Valletti (University of Siena, Italy), S. Kurunczi, R. Horvath, F. Rossi (University of Siena, Siena, Italy), I. Lagzi (BME)

Investigating and designing reaction networks and their emergent phenomena are the backbone of systems chemistry. Designing chemical oscillators in homogeneous systems utilizing enzymatic reactions is challenging due to the consumption of the substrates over one reaction cycle. Here, we show that an antagonistic enzymatic reaction network comprising urea-urease and ester-esterase reactions can generate temporal pH variations in a batch. We developed a coupled reaction kinetic model to elucidate the mechanism that accurately captures the experimentally observed pH variation over time. To demonstrate the remarkable potential of the enzymatic reaction network, we expanded on this discovery by generating front propagation and presenting several applications by coupling this enzymatic reaction network to fuel pH-dependent processes (gelation of pH-sensitive monomers and emulsion-vesicle transformation). By employing the coupling strategy of antagonistic enzymatic reactions, we engineered a single pH pulse in cell-sized microcompartments, which could contribute to developing synthetic cells with multiple functions [Ref.6.9].

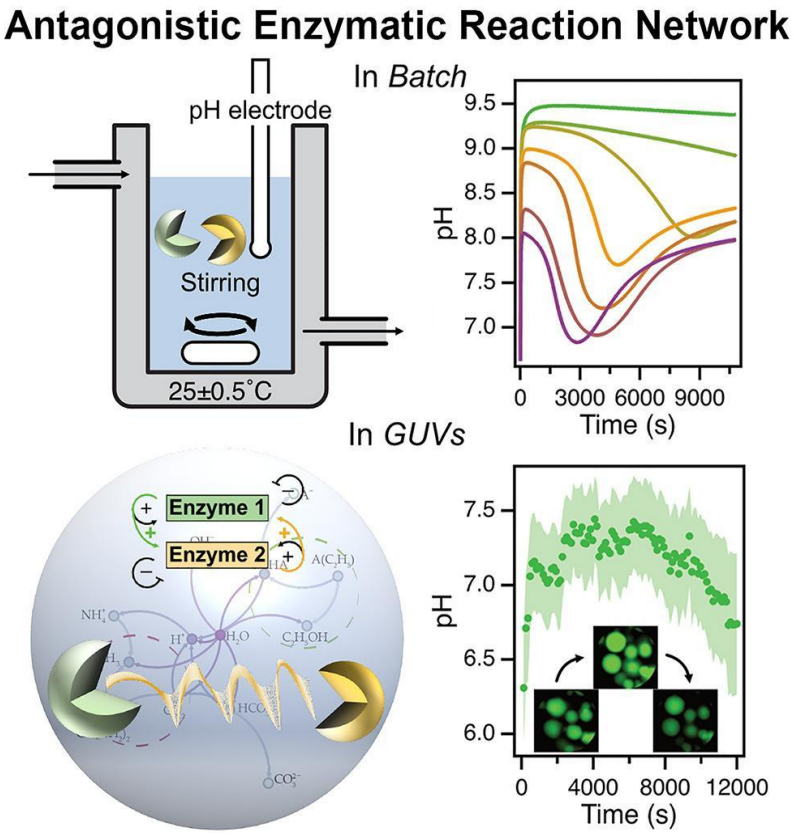

Figure 6.9 Schematic illustration of the antagonistic enzymatic reaction network.

Complex Systems Department

Head: Dr. Géza Ódor D.Sc., Scientific advisor

Research Staff:
György Szabó, D.Sc., Professor emeritus
Attila Szolnoki, D.Sc., Scientific advisor
Zoltán Juhász, Ph.D.
Balázs Király, Ph.D.
István Papp, Ph.D.
István Borsos +
Kristóf Benedek, Ph.D. student

Diploma workers:
Dávid Király, LFZE
Katalin Krisztina Kovács, LFZE
Zsombor Tóth, LFZE
Áron Weidinger, BME

The research field of the group is the investigation of complex systems by the methods of statistical physics. In 2024 they focused on the following topics:

- One of their study investigated how to mitigate cascade failures in European power grids by analyzing their network structure and dynamics. Cascade failures may occur when one component's failure triggers a chain reaction, potentially leading to widespread outages.
- They used theoretical toolkits for understanding cooperation and strategic dynamics in structured populations. They presented an analytical framework for studying n-strategy multiplayer evolutionary games on graphs under weak selection using pair approximation.
- They also extended the traditional game theory which assumes symmetric interactions. In real-world roles and traits often create asymmetries better captured by bimatrix games.

Improving power-grid systems via topological changes or how self-organized criticality can help power grids

G. Ódor

Cascade failures in power grids occur when the failure of one component or subsystem causes a chain reaction of failures in other components or subsystems, ultimately leading to a widespread blackout or outage. Controlling cascade failures on power grids is important for many reasons like economic impact, national security, public safety and even rippled effects like troubling transportation systems. Monitoring the networks on node level has been suggested by many, either controlling all nodes of a network or by subsets.

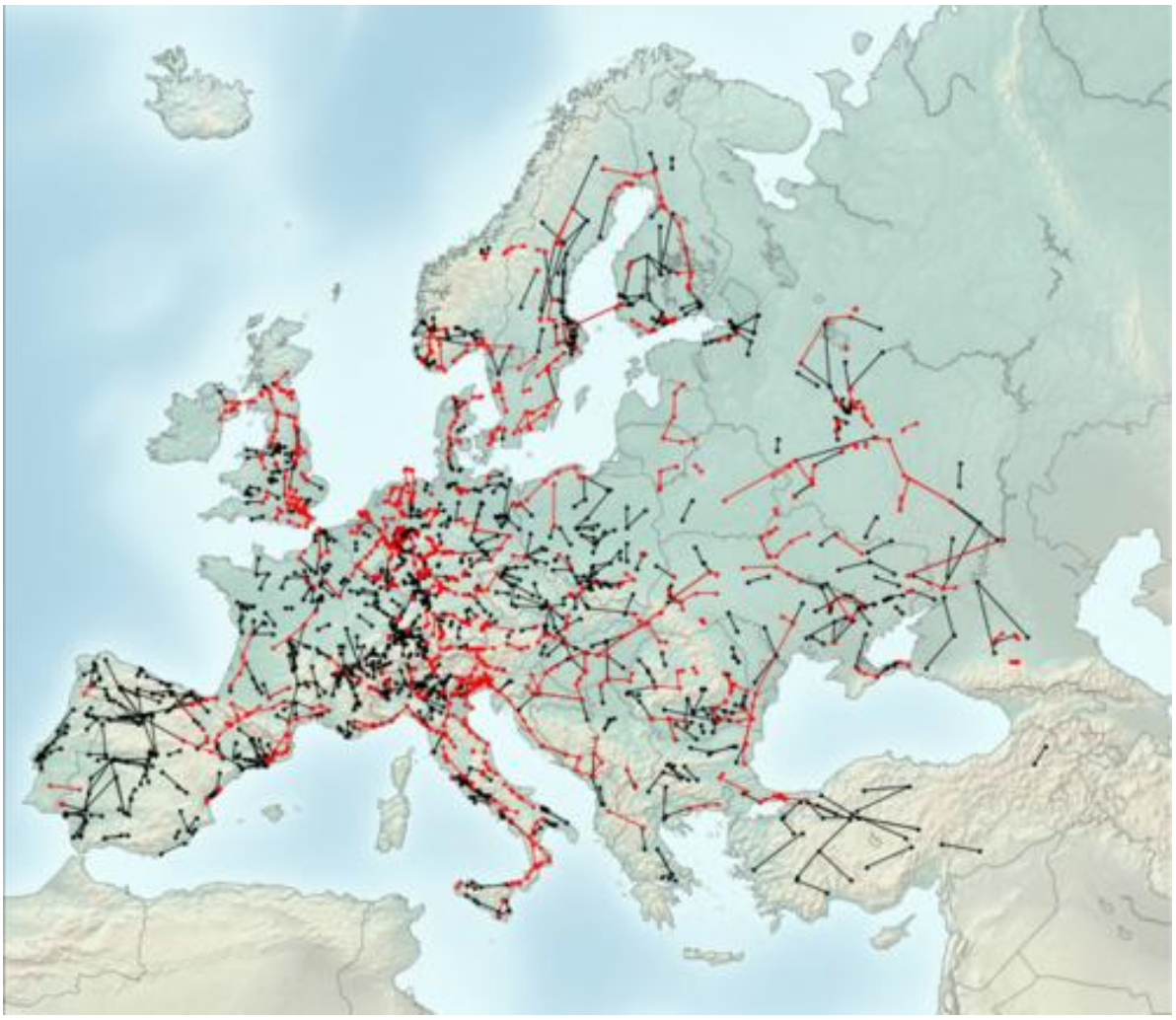

Figure 7.1 The figure shows the difference between the set of (red) nodes, links selected with the bypass method for EU16 network and the set of black nodes, links that are on the bridges. The edges were inserted between the nodes selected by the bypass method, increasing the network's modularity score.

We identified sensitive graph elements of the weighted European power-grids (from 2016 and 2022) by two different methods. Bridges are determined between communities and “weak” nodes are selected by the lowest local synchronization of the swing equation. In the latter case we added bypasses of the same number as the bridges at weak nodes, and we compared the synchronization, cascade failure behavior by the dynamical improvement with the purely topological changes. The results were also compared if bridges were removed from networks, which results in a case similar to islanding, and with the addition of links at randomly selected places. Bypassing was found to improve synchronization the best, while the average cascade sizes were the lowest with bridge additions. However, for very large or small global couplings these network changes do not help, they seem to be useful near the synchronization transition region, where self-organization drives the power grid. Thus, we provided a demonstration for the Braess' Paradox on continent-sized power-grid simulations and uncover the limitations of this phenomenon. We also determined the cascade size distributions and justify the power-law tails near the transition point on these grids. [Ref.7.1]

Evolutionary dynamics of any multiplayer game on regular graphs

OTKA K 128989

C. Wang, M. Perc, and A. Szolnoki

Our work developed the replicator equation for any n-strategy multiplayer game under weak selection and pair approximation, which can be obtained in polynomial time. Using combinatorial methods, we have shown that the local configuration of multiplayer games on graphs is equivalent to distributing k identical co-players among n distinct strategies.

This analytical method makes possible to revisit some celebrated problems where only numerical solutions are available for several interaction graphs. The introduction of the third strategy in the second-order free-riding problem cannot truly resolve social dilemmas in a community where interacting groups are formed at random. For local neighbourhood, however, this new calculation can derive an accurate threshold for the punishment strength, beyond which punishment can either lead to the extinction of defection or transform the system into a rock-paper-scissors-like cycle. The analytical solution agrees qualitatively with the prediction of numerical simulations obtained previously for non-marginal selection strengths. Similar qualitative agreement was found when other versions (e.g., pool or institutional) punishment is used to minimize defection. These results shed light on general relationships that were indicated previously in independent research efforts obtained for weak and non-marginal selection limits. [Ref.7.2]

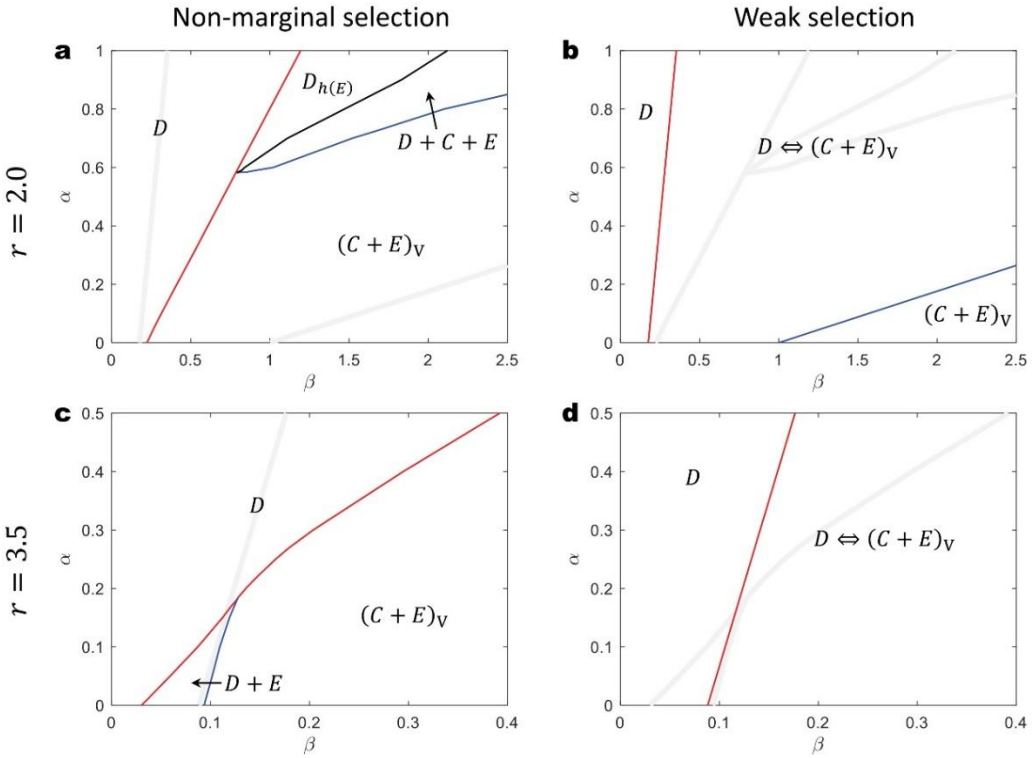

Figure 7.2 Phase diagrams of the system behavior with respect to punishing cost α and fine β are qualitatively similar under non-marginal and weak selection strength. D,C,E denotes defector, pure cooperator and peer-punisher players, respectively. Phase diagrams of the system behavior with respect to punishing cost α and fine β are qualitatively similar under non-marginal and weak selection strength. V marks the region where there is a voter-model like coarsening between C and E neutral strategies

Orthogonal elementary interactions for bimatrix games

OTKA PD 138571

Gy. Szabó, B. Király

Although game theory has traditionally focused on interactions in which an exchange of strategies between players leads to an exchange of outcomes, real interactions are rarely this symmetric. The interacting parties often play fundamentally different roles (incumbent–challenger, host–parasite, etc.), but the natural variance and adaptation of certain capabilities or traits (e.g., strength, wealth, influence, authority) can also introduce differences between players and outcomes. The simplest general models of such pair interactions are so-called bimatrix games, which tabulate the outcomes of the participants in two separate payoff matrices. For symmetric interactions, the two payoff matrices are equal.
Previous research has revealed that symmetric matrix games can be decomposed into orthogonal elementary components describing just four archetypal interaction situations: self-dependent, cross-dependent, coordination-type, and rock–paper–scissors-like cyclic interactions. Our latest results extend this analysis to general bimatrix games.

We identified two new basis game types not present in symmetric matrix games, elementary matching pennies and elementary directed anticoordination games. The former, the zero-sum counterparts of elementary coordination games, generate cyclic dominance between the strategies similarly to rock–paper–scissors-like games, and thus also preclude the game from admitting a potential or exhibiting thermodynamics behaviour. The latter, the fraternal counterparts of elementary rock–paper–scissors-like games, have more in common with partnership games, but unlike any symmetric game have a non-Hermitian potential matrix. The spatial version of this type of evolutionary game shows a phase transition (see Figure 7.3) that deviates slightly from the one characterizing the three-state Potts model. Zero-sum combinations of self- and cross-dependent components can also contribute non-symmetric components to the potential.

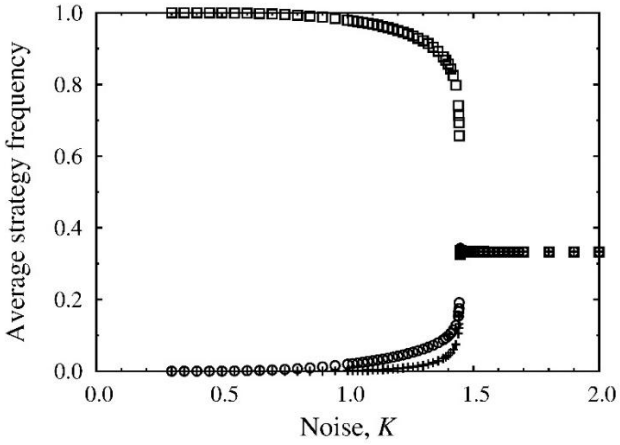

Figure 7.3 Monte Carlo simulation results illustrate the noise-dependent thermodynamic behaviour and order–disorder phase transition in a multiagent game in which players located at the sites of a square lattice repeatedly play the three-strategy elementary directed anticoordination game against their nearest neighbours following the logit strategy update rule.

The above outlined decomposition scheme provides a simple mathematical framework for the systematic analysis of not only how pair interactions determine the macroscopic properties of multiagent systems in general, but also the exploration of the various causes of social dilemmas, the novel characteristics of non-reciprocal interactions, and the effects of the coevolution of the payoffs in particular.

REFERENCES

[Ref.1.1.] Pálinkás, A. et al. Identification of graphite with perfect rhombohedral stacking by electronic Raman scattering. Carbon 230, 119608 (2024).
[Ref.2.1] Borg, H.; Zámbó, D.; Bessel, P.; Kranz, D.; Rosebrock, M.; Lübkemann-Warwas, F.; Bigall, N. C.; Dorfs, D. Tailoring Bimetallic Pt/Pd Cryogels for Efficient Ethanol Electro-Oxidation. *ChemElectroChem* 2024, e202400552. https://doi.org/10.1002/celc.202400552.
[Ref.2.2] Zámbó, D.; Kovács, D.; Radnóczi, GyörgyZ.; Horváth, Z. E.; Sulyok, A.; Tolnai, I.; Deák, A. Structural Control Enables Catalytic and Electrocatalytic Activity of Porous Tetrametallic Nanorods. *Small* 2024, *20* (31), 2400421. https://doi.org/10.1002/smll.202400421.
[Ref.2.3] Omondi, A. S.; Kovács, D.; Radnóczi, G. Z.; Horváth, Z. E.; Tolnai, I.; Deák, A.; Zámbó, D. Symmetry Breaking Enhances the Catalytic and Electrocatalytic Performance of Core/Shell Tetrametallic Porous Nanoparticles. *Nanoscale* 2025, *17* (1), 261–275. https://doi.org/10.1039/D4NR03589E.
[Ref.2.4] Kovács, D.; Deák, A.; Radnóczi, G. Z.; Horváth, Z. E.; Sulyok, A.; Schiller, R.; Czömpöly, O.; Zámbó, D. Position of Gold Dictates the Photophysical and Photocatalytic Properties of Cu_2O in Cu_2O/Au Multicomponent Nanoparticles. *J. Mater. Chem. C* 2023, *11* (26), 8796–8807. https://doi.org/10.1039/D3TC01213A.
[Ref.2.5] Zámbó, D.; Kovács, D.; Deák, A. Optical and Structural Properties of Cuprous Oxide Shell Coated Gold Nanoprisms. *Part & Part Syst Charact* 2024, 2400082. https://doi.org/10.1002/ppsc.202400082.
[Ref.2.6] N. Nagy "Determination of solid-liquid adhesion work on flat surfaces in a direct and absolute manner" *Scientific Reports*, 14:29991 2024. https://doi.org/10.1038/s41598-024-81710-6
[Ref.2.7] N. Nagy „Eljárás és berendezés folyadék-szilárd adhéziós munka meghatározására" *Hungarian patent* (231 506)
[Ref.2.8] N. Nagy „Method and Apparatus for Determining Liquid-Solid Adhesion Work", *WIPO PCT patent application* (WO2023094846) https://patentscope.wipo.int/search/en/detail.jsf?docId=WO2023094846
[Ref.2.9] C. Major, G. Juhasz, Z. Labadi, M. Fried, "High speed spectroscopic ellipsometry technique for on-line monitoring in large area thin layer production," 2015 IEEE 42nd Photovoltaic Specialist Conference (PVSC), 2015, pp. 1-6, doi: 10.1109/PVSC.2015.7355640
[Ref.2.10] G. Juhász, Z. Horváth, C. Major, P. Petrik, O. Polgár, M. Fried, Non-collimated beam ellipsometry, physica status solidi c Volume 5, Issue 5 p. 1081-1084, https://doi.org/10.1002/pssc.200777862
[Ref.2.11] Horváth Z Gy, Juhász G, Fried M, Major C, Petrik P: Imaging optical inspection device with a pinhole camera; EP2160591B1, Submission Number: PCT/HU2008/000058, NSZO: G01N21/8422, Country of patent: Europe
[Ref.2.12] J. W. P. Bakker, H. Arwin, I. Lundström, and D. Filippini: Computer screen photoassisted off-null ellipsometry, Applied Optics Vol. 45, Issue 30, pp. 7795-7799 (2006), https://doi.org/10.1364/AO.45.007795
[Ref.2.13] Zereay, Berhane N. ; Kálvin, Sándor ; Juhász, György ; Major, Csaba ; Petrik, Péter ; Horváth, Zoltán G. ; Fried, Miklós: Optical Calibration of a Multi-Color Ellipsometric Mapping Tool Fabricated Using Cheap Parts, PHOTONICS 11 : 11 Paper: 1036 , 11 p. (2024) https://doi.org/10.3390/photonics11111036
[Ref.2.14] R.S. Moirangthem, Y.-C. Chang, P.-K. Wei, Ellipsometry study on gold- nanoparticle-coated gold thin film for biosensing application, Biomed. Opt. Express (2011) 2569.
[Ref.2.15] S. Kim, S. Park, S. Park, C. Lee, Acetone sensing of Au and Pd-decorated WO3 nanorod sensors, Sensors Actuators B 209 (2015) 180.
[Ref.2.16] B. Kalas, Z. Zolnai, G. Sáfrán, M. Serényi, E. Agocs, T. Lohner, A. Nemeth, N.Q. Khánh, M. Fried, P. Petrik, Micro-combinatorial sampling of the optical properties of hydrogenated amorphous Si1−xGex for the entire range of compositions towards a database for optoelectronics, Sci. Rep. 10 (2020) 19266.
[Ref.2.17] G. Sáfrán, ''One-sample concept'' micro-combinatory for high throughput TEM of binary films, Ultramicroscopy 187 (2018) 50.
[Ref.2.18] M. Loncaric, J. Sancho-Parramon, H. Zorc, Optical properties of gold island films—a spectroscopic ellipsometry study, Thin Solid Films 519 (2011) 2946.
[Ref.2.19] F. Binkowski, T. Wu, P. Lalanne, S. Burger, A.O. Govorov, Hot electron generation through near-field excitation of plasmonic nanoresonators, ACS Photonics 8 (2021) 1243.
[Ref.2.20] M. Kang, S.-G. Park, K.-H. Jeong, Repeated solid-state dewetting of thin gold films for nanogap-rich plasmonic nanoislands, Sci. Rep. 5 (2015) 14790.
[Ref.2.21] Granqvist, C.G. Handbook of Inorganic Electrochromic Materials, Elsevier: Amsterdam, The Netherlands, (1995)
[Ref.2.22] Noor, Taha Ismaeel; Lábadi, Zoltán ; Petrik, Peter ; Fried, Miklós, Investigation of Electrochromic, Combinatorial TiO2-SnO2 Mixed Layers by Spectroscopic Ellipsometry Using Different Optical Models

Materials 2023, 16(12), 4204.
[Ref.2.23] Lábadi, Zoltán ; Ismaeel, Noor T. ; Petrik, Péter ; Fried, Miklós, Compositional Optimization of Sputtered SnO2/ZnO Films for High Coloration Efficiency, INTERNATIONAL JOURNAL OF MOLECULAR SCIENCES 25 : 19 Paper: 10801 , 11 p. (2024)
[Ref.2.24] S.P. Thompson, "Ye Magick Mirrour of Old Japan", London, private edition (1893).
[Ref.2.25] Luo Xiangang, Pu Mingbo, Guo Yinghui, Li Xiong, Ma Xiaoliang, "Electromagnetic architectures: Structures, properties, functions and their intrinsic relationships in subwavelength optics and electromagnetics", Adv. Photonics Res. 2 (2021) 2100023.
[Ref.2.26] Kim Wooyoun, B. Cassarly, J.P. Rolland, "Connecting tolerancing of freeform surface deformation in illumination optics with the Laplacian magic mirror", Optics Express 29 (2021) 40559.
[Ref.2.27] A.S. Adnan, V. Ramalingam, J.H. Ko, S. Subbiah, "Nano texture generation in single point diamond turning using backside patterned workpiece", Manufact. Letters 2 (2014) 44.
[Ref.2.28] S. Vinothkumar, S. Subbiah, S. Sankaran, "Subsurface pore-induced quilting during machining of metal foams", J. Micro- Nano-Manufact. 8 (2020) 024509-1.
[Ref.2.29] S.M. Kennedy, C.X. Zheng, W.X. Tang, D.M. Paganin, D.E. Jesson, "Addendum. Laplacian image contrast in mirror electron microscopy", Proc. R. Soc. A 467 (2011) 3332
[Ref.2.30] S.W. Wilkins, Y.I. Nesterets, T.E. Gureyev, S.C. Mayo, A. Pogany, A.W. Stevenson, "On the evolution and relative merits of hard X-ray phase-contrast imaging methods", Phil. Trans. R. Soc. A 372 (2014) 20130021.
[Ref.2.31] Mak Se-yuen, Yip Din-yan, "Secrets of the Chinese magic mirror replica", Phys. Educ. 36 (2001) 102.
[Ref.3.1] Dumas, P., F. Gustavo, M. Opprecht, G. Freychet, P. Gergaud, S. Kerdilès, S. Guillemin, J. L. Lábár, B. Pécz, F. Lefloch and F. Nemouchi. "Enhancing Superconductivity in CoSi2 Films with Laser Annealing."JAP 136 (10) 105103 (2024). https://doi.org/10.1063/5.0218950.
[Ref.3.2.] T. Stasiak, S. Debnárová, S. Lin, N. Koutná, Zs. Czigány, K. Balázsi, V. Buršíková, P. Vašina, P. Souček Synthesis and characterization of ceramic high entropy carbide thin films from the Cr-Hf-Mo-Ta-W refractory metal system Surface & Coatings Technology 485 (2024) 130839
[Ref.3.3.] Zs. Czigány, H. Rachid Ben Zine, K. Balázsi, C. Balázsi Cr-Al spinel phase formation in 316l alumina dispersed stainless steel processed by spark plasma sintering, Scientific Reports 15(2025) 7311
[Ref.3.4] I. Khan, A. Ibrahim; S. Satake; K. A. Béres; M. Mohai, Zs. Czigány, K. Sinkó, Z. Homonnay, E. Kuzmann, S. Krehula, M. Marciuš, L. Pavić, A. Šantić, S. Kubuki, 57 Fe-Mössbauer, XAFS and XPS Studies of Photo-Fenton Active xMO•40Fe2O3•(60-x)SiO2 (M:Ni, Cu, Zn) Nano-Composite Prepared by Sol-Gel Method, Ceramic International 50 (2024) 55177
[Ref.3.5.] D. Lenaz and H, Skogby, Structural changes in the FeAl2O4–FeCr2O4 solid solution series and their consequences on natural Cr-bearing spinels, Phys Chem Minerals 40 (2013) 587–595
[Ref.3.6.] O. Shtyka, W. Maniukiewicz, R. Ciesielski, A. Kedziora, V. Shatsila, T. Sierański, and T. Maniecki. "The Formation of Cr-Al Spinel under a Reductive Atmosphere" Materials 14 (2021) 3218
[Ref.3.7.] Dániel Olasz, Noémi Szász , Tamás Kolonits, György Radnóczi, Nguyen Quang Chinh, György Sáfrán Comprehensive characterisation of the Al-Cu binary thin film system: Correlation between composition, microstructure and mechanical properties Mater. Lett. 330 (2023) 133409
https://doi.org/10.1016/j.jallcom.2026.186114
[Ref.3.8.] N.Q. Chinh et al., MSEA 2025, 923, 147733
[Ref.3.9.] S. E. Panasci, E. Schilirò, A. Koos, F. Roccaforte, M. Cannas, S. Agnello, B. Pécz, F. Giannazzo, Tailoring MoS2 domains size, doping, and light emission by the sulfurization temperature of ultra-thin MoOx films on sapphire, Appl. Phys. Lett. 124, 243101 (2024). https://doi.org/10.1063/5.0214274
[Ref.3.10.] S. E. Panasci, I. Deretzis, E. Schilirò, A. La Magna, F. Roccaforte, A. Koos, M. Nemeth, B. Pécz, M. Cannas, S. Agnello, F. Giannazzo, Interface Properties of MoS2 van der Waals Heterojunctions with GaN, Nanomaterials 14, 133 (2024); https://doi.org/10.3390/nano14020133
[Ref.3.11.] F. Roccaforte, M. Vivona, S. E. Panasci, G. Greco, P. Fiorenza, A. Sulyok, A. Koos, B. Pecz, F. Giannazzo, Schottky contacts on sulfurized silicon carbide (4H-SiC) surface, Appl. Phys. Lett. 124, 102102 (2024). https://doi.org/10.1063/5.0192691
[Ref.3.12.] F. Giannazzo, S. E. Panasci, E. Schilirò, A. Koos, B Pécz, Integration of graphene and MoS2 on silicon carbide: Materials science challenges and novel devices, Materials Science in Semiconductor Processing 174, 108220 (2024). https://doi.org/10.1016/j.mssp.2024.108220.
[Ref.3.13.] B. Galizia, P. Fiorenza, C. Bongiorno, B. Pécz, Z. Fogarassy, E. Schilirò, F. Giannazzo, F. Roccaforte, R. Lo Nigro, Structural and electrical correlation in aluminum nitride thin films grown by plasma enhanced atomic layer deposition as interface insulating layers on silicon carbide (4H-SiC), Microelectronic Engineering 283, 112103 (2024). https://doi.org/10.1016/j.mee.2023.112103
[Ref.3.14.] S. E. Panasci, E. Schilirò, M. Cannas, S. Agnello, A. Koos, M. Nemeth, B. Pécz, F. Roccaforte, F. Giannazzo, Vertical Current Transport in Monolayer MoS2 Heterojunctions with 4H-SiC Fabricated by Sulfurization of Ultra-Thin MoOx Films, Solid State Phenomena 362, 7 (2024). https://doi.org/10.4028/p-dInd9N

[Ref.3.15.] A.S. Racz, M. Menyhard XPS depth profiling of nano-layers by a novel trial-and-error evaluation procedure, Scientific Reports, 14, 2024, 18497,
[Ref.3.16.] A.S. Racz Atomistic insights into salicylic acid treatment on human keratinized skin by XPS combined with argon gas cluster sputtering, Surf. Interfaces, 55, 2024, 105452,
[Ref.4.1] Z. Baji, Z. Fogarassy, O. Hakkel, and Z. Szabó, "Enhancing the nucleation in atomic layer deposition: A study on vanadium sulfide and oxide layers," Journal of Vacuum Science & Technology A, vol. 43, no. 2, p. 022408, Mar. 2025, doi: 10.1116/6.0004247.
[Ref.4.2] Z. Baji, Z. Fogarassy, A. Sulyok, Z. E. Horváth, and Z. Szabó, "Novel precursor for the preparation of vanadium sulfide layers with atomic layer deposition," Journal of Vacuum Science & Technology A, vol. 43, no. 2, p. 022405, Mar. 2025, doi: 10.1116/6.0004127.
[Ref.4.3] U. Gösele, K. N. Tu Growth kinetics of planar binary diffusion couples: ''Thin-film case'' versus ''bulk cases'' J. Appl. Phys. 53, 3252–3260 (1982) https://doi.org/10.1063/1.331028
[Ref.4.4] László Pósa*, Péter Hornung, Tímea Nóra Török, Sebastian Werner Schmid, Sadaf Arjmandabasi, György Molnár, Zsófia Baji, Goran Dražić, András Halbritter, and János Volk Interplay of Thermal and Electronic Effects in the Mott Transition of Nanosized VO2 Phase Change Memory Devices ACS Applied Nano Materials 2023, 6, 11, 9137-9147
[Ref.4.5] Sebastian Werner Schmid, László Pósa, Tímea Nóra Török, Botond Sánta, Zsigmond Pollner, György Molnár, Yannik Horst, János Volk, Juerg Leuthold, András Halbritter, Miklós Csontos Picosecond femtojoule resistive switching in nanoscale VO2 memristors ACS Nano, 18, 33, 21966 (2024) https://doi.org/10.1021/acsnano.4c03840
[Ref.4.6] Scherübl Z., et al. Determination of the current-phase relation of an InAs 2DEG Josephson junction with a microwave resonator. Phys. Rev. Research 7, 023173 (2025)
[Ref.5.1] Kitti Pankász, Cs. Dücső, Chip-set for Chemoresistive Gas Sensors, Eurosensors 2024 Conference, Debrecen, Hungary, 2024 (poster presentation)
[Ref.5.2] János Márk Bozorádi, Géza Papp, Zsófia Sz Bérces, Péter Fürjes, Characterization of Gastric Tissue Samples with MEMS Force Sensor Based Indentation method, Eurosensors 2024 Conference, Debrecen, Hungary, 2024 (poster presentation)
[Ref.5.3] János Volk, János M. Bozorádi, Ferenc Braun, Attila Nagy, Levente Illés, János Radó, Ultra-Sensitive Force Gauge Accessory for Microscope Micromanipulators, Eurosensors 2024 Conference, Debrecen, Hungary, 2024 (oral presentation)
[Ref.5.4] Géza Papp, János Márk Bozorádi, Zsófia Sz Bérces, Péter Fürjes, Laparoscopic staplers - time to be in safe, Colorectal THRIVE 2024 Congress, Fribourg, Switzerland, 2024 (BEST PAPER AWARD)
[Ref.5.5] Levente Víg, Anita Zátonyi, Bence Csernyus, Ágoston C. Horváth,Márton Bojtár, Péter Kele, Miklós Madarász, Balázs Rózsa, Péter Fürjes, Petra Hermann, Orsolya Hakkel, László Péter, Zoltán Fekete, Optically Controlled Drug Delivery Through Microscale Brain–Machine Interfaces Using Integrated Upconverting Nanoparticles, SENSORS 24 (24) 7987, 2024 https://doi.org/10.3390/s24247987
[Ref.5.6] Ágoston Csaba Horváth, Ákos Mórocz, Borbála Csomai, Ágnes Szabó,Zsófia Balogh-Lantos, Péter Fürjes, Estilla Zsófia Tóth, Richárd Fiáth, and Zoltán Fekete, Silicon Optrode with a Micromirror-Tip Providing TunableBeam Profile During Infrared Neuromodulation of the Rat Neocortex, Advanced Materials Technologies, 9 (20), 2400044, https://doi.org/10.1002/admt.202400044
[Ref.5.7] Ágoston Csaba Horváth, Borbála Csomai, Ákos Mórocz, Ágnes Szabó, Zsófia Balogh-Lantos, Péter Fürjes, Estilla Zsófia Tóth, Richárd Fiáth, Zoltán Fekete, On the way to layer-by-layer infrared neuromodulation: presentation and functional characterisation of an intracortical optrode needle featured with a micromirror tip ending, FENS (Federation of European Neuroscience Societies) Forum 2024, Vienna, Austria, 2024 (poster presentation)
[Ref.5.8] Á. Cs. Horváth, B. Csomai, Á. Mórocz, Á. Szabó, Zs. Balogh-Lantos, P. Fürjes, E. Zs. Tóth, R. Fiáth, Z. Fekete, Towards layer-by-layer infrared neuromodulation: presentation and functional characterisation of an intracortical optrode needle featured with a micromirror tip ending, IBRO-MITT International Neuroscience Conference 2024, Pécs, Hungary, 2024 (poster presentation)
[Ref.5.9] Lilia Bató, P. Fürjes, Diffusion coefficient measurement with fluorescent detection in free-diffusion based microfluidics, Microfluidics and Nanofluidics, 28 (8) 56, 2024 (IF 2.3 / Q3) https://doi.org/10.1007/s10404-024-02752-w
[Ref.5.10] Lilia Bató, Péter Fürjes, Vertical Microfluidic Trapping System for Capturing and Simultaneous Electrochemical Detection of Cells, SENSORS 24 (20) 6638, 2024 (IF 3.4 / Q1) https://doi.org/10.3390/s24206638
[Ref.5.11] Zoltan Vizvari, Nina Gyorfi, Gergo Maczko, Reka Varga, Rita Jakabfi-Csepregi, Zoltan Sari, Andras Furedi, Eszter Bajtai, Flora Vajda, Vladimir Tadic, Peter Odry, Zoltan Karadi, Attila Toth, Reproducibility

analysis of bioimpedance-based self-developed live cell assays, Scientific Reports (2024) 14:16380, https://doi.org/10.1038/s41598-024-67061-2 (IF: 3.8 / Q1)
[Ref.5.12] Beiler Barbara, Sáfrány Ágnes, Bató Lilia, Szomor Zsombor, Veres Miklós, Effect of binary porogen mixtures on polymer monoliths prepared by gamma-radiation initiated polymerization, HELIYON (2405-8440): 10 19 Paper e38852. 8 p. (2024) DOI: 10.1016/j.heliyon.2024.e38852 (IF 3.4 / Q1)
[Ref.5.12] Lilia Bató, János M. Bozorádi, Zoltán Vizvári, Péter Fürjes, Microfluidic device with integrated microelectrodes for enhanced EIS sensitivity, Eurosensors 2024 Conference, Debrecen, Hungary, 2024 (oral presentation)
[Ref.5.13] Lilia Bató, János M. Bozorádi, Péter Fürjes, Microfluidic device for EIS and optical monitoring of cells, EUROoCS Annual Meeting 2024, Milan, Italy, 2024 (poster presentation)
[Ref.5.14] Lilia Bató, János M. Bozorádi, Zoltán Vizvári, Péter Fürjes, Microfluidic device for impedance tomography, Mátrafüred International Conference on Chemical Sensors 2024, Visegrád, Hungary, 2024 (poster presentation)
[Ref.5.15] Zsombor Szomor, Eszter L. Tóth, Péter Fürjes, 3D Modelling of droplet formation in two-phase microfluidics for single-cell manipulation, Eurosensors 2024 Conference, Debrecen, Hungary, 2024 (oral presentation)
[Ref.5.16] Zsombor Szomor, Nafisat Gyimah, Péter Fürjes, Tamás Pardy, 3D Finite Element Modelling of Mixing Phenomena in Droplet-based Microfluidic Systems, Baltic Electronics Conference 2024 (BEC 2024), Tallinn, Estonia, 2024 (oral presentation)
[Ref.5.17] Anita Bányai, Enikő Farkas, Hajnalka Jankovics, Inna Székács, Eszter Leelőssyné Tóth, Ferenc Vonderviszt, Róbert Horváth, Máté Varga and Péter Fürjes, Cells and Model Particles in Lateral Focusing Microfluidics, Eurosensors 2024 Conference, Debrecen, Hungary, 2024 (poster presentation)
[Ref.5.18] Flóra Vajda, Áron Szepesi, Zsuzsa Erdei, Edit Szabó, György Várady, Dániel Kiss, László Héja, Katalin Német, Gergely Szakács, András Füredi, Mesenchymal Stem Cells Increase Drug Tolerance of A431 Cells Only in 3D Spheroids, Not in 2D Co-Cultures, Int. J. Molecular Sciences 2024, 25(8), 4515; https://doi.org/10.3390/ijms25084515 (IF: 4.9 / Q1)
[Ref.5.19] András Füredi, Dóra Bereczki, Balázs Gombos, Pál Szabó, Péter Vajdovich, Péter Fürjes. A Simple Microfluidic System for Point-of-Care Therapeutic Drug Monitoring of Anticancer Drugs, Eurosensors 2024 Conference, Debrecen, Hungary, 2024 (oral presentation)
[Ref.6.1] B. Péter, I. Székács, R. Horvath, „Label-free biomolecular and cellular methods in small molecule epigallocatechin-gallate research". HELIYON, vol. 10, 2024.
[Ref.6.2] A. Bonyár, Á. G. Nagy, H. Gunstheimer, G. Fläschner, R. Horvath, „Hydrodynamic function and spring constant calibration of FluidFM micropipette cantilevers." MICROSYSTEMS & NANOENGINEERING, vol. 10, 2024.
[Ref.6.3] H. Cheraghi (ELTE), K. D. Kovács, I. Székács, R. Horvath, B. Szabó, „Continuous distribution of cancer cells in the cell cycle unveiled by AI-segmented imaging of 37,000 HeLa FUCCI cells". HELIYON, vol. 10, 2024.
[Ref.6.4] K. D. Kovács, Z. Szittner, B. Magyaródi, B. Péter, B. Szabó, A. Vörös, N. Kanyó, I. Székács, R. Horvath, „Optical sensor reveals the hidden influence of cell dissociation on adhesion measurements". SCIENTIFIC REPORTS, vol. 14, 2024.
[Ref.6.5] K. D. Kovacs, B. Beres, N. Kanyo, B. Szabó, B. Peter, Sz. Bősze, I. Szekacs, R. Horvath, , „Single-cell classification based on label-free high-resolution optical data of cell adhesion kinetics", SCIENTIFIC REPORTS, vol. 14, 2024.
[Ref.6.6] B. Beres, K. D. Kovacs, N. Kanyo, B. Peter, I. Szekacs, R. Horvath, „Label-free single-cell cancer classification from the spatial distribution of adhesion contact kinetics ", ACS SENSORS, vol. 9, 2024.
[Ref.6.7] E. Farkas, K. D. Kovács, I. Szekacs, B. Peter, I. Lagzi, H. Kitahata, N. J. Suematsu, R. Horvath, „Kinetic monitoring of molecular interactions during surfactant-driven self-propelled droplet motion by high spatial resolution waveguide sensing", JOURNAL OF COLLOID AND INTERFACE SCIENCE, vol. 677, 2024.
[Ref.6.8] I. Sallai, „Resonant waveguide grating biosensors based on label-free optical principle", PERIODICA POLYTECHNICA ELECTRICAL ENGINEERING AND COMPUTER SCIENCE, vol. 68, 2024.
[Ref.6.9] M. Itatani, G. Holló, P. Albanese, N. Valletti S. Kurunczi, R. Horvath, F. Rossi, I. Lagzi „Temporal pH waveforms generated in an enzymatic reaction network in batch and cell-sized microcompartments", CELL REPORTS PHYSICAL SCIENCE, 102367, 2024
[Ref.7.1] Phys. Rev. Research 6, 013194 – Published 22 February, 2024
https://doi.org/10.1103/PhysRevResearch.6.013194
[Ref.7.2] https://www.nature.com/articles/s41467-624-49505-5 Nature Communications 15 (2024) 326

MFA'S FULL LIST OF PUBLICATION IN 2024

[1] A. Q. Ahmed, D. Olasz, E. V. Bobruk, R. Z. Valiev, and N. Q. Chinh, "Microstructure Evolution during High-Pressure Torsion in a 7xxx AlZnMgZr Alloy," MATERIALS, vol. 17, no. 3, 2024.
[2] W. Alkaron, A. Almansoori, C. Balázsi, and K. Balázsi, "A Critical Review of Natural and Synthetic Polymer-Based Biological Apatite Composites for Bone Tissue Engineering," *JOURNAL OF COMPOSITES SCIENCE*, vol. 8, no. 12, 2024.
[3] W. Alkaron, A. Almansoori, K. Balázsi, and C. Balázsi, "Hydroxyapatite-Based Natural Biopolymer Composite for Tissue Regeneration," *MATERIALS*, vol. 17, 2024.
[4] A. Almansoori and W. Alkaron, "Effect of low-pressure plasma treatment on the thermal behaviour of organo-modified montmorillonite nanoclay," *ARCHIVES OF MATERIALS SCIENCE AND ENGINEERING*, vol. 125, no. 1, pp. 5–14, 2024.
[5] A. Almansoori, K. Balázsi, and C. Balázsi, "Advances, Challenges, and Applications of Graphene and Carbon Nanotube-Reinforced Engineering Ceramics," *NANOMATERIALS*, vol. 14, no. 23, 2024.
[6] S. B. Anooz, P. Petrik, Y. Wang, D. Mukherjee, M. Schmidbauer, and J. Schwarzkopf, "Dielectric function and interband critical points of compressively strained ferroelectric K 0.85 Na 0.15 NbO 3 thin film with monoclinic and orthorhombic symmetry," *OPTICS EXPRESS*, vol. 32, no. 9, pp. 15597–15609, 2024.
[7] T. Arjmandabasi, Á. Révész, V. K. Kis, D. Ugi, E. Schafler, and Z. Kovács, "Radial dependence of thermal, structural and micro deformation characteristics in Cu-Zr-Al bulk metallic glass subjected to high pressure torsion," *MATERIALS AND DESIGN*, vol. 244, 2024.
[8] I. Ayyubov, C. Berghian-Grosan, E. Dodony, Z. Pászti, I. Borbáth, A. Szegedi, A. Vulcu, A. Tompos, and E. Tálas, "Structure–Catalytic Behavior Relationships in TiO2-Carbon Composite Supported Pt Electrocatalysts: A Case Study," *ANALYTICAL LETTERS*, vol. 67, no. 19–20, pp. 1348–1367, 2024.
[9] A. Azarov, A. Galeckas, I. Cora, Z. Fogarassy, V. Venkatachalapathy, E. Monakhov, and A. Kuznetsov, "Optical Activity and Phase Transformations in γ/β Ga2O3 Bilayers Under Annealing," *ADVANCED OPTICAL MATERIALS*, vol. 12, no. 29, 2024.
[10] Z. Baji, L. Pósa, G. Molnár, J. Á. Vándorffy, P. Neumann, Z. Szabó, A. Sulyok, Z. Fogarassy, and J. Volk, "Technological applicability of VO2 layers prepared with different approaches," in *19th Joint Vacuum Conference*, 2024, pp. 85–85.
[11] Z. Baji, B. Pécz, Z. Fogarassy, Z. Szabó, and I. Cora, "Atomic layer deposited Fe-sulphide layers with pyrrhotite structure controlled by the deposition temperature," *THIN SOLID FILMS*, vol. 794, 2024.
[12] K. Bajnok, Z. Kovács, and A. A. Nagy, "BETTER LATE (ROMAN) THAN NEVER! A POSSIBLE AMPHORA FRAGMENT FROM 6TH CENTURY BALATONLELLE, WESTERN HUNGARY/ [EGY LEHETSÉGES AMPHORA TÖREDÉK A 6. SZÁZADI BALATONLELLÉRŐL," *ARCHEOMETRIAI MŰHELY*, vol. 21, no. 2, pp. 201–216, 2024.
[13] K. Balázsi, A. Almansoori, and C. Balázsi, "Superior Ceramics: Graphene and Carbon Nanotube (CNT) Reinforcements," *CERAMICS (SWITZERLAND)*, vol. 7, no. 4, pp. 1758–1778, 2024.
[14] Z. Bálint, G. Katona, K. Kertész, G. Piszter, B. Tóth, and L. P. Biró, "Not all apparently gynandromorphic butterflies are gynandrous: The case of Polyommatus icarus and its relatives (Lepidoptera: Lycaenidae)," *ARTHROPOD STRUCTURE & DEVELOPMENT*, vol. 80, 2024.
[15] A. Balogh, K. D. Kovács, B. Kovács, I. Rajmon, K. Molnár, I. Székács, B. É. Péter, and R. Horváth, "Funkcionalizált nanorészecskék és élő sejtek kölcsönhatásainak jelölésmentes vizsgálata modern biofizikai módszerekkel." 2024.
[16] Z. Balogh, A. Nyáry, B. Sánta, J. G. Fehérvári, S. W. Schmid, L. Pósa, M. Csontos, and A. Halbritter, "Noise-Spectroscopy-Motivated Improvements in Memristor-Based Neuromorphic Applications: From Comprehensive Noise Analysis to Controlled Noise Manipulation Strategies," in *Proceedings of the Neuronics Conference, 2024*, 2024.
[17] Z. Balogh, A. Len, V. Baksa, A. Krajnc, P. Herman, G. Szemán-Nagy, Z. Czigány, I. Fábián, J. Kalmár, and Z. Dudás, "Nanoscale structural characteristics and in vitro bioactivity of borosilicate – polyvinyl alcohol (PVA) hybrid aerogels for bone regeneration," *ACS APPLIED NANO MATERIALS*, vol. 7, no. 4, pp. 4092–4102, 2024.
[18] A. Bányai, E. Farkas, H. Jankovics, I. Székács, E. Leelőssyné Tóth, F. Vonderviszt, R. Horváth, M. Varga, and P. Fürjes, "Cells and Model Particles in Lateral Focusing Microfluidics." 2024.
[19] Y. Baron, J. L. Lábár, S. Lequien, B. Pécz, R. Daubriac, S. Kerdilès, P. Acosta Alba, C. Marcenat, D. Débarre, F. Lefloch, and F. Chiodi, "Nanosecond laser annealing: Impact on superconducting silicon on insulator monocrystalline epilayers," *APL MATERIALS*, vol. 12, 2024.
[20] T. Baross, H. Rachid, P. Bereczki, M. Palánkai, K. Balázsi, C. Balázsi, and G. Veres, "Diffusion Bonding of Al2O3 Dispersion-Strengthened 316L Composite by Gleeble 3800," *MATERIALS*, vol. 17, no. 10, 2024.

[21] I. Bársony, "Fejlődésünk záloga: a félvezető-technológia," *MŰSZAKI TUDOMÁNYOS KÖZLEMÉNYEK (HU)*, vol. 20, no. 20, pp. 1–6, 2024.
[22] I. Bársony, "Key to Progress: the Semiconductor Technology," *MŰSZAKI TUDOMÁNYOS KÖZLEMÉNYEK (EN)*, vol. 20, no. 20, pp. 1–6, 2024.
[23] L. Bató, J. M. Bozorádi, P. Fürjes, and Z. Vizvári, "OT6.160 - Microfluidic device with integrated microelectrodes for enhanced EIS sensitivity," in *Abstract book Eurosensors XXXVI*, 2024, pp. 173–174.
[24] L. Bató, J. M. Bozorádi, and P. Fürjes, "Microfluidic device for EIS and optical monitoring of cells." 2024.
[25] L. Bató, J. M. Bozorádi, Z. Vizvári, and P. Fürjes, "Microfluidic device for impedance tomography." 2024.
[26] L. Bató and P. Fürjes, "Microfluidic System with Integrated Electrode Array for High-Throughput Electrochemical Impedance Spectroscopy Analysis of Localised Cells." 2024.
[27] L. Bató and P. Fürjes, "Vertical Microfluidic Trapping System for Capturing and Simultaneous Electrochemical Detection of Cells," *SENSORS*, vol. 24, no. 20, 2024.
[28] L. Bató and P. Fürjes, "Diffusion coefficient measurement with fluorescent detection in free-diffusion based microfluidics," *MICROFLUIDICS AND NANOFLUIDICS*, vol. 28, no. 8, 2024.
[29] L. Bató and P. Fürjes, "Microfluidic System with Integrated Electrode Array for High-Throughput Electrochemical Impedance Spectroscopy Analysis of Localised Cells," *PROCEEDINGS*, vol. 97, no. 1, 2024.
[30] G. Battistig, "Az ionsugaras adalékolás és analitika alkalmazása a félvezető-technológiában, avagy, Gyulai József munkásságának hatása a KFKI-ban és utódintézeteiben," *FIZIKAI SZEMLE*, vol. 74, no. 3, pp. 88–91, 2024.
[31] B. Beiler, Á. Sáfrány, L. Bató, Z. Szomor, and M. Veres, "Effect of binary porogen mixtures on polymer monoliths prepared by gamma-radiation initiated polymerization," *HELIYON*, vol. 10, no. 19, 2024.
[32] T. Benkó, S. Shen, M. Németh, D. Lukács, Y. Xu, I. Khan, Z. Czigány, Z. E. Horváth, Z. Kovács, J. Su, and J. S. Pap, "Photoelectrocatalytic Water Splitting by Conformal Copper-Oxide on Hematite Nanostructures: Dependence on Surface-States," *CHEMELECTROCHEM*, vol. 11, no. 13, 2024.
[33] B. Beres, K. D. Kovacs, N. Kanyo, B. Peter, I. Szekacs, and R. Horvath, "Label-Free Single-Cell Cancer Classification from the Spatial Distribution of Adhesion Contact Kinetics," *ACS SENSORS*, vol. 9, no. 11, pp. 5815–5827, 2024.
[34] L. P. Biró, G. Piszter, K. Kertész, Z. Baji, Z. Vértesy, Z. E. Horváth, G. I. Márk, D. Kovács, D. Zámbó, Z. Bálint, G. Nagy, and J. S. Pap, "Structural color on butterfly wings: from sexual communication to photocatalysis," in *A MMT éves konferenciájának kivonatkönyve 2024*, 2024, pp. 19–21.
[35] L. P. Biró, L. Tapasztó, and P. Nemes-Incze, "Pásztázószondás módszerek az MFA-ban," *FIZIKAI SZEMLE*, vol. 74, no. 3, pp. 74–79, 2024.
[36] L. P. Biró and B. Pécz, "Gyulai József öröksége a funkcionális anyagok tudományában," *FIZIKAI SZEMLE*, vol. 74, no. 3, pp. 73–73, 2024.
[37] A. Bonyár, Á. G. Nagy, H. Gunstheimer, G. Fläschner, and R. Horvath, "Hydrodynamic function and spring constant calibration of FluidFM micropipette cantilevers," *MICROSYSTEMS & NANOENGINEERING*, vol. 10, 2024.
[38] I. Borbáth, K. Salmanzade, Z. Pászti, A. Kuncser, D. Radu, Ş. Neaţu, E. Tálas, I. E. Sajó, D. Olasz, G. Sáfrán, Á. Szegedi, M. Florea, and A. Tompos, "Strategies to improve CO tolerance and corrosion resistance of Pt electrocatalysts for polymer electrolyte membrane fuel cells: Sn-doping of the mixed oxide–carbon composite support," *CATALYSIS TODAY*, vol. 438, 2024.
[39] J. M. Bozorádi, Z. S. Bérces, P. Fürjes, and G. Papp, "PT4.238 - Characterization of Gastric Tissue Samples with MEMS Force Sensor Based Indentation method," in *Abstract book Eurosensors XXXVI*, 2024, pp. 317–318.
[40] H. Cheraghi, K. D. Kovács, I. Székács, R. Horvath, and B. Szabó, "Continuous distribution of cancer cells in the cell cycle unveiled by AI-segmented imaging of 37,000 HeLa FUCCI cells," *HELIYON*, vol. 10, no. 9, 2024.
[41] T.-S. Chou, S. Bin Anooz, R. Grüneberg, J. Rehm, A. Akhtar, D. Mukherjee, P. Petrik, and A. Popp, "In-situ spectral reflectance investigation of hetero-epitaxially grown β-Ga2O3 thin films on c-plane Al2O3 via MOVPE process," *APPLIED SURFACE SCIENCE*, vol. 652, 2024.
[42] I. Cora, Z. Baji, Z. E. Horváth, Z. Szabó, J. Volk, and Z. Fogarassy, "In situ TEM examination of the monoclinic VO2 thin layer phase transformation to tetragonal VO2," in *19th Joint Vacuum Conference*, 2024, pp. 88–88.
[43] I. Cora, Z. Fogarassy, A. Azarov, G. Z. Radnóczi, B. Pécz, and A. Kuznetsov, "Phase transformations in Ni implanted Ga-oxide studied by electron microscopy," in *A MMT éves konferenciájának kivonatkönyve 2024*, 2024, pp. 22–24.
[44] ldiko Cora, Z. Fogarassy, M. Bosi, R. Fornari, A. Azarov, A. Kuznetsov, and B. Pécz, "Advanced structural characterization of Gallium Oxide by transmission electron microscopy," in *19th Joint Vacuum Conference*, 2024, pp. 77–77.

[45] M. Costa, Á. L. Viloria, S. Attal, M. Benmesbah, A. Neild, N. Grishin, K. Kertész, and Z. Bálint, "Lepidoptera from the Pantepui. Part XVI: A new species of Thaeides Johnson, Kruse & Kroenlein, 1997 (Lycaenidae: Theclinae: Eumaeini).," *ANNALES HISTORICO-NATURALES MUSEI NATIONALIS HUNGARICI*, vol. 116, pp. 275–295, 2024.
[46] Z. Czigány, J. Ženíšek, P. Souček, P. Ondračka, V. Buršíková, D. Holec, K. Balázsi, and P. Vašina, "Relation of orthorhombic and fcc transition metal carbide phases based on electron diffraction investigation," in *A MMT éves konferenciájának kivonatkönyve 2024*, 2024, pp. 26–28.
[47] Z. Czigány, H. R. Ben Zine, K. Balázsi, and C. Balázsi, "Cr-rich spinel phase formation in alumina dispersed 316L stainless steel processed by spark plasma sintering," in *CMCEE14 : 14th International Conference on Ceramic Materials and Components for Energy and Environmental Systems*, 2024, pp. 307–307.
[48] O. Czömpöly, F. Szabó, M. Fábián, T. Kolonits, Z. Fogarassy, D. Zámbó, M. Aertsens, and J. Osán, "Retention of Nickel and Cobalt in Boda Claystone Formation," *MINERALS*, vol. 14, no. 12, 2024.
[49] L. P. Csernai, T. Csorgo, I. Papp, K. Tamosiunas, M. Csete, A. Szenes, D. Vass, T. S. Biro, and N. Kroo, "Femtoscopy for the NAno-Plasmonic Laser Inertial Fusion Experiments (NAPLIFE) Project," *UNIVERSE*, vol. 10, no. 4, 2024.
[50] Z. Dallos, P. Golle-Leidreiter, Z. Molnár, F. Kristály, V. Kovács Kis, and I. Dódony, "Structural Changes of Bioapatite during Heat Treatment," *CRYSTAL GROWTH & DESIGN*, vol. 24, no. 5, pp. 2058–2063, 2024.
[51] D. Datz, G. Németh, L. Rátkai, Á. Pekker, and K. Kamarás, "Generalized Mie Theory for Full-Wave Numerical Calculations of Scattering Near-Field Optical Microscopy with Arbitrary Geometries," *PHYSICA STATUS SOLIDI - RAPID RESEARCH LETTERS*, vol. 18, no. 4, 2024.
[52] S. Deng and G. Ódor, "Chimera-like states in neural networks and power systems," *CHAOS*, vol. 34, no. 3, 2024.
[53] E. Dodony, I. Dódony, P. Pekker, and G. Sáfrán, "A step forward in understanding γ-nickel silicide," in *A MMT éves konferenciájának kivonatkönyve 2024*, 2024, pp. 32–33.
[54] E. Dodony, B. Rudd, I. Dodony, and G. Sáfrán, "EDIC intensity correction of electron diffraction," in *19th Joint Vacuum Conference*, 2024, pp. 33–33.
[55] E. Dodony and I. Dódony, "TEM study of copper silicides," in *Symposium on Materials Science 2023*, 2024, pp. 31–32.
[56] E. Dodony, I. Dódony, and G. Sáfrán, "EDIC intensity correction of electron diffraction," *MICRON*, vol. 183, 2024.
[57] T. Dózsa, V. Jurdana, S. B. Segota, J. Volk, J. Radó, A. Soumelidis, and P. Kovács, "Road Type Classification Using Time-Frequency Representations of Tire Sensor Signals," *IEEE ACCESS*, vol. 12, pp. 53361–53372, 2024.
[58] R. Drevet, P. Souček, P. Mareš, P. Ondračka, M. Dubau, T. Kolonits, Z. Czigány, K. Balázsi, and P. Vašina, "Aluminum tantalum oxide thin films deposited at low temperature by pulsed direct current reactive magnetron sputtering for dielectric applications," *VACUUM*, vol. 221, 2024.
[59] P. Dumas, F. Gustavo, M. Opprecht, G. Freychet, P. Gergaud, S. Kerdilès, S. Guillemin, J. L. Lábár, B. Pécz, F. Lefloch, and F. Nemouchi, "Enhancing superconductivity in CoSi2 films with laser annealing," *JOURNAL OF APPLIED PHYSICS*, vol. 136, no. 10, 2024.
[60] K. Edalati, A. Q. Ahmed, S. Akrami, K. Ameyama, V. Aptukov, R. N. Asfandiyarov, M. Ashida, V. Astanin, A. Bachmaier, V. Beloshenko, E. V. Bobruk, K. Bryła, J. M. Cabrera, A. P. Carvalho, N. Q. Chinh, I.-C. Choi, R. Chulist, J. M. Cubero-Sesin, G. Davdian, M. Demirtas, S. Divinski, K. Durst, J. Dvorak, P. Edalati, S. Emura, N. A. Enikeev, G. Faraji, R. B. Figueiredo, R. Floriano, M. Fouladvind, D. Fruchart, M. Fuji, H. Fujiwara, M. Gajdics, D. Gheorghe, Ł. Gondek, J. E. González-Hernández, A. Gornakova, T. Grosdidier, J. Gubicza, D. Gunderov, L. He, O. F. Higuera, S. Hirosawa, A. Hohenwarter, Z. Horita, J. Horky, Y. Huang, J. Huot, Y. Ikoma, T. Ishihara, Y. Ivanisenko, J. Jang, A. M. Jorge, M. Kawabata-Ota, M. Kawasaki, T. Khelfa, J. Kobayashi, L. Kommel, A. Korneva, P. Kral, N. Kudriashova, S. Kuramoto, T. G. Langdon, D.-H. Lee, V. I. Levitas, C. Li, H.-W. Li, Y. Li, Z. Li, H.-J. Lin, K.-D. Liss, Y. Liu, D. M. M. Cardona, K. Matsuda, A. Mazilkin, Y. Mine, H. Miyamoto, S.-C. Moon, M. Müller, J. A. Muñoz, M. Y. Murashkin, M. Naeem, M. Novelli, D. Olasz, R. Pippan, V. V. Popov, E. N. Popova, G. Purcek, P. de Rango, O. Renk, D. Retraint, Á. Révész, V. Roche, P. Rodriguez-Calvillo, L. Romero-Resendiz, X. Sauvage, T. Sawaguchi, H. Sena, H. Shahmir, X. Shi, V. Sklenicka, W. Skrotzki, N. Skryabina, F. Staab, B. Straumal, Z. Sun, M. Szczerba, Y. Takizawa, Y. Tang, R. Z. Valiev, A. Vozniak, A. Voznyak, B. Wang, J. T. Wang, G. Wilde, F. Zhang, M. Zhang, P. Zhang, J. Zhou, X. Zhu, and Y. T. Zhu, "Severe plastic deformation for producing Superfunctional ultrafine-grained and heterostructured materials: An interdisciplinary review," *JOURNAL OF ALLOYS AND COMPOUNDS*, vol. 1002, 2024.
[61] T. Elalaily, M. Berke, I. Lilja, A. Savin, G. Fülöp, L. Kupás, T. Kanne, J. Nygård, P. Makk, P. Hakonen, and S. Csonka, "Switching dynamics in Al/InAs nanowire-based gate-controlled superconducting switch," *NATURE COMMUNICATIONS*, vol. 15, no. 1, 2024.

[62] J. G. Fehérvári, Z. Balogh, T. N. Török, and A. Halbritter, “Noise tailoring, noise annealing, and external perturbation injection strategies in memristive Hopfield neural networks,” *APL machine learning.*, vol. 2, no. 1, 2024.
[63] K. Feng, S. Han, M. Feng, and A. Szolnoki, “An evolutionary game with reputation-based imitation-mutation dynamics,” *APPLIED MATHEMATICS AND COMPUTATION*, vol. 472, 2024.
[64] H. A. Flayyih, F. A. Abdulla, and A. Almansoori, “Studying the Hygrothermal Effects on the Impact Responses of Composite Materials Under Various Environmental Conditions,” *JOURNAL OF ENGINEERING AND SUSTAINABLE DEVELOPMENT*, vol. 28, no. 5, pp. 681–690, 2024.
[65] Z. Fogarassy, A. Wójcicka, I. Cora, A. S. Rácz, S. Grzanka, E. Dodony, P. Perlin, and M. A. Borysiewicz, “Structural investigation of the heat-treated Ti/Al/TiN/Au contact layer on n-GaN - role of TiN,” in *19th Joint Vacuum Conference*, 2024, pp. 75–75.
[66] Z. Fogarassy, A. Wójcicka, I. Cora, A. S. Rácz, S. Grzanka, E. Dodony, P. Perlin, and M. A. Borysiewicz, “Structural and electrical investigation of Al/Ti/TiN/Au based N-face n-GaN contact stack,” *MATERIALS SCIENCE IN SEMICONDUCTOR PROCESSING*, vol. 175, 2024.
[67] P. Fürjes, F. Simon, and J. Volk, “Gordon Moore öröksége,” *FIZIKAI SZEMLE*, vol. 74, no. 5, pp. 169–172, 2024.
[68] M. Furko, Z. E. Horváth, I. Tolnai, K. Balázsi, and C. Balázsi, “Investigation of Calcium Phosphate-Based Biopolymer Composite Scaffolds for Bone Tissue Engineering,” *INTERNATIONAL JOURNAL OF MOLECULAR SCIENCES*, vol. 25, no. 24, 2024.
[69] M. Furko, R. Detsch, Z. E. Horvath, K. Balazsi, A. R. Boccaccini, and C. Balazsi, “Amorphous, Carbonated Calcium Phosphate and Biopolymer-Composite-Coated Si3N4/MWCNTs as Potential Novel Implant Materials,” *NANOMATERIALS*, vol. 14, no. 3, 2024.
[70] A. Füredi, D. Bereczki, and P. Fürjes, “OT6.228 - Simple Microfluidic System for Point-of-Care Therapeutic Drug Monitoring of Anticancer Drugs,” in *Abstract book Eurosensors XXXVI*, 2024, pp. 185–186.
[71] M. Gajdics, I. Cora, and B. Pécz, “Crystallization of sputtered Ga2O3 thin films studied by in situ transmission electron microscopy,” in *A MMT éves konferenciájának kivonatkönyve 2024*, 2024, pp. 40–41.
[72] M. Gajdics, M. Serényi, G. Sáfrán, and B. Pécz, “GaON thin films prepared by reactive sputtering of a liquid Ga target,” in *19th Joint Vacuum Conference*, 2024, pp. 95–95.
[73] B. Galizia, P. Fiorenza, E. Schilirò, B. Pecz, Z. Foragassy, G. Greco, M. Saggio, S. Cascino, N. R. Lo, and F. Roccaforte, “Towards aluminum oxide/aluminum nitride insulating stacks on 4H–SiC by atomic layer deposition,” *MATERIALS SCIENCE IN SEMICONDUCTOR PROCESSING*, vol. 174, 2024.
[74] B. Galizia, P. Fiorenza, C. Bongiorno, B. Pécz, Z. Fogarassy, E. Schilirò, F. Giannazzo, F. Roccaforte, and R. L. Nigro, “Structural and electrical correlation in aluminum nitride thin films grown by plasma enhanced atomic layer deposition as interface insulating layers on silicon carbide (4H-SiC),” *MICROELECTRONIC ENGINEERING*, vol. 283, 2024.
[75] F. Giannazzo, S. E. Panasci, E. Schilirò, A. Koos, and B. Pécz, “Integration of graphene and MoS2 on silicon carbide: Materials science challenges and novel devices,” *MATERIALS SCIENCE IN SEMICONDUCTOR PROCESSING*, vol. 174, 2024.
[76] J. M. Gong, X. Liu, L. H. Yang, A. Sulyok, Z. Baji, V. Kis, K. Tőkési, R. G. Zeng, G. J. Fang, J. B. Gong, X. D. Xiao, B. Da, and Z. J. Ding, “Optical properties of hafnium-dioxide derived from reflection electron energy loss spectroscopy spectra,” *JOURNAL OF ALLOYS AND COMPOUNDS*, vol. 1005, 2024.
[77] K. Hajagos-Nagy, Z. Czigány, F. Misják, and G. Radnóczi, “Mapping of growth and structure of α-Mn(Cu) thin films,” in *A MMT éves konferenciájának kivonatkönyve 2024*, 2024, pp. 42–43.
[78] K. Hajagos-Nagy, Z. Czigány, F. Misják, and G. Radnóczi, “Non-equilibrium solubility of Cu in α-Mn structure – microstructure and growth of α-Mn(Cu) films,” in *19th Joint Vacuum Conference*, 2024, pp. 24–24.
[79] K. Hajagos-Nagy, G. Z. Radnóczi, and G. Radnóczi, “The effect of impurities on the structure and mechanical properties of CoCrCuFeNi alloy films,” in *19th Joint Vacuum Conference*, 2024, pp. 90–90.
[80] K. Hajagos-Nagy, G. Z. Radnóczi, Q. C. Nguyen, and G. Radnóczi, “Microstucture and mechanical properties of carbon containing high entropy alloy films,” in *CMCEE14 : 14th International Conference on Ceramic Materials and Components for Energy and Environmental Systems*, 2024, pp. 660–661.
[81] A. Halbritter, M. Csontos, T. N. Török, R. Kövecs, L. Pósa, P. Balázs, D. Molnár, N. J. Olalla, Z. Balogh, J. Leuthold, J. Volk, and G. Molnár, “Autonomous Neural Information Processing by a Dynamical Memristor Circuit,” in *Proceedings of the Neuronics Conference, 2024*, 2024.
[82] J. Han, X. Chen, and A. Szolnoki, “When selection pays: Structured public goods game with a generalized interaction mode,” *CHAOS*, vol. 34, no. 3, 2024.
[83] L. HARASZTOSI, R. KISS, and G. BATTISTIG, “Mikrokaloriméteres mérőrendszer referencia paramétereinek meghatározása,” *ENELKO - SZÁMOKT*, vol. XXV. Enelko – XXXIV. SzámOkt, pp. 5–11, 2024.
[84] B. Hartmann, G. Ódor, I. Papp, K. Benedek, S. Deng, and J. Kelling, “Dynamical heterogeneity and universality of power-grids,” *SUSTAINABLE ENERGY GRIDS & NETWORKS*, vol. 39, 2024.

[85] C. Hauert and G. Szabó, “Spontaneous symmetry breaking of cooperation between species,” *PNAS NEXUS*, vol. 3, no. 9, 2024.
[86] M. Hegedűs, V. Kis, and Z. Kovács, “A fogzománc szerkezeti és mechanikai tulajdonságai,” *FIZIKAI SZEMLE*, vol. 74, no. 2, pp. 56–61, 2024.
[87] M. Hegedűs, V. K Kis, N. Rózsa, and Z. Kovács, “A novel image processing procedure for the quantitative evaluation of dental enamel prism arrangement,” *MICROSCOPY RESEARCH AND TECHNIQUE*, vol. 87, no. 4, pp. 808–817, 2024.
[88] A. Horváth, A. Beck, M. Németh, G. Sáfrán, M. Roškarič, G. Žerjav, and A. Pintar, “Influence of 0.25% Indium Addition to Ni/CeO2 Catalysts for Dry Reforming of Methane,” *CATALYSTS*, vol. 14, no. 6, 2024.
[89] A. Horváth, M. Németh, A. Beck, G. Sáfrán, Z. Horváth, I. Rigó, Z. May, and T. Korányi, “Methane pyrolysis on NiMo/MgO catalysts: The significance of equimolar NiMo alloy resisting nanosize segregation during the reaction,” *APPLIED CATALYSIS A-GENERAL*, vol. 676, 2024.
[90] A. Horváth, M. Németh, A. Beck, G. Sáfrán, P. V. La, L. Liotta, G. Žerjav, M. Roškarič, and A. Pintar, “Longevity increase of an impregnated Ni/CeO2-Al2O3 dry reforming catalyst by indium,” *APPLIED CATALYSIS A-GENERAL*, vol. 669, 2024.
[91] Á. C. Horváth, Á. Mórocz, B. Csomai, Á. Szabó, Z. Balogh-Lantos, P. Fürjes, E. Z. Tóth, R. Fiáth, and Z. Fekete, “Silicon Optrode with a Micromirror-Tip Providing Tunable Beam Profile During Infrared Neuromodulation of the Rat Neocortex,” *ADVANCED MATERIALS TECHNOLOGIES*, vol. 9, no. 20, 2024.
[92] Z. Hózer, T. Hinoki, E. Slonszki, A. Pintér-Csordás, L. Illés, M. Király, Z. Kovács, M. Horváth, R. Farkas, E. Perez-Feró, T. Novotny, and P. Szabó, “Mechanical testing of SiCf/SiC cladding tubes for gas-cooled fast reactors,” in *CMCEE14 : 14th International Conference on Ceramic Materials and Components for Energy and Environmental Systems*, 2024, pp. 112–113.
[93] N. T. Ismaeel, Z. Lábadi, and M. Fried, “Investigation of Combinatorial TiO2-MoO3 Mixed Layers to Optimize the Electrochromic Properties,” in *XXXIX. Kandó Konferencia 2023*, 2024, pp. 394–406.
[94] H. Jankovics, É. Tóth, Z. Lábadi, P. Petrik, and F. Vonderviszt, “Development of flagellin protein-based heavy metal sensing layers for biosensors,” in *Víz- és szennyvízkezelés az iparban (VSZI ’23) : IX. Soós Ernő Nemzetközi Tudományos Konferencia = Water and wastewater treatment in the industry 2023 : IX. Soós Ernő International Scientific Conference*, 2024, pp. 36–36.
[95] P. Joó, Z. Szittner, B. Péter, I. Székács, and R. Horváth, “Sejtaktivációs folyamatok vizsgálatának lehetősége az egyesi sejt szintjén jelölésmentes optikai bioszenzorokkal.” 2024.
[96] Z. Juhász and T. Török, *Zenegenetika*. Győr: Magyar Kultúra Kiadó, 2024.
[97] Z. Juhász, “Revealing Footprints of Ancient Sources in Recent Eurasian and American Folk Music Cultures Using PCA of the Culture-Dependent Moment Vectors of Shared Melody Types,” *MUSIC & SCIENCE*, vol. 7, pp. 1–26, 2024.
[98] G. Kádár, “Emberi tudat és természettudomány,” *MAGYAR TUDOMÁNY*, vol. 185, no. 9, pp. 1178–1187, 2024.
[99] N. Kanyo, K. D. Kovacs, B. Peter, I. Szekacs, I. Rajmona, and R. Horvath, “Cancer cell adhesion and glycocalyx degradation measurement via FluidFM and single-cell optical biosensor.” 2024.
[100] M. H. Kaou, M. Furko, B. Z. H. Rachid, K. Balazsi, and C. Balazsi, “Morphological and structural evaluation of spark plasma sintered calcium silicate ceramics,” *INTERNATIONAL JOURNAL OF APPLIED CERAMIC TECHNOLOGY*, vol. 21, no. 4, pp. 2623–2635, 2024.
[101] M. Kedves, T. Pápai, G. Fülöp, K. Watanabe, T. Taniguchi, P. Makk, and S. Csonka, “Self-heating effects and switching dynamics in graphene multiterminal Josephson junctions,” *PHYSICAL REVIEW RESEARCH*, vol. 6, no. 3, 2024.
[102] S. Keszei, Y. Wang, H. Zhou, T. Ollár, É. Kováts, K. Frey, L. Tapasztó, S. Shen, and J. S. Pap, “Hydrogen evolution driven by heteroatoms of bidentate N-heterocyclic ligands in iron(ii) complexes,” *DALTON TRANSACTIONS*, vol. 53, no. 35, pp. 14817–14829, 2024.
[103] N. Q. Khánh, Z. E. Horváth, Z. Zolnai, P. Petrik, L. Pósa, and J. Volk, “Effect of process parameters on co-sputtered Al(1-x)ScxN layer’s properties: Morphology, crystal structure, strain, band gap, and piezoelectricity,” *MATERIALS SCIENCE IN SEMICONDUCTOR PROCESSING*, vol. 169, 2024.
[104] I. Khan, A. Ibrahim, S. Satake, K. A. Béres, M. Mohai, Z. Czigány, K. Sinkó, Z. Homonnay, E. Kuzmann, S. Krehula, M. Marciuš, L. Pavić, A. Šantić, and S. Kubuki, “57Fe-Mössbauer, XAFS and XPS studies of photo-Fenton active xMO•40Fe2O3•(60-x)SiO2 (M: Ni, Cu, Zn) nano-composite prepared by sol-gel method,” *CERAMICS INTERNATIONAL*, vol. 50, no. 24, pp. 55177–55189, 2024.
[105] I. Khan, T. Benko, A. Horvath, S. Shen, J. Su, Y. Wang, Z. E. Horvath, M. Nemeth, Z. Czigany, D. Zambo, and J. S. Pap, “Photoelectrochemical water splitting by hematite boosted in a heterojunction with B-doped g-C3N4 nanosheets and carbon nanotubes,” *JOURNAL OF MATERIALS CHEMISTRY A*, vol. 12, no. 30, pp. 19247–19258, 2024.

[106] B. Király, T. Varga, G. Szabó, and J. Garay, "Evolutionarily stable payoff matrix in hawk–dove games," *BMC ECOLOGY AND EVOLUTION*, vol. 24, no. 1, 2024.
[107] B. Király, "A tensor renormalization group analysis of an evolutionary game of competing Ising and Potts subgames," *PHYSICS LETTERS A*, vol. 502, 2024.
[108] R. G. Kiss, L. Harasztosi, I. A. Szabó, and G. Battistig, "Microhotplate as a Platform for Calorimetry," *PROCEEDINGS*, vol. 97, no. 1, 2024.
[109] V. K. Kis, Z. Kovács, and Z. Czigány, "Improved Method for Electron Powder Diffraction-Based Rietveld Analysis of Nanomaterials," *NANOMATERIALS*, vol. 14, no. 5, 2024.
[110] M. Kocsis, Z. Scherübl, G. Fülöp, P. Makk, and S. Csonka, "Strong nonlocal tuning of the current-phase relation of a quantum dot based Andreev molecule," *PHYSICAL REVIEW B*, vol. 109, no. 24, 2024.
[111] S. Kollarics, B. G. Márkus, R. Kucsera, G. Thiering, Á. Gali, G. Németh, K. Kamarás, L. Forró, and F. Simon, "Terahertz emission from diamond nitrogen-vacancy centers," *SCIENCE ADVANCES*, vol. 10, no. 22, 2024.
[112] B. Kovacs, K. Borbely, B. Peter, S. Kurunczi, and R. Horvath, "GCI in the Nanobiosensorics Laboratory: From Ionic Interactions to Small Molecule-Protein Binding." 2024.
[113] D. Kovács, A. Deák, and D. Zámbó, "Spatial distribution of photoexcited electrons and holes in Cu2O/Au multicomponent nanoparticles," in *Symposium on Materials Science 2023*, 2024, pp. 20–24.
[114] K. D. Kovács, B. Beres, N. Kanyo, B. Szabó, B. Peter, S. Bősze, I. Szekacs, and R. Horvath, "Single-cell classification based on label-free high-resolution optical data of cell adhesion kinetics." 2024.
[115] K. D. Kovács, B. Béres, N. Kanyo, B. Szabó, B. Peter, S. Bősze, I. Székács, and R. Horvath, "Single-cell classification based on label-free high-resolution optical data of cell adhesion kinetics." 2024.
[116] K. D. Kovács, Z. Szittner, B. Magyaródi, B. Péter, B. Szabó, A. Vörös, N. Kanyó, I. Székács, and R. Horvath, "Optical sensor reveals the hidden influence of cell dissociation on adhesion measurements," *SCIENTIFIC REPORTS*, vol. 14, no. 1, 2024.
[117] K. D. Kovacs, B. Beres, N. Kanyo, B. Szabó, B. Peter, S. Bősze, I. Szekacs, and R. Horvath, "Single-cell classification based on label-free high-resolution optical data of cell adhesion kinetics," *SCIENTIFIC REPORTS*, vol. 14, no. 1, 2024.
[118] Z. Kovács-Krausz, D. Nagy, A. Márffy, B. Karpiak, Z. Tajkov, L. Oroszlány, J. Koltai, P. Nemes-Incze, S. P. Dash, P. Makk, S. Csonka, and E. Tóvári, "Signature of pressure-induced topological phase transition in ZrTe5," *NPJ QUANTUM MATERIALS*, vol. 9, no. 1, 2024.
[119] L. Kovács, T. Ferenci, B. Gombos, A. Füredi, I. Rudas, G. Szakács, and D. A. Drexler, "Positive Impulsive Control of Tumor Therapy—A Cyber-Medical Approach," *IEEE TRANSACTIONS ON SYSTEMS MAN AND CYBERNETICS: SYSTEMS*, vol. 54, no. 1, pp. 597–608, 2024.
[120] N. Kroó, L. P. Csernai, I. Papp, M. A. Kedves, M. Aladi, A. Bonyár, M. Szalóki, K. Osvay, P. Varmazyar, and T. S. Biró, "Indication of p + 11B reaction in Laser Induced Nanofusion experiment," *SCIENTIFIC REPORTS*, vol. 14, no. 1, 2024.
[121] Z. Lábadi, N. T. Ismaeel, P. Petrik, and M. Fried, "Compositional Optimization of Sputtered SnO2/ZnO Films for High Coloration Efficiency," *INTERNATIONAL JOURNAL OF MOLECULAR SCIENCES*, vol. 25, no. 19, 2024.
[122] Z. Lábadi, D. Takács, Z. Zolnai, P. Petrik, and M. Fried, "Compositional Optimization of Sputtered WO3/MoO3 Films for High Coloration Efficiency," *MATERIALS*, vol. 17, no. 5, 2024.
[123] J. Lábár and B. Pécz, "Transzmissziós elektronmikroszkópia az MFA-ban," *FIZIKAI SZEMLE*, vol. 74, no. 3, pp. 84–87, 2024.
[124] J. L. Lábár, B. Pécz, Y. Yao, F. F. Daniel, K. Tereza, K. Tomas, Z. Zhen, L. Francois, G. Frédéric, L. Axel, and Z. Shi-Li, "TEM of PtSi, a known contact material in new (superconducting) role," in *A MMT éves konferenciájának kivonatkönyve 2024*, 2024, pp. 56–57.
[125] T. P. Lange, P. Vancsó, Z. Popov, M. Pósfai, P. Pekker, C. Szabó, I. J. Kovács, and M. Berkesi, "Fluidum-szilárd nanofelületek a Persány-hegység alatti litoszféra köpenyben," in *14. Kőzettani és Geokémiai Vándorgyűlés absztrakt kötet*, 2024, p. 68.
[126] K. László, O. Czakkel, A. Domján, G. Sáfrán, Z. Sebestyén, A. Bulátkó, S. Villar-Rodil, J. M. D. Tascón, and E. Geissler, "Water adsorbed in a commercial carbon: Role of nanostructure and surface chemistry," *CARBON*, vol. 229, 2024.
[127] K. Lázár, Z. Máthé, T. Németh, V. Kovács-Kis, S. Stichleutner, and I. Kovács, "Iron-Bearing Minerals in the Boda Claystone Formation: Correspondences with Stages of Evolution Revealed by Mössbauer Spectroscopy," *MINERALS*, vol. 14, no. 2, 2024.
[128] H.-W. Lee, C. Cleveland, and A. Szolnoki, "Suppressing defection by increasing temptation: The impact of smart cooperators on a social dilemma situation," *APPLIED MATHEMATICS AND COMPUTATION*, vol. 479, 2024.

[129] H.-W. Lee, C. Cleveland, and A. Szolnoki, “Supporting punishment via taxation in a structured population,” *CHAOS SOLITONS & FRACTALS*, vol. 178, 2024.
[130] B. Magyaródi, K. D. Kovács, B. Kovács, E. Farkas, I. Székács, F. Vonderviszt, and R. Horváth, “Applications of label-free biophysical methods in studying living cells.” 2024.
[131] Y. E. Maidebura, V. G. Mansurov, T. V. Malin, A. N. Smirnov, K. S. Zhuravlev, and B. Pecz, “Droplet epitaxy of 3D zinc-blende GaN islands on a 2D van der Waals SiN structure,” *APPLIED SURFACE SCIENCE*, vol. 655, 2024.
[132] P. Márton, B. Szolnoki, N. Nagy, A. Deák, D. Zámbó, G. S. Szabó, and Z. Hórvölgyi, “Wetting and swelling behaviour of N-acetylated thin chitosan coatings in aqueous media,” *HELIYON*, vol. 10, no. 1, 2024.
[133] P. Márton, A. Rácz, B. Szolnoki, J. Madarász, N. Nagy, B. Fodor, P. Basa, J. Rohonczy, and Z. Hórvölgyi, “Chitosan nanocoatings N-acylated with decanoic anhydride: Hydrophobic, hygroscopic and structural properties,” *CARBOHYDRATE POLYMERS*, vol. 343, 2024.
[134] P. Márton, L. Áder, D. M. Kemény, A. Rácz, D. Kovács, N. Nagy, G. S. Szabó, and Z. Hórvölgyi, “Chitosan–Surfactant Composite Nanocoatings on Glass and Zinc Surfaces Prepared from Aqueous Solutions,” *MOLECULES*, vol. 29, no. 13, 2024.
[135] L. McDonough, M. Campbell, P. Treble, C. Marjo, S. Frisia, J. Vongsvivut, A. Klein, V. Kovacs-Kis, and A. Baker, “Fire-induced shifts in stalagmite organic matter mapped using Synchrotron infrared microspectroscopy,” *ORGANIC GEOCHEMISTRY*, vol. 195, 2024.
[136] D. G. Merkel, M. A. Gracheva, G. Z. Radnóczi, G. Hegedűs, D. L. Nagy, Z. E. Horváth, and A. Lengyel, “Temperature induced A1 to B2 structural and magnetic transition in FeRh thin film,” *MATERIALS RESEARCH EXPRESS*, vol. 11, no. 8, 2024.
[137] D. G. Miklós, S. Józsa, Z. Kasztovszky, K. Gméling, I. Harsányi, Z. Kovács, F. Horváth, S. Elisabetta, and G. Szakmány, “A Hódmezővásárhely-Gorzsa lelőhely homokkő szerszámkőanyagának teljeskörű petrográfiai és geokémiai szempontú értékelése,” in *XIV. Kőkor Kerekasztal*, 2024, pp. 7–9.
[138] D. G. Miklós, S. Józsa, Z. Kasztovszky, I. Harsányi, K. Gméling, Z. Kovács, E. Starnini, F. Horváth, and G. Szakmány, “Provenance analysis of red sandstone ground stone tools from the tell site of Hódmezővásárhely-Gorzsa (SE Hungary),” *ARCHAEOLOGICAL AND ANTHROPOLOGICAL SCIENCES*, vol. 16, no. 7, 2024.
[139] D. Mukherjee, S. Burger, T. Siefke, J. Gour, B. Bodermann, and P. Petrik, “Modeling of dimensions and sensing properties of gold gratings by spectroscopic ellipsometry and finite element method,” *EPJ WEB OF CONFERENCES*, vol. 309, 2024.
[140] K. Mukhtarova, M. Kawasaki, Z. Dankházi, M. Windisch, G. Z. Radnóczi, W. Serafimowicz, and J. Gubicza, “Nanostructuring of an additively manufactured CoCrFeNi multi-principal element alloy using severe plastic deformation: Comparison of two materials processed by different laser scan speeds,” *INTERMETALLICS*, vol. 170, 2024.
[141] N. Nagy, “Determination of solid-liquid adhesion work on flat surfaces in a direct and absolute manner,” *SCIENTIFIC REPORTS*, vol. 14, no. 1, 2024.
[142] N. Nagy, “Eljárás és berendezés folyadék-szilárd adhéziós munka meghatározására,” 2024.
[143] P. Nagy, L. Péter, T. Kolonits, A. Nagy, and J. Gubicza, “Combinatorial Design of an Electroplated Multi-Principal Element Alloy: A Case Study in the Co-Fe-Ni-Zn Alloy System,” *METALS*, vol. 14, no. 6, 2024.
[144] P. Nagy, M. Wątroba, Z. Hegedűs, J. Michler, L. Pethö, J. Schwiedrzik, Z. Czigány, and J. Gubicza, “Mapping the microstructure and the mechanical performance of a combinatorial Co–Cr–Cu–Fe–Ni–Zn high-entropy alloy thin film processed by magnetron sputtering technique,” *JOURNAL OF MATERIALS RESEARCH AND TECHNOLOGY*, vol. 31, pp. 47–61, 2024.
[145] A. Nyáry, Z. Balogh, M. Vigh, B. Sánta, L. Pósa, and A. Halbritter, “Voltage-time dilemma and stochastic threshold-voltage variation in pure-silver atomic switches,” *PHYSICAL REVIEW APPLIED*, vol. 21, no. 1, 2024.
[146] G. Ódor, I. Papp, K. Benedek, and B. Hartmann, “Improving power-grid systems via topological changes or how self-organized criticality can help power grids,” *PHYSICAL REVIEW RESEARCH*, vol. 6, no. 1, 2024.
[147] G. Ódor, S. Deng, and J. Kelling, “Frustrated Synchronization of the Kuramoto Model on Complex Networks,” *ENTROPY*, vol. 26, no. 12, 2024.
[148] D. Olasz, V. Kis, I. Cora, M. Németh, and G. Sáfrán, “High-Throughput Micro-Combinatorial TEM Phase Mapping of the DC Magnetron Sputtered YxTi1−xOy Thin Layer System,” *NANOMATERIALS*, vol. 14, no. 11, 2024.
[149] D. Olasz, G. Sáfrán, N. Szász, T. Kolonits, and N. Q. Chinh, “Microstructure and mechanical properties of AlCu thin films in a wide range of composition,” *BIO WEB OF CONFERENCES*, vol. 129, 2024.
[150] A. Pálinkás, K. Márity, K. Kandrai, Z. Tajkov, M. Gmitra, P. Vancsó, L. Tapasztó, and P. Nemes-Incze, “Identification of graphite with perfect rhombohedral stacking by electronic Raman scattering,” *CARBON*, vol. 230, 2024.

[151] S. E. Panasci, I. Deretzis, E. Schilirò, M. A. La, F. Roccaforte, A. Koos, M. Nemeth, B. Pécz, M. Cannas, S. Agnello, and F. Giannazzo, "Interface Properties of MoS2 van der Waals Heterojunctions with GaN," *NANOMATERIALS*, vol. 14, no. 2, 2024.
[152] S. E. PANASCI, E. Schilirò, A. Koos, S. Agnello, B. Pécz, F. Roccaforte, and F. Giannazzo, "Integration strategies and nanoscale electrical characterization of MoS2 on wide bandgap semiconductors." 2024.
[153] S. E. Panasci, E. Schilirò, M. Cannas, S. Agnello, A. Koos, M. Nemeth, B. Pécz, F. Roccaforte, and F. Giannazzo, "Vertical Current Transport in Monolayer MoS2 Heterojunctions with 4H-SiC Fabricated by Sulfurization of Ultra-Thin MoOx Films," in *Solid State Phenomena*, vol. 362, 2024, pp. 7–12.
[154] S. E. Panasci, E. Schilirò, A. Koos, F. Roccaforte, M. Cannas, S. Agnello, B. Pécz, and F. Giannazzo, "Tailoring MoS2 domains size, doping, and light emission by the sulfurization temperature of ultra-thin MoOx films on sapphire," *APPLIED PHYSICS LETTERS*, vol. 124, no. 24, 2024.
[155] K. Pankász and C. Dücső, "PT5.174 - Chip-set for Chemoresistive Gas Sensors," in *Abstract book Eurosensors XXXVI*, 2024, pp. 385–386.
[156] E. Pásztor, V. Szilágyi, D. Gerber, A. Gémes, T. Hajdu, G. Hajduné Darabos, B. Heltai, A. Horváth, L. Illés, I. Károly, Z. Kovács, G. Kulcsár, I. Major, M. R. Merkl, J. Sándorné Kovács, E. Sipos, P. Sümegi, G. Szakmány, A. Szécsényi-Nagy, Z. Szoldán, K. T. Biró, and V. Kiss, "Archeometriai vizsgálatok a Sükösd–Árpás-dűlői bronzkori temetőből – előzetes eredmények [Archaeometric investigations of the Bronze Age cemetery at Sükösd–Árpás-dűlő – preliminary results]," *ARCHEOMETRIAI MŰHELY*, vol. 21, no. 4, pp. 445–482, 2024.
[157] L. Patkó, N. Liptai, L. E. Aradi, K. Török, Z. Kovács, Á. Kővágó, S. Gergely, I. J. Kovács, C. Szabó, and M. Berkesi, "Fossil metasomatized and newly-accreted fertile lithospheric mantle volumes beneath the Bakony-Balaton Highland Volcanic Field (central Carpathian-Pannonian region)," *LITHOS*, vol. 482–483, 2024.
[158] B. Péter, I. Szekacs, and R. Horvath, "Label-free biomolecular and cellular methods in small molecule epigallocatechin-gallate research," *HELIYON*, vol. 10, no. 3, 2024.
[159] L. Péter, S. Kugler, T. Kolonits, and A. Nagy, "Composition Profiles at the Metal Substrate–Deposit Interface Produced in Laser-Assisted Additive Manufacturing Processes," *MATERIALS*, vol. 17, no. 13, 2024.
[160] P. Petrik, D. Mukherjee, K. Kertész, Z. Zolnai, Z. Kovács, A. Deák, A. Pálinkás, Z. Osváth, D. Olasz, A. Romanenko, M. Fried, and G. Sáfrán, "PT7.123 - The power of using combinatorial materials science and finite element methods in the optimization of sensing by gold nanostructures," in *Abstract book Eurosensors XXXVI*, 2024, pp. 477–478.
[161] P. Petrik, M. Fried, and T. Lohner, "Optikai módszerek az MFA-ban," *FIZIKAI SZEMLE*, vol. 74, no. 3, pp. 80–83, 2024.
[162] É. K. Pfeifer, L. Trif, P. Petrik, J. Mink, I. G. Gyurika, and J. Telegdi, "Influence of gamma radiation on self-assembled molecular layers developed on different metals," *SURFACE AND COATINGS TECHNOLOGY*, vol. 489, 2024.
[163] G. Piszter, K. Kertész, G. Nagy, D. Kovács, D. Zámbó, Z. Baji, J. S. Pap, and L. P. Biró, "Photocatalytic bioheteronanostructures by integrating multicomponent Cu2O–Au nanoparticles into ZnO-coated butterfly wings colored by photonic nanoarchitectures," *JOURNAL OF MATERIALS SCIENCE*, vol. 59, no. 38, pp. 17877–17896, 2024.
[164] G. Piszter, K. Kertész, D. Kovács, D. Zámbó, A. Cadena, K. Kamarás, and L. P. Biró, "Integrating Cu2O Colloidal Mie Resonators in Structurally Colored Butterfly Wings for Bio-Nanohybrid Photonic Applications," *MATERIALS*, vol. 17, no. 18, 2024.
[165] A. S. Racz, "Atomistic insights into salicylic acid treatment on human keratinized skin by XPS combined with argon gas cluster sputtering: A pilot study," *SURFACES AND INTERFACES*, vol. 55, 2024.
[166] A. S. Racz and M. Menyhard, "XPS depth profiling of nano-layers by a novel trial-and-error evaluation procedure," *SCIENTIFIC REPORTS*, vol. 14, no. 1, 2024.
[167] G. Z. Radnóczi, "Electron diffraction simply explained," in *A MMT éves konferenciájának kivonatkönyve 2024*, 2024, pp. 77–78.
[168] I. Rajmon, A. Balogh, K. D. Kovács, I. Székács, and R. Horváth, "A fluidikai erőmikroszkóp főbb alkalmazásai." 2024.
[169] J. B. Renkó, A. Romanenko, T. Bíró, P. J. Szabó, P. Petrik, and A. Bonyár, "Investigating the kinetics of layer development during the color etching of low-carbon steel with in-situ spectroscopic ellipsometry," *HELIYON*, vol. 10, no. 3, 2024.
[170] F. Roccaforte, M. Vivona, S. E. Panasci, G. Greco, P. Fiorenza, A. Sulyok, A. Koos, B. Pecz, and F. Giannazzo, "Schottky contacts on sulfurized silicon carbide (4H-SiC) surface," *APPLIED PHYSICS LETTERS*, vol. 124, no. 10, 2024.
[171] F. Roccaforte, M. Vivona, S. E. Panasci, G. Greco, P. Fiorenza, A. Sulyok, A. Koos, B. Pécz, and F. Giannazzo, "Effects of Sulfurization on the Properties of 4H-SiC Schottky Contacts." pp. 97–99, 2024.
[172] S. Sáfrán, S. C. Collins, H. Takano, Z. Faltynek Fric, B. Tóth, G. Katona, G. Piszter, and Z. Bálint, "Descriptions of four new species of Capys from East and West Africa with notes on adult morphology and

biogeography (Lepidoptera: Lycaenidae: Theclinae)," *ANNALES MUSEI HISTORICO-NATURALIS HUNGARICI*, vol. 116, pp. 131–165, 2024.
[173] I. Sallai, Z. Szittner, B. Béres, Á. Kiss, B. Plegányi, I. Székács, and R. Horvath, "Development of methods compatible with label-free optical biosensors for immunidagnostics," in *12. Környezetkémiai Szimpózium*, 2024, pp. 23–23.
[174] I. Sallai, "Resonant Waveguide Grating Biosensors Based on Label-free Optical Principle," *PERIODICA POLYTECHNICA-ELECTRICAL ENGINEERING AND COMPUTER SCIENCE*, vol. 68, no. 1, pp. 107–114, 2024.
[175] S. W. Schmid, L. Posa, T. N. Torok, B. Santa, Z. Pollner, G. Molnar, Y. Horst, J. Volk, J. Leuthold, A. Halbritter, and M. Csontos, "Picosecond Femtojoule Resistive Switching in Nanoscale VO2 Memristors," *ACS NANO*, vol. 18, no. 33, pp. 21966–21974, 2024.
[176] H. P. Schwarcz, N. Nassif, and V. Kovacs Kis, "Curved mineral platelets in bone," *ACTA BIOMATERIALIA*, vol. 183, pp. 201–209, 2024.
[177] M. Serényi, D. Olasz, and G. Sáfrán, "On the challenges in reactive HiPIMS co-sputtering of Y and Ti for oxide layers," in *19th Joint Vacuum Conference*, 2024, pp. 76–76.
[178] L. S. Shankar, S. K. Samaniego Andrade, K. László, D. Zalka, P. B. Nagy, M. Szabados, Z. Pászti, K. Balázsi, Z. Czigány, L. Illés, and R. Kun, "A fresh perspective to synthesizing and designing carbon/sulfur composite cathodes using supercritical CO2 technology for advanced Li-S battery cathodes," *JOURNAL OF ALLOYS AND COMPOUNDS*, vol. 1008, 2024.
[179] T. Sopcak, L. Medvecky, T. Csanadi, M. Giretova, R. Stulajterova, R. Sedlak, F. Kromka, M. Streckova, M. Vojtko, and K. Balazsi, "Reinforcement of hydroxyapatite bone cement via thin glycerol-citrate polyester infiltration: Microstructural, mechanical and in-vitro evaluation," *SURFACES AND INTERFACES*, vol. 52, 2024.
[180] T. Stasiak, S. Debnárová, S. Lin, N. Koutná, Z. Czigány, K. Balázsi, V. Buršíková, P. Vašina, and P. Souček, "Synthesis and characterization of ceramic high entropy carbide thin films from the Cr-Hf-Mo-Ta-W refractory metal system," *SURFACE AND COATINGS TECHNOLOGY*, vol. 485, 2024.
[181] P. Süle, "Resolving heterogeneous particle mobility in deeply quenched liquid iron: an ultra-fast assembly-free two-step nucleation mechanism," *PHYSICAL CHEMISTRY CHEMICAL PHYSICS*, vol. 26, no. 40, pp. 26091–26108, 2024.
[182] Z. Szabó, K. Pankász, J. Bozorádi, O. Hakkel, S. Bella, B. Fabinyi, S. Meucci, and P. Fürjes, "Microfluidic Cuvette for Near-Infrared Spectroscopy," *PROCEEDINGS*, vol. 97, no. 1, 2024.
[183] K. Szakolczai, *EK MFA Yearbook 2023*. Budapest: HUN-REN EK MFA, 2024.
[184] Á. Szamosvölgyi, Á. Pitó, A. Efremova, K. Baán, B. Kutus, M. Suresh, A. Sápi, I. Szenti, J. Kiss, T. Kolonits, Z. Fogarassy, B. Pécz, Á. Kukovecz, and Z. Kónya, "Optimized Pt–Co Alloy Nanoparticles for Reverse Water–Gas Shift Activation of CO2," *ACS APPLIED NANO MATERIALS*, vol. 7, no. 9, pp. 9968–9977, 2024.
[185] I. Szekacs, E. Farkas, B. Kovacs, E. Takacs, M. Olah, A. Szekacs, and R. Horvath, "Discovery of cell adhesion-modifying effects of glyphosate on living cells by label-free optical biosensing." 2024.
[186] Z. Szekanecz, A. Besnyi, P. Kónya, J. Füri, E. Király, É. Bertalan, G. Falus, B. Udvardi, V. Kovács-Kis, L. Andrássy, G. Maros, T. Fancsik, Z. Pethő, I. Gomez, Á. Horváth, K. Gulyás, B. Juhász, K. Hodosi, Z. Sándor, H. P. Bhattoa, and I. J. Kovács, "Bones or Stones: How Can We Apply Geophysical Techniques in Bone Research?," *INTERNATIONAL JOURNAL OF MOLECULAR SCIENCES*, vol. 25, no. 19, 2024.
[187] A. Szekeres, S. Alexandrova, M. Anastasescu, H. Stroescu, M. Gartner, and P. Petrik, "Optical and Morphological Characterization of Nanoscale Oxides Grown in Low-Energy H+-Implanted c-Silicon," *MICRO*, vol. 4, no. 3, pp. 426–441, 2024.
[188] E. Szilágyi, M. K. Pal, E. Kótai, Z. Zolnai, and I. Bányász, "Fluence evolution of defects in α-SiO2 determined by ionoluminescence," *NUCLEAR INSTRUMENTS & METHODS IN PHYSICS RESEARCH SECTION B-BEAM INTERACTIONS WITH MATERIALS AND ATOMS*, vol. 555, 2024.
[189] A. Szolnoki and X. Chen, "When faster rotation is harmful: The competition of alliances with inner blocking mechanism," *PHYSICAL REVIEW RESEARCH*, vol. 6, no. 2, 2024.
[190] Z. Szomor, N. Gyimah, P. Fürjes, and T. Pardy, "3D Finite Element Modelling of Mixing Phenomena in Droplet-based Microfluidic Systems," in *Proceedings of the Biennial Baltic Electronics Conference, BEC*, 2024.
[191] Z. Szomor, N. Gyimah, T. Pardy, and P. Fürjes, "3D Finite Element Modelling of Mixing Phenomena in Droplet-based Microfluidic Systems." 2024.
[192] Z. Szomor, T. E. L., and P. Fürjes, "3D Modelling of droplet formation in two-phase microfluidics for single-cell manipulation." 2024.
[193] Z. Szomor, L. Bató, Z. Baji, J. M. Bozorádi, K. Balázsi, E. Dodony, Z. Kovács, A. Sulyok, and P. Fürjes, "Characterisation of Titanium-Oxide layers for low-power pH Sensors." 2024.
[194] Z. Szomor, L. Bató, S. Stágl, O. Hakkel, A. Sulyok, C. Dücső, Z. Baji, and P. Fürjes, "Non-Stoichiometric Titanium-Oxide Gate Electrodes for EGFET Based pH Sensors," *PROCEEDINGS*, vol. 97, no. 1, 2024.

[195] N. Taha Ismaeel, Z. Lábadi, P. Petrik, and M. Fried, "Combinatorial Preparation and Electrochromic Investigation of Metal Oxide Mixtures," in *Symposium on Materials Science 2023*, 2024, pp. 15–19.
[196] B. Tegze, G. Tolnai, E. Albert, D. Hessz, M. Kubinyi, J. Madarász, Z. May, D. Olasz, G. Sáfrán, and Z. Hórvölgyi, "Optimizing the composition of LaF3:Yb,Tm upconverting nanoparticles synthesised by the co-precipitation method to improve the emission intensity," *NANOSCALE*, vol. 16, no. 46, pp. 21554–21560, 2024.
[197] T. N. Török, R. Kövecs, L. Pósa, F. Braun, G. Molnár, N. Q. Khánh, A. Halbritter, and J. Volk, "Applying Neurodynamic Behavior of Mott Memristors for Auditory Sensing," in *Proceedings of the Neuronics Conference, 2024*, 2024.
[198] T. N. Török, L. Pósa, D. Molnár, J. G. Fehérvári, R. Kövecs, Z. Balogh, J. Volk, and A. Halbritter, "Információfeldolgozás nanoskálájú memrisztív eszközökkel," *SCIENTIA ET SECURITAS*, vol. 4, no. 4, pp. 312–320, 2024.
[199] D. Ugi, K. Zoller, K. Lukács, Z. Fogarassy, I. Groma, S. Kalácska, K. Schulz, and P. D. Ispánovity, "Irreversible evolution of dislocation pile-ups during cyclic microcantilever bending," *MATERIALS AND DESIGN*, vol. 238, 2024.
[200] A. Váczi-Lovász, Z. Kovács, and G. B. Kiss, "Genesis of Gabbroic Hosted Copper Mineralisations in the Albanian Mirdita Zone (Kçira, Thirra)," *MINERALS*, vol. 14, no. 2, 2024.
[201] D. Vadas, K. Bocz, T. Igricz, J. Volk, S. Bordács, L. Madarász, and G. Marosi, "Novel manufacturing method for highly flexible poly(lactic acid) foams and ferroelectrets," *ADVANCED INDUSTRIAL AND ENGINEERING POLYMER RESEARCH*, vol. 7, no. 2, pp. 215–225, 2024.
[202] F. Vajda, Á. Szepesi, Z. Erdei, E. Szabó, G. Várady, D. Kiss, L. Héja, K. Német, G. Szakács, and A. Füredi, "Mesenchymal Stem Cells Increase Drug Tolerance of A431 Cells Only in 3D Spheroids, Not in 2D Co-Cultures," *INTERNATIONAL JOURNAL OF MOLECULAR SCIENCES*, vol. 25, no. 8, 2024.
[203] M. Váradi, S. J. Keszei, Á. Gömöry, M. Kovács, T. Kégl, L. Fodor, and R. Skoda-Földes, "Investigation of Host–Guest Interactions in 2-Ureido-4-ferrocenylpyrimidine Derivatives," *INTERNATIONAL JOURNAL OF MOLECULAR SCIENCES*, vol. 25, no. 24, 2024.
[204] G. Vértesy, M. Rabung, A. Gasparics, I. Uytdenhouwen, J. Griffin, D. Algernon, S. Grönroos, and J. Rinta-Aho, "Evaluation of the Embrittlement in Reactor Pressure-Vessel Steels Using a Hybrid Nondestructive Electromagnetic Testing and Evaluation Approach," *MATERIALS*, vol. 17, no. 5, 2024.
[205] L. Víg, A. Zátonyi, B. Csernyus, Á. C. Horváth, M. Bojtár, P. Kele, M. Madarász, B. Rózsa, P. Fürjes, P. Hermann, O. Hakkel, L. Péter, and Z. Fekete, "Optically Controlled Drug Delivery Through Microscale Brain–Machine Interfaces Using Integrated Upconverting Nanoparticles," *SENSORS*, vol. 24, no. 24, 2024.
[206] Z. Vizvari, N. Gyorfi, G. Maczko, R. Varga, R. Jakabfi-Csepregi, Z. Sari, A. Furedi, E. Bajtai, F. Vajda, V. Tadic, P. Odry, Z. Karadi, and A. Toth, "Reproducibility analysis of bioimpedance-based self-developed live cell assays," *SCIENTIFIC REPORTS*, vol. 14, no. 1, 2024.
[207] J. Volk, J. M. Bozorádi, F. Braun, A. Nagy, L. Illés, and J. Radó, "OT4.209 - Ultra-Sensitive Force Gauge Accessory for Microscope Micromanipulators," in *Abstract book Eurosensors XXXVI*, 2024, pp. 81–82.
[208] J. Volk, "Rendezett cink-oxid nanoszálak," Energiatudományi Kutatóközpont, 2024.
[209] C. Wang, M. Perc, and A. Szolnoki, "Evolutionary dynamics of any multiplayer game on regular graphs," *NATURE COMMUNICATIONS*, vol. 15, no. 1, 2024.
[210] C. Wang and A. Szolnoki, "Competition between self- and other-regarding preferences in resolving social dilemmas," *NEW JOURNAL OF PHYSICS*, vol. 26, no. 5, 2024.
[211] Q. Wang, X. Chen, N. He, and A. Szolnoki, "Evolutionary Dynamics of Population Games With an Aspiration-Based Learning Rule," *IEEE TRANSACTIONS ON NEURAL NETWORKS AND LEARNING SYSTEMS*, vol. in press, p. in press, 2024.
[212] A. Wójcicka, M. Borysiewicz, and Z. Fogarassy, "Method of producing transparent thin-film conductive coatings," 2024.
[213] A. Wójcicka, M. Borysiewicz, and Z. Fogarassy, "Method of deposition of transparent, low-resistance, thin conductive layers," 2024.
[214] A. Wójcicka, Z. Fogarassy, T. Kravchuk, C. Saguy, E. Kamińska, P. Perlin, S. Grzanka, and M. A. Borysiewicz, "Transparent (Ni,Au)/ZnO:Al-Based Ohmic Contacts to p-Type GaN as an Insight into the Role of Ni and Au in Standard p-Type GaN Contacts," *ACS APPLIED MATERIALS & INTERFACES*, vol. 16, no. 44, pp. 61284–61292, 2024.
[215] X. Xiaojin, Z. Ziyan, F. Minyu, and S. Attila, "Coevolution of relationship and interaction in cooperative dynamical multiplex networks," *CHAOS*, vol. 34, no. 2, 2024.
[216] M. Xu, X. Chen, and A. Szolnoki, "Nash Equilibrium in Macro-Task Crowdsourcing Systems With Collective-Effort-Dependent Rewarding," *IEEE TRANSACTIONS ON NETWORK SCIENCE AND ENGINEERING*, vol. 11, no. 3, pp. 2689–2702, 2024.

[217] Y. Yao, D. F. Fernandes, T. Košutová, T. Kubart, Z. Zhang, F. Lefloch, F. Gustavo, A. Leblanc, J. L. Lábár, B. Pécz, and S.-L. Zhang, "Self-aligned formation of superconducting sub-5 nm PtSi films," *APL Quantum*, vol. 1, no. 2, 2024.
[218] D. Zámbó, "Félvezető nanorészecskékkel a modern optikába," *INNOTÉKA: TUDOMÁNY INNOVÁCIÓ ZÖLDKÖRNYEZET*, vol. XIV, no. 2024. április, pp. 16–17, 2024.
[219] D. Zámbó, D. Kovács, and A. Deák, "Optical and Structural Properties of Cuprous Oxide Shell Coated Gold Nanoprisms," *PARTICLE & PARTICLE SYSTEMS CHARACTERIZATION*, vol. 41, no. 12, 2024.
[220] D. Zámbó, D. Kovács, G. Z. Radnóczi, Z. E. Horváth, A. Sulyok, I. Tolnai, and A. Deák, "Structural Control Enables Catalytic and Electrocatalytic Activity of Porous Tetrametallic Nanorods," *SMALL*, vol. 20, no. 31, 2024.
[221] T. Zeffer, T. N. Török, L. Pósa, F. Braun, A. Halbritter, and J. Volk, "PT2.210 - Towards fully hardware-based neuromorphic encoding for efficient vibration signal recognition," in *Abstract book Eurosensors XXXVI*, 2024, pp. 265–266.
[222] J. Ženíšek, P. Souček, P. Ondračka, Z. Czigány, V. Buršíková, D. Holec, K. Balázsi, and P. Vašina, "Effect of Nb incorporation in Mo 2 BC coatings on structural and mechanical properties — Ab initio modelling and experiment," *ACTA MATERIALIA*, vol. 268, 2024.
[223] B. N. Zereay, S. Kálvin, G. Juhász, C. Major, P. Petrik, Z. G. Horváth, and M. Fried, "Optical Calibration of a Multi-Color Ellipsometric Mapping Tool Fabricated Using Cheap Parts," *PHOTONICS*, vol. 11, no. 11, 2024.
[224] Z. Zolnai, Z. Kis, N. Q. Khánh, Z. Kovács, G. Battistig, L. Szentmiklósi, and J. Volk, "PT3.299 - Effective neutron absorption and conversion with thin 10B4C layers," in *Abstract book Eurosensors XXXVI*, 2024, pp. 287–288.
[225] Z. Zolnai, M. K. Pal, E. Kótai, and E. Szilágyi, "Helium ion beam-induced luminescence from defect centers in Al2O3," in *Symposium on Materials Science 2023*, 2024, pp. 25–26.